THE INTERACTION OF XENON DIFLUORIDE WITH Si(100)

by

JUDSON ROBERT HOLT

B.A. CHEMICAL PHYSICS
RICE UNIVERSITY
(1996)

SUBMITTED TO THE DEPARTMENT OF CHEMISTRY
IN PARTIAL FULFILLMENT OF THE REQUIREMENTS
FOR THE DEGREE OF

DOCTOR OF PHILOSOPHY

at the

MASSACHUSETTS INSTITUTE OF TECHNOLOGY

MAY 2002

Signature of Author _____

Department of Chemistry
24 May 2002

Certified by _____

Sylvia T. Ceyer
Professor of Chemistry
Thesis Supervisor

Accepted by _____

Robert Field
Chairman, Departmental Committee on Graduate Students

This doctoral thesis has been examined by a Committee of the Department of Chemistry as follows:

Professor Keith A. Nelson _____

Chairman

Professor Sylvia T. Ceyer _____

Thesis Supervisor

Professor Robert J. Silbey _____   _____

The Interaction of Xenon Difluoride with Si(100)

by

Judson Robert Holt

Submitted to the Department of Chemistry
on 24 May 2002
in Partial Fulfillment of the Requirements
for the Degree of
Doctor of Philosophy in Chemistry

ABSTRACT

The interaction of low energy XeF_2 with Si(100)2×1 has been investigated by studying both the surface-bound and gas-phase products of the reaction.

Helium atom diffraction, beam-surface scattering and thermal desorption measurements are the major techniques used to probe the surface-bound products of the reaction. It is found that XeF_2 dissociatively chemisorbs with high probability solely on the Si dangling bonds up to a coverage of about one monolayer (ML). Molecular fluorine has previously been observed to react similarly, saturating the dangling bonds at 1 ML coverage. The thermal desorption products and kinetics from the fluorinated layer produced by XeF_2 exposure are identical to that produced by F_2 exposure. The interactions of XeF_2 and F_2 are also strikingly similar with respect to the order of the Si surface up to about 1 ML coverage. The surface order is monitored by He diffraction detected by a line-of-sight, differentially pumped mass spectrometer. In both systems, the diffracted He beams exhibit a sharp decrease in intensity due to the disorder produced by the fluorination of random surface unit cells as the coverage increases from zero to about 0.3 ML. The intensity then increases until the fluorine overlayer has fully recovered its 2×1 periodicity at about 1 ML. This recovery corresponds to the decoration of each Si dangling bond with a fluorine atom. A critical observation of this study is that despite the large exothermicity of the dissociative chemisorption of XeF_2 or F_2, which is approximately 230-250 kcal/mol, the order of the surface is not destroyed in either system. After saturation of the dangling bonds, F_2 ceases to react with the surface while XeF_2 continues to deposit fluorine by reacting with the Si-Si σ dimer bonds and the Si-Si lattice bonds. The order is destroyed as a result of the continued fluorine deposition and ultimately etching occurs by the formation of volatile SiF_4.

The gas-phase products of the reaction are studied using the time-of-flight (TOF) technique. The translational excitation of XeF from single atom abstraction is observed to be only a small fraction of the reaction exothermicity, implying that the abstraction reaction can be described by a potential energy surface with a transition state in the entrance channel. Furthermore, the angular distribution of the XeF becomes peaked towards normal on a fluorinated surface, suggesting that the combined influence of molecular steering and steric hindrance serve to align the XeF_2 into a more favorable perpendicular orientation prior to the

reaction. The observation of reactively scattered F atoms indicates that some of the XeF from atom abstraction dissociates to produce a F atom and a Xe atom. This dissociation is modeled using the conservation of energy and momentum to predict the trajectory of the scattered F and Xe atoms from the gas-phase dissociation of XeF in a forward convolution calculation that takes into account the initial velocity, scattering angle, orientation and energy distributions of the XeF prior to dissociation. The calculation successfully predicts the observed F and Xe atom TOF distributions at all angles and coverages. The results of the calculation suggest that the dissociation occurs primarily through excitation into a rovibrational state in the ground electronic state that is above the dissociation threshold, and that the orientation of the XeF in the transition state is such that the F atom is pointed into the vacuum. The calculation also suggests that atom abstraction occurs primarily at the dangling bond reactive sites, even at high coverage. The two-atom adsorption signal is identified by that part of the observed Xe TOF distribution that is not predicted to be due to Xe from XeF dissociation. The angular distribution of one of the components of Xe from two-atom adsorption suggests that molecular steering influences the orientation of the XeF during the reaction. Moreover, the low translational energy of the Xe from two-atom adsorption is likely due to the extremely weak XeF bond and the large attractive potential between the fluorine atom end of the XeF and the Si dangling bond.

Thesis Supervisor: Sylvia T. Ceyer
Title: J.C. Sheehan Professor of Chemistry

To My Parents

Acknowledgements

It is nearly impossible to sum up, in a mere two pages, the contributions that so many people have made to my development as a scientist and as a person. The people who I have interacted with to bring me to this point deserve far more credit than I can give. To each of you, I say thank you.

My advisor, Sylvia Ceyer, has without a doubt been the single greatest influence on my development as a scientist in general, and the contents of this thesis in particular. I will forever remember her unflinching dedication to the ideals of science, a dedication that has been an example to all who have known her. She has held me, and indeed everyone who has worked with her, to exacting standards of excellence. It was she who insisted that we do the best experiment that we could, and that experience has taught me the meaning of the phrase, "The devil is in the details." It has been a privilege to work with her.

During my years as a graduate student I had the opportunity to work with many talented, dedicated people. During the first three years, Matthew Tate was my mentor on the Big Machine. Working with him on a daily basis was one of the best experiences in my life, due to his intelligence, work ethic, and sense of humor. Through Matthew I learned the meaning of the phrase, "Do or do not. There is no try." I will always remember him both as a mentor, and as a friend. Stacey Eckman was my colleague and welcomed me from the first day that I joined the group. I always admired her positive attitude, and later, her courage and conviction in the face of a difficult situation. Massimo Bertino was one of the more colorful post-docs that have joined the group, and I will remember him for his love of science, and his very Italian personality. David Gosalvez impressed me from the beginning with his scientific knowledge. His honesty and candor greatly influenced my decision to join the group. Bob Hefty has been a great help in obtaining the data presented in this thesis. He suffered through many experimental difficulties with me, and I am happy to leave the machine in his capable hands. It was also a great learning experience to play volleyball with Bob, and a pleasure to participate in the dominant Ceyer group volleyball team that he spearheaded. Finally, I wish to thank Dave Lahr for many interesting (and occasionally heated) conversations about science and world politics.

Phil Brooks was my undergraduate research advisor. He taught me much about the vagaries of working with molecular beams, high vacuum, and children's toys. From him I also learned that if an experiment isn't difficult, it probably has been done previously, or it is not worth doing in the first place. The graduate students in Phil's group, Larry Lewis and Sue Wiediger, welcomed me into the group and made me feel quite at home in the lab. Dock Chil Che, a post-doc in the Brooks group, deserves special mention as he worked closely with me for many months, and introduced me to the joys of sushi.

Outside of MIT, I have enjoyed spending time with Cornelia Brenninkmeyer and Chris Davis. I have especially enjoyed their love of good food, good wine, and good friends, not necessarily in that order.

I would like to specifically thank two of my friends from Rice University. Wendy Lane, who kept me sane through my initial adjustment to MIT, and Peter Rogers, who kept me sane

during the push to finish my thesis. Likewise, I want to thank my two best friends from high school, Richard Scalzo and Joshua Madden, for good times and many intellectually stimulating discussions.

I also want to thank my brother Martin, who throughout my graduate career has been happy to offer his advice on issues both academic and not, often giving me a much-needed sense of perspective and a good dose of common sense. I know how rare it is to be able to count your sibling as your best friend - for me, Martin is both.

My parents I want to thank for having literally made me who I am now, with their constant love and unconditional positive regard. They have helped me in every way possible, and given me every reason to succeed. It is to them that this thesis is dedicated, and with good reason – if it were not for their encouragement, I very well may not have made it to where I am now.

Last, I want to thank my wife Sarah, who has given me her unwavering support, encouragement, motivation, and love through some very difficult times. The process of completing my thesis was if anything harder for her than it was for me, but she was always there for me when I needed her, and able to make me smile when I needed it most. I simply cannot imagine being without her, and I look forward to the new life that we will build together.

Table of Contents

List of Figures

Appendix A: Counting Electronics and Computer Interface

Chapter 1: Introduction

I. Background

I.A. Industrial relevance

One of the factors that has catalyzed the recent revolution in the computer industry is the ability of hardware manufacturers to consistently increase computational speeds while concomitantly maintaining or reducing the price at which that technology is available. This progression, loosely described by "Moore's Law," which predicts that the number of transistors on an etched silicon microchip will double approximately every 18 months,[1] is intimately related to the ability of manufacturers to shrink the "feature size" of the etched channels that form each individual transistor on the microprocessor. Despite the fact that etching plays a central role in semiconductor processing, the underlying mechanism is not well understood. In industry, complex etching "recipes" are concocted by trial and error. In order to better understand the etching process, many investigations have replaced the complex plasma environment used in industry with a model system consisting of a fluorine source coupled to a silicon single crystal. One such source of fluorine is XeF_2. Xenon difluoride is a gas phase, room temperature, plasmaless etchant that reacts rapidly and isotropically with Si, neither leaving an adsorbed by-product on nor radiatively damaging the Si. Since the discovery that XeF_2 spontaneously etches silicon under ambient conditions[2] several investigators have sought to understand the way in which XeF_2 reacts with silicon.[3] Recently, there has been renewed interest in XeF_2 as an isotropic etchant for the fabrication of microscopic three-dimensional mechanical structures known as microelectromechanical systems (MEMS).[4-8] Among the advantages offered by XeF_2 are compatibility with CMOS processing and high selectivity against silicon dioxide, aluminum and photoresist.[9]

I.B. Atom abstraction

In addition to its industrial relevance, the reaction of XeF_2 with Si is also of interest from the standpoint of surface dynamics. The reaction proceeds via a novel gas-surface interaction pathway known as atom abstraction, which was originally demonstrated in the case of the interaction of F_2 with Si(100).[10-16] In atom abstraction, only one surface-adsorbate bond is formed, while the complementary fragment is scattered into the gas phase. Atom abstraction differs from classic dissociative chemisorption in that classic dissociative chemisorption requires the simultaneous formation of two surface-adsorbate bonds along with the cleavage of a molecular bond of the incident gas molecule. Atom abstraction is energetically allowed in the interactions of XeF_2 and F_2 with Si(100) because the energy released upon the formation of a single Si-F bond is greater than the energy required to cleave the F-F and F-XeF bond. It is believed that atom abstraction is a universal gas-surface interaction mechanism, and is operative whenever the strength of a single surface-adsorbate bond is larger than the strength of the molecular bond of the incident gas-phase molecule.

In the case of the interaction of F_2 with Si(100), an atom abstraction event results in the liberation of a single gas phase F atom. However, this liberated F atom does not necessarily have to survive as an ejected gas phase particle. It is possible for this F atom to also adsorb on a second empty reaction site, a process known as two-atom adsorption. In contrast to classic dissociative chemisorption, which is a concerted process, two-atom adsorption occurs in a stepwise fashion, with an atom abstraction event being the necessary first step to two-atom adsorption. The probability of single atom abstraction and two atom adsorption in the case of F_2 interacting with Si(100) were determined as a function of coverage,[11,14,15] and a statistical model

was proposed to account for the observed reaction probabilities and to gain insight into the reaction mechanism.[12,16] These results are reviewed in greater detail below.

I.C. Etch rates

One of the most interesting aspects of the XeF_2/Si interaction is a simple comparison of etch rate of XeF_2 with that of two related species, atomic and molecular fluorine. This seemingly simple comparison yields results that have defied simple explanation. Under similar conditions, the etch rates are ranked $XeF_2 \geq F \gg F_2$.[17,18] This is surprising, since a thermodynamic ranking based on the bond strength of the reactants would predict $F \gg F_2 > XeF_2$. Understanding why the relative etch rates of these species differs from the thermodynamically predicted ranking is one of the major goals of our research.

The etch rate of XeF_2 was found to have an unusual temperature dependence.[18] It was found that above 450 K the etch rate exhibits normal Arrhenius behavior and increases with increasing temperature. However, below 400 K the etch rate was actually found to increase monotonically with decreasing temperature, indicative of a negative activation energy. This low-temperature non-Arrhenius behavior was interpreted in terms an extrinsic precursor, which is a species physisorbed on top of filled sites.[19] An extrinsic precursor diffuses on top of the filled sites until it encounters an empty site, such as a dangling bond, and reacts. A later study[20] confirmed this result and extended the temperature range to lower temperatures, finding that at temperatures below 150 K, XeF_2 would condense on the surface leading to passivation.

I.D. Etch products

The etch products of the reaction of XeF_2 with Si have also been studied.[2,18,21-24] Although there has been disagreement about the relative abundances, it is generally agreed that the major etch product at low surface temperatures ($T_s < 600$ K) is SiF_4, tetrafluorosilane.

Similarly, the reaction of atomic fluorine with Si produces SiF_4 as the major etch product. Minor etch products include higher fully coordinated fluorosilanes like Si_2F_6 and Si_2F_8, and radicals like SiF_x (x = 1,2,3). This product distribution is in contrast to that of the reaction of atomic fluorine with Si, which has a higher abundance of SiF_2 relative to the other minor etch products. Various time-of-flight measurements on the SiF_4 etch product have shown a bimodal distribution, suggesting that some of the exothermicity of the reaction is partitioned into translational excitation of the etch product.[15] Chemiluminescence was observed as a result of the reaction,[25] including a diffuse 500 nm feature ascribed to excited SiF_3 and a distinct feature at 350 nm from the excimer B state of XeF, attributed to reaction of unsaturated gas-phase SiF_2 or SiF_3 with ambient XeF_2. Although it is in principle possible that the exothermicity of the atom abstraction reaction produces electronically excited XeF, a possibility that was not considered, it turns out that such an excitation is unlikely. The involvement of the electronic states in the production of excited XeF will be discussed in greater detail in Chapter 3.

I.E. Comparison to plasma etching

Because of its relevance to plasma etching, some studies have incorporated additional energetic particles to better mimic the plasma environment. It was found that the reactivity of XeF_2 with Si is greatly enhanced by both coincident ions[26-30] and photons.[31-37] In fact, the etch rate enhancement due to coincident ions was dramatically greater than the sum of the etch rates from either XeF_2 or energetic ion sputtering alone.[38,39] This synergistic effect has been given the label "chemical sputtering." In addition to the etch rate enhancements due to coincident ions and photons, it was found that the etch rate could was enhanced by heavily n-doped silicon and inhibited in heavily p-doped silicon.[40]

I.F. Analysis of the fluorinated surface layer

To better understand the etching mechanism, many investigations have focused on the characterization of the silicon surface after exposure to XeF_2. Chuang measured low-resolution X-ray photoelectron spectra of a silicon surface exposed to a small fluence of XeF_2 and found that the spectra were suggestive of a fluorine layer with an average stoichiometry of SiF_2.[41] McFeely and coworkers have extensively investigated the SiF_x layer using XPS measurements on a Si(100) surface exposed to a low fluence (~50 L) of XeF_2.[42,43] The resultant spectra indicated that the majority surface species is SiF, with minor amounts of SiF_2 and SiF_3. They also found a uniformly diffuse (2x1) LEED pattern upon fluorination of the surface at 80 K, although the interpretation of this result is ambiguous due to the efficient electron stimulated desorption of F on Si.

Aliev and Kruchinin performed an ellipsometric study of F_2 and XeF_2 etching the Si(100) surface. They divide their results into two distinct reaction regimes. The initial regime was attributed to formation of the SiF_x (x = 1, 2, and 3) adsorption layer prior to the onset of etching, and the secondary regime was attributed to etching.[44]

Yarmoff and co-workers have performed XPS[45] and ESDIAD[46] studies of the Si surface fluorinated by XeF_2. They concluded from XPS data taken on a Si(111) surface that defects created by the exothermicity of the reaction were critical to etching, a conclusion also reached by Carter and co-workers in their theoretical investigations.[47] The ESDIAD study[9] of fluorinated Si(100)2x1 showed that at very low XeF_2 dose (between 0.1 and 0.25 ML surface coverage) the Si-F bond angle was 20° from the surface normal. The large spread in energy and angle of the desorbing F^+ was taken as evidence that etching was disordering the surface even at extremely low coverages. This conclusion is incorrect, as will be demonstrated in chapter 2.

I.G. Thesis overview

The remainder of Chapter 1 reviews the previous work done on the interaction of F_2 and XeF_2 with Si(100) in our laboratory. First, the interaction of F_2 with Si(100) will be summarized, including the determination of the absolute reaction probabilities of atom abstraction and two-atom adsorption, and a description of the model which was used to account for the observed reaction probabilities. Second, the interaction of XeF_2 with Si(100) will be summarized, including the observation of reactively scattered F atoms from XeF dissociation.

Chapter 2 presents a fundamental description of the interaction of XeF_2 with Si(100), including the surface fluorine coverage during the reaction, the evolution of the dissociative chemisorption probability with respect to coverage, and the evolution of the surface order with respect to coverage. It is shown that the reaction of XeF_2 with Si(100) is quite similar to the reaction of F_2 with Si(100) up to approximately 1 monolayer (ML) coverage. That is, both react with the Si dangling bonds to produce a well-ordered surface where each Si atom is decorated with a fluorine atom. Above 1 ML coverage however, the reactivities differ greatly. Molecular fluorine ceases to react with the surface, while XeF_2 continues to react, breaking Si-Si lattice bonds, destroying the surface order, and ultimately etching the surface via production of volatile SiF_4.

Chapter 3 presents a set of time-of-flight spectra of the scattered products of the reaction of XeF_2 with Si(100). The analysis of these spectra includes a momentum-matching calculation that successfully accounts for the observed F atoms from XeF dissociation. This momentum-matching calculation is also used to predict the expected Xe atoms from XeF dissociation, and the prediction is compared to the observed Xe time-of-flight spectra.

II. Previous results for the interaction of F_2 and XeF_2 with Si(100)

II.A. Introduction

There are three possible scattering channels during the interactions of F_2 and XeF_2 with Si. One channel is unreactive scattering, where the molecule simply reflects from the surface without breaking or creating any chemical bonds. A second channel is single atom abstraction, where one fluorine atom bonds to the surface while the remaining fluorine atom or XeF fragment scatters into the gas phase. The third channel is two-atom adsorption, where both fluorine atoms form bonds to the surface. However, two-atom adsorption is distinct from classic dissociative chemisorption in that two-atom adsorption is a stepwise process, whereas dissociative chemisorption is a concerted process. Two-atom adsorption results when the complementary fragment that was initially a gas phase species also adsorbs. Thus atom abstraction and two-atom adsorption are intimately linked as both share an abstraction event as the necessary first step.

The existence of the atom abstraction and two-atom dissociative chemisorption mechanisms has only recently been conclusively shown, first in the reaction of F_2 with Si(100),[10,11,14] and subsequently in the reaction of XeF_2 with Si(100).[15,16] The difficulties inherent in demonstrating atom abstraction are similar to those that precluded the direct observation of the Eley-Rideal mechanism until half a century after it was proposed. Despite the dearth of experimental evidence demonstrating atom abstraction, it ought to be present in any gas-surface system in which the energy liberated by the formation of a single suface-adsorbate bond is greater than the energy required to break the bond of the incident gas molecule.

II.B. The interaction of F_2 with Si(100)

Recently, the mechanism for the dissociative chemisorption of F_2 on Si(100) was shown to proceed by atom abstraction. As a F_2 molecule approaches the Si surface, a Si dangling bond abstracts one of the F atoms, which is then adsorbed at that site, while the complementary F atom is expelled. The fate of the complementary F atom can be influenced by both the orientation of the incident F_2 molecule relative to the surface, and the occupancy of the neighboring reactive sites, as described below. The reaction proceeds until all available dangling bonds have reacted to form Si-F, at which point the reaction ceases. The saturation coverage is 1 monolayer (ML) of fluorine arranged in an ordered overlayer that preserves the original (2x1) reconstruction of the surface.

The absolute reaction probabilities of unreactive scattering, single atom abstraction, and two-atom adsorption have been measured[11] for the interaction of F_2 with Si(100) and are shown as open circles in Figure 1 as a function of fluorine coverage. It can be seen that the probability of unreactive scattering, P_0, starts close to zero and then increases monotonically. The probability of two-atom adsorption, P_2, starts close to 1, and decreases monotonically. The initial decrease in P_2 is quite linear. The probability of single atom abstraction, P_1, on the other hand, starts at an intermediate value, increases to a maximum, and subsequently decays to zero. Both the behavior of P_1 and the behavior of P_2 are unexpected from the viewpoint of traditional Langmuirian chemical kinetics, which predicts that the probability of single atom abstraction should be linearly dependent on the number of empty sites, while two atom adsorption should depend quadratically on the number of empty sites. The experimental results clearly demand a non-traditional approach in order to correctly fit the data.

A statistical model for the reaction probabilities was proposed based on two main premises.[11,16] First, it was proposed that that the two dissociative chemisorption channels, atom abstraction and two atom adsorption, share a common initial step, F atom abstraction. The subsequent interaction, if any, of the complementary F atom with the surface determines if the overall result is single atom abstraction or two-atom adsorption. Second, the reactivity of each dangling bond site was linked to the occupancy of the complementary Si atom in the dimer pair. The model differentiates each reactive site into one of four categories based on the occupancy of the dimer pair to which the reactive site belongs. A reactive site can either be an empty site on an unfilled dimer, an empty site on a half-filled dimer, a filled site on a half-filled dimer or a filled site on a filled dimer. The results of the model are shown in Figure 1 as the solid lines. There is good agreement between the experimental data and the model.

The results of the model suggest that the fate of the complementary F atom is determined, in part, by the orientation of the incident F_2 molecular axis with respect to the surface. If the incident F_2 molecule has a perpendicular orientation with respect to the surface, the complementary F atom will likely be ejected away from the surface, making two atom adsorption impossible. This mechanism is termed "neighbor-independent" because the fate of the complementary F atom is independent of the occupancy of the other sites on the surface. At zero coverage, it is this mechanism that yields the nonzero probability for single atom abstraction. On the other hand, if the incident F_2 molecule has a parallel orientation with respect to the surface, the complementary F atom will likely interact with the surface. If the F atom interacts with an unoccupied site, adsorption may occur. This mechanism is termed "neighbor-dependent" because the occupancy of the site with which the F atom interacts determines whether the overall result is single atom abstraction or two atom adsorption. It is the competition

between the need for an unoccupied site for the initial atom abstraction, and the subsequent need for an occupied site to prevent adsorption of the complementary F atom that yields the unusual coverage dependence of the probability of single atom abstraction, which is signified by a maximum likelihood at about 0.5 ML coverage.

The results of the model also show that the reaction proceeds without significant energy barriers. A comparison of the reaction cross sections shows that an unoccupied site on a half-filled dimer is particularly reactive, about twice as reactive as the unoccupied sites on empty dimers, with a reaction cross section that is significantly larger than the cross sectional area of a surface site. This result is consistent with a de-stabilizing effect resulting from the loss of the stabilizing π interaction between unfilled dangling bonds on an empty dimer, which results in a more radical-like dangling bond. In fact, the results of the model suggest that the unoccupied sites on the half-filled dimer are so reactive that they are able to attract the incident F_2 molecule from a distance extending beyond the cross sectional area of the site itself. These results likely reflect the phenomenon of molecular steering in which the incident molecules are aligned into a favorable orientation for reaction.
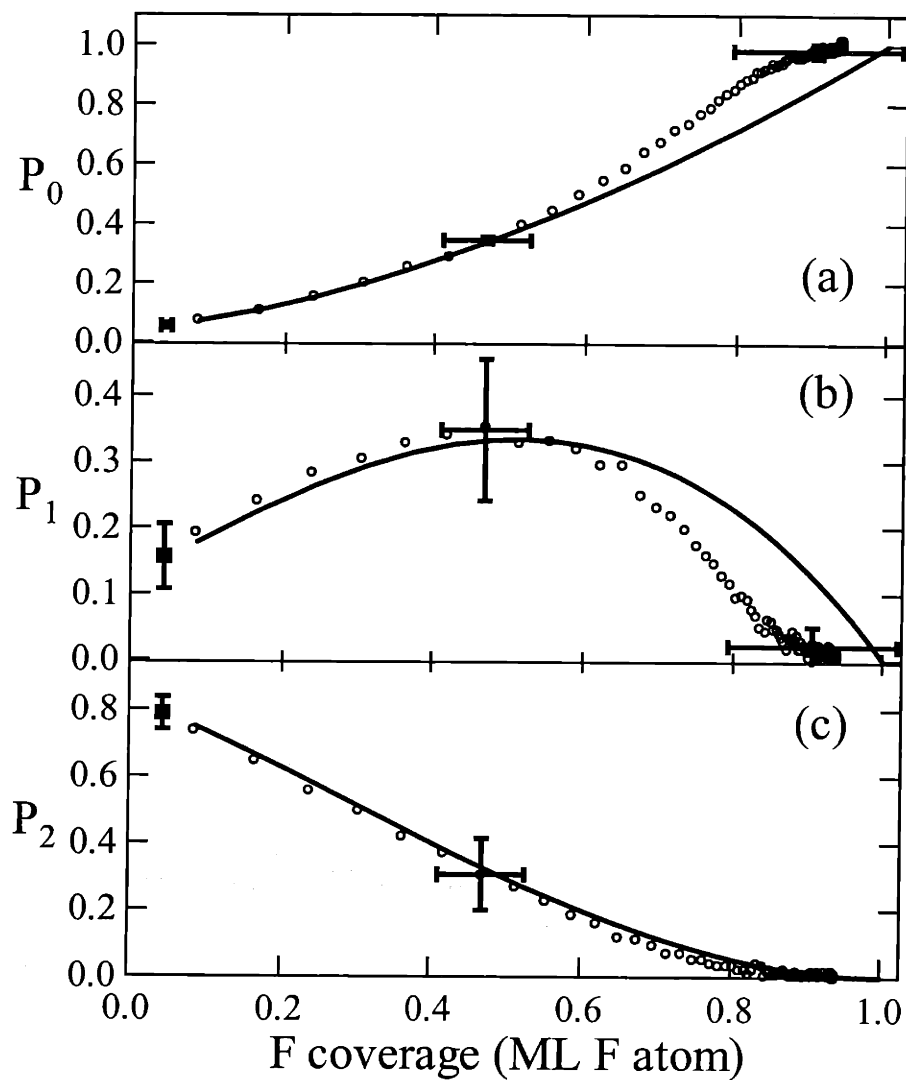
Figure 1 Reaction probabilities predicted by model as a function of fluorine coverage

Reaction probability of F_2 with Si(100) as a function of fluorine coverage derived from the best fit of the model [solid line] to the experimental data [circles] for (a) unreactive scattering P_0, (b) single atom abstraction P_1, (c) two atom adsorption P_2. Error bars reflect a 95% confidence limit.

II.C. The Interaction of XeF$_2$ with Si(100)

This section summarizes the observed time-of-flight (TOF) spectra of the scattered products of the reaction of XeF$_2$ with Si(100) at a surface temperature of 250 K.[16] The observed time-of-flight spectra at 250 K give a basis for understanding the results presented in Chapter 3 for the time-of-flight spectra of the scattered products of the reaction of XeF$_2$ with Si(100) at a surface temperature of 150 K.

The time-of-flight distributions of the scattered products were measured as a function of surface coverage at nine different scattering angles, spanning the forward scattering plane from 0-80° as measured from the surface normal. Five distinct species are expected to scatter from the surface during the course of the reaction. These species are XeF$_2$, XeF, Xe, F, and SiF$_4$. The TOF spectra of each of these except SiF$_4$ were recorded as a function of surface coverage and will be described below.

II.C.1. m/e = 167

The TOF distributions at m/e=167, corresponding to the unreactively scattered product, XeF$_2$, have been measured at nine detection angles spanning the forward scattering region from 0° to 80° detection angle. The observed TOF spectrum at 0° detection angle averaged over the coverage range 0-1.1 ML, shown in Figure 2, illustrates the bimodal nature of the m/e=167 TOF spectra. A fast peak corresponds to direct inelastic (DI) scattering, while a slower peak corresponds to molecular species that have entered the trapping-desorption (TD) channel, which is the result of XeF$_2$ that has thermally equilibrated with the surface and subsequently desorbed.

The flux for each component may be obtained by integrating the velocity-weighted TOF distribution. A detailed description of the equations involved has been given previously.[16] The flux of each component is shown in Figure 3 as a function of detector angle for four different

coverage regimes, 0-0.4 ML F, 0.4-0.7 ML F, 0.7-0.9 ML F, and 0.9-1.1 ML F. The angular distribution of the direct inelastic feature is peaked towards the super-specular, while the angular distribution of the trapping-desorption feature is cosine-like.

The intensity of the TD component changes dramatically with increasing coverage. On a clean surface there is virtually no unreactively scattered XeF_2 from the trapping-desorption scattering channel. On a fluorinated surface, on the other hand, the TD component is approximately equal to the DI component, suggesting that on a fluorinated surface the energy transfer of the incident XeF_2 to the surface is greater, thereby resulting in a larger TD component.
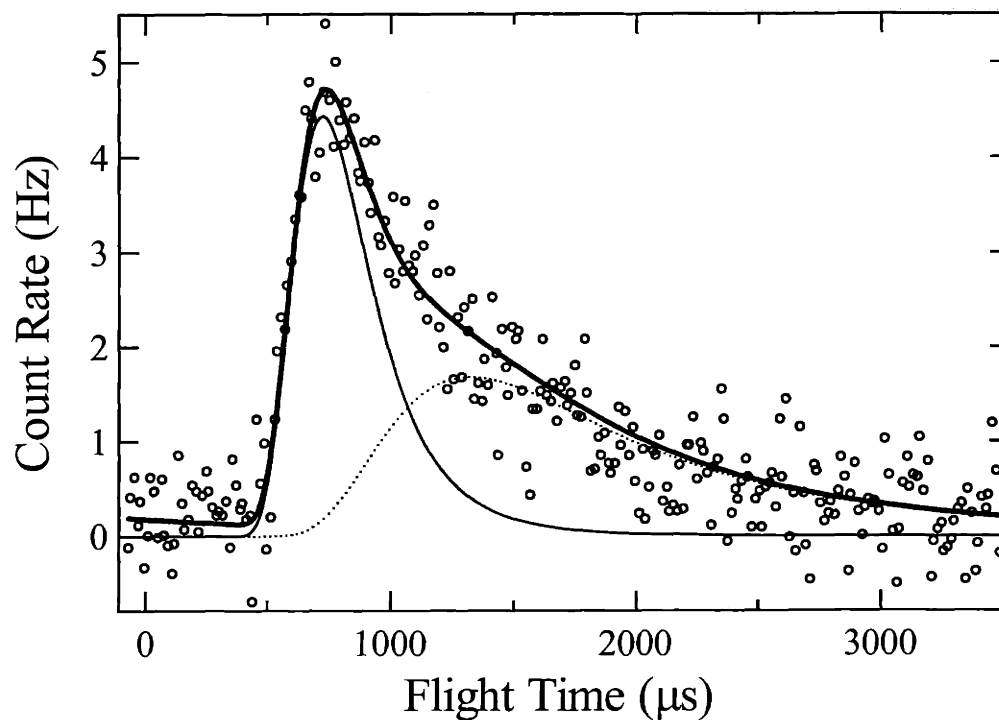
Figure 2 TOF distribution of scattered products at m/e=167

TOF spectrum of signal at m/e=167 scattered along the surface normal, θ_d=0°, from Si(100) at 250 K upon exposure to XeF$_2$ at θ_i=35°. Thick solid line shows a least squares fit of a two component velocity distribution. The fast component (thin solid line) at short flight times corresponds to direct-inelastic (DI) scattering. The slow component (dashed line) at long flight times corresponds to trapping-desorption (TD). Spectrum is averaged over XeF$_2$ exposure corresponding to a fluorine coverage range of 0-1.1 ML F.
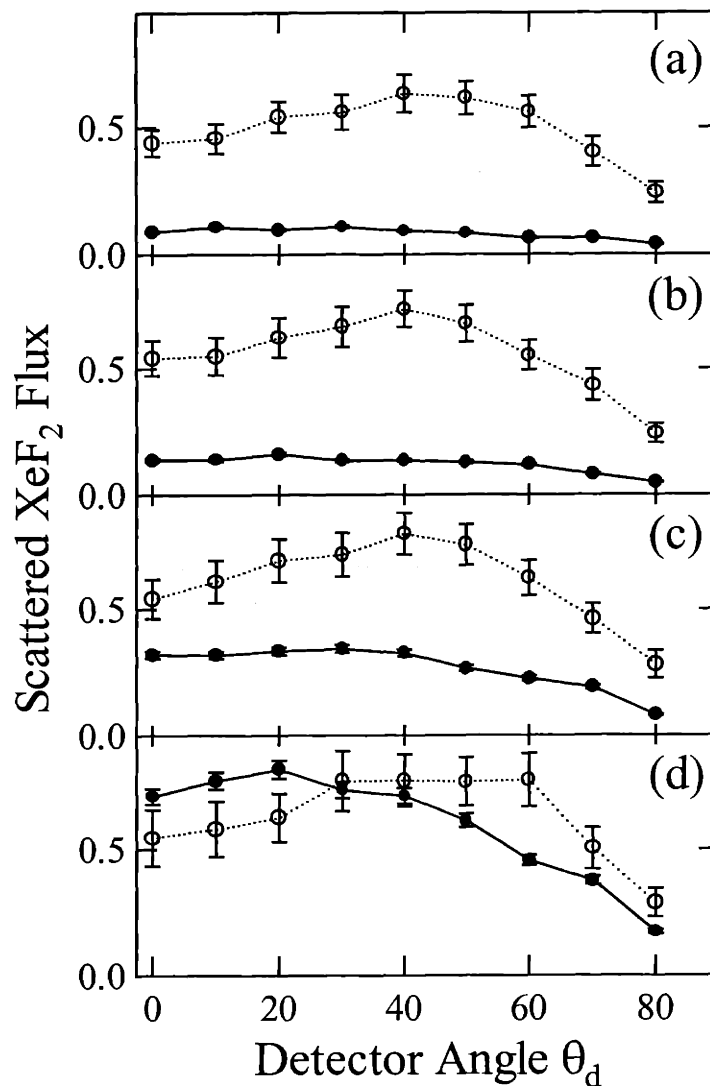
Figure 3 Angular distribution of flux of XeF$_2$ scattered from Si(100)

Scattered flux of XeF$_2$ determined from velocity-weighted integration of the fit to the TOF distribution at m/e=167 attributable to DI scattering (hollow circles) and TD scattering (solid circles) as a function of detector angle over successive 10 s high energy XeF$_2$ exposure intervals corresponding to coverage ranges of (a) 0-0.4 ML F, (b) 0.4-0.7 ML F, (c) 0.7-0.9 ML F, and (d) 0.9-1.1 ML F. Error bars represent uncertainty of the integral of the velocity-weighted fit to the TOF distributions.

II.C.2. m/e = 148

Analogous to the TOF measurements at m/e=167, TOF distributions at m/e=148 have been measured at nine detection angles spanning the forward scattering region from 0° to 80° detection angle. Figure 4a shows the observed TOF spectrum at 0° detection angle averaged over the coverage range 0-1.1 ML.

The nature of the electron impact bombardment ionizer used in the quadrupole mass spectrometer detector is such that significant amounts of fragmentation can occur in the ionizer region. This fragmentation complicates the interpretation of the TOF spectra, since the ionization of the parent XeF_2 molecule gives rise to species that can be detected as XeF^+, Xe^+ or F^+. This fragmentation can be readily observed by the fact that the overall m/e=148 TOF spectrum shown in Figure 4a is bimodal. The XeF_2 TOF spectrum taken under the same experimental conditions multiplied by the cracking ratio 1.9:1 is overlaid on the plot. This contribution is removed by point-by-point subtraction, and Figure 4b shows the resultant TOF spectrum of the abstraction product, XeF. The average energy of the XeF shown in Figure 4b is $E_{avg} = 7.8\pm0.7$ kcal/mol, which is less than 10% of the total reaction exothermicity. The small fraction of the reaction exothermicity that is channeled into the translational energy of the abstraction product can be contrasted to the recent observations of the gas phase products of a direct gas-surface reaction, which were observed to carry away significant fractions (>25%) of the reaction exothermicity.[48] The low translational energy of the abstraction product is consistent with an "early barrier" or "attractive potential" type of potential energy surface first described by Evans and Polanyi for gas phase reactions.[49] In the prototypical three atom reaction $A+B_2 \rightarrow AB+B$, an "attractive potential" surface leads to low translational energy in the products and high vibrational energy in the product AB. In the case of the interactions of XeF_2

with Si(100), the vibrational excitation is in the newly formed Si-F bond. Indeed, in the interaction of XeF_2 with Si, emission at about 1400 cm^{-1} has been attributed to the decay of a vibrationally excited fluorinated Si surface species.[50]

Similar to the analysis of the XeF_2 TOF spectra, the flux of XeF can be obtained by integrating the velocity-weighted TOF spectra at each angle and coverage. The resulting angular distribution is shown in Figure 5. Up until 0.7 ML coverage (corresponding to Figure 5a and Figure 5b) the angular distribution of the abstraction product is broad and essentially isotropic. However, above 0.7 ML coverage, the XeF angular distribution changes dramatically, becoming quite peaked towards normal. The anisotropy of the XeF angular distribution is remarkable given that in the interaction of F_2 with Si(100), the F atom angular distribution is isotropic and cosine-like over the entire coverage range.[11]

A possible explanation for the coverage dependence of the angular distribution of the scattered XeF is based on steric hindrance. On the clean surface, a XeF_2 molecule readily loses a F atom to any unoccupied site in almost any orientation because there is free access to the dangling bonds. On the other hand, the fluorinated surface is more crowded, and access to the few unoccupied bonds will be hindered by the surrounding adsorbed fluorine. If the XeF_2 molecular axis is perpendicular to the surface, steric hindrance from the adsorbed F will block the XeF_2 from accessing the dangling bond reactive site. However, a reaction geometry where the molecular axis is tilted allows for free access to the reaction site, leading to ejection of the XeF abstraction product preferentially along the surface normal. On the other hand, steric effects are not likely to play a role in the interaction of F_2 with Si(100) because of the much smaller size of the F_2 molecule.

The average energy of the scattered XeF also shows a strong dependence on the coverage. Figure 6 shows the average energy of XeF averaged over all scattering angles as a function of fluorine coverage. It can be seen that the average energy decreases dramatically, beginning above 10 kcal/mol on a clean surface and decreasing monotonically to below 6 kcal/mol on a fluorinated surface. Van der Waals interactions could explain the observed decrease in average energy with increasing coverage. The exiting XeF fragment may experience an attractive interaction with the nearest adsorbed F atoms, resulting in a frictional force that slows the exit trajectory of the XeF.
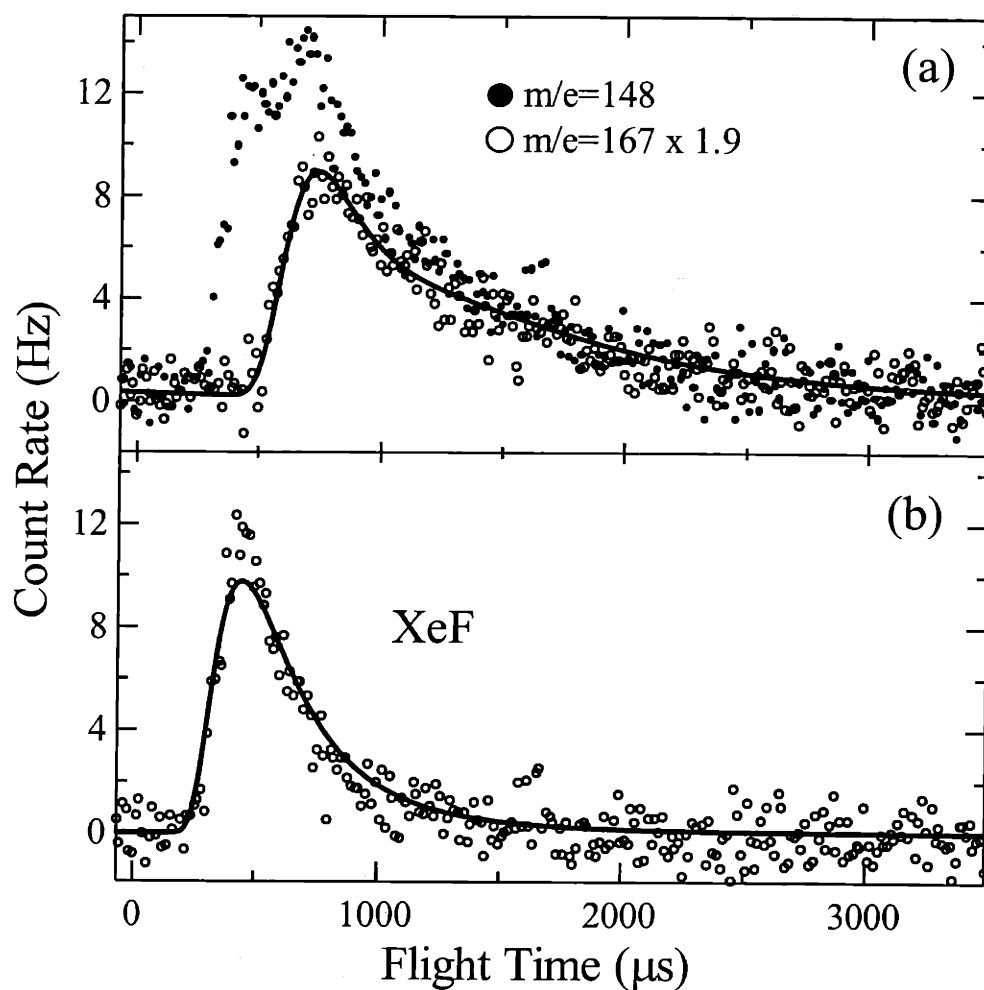
Figure 4 TOF distribution of scattered products at m/e=148

(a) TOF spectra at m/e=167 multiplied by the XeF_2 cracking ratio and at m/e=148 measured at $\theta_d=0°$ and $T_s=250$ K upon exposure to XeF_2 at $\theta_i=35°$. The solid line in (a) shows the fit to the TOF distribution at m/e=167 multiplied by the XeF_2 cracking ratio. (b) Net scattered XeF TOF distribution obtained by point-by-point subtraction of m/e=167 signal multiplied by XeF_2 cracking ratio from m/e=148 signal in (a). The solid line in (b) shows a fit to the data of a single component Maxwell-Boltzmann function. Spectra are averaged over XeF_2 exposure corresponding to a fluorine coverage range of 0-1.1 ML F.
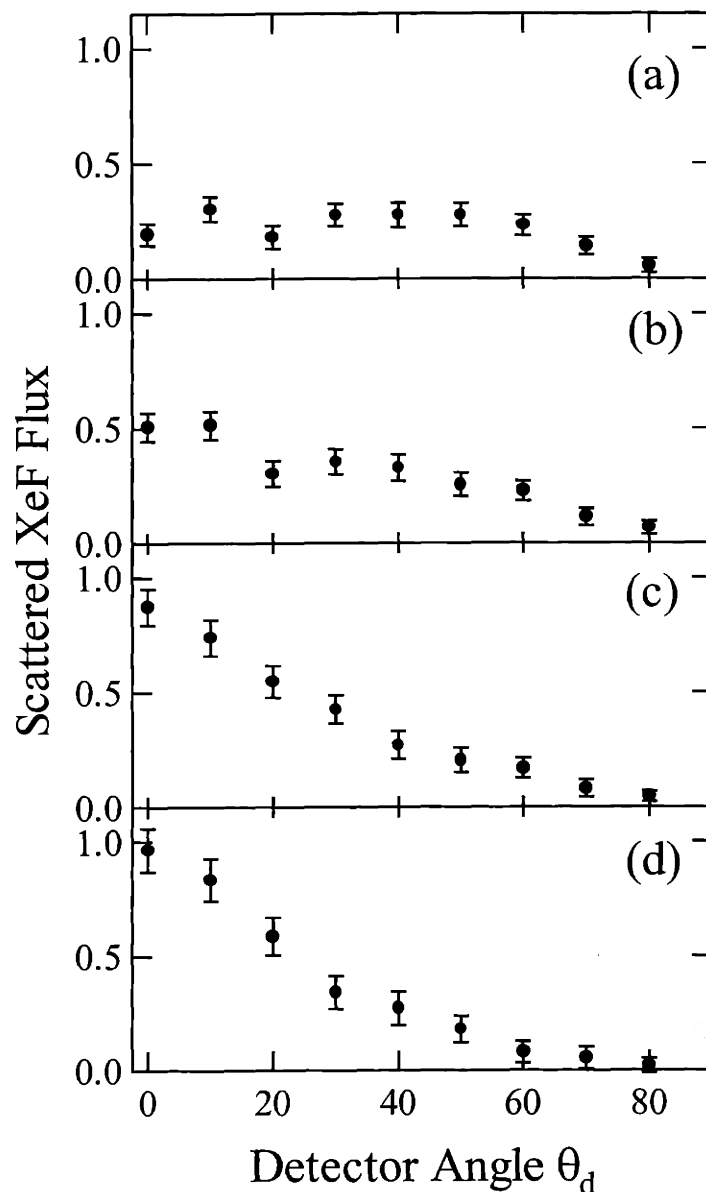
Figure 5 Angular distribution of flux of XeF scattered from Si(100)
Flux of scattered XeF as a function of detector angle determined by integration of velocity-weighted TOF distributions of scattered XeF over a sequence of 10 s exposures to high energy XeF_2 which corresponds to coverage ranges of (a) 0-0.4 ML F, (b) 0.4-0.7 ML F, (c) 0.7-0.9 ML F, and (d) 0.9-1.1 ML F. Error bars represent the uncertainty of integral of the velocity-weighted fit to the TOF distributions.
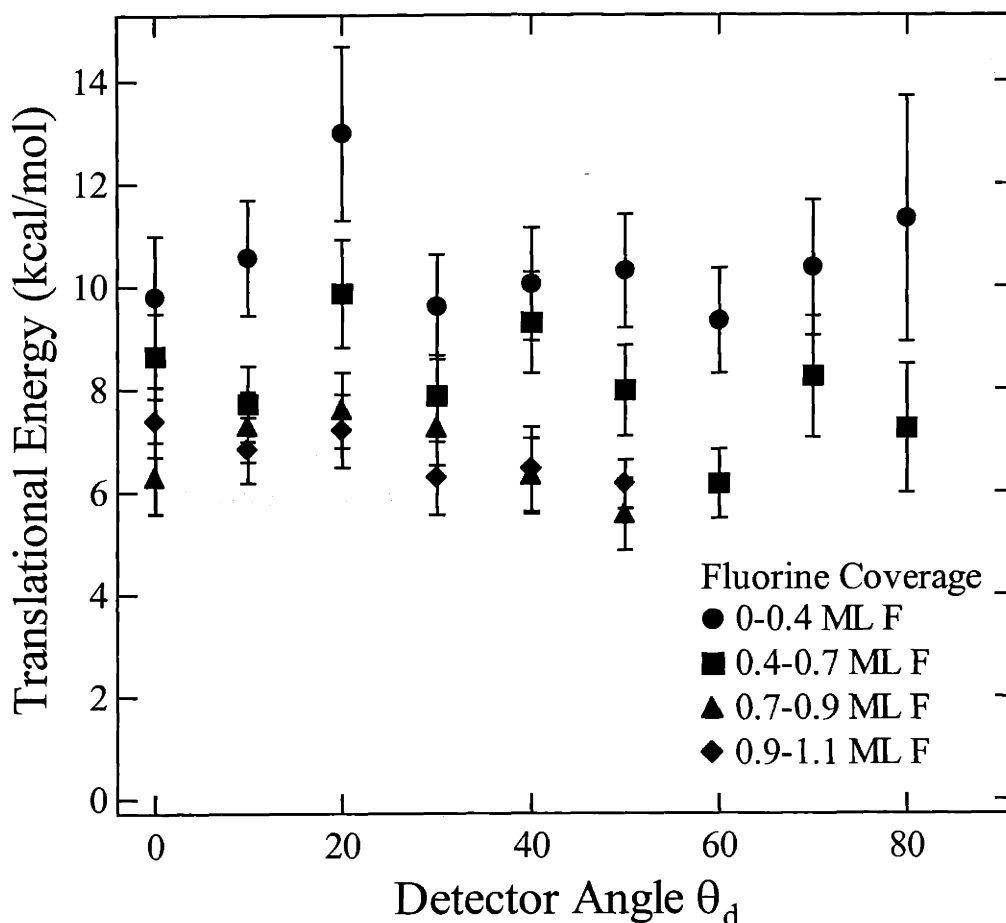
Figure 6 Translational energy of XeF scattered from Si(100) as a function of detector angle
Average translational energy of scattered XeF as a result of exposure to high energy XeF_2 as a function of detector angle over four different fluorine coverage ranges. The average translational energy is determined from the velocity-weighted TOF distributions. Error bars represent the uncertainty of the determination of the average translational energy from the fits to the TOF distributions. The translational energy of the scattered XeF into detector angles $\theta_d > 50°$ at coverages greater than 0.7 ML F are not shown because the uncertainty of these values resulting from extremely low signal intensity.

II.C.3. m/e = 19

It is likely that the XeF produced as a result of single atom abstraction will dissociate if just a small fraction of the tremendous exothermicity of the reaction is channeled into the internal energy of the weakly bound XeF (3 kcal/mol), resulting in a scattered F and Xe atom. To test this possibility, the TOF distributions of the scattered products at m/e=19 were measured. Figure 7a shows the TOF distribution of the scattered products at m/e=19 at 0° detection angle, averaged over the coverage range 0-1.1 ML. Three other species are overlaid on the graph and contribute to the signal at m/e=19. First, cracking from XeF_2 and XeF both result in signal at m/e=19. Also, there is a contribution from doubly ionized $^{38}Ar^{2+}$ from the Ar carrier gas. After these contributions are subtracted, the remaining fast narrow TOF spectrum shown in Figure 7b is directly attributable to scattered F atoms from XeF dissociation.

The phenomenon of gas-phase XeF dissociation is analyzed and discussed in detail in Chapter 3.
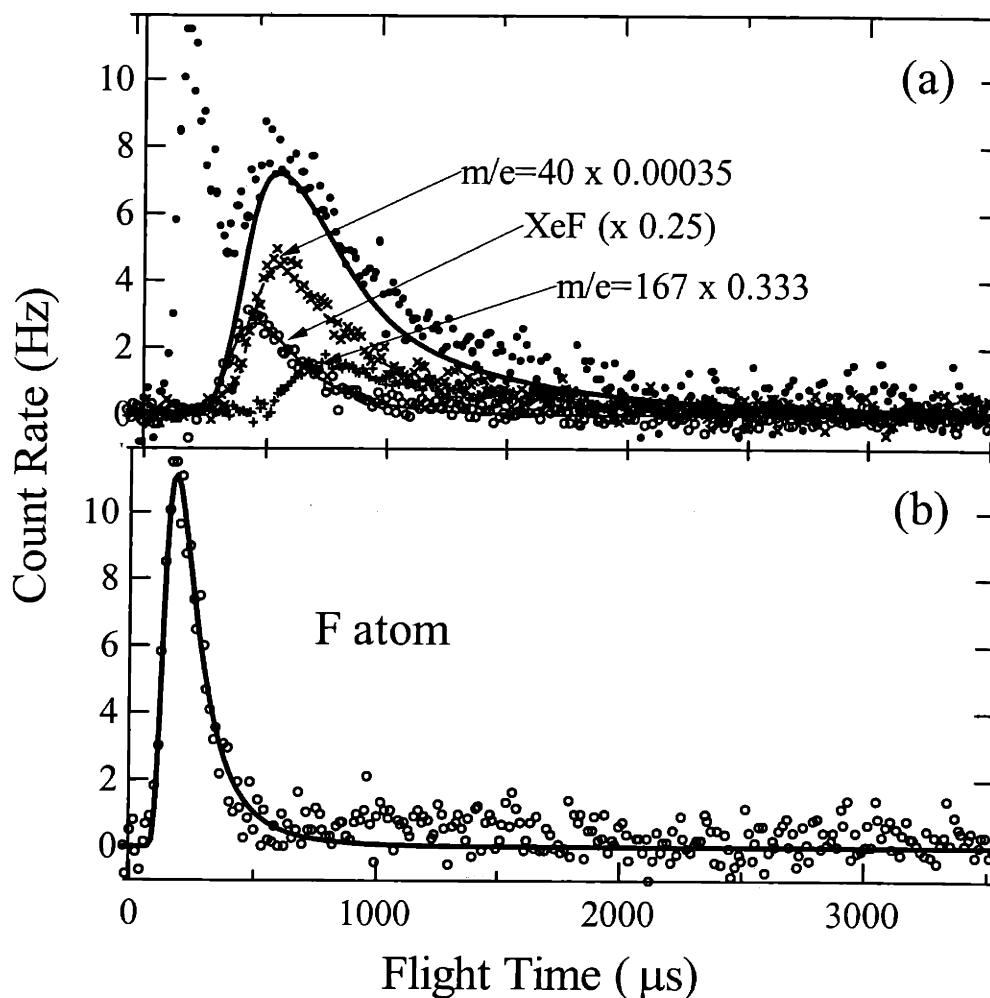
Figure 7 TOF distribution of scattered products at m/e=19

(a) TOF spectra at m/e=19 measured at $\theta_d=0°$ and $T_s=250$ K upon exposure to XeF_2 at $\theta_i=35°$. Signal at m/e=167 multiplied by XeF_2 cracking ratio, signal at m/e=40 multiplied by scaling factor of 0.00035 to account for isotopic abundance and ionization cross section, and XeF signal multiplied by optimal scaling factor of 0.25 are superimposed for comparison. (b) Net scattered F atom TOF distribution obtained by point-by-point subtraction of contributions from XeF_2, Ar, and XeF from m/e=19 signal in (a). Spectra are averaged over XeF_2 exposure corresponding to a fluorine coverage range of 0-1.1 ML F.

II.C.4. m/e = 129

For the interaction of F_2 with Si(100), it was shown that two-atom adsorption proceeds in a stepwise fashion. The absolute probability of two-atom adsorption was determined as a function of coverage using normalization, not by direct observation. In other words, if a F_2 molecule was *not* observed to undergo unreactive scattering or single atom abstraction, then it must have undergone two-atom adsorption. In the interaction of XeF_2 with Si(100), two atom adsorption will necessarily result in a Xe atom scattered into the gas phase. This reactively scattered Xe atom acts as an "atomic spectator" to the two-atom adsorption reaction, possibly yielding information that would further our understanding of the two-atom adsorption reaction mechanism.

However, conclusive assignment of Xe due to two-atom adsorption is hampered by the multiple sources of signal that give rise to the observed m/e=129 TOF spectra. These are 1) cracking from unreactively scattered XeF_2; 2) cracking from the XeF abstraction product; 3) Xe atoms from XeF dissociation; 4) Xe atoms from two-atom adsorption; 5) unreactively scattered Xe from contamination present in the incident beam, which could occur if the steady-state reaction of XeF_2 with the stainless steel manifold or Ni nozzle is significant. The only one of these five sources that is known is the dissociative ionization of XeF_2, which can be accounted for by subtracting the observed XeF_2 signal multiplied by the $Xe^+:XeF_2^+$ cracking ratio from the observed m/e=129 signal.

The problem of separating the multiple contributions to the m/e=129 signal is discussed in detail in Chapter 3.

REFERENCES

[1] G.E. Moore, *Electronics* **38**, 114 (1965).

[2] H.F. Winters and J.W. Coburn, *Appl. Phys. Lett.* **34**, 70 (1979).

[3] H.F. Winters and J.W. Coburn, *Surf. Sci. Rep.* **14**, 165 (1992).

[4] I.C. Ressejac, L.M. Landsberger, J.F. Currie, *J. Vac. Sci. Technol. A* **18**, 746 (2000).

[5] N.H. Tea, V. Milanović, C.A. Zincke, J.S. Suehle, M. Gaitan, M.E. Zaghloul, J. Geist, *J. Microelec. Sys.* **6**, 363 (1997).

[6] F.I. Chang, R. Yeh, G. Lin, P.B. Chu, E. Hoffman, E.J.J. Kruglick, K.S.J. Pister, M.H. Hecht, *SPIE* **2641**, 117 (1995).

[7] P.B. Chu, J.T. Chen, R. Yeh, G. Lin, J.C.P. Huang, B.A. Warneke, K.S.J. Pister, *Transducers* **97**, 665 (1997).

[8] R. Toda, K. Minami, M. Esashi, *Transducers* **97**, 671 (1997). *Sensors and Actuators A* **66**, 268 (1998).

[9] G.T.A. Kovacs, N.I. Maluf and K.E. Petersen, *Proc. IEEE* **86**, 1536 (1998).

[10] Y.L. Li, D.P. Pullman, J.J. Yang, A.A. Tsekouras, D.B. Gosalvez, K.B. Laughlin, Z. Zhang, M.T. Schulberg, D.J. Gladstone, S.T. Ceyer, *Phys. Rev. Lett.* **74**, 2603 (1995).

[11] M.R. Tate, D. Gosalvez-Blanco, D.P. Pullman, A.A. Tsekouras, Y.L. Li, J.J. Yang, K.B. Laughlin, S.C. Eckman, M.F. Bertino, and S.T. Ceyer, *J. Chem. Phys.* **111**, 3679 (1999).

[12] M.R. Tate, D.P. Pullman, Y.L. Li, D. Gosalvez-Blanco, A.A. Tsekouras, S.T. Ceyer, *J. Chem. Phys.* **112**, 5190 (2000).

[13] D.P. Pullman, A.A. Tsekouras, Y.L. Li, J.J. Yang, M.R. Tate, D.B. Gosalvez, K.B. Laughlin, M.T. Schulberg, and S.T. Ceyer, *J. Phys. Chem. B* **105**, 486 (2001).

[14] J.J. Yang, Ph. D. Thesis, Massachusetts Institute of Technology, Cambridge, MA, 1993.

[15] D. Gosalvez-Blanco, Ph. D. Thesis, Massachusetts Institute of Technology, Cambridge, MA, 1997.

[16] M.R. Tate, Ph. D. Thesis, Massachusetts Institute of Technology, Cambridge, MA, 1999.

[17] D.L. Flamm, V.M. Donnelly, and J.A. Mucha, *J. Appl. Phys.* **52**, 3633 (1981).

[18] D.E. Ibbotson, D.L. Flamm, J.A. Mucha, and V.M. Donnelly, *Appl. Phys. Lett.* **44**, 1129 (1984).

[19] Kisliuk, P. *J. Phys. Chem. Solids* **3**, 95 (1957).

[20] M.J.M. Vugts, G.L.J. Verschueren, M.F.A. Eurlings, L.J.F. Hermans, and H.C.W. Beijerinck, *J.Vac. Sci. Tech. A* **14**, 2766 (1996).

[21] H.F. Winters and F.A. Houle, *J. Appl. Phys.* **54**, 1218 (1983).

[22] F.A. Houle, *J. Chem. Phys.* **87**, 1866 (1987).

[23] J.A. Dagata, D.W. Squire, C.S. Dulcey, D.S.Y. Hsu, and M.C. Lin, *J. Vac. Sci. Tech. B* **5**, 1495 (1987).

[24] F.A. Houle, *J. Appl. Phys.* **60**, 3018 (1986).

[25] M.J. Mitchell, M. Suto, L.C. Lee, and T.J. Chuang, *J. Vac. Sci. Tech. B* **5**, 1444 (1987).

[26] Y.Y. Tu, T.J. Chuang, and H.F. Winters, *Phys. Rev. B.* **23**, 823 (1981)

[27] R.A. Haring, A. Haring, F.W. Saris, and A.E. de Vries, *Appl. Phys. Lett.* **41**, 174 (1982)

[28] F.A. Houle, *Appl. Phys. Lett.* **50**, 1838 (1987)

[29] M.J.M. Vugts, L.J.F. Hermans, and H.C.W. Beijerinck, *J. Vac. Sci. Tech. A* **14**, 2138 (1996)

[30] M.J.M. Vugts, L.J.F. Hermans, and H.C.W. Beijerinck, *J. Vac. Sci. Tech. A* **14**, 2820 (1996)

[31] T.J. Chuang, *J. Chem. Phys.* 74, 1461 (1981)

[32] F.A. Houle, *Chem. Phys. Lett.* **95**, 5 (1983)

[33] F.A. Houle, *J. Chem. Phys.* **79**, 4237 (1983)

[34] F.A. Houle, *J. Chem. Phys.* **80**, 4851 (1984)

[35] F.A. Houle, *Phys. Rev. Lett.* **61**, 1871 (1988)

[36] F.A. Houle, *Phys. Rev. B* **39**, 10120 (1989)

[37] B. Li, U. Streller, H.P. Krause, I. Twesten, and N. Schwentner, *J. Appl. Phys.* **77**, 350 (1995)

[38] J.W. Coburn and H.F. Winters, *J. Appl. Phys.* **50**, 3189 (1979).

[39] Y.Y. Tu, T.J. Chuang, and H.F. Winters, *Phys. Rev. B* **23**, 823 (1981).

[40] H.F. Winters and D. Haarer, *Phys. Rev. B* **36**, 6613 (1987).

[41] T.J. Chuang, *J. Appl. Phys.* **51**, 2614 (1980).

[42] F.R. McFeely, J.F. Morar, N.D. Shinn, G. Landgren, and F.J. Himpsel, *Phys Rev. B* **30**, 764 (1984)

[43] N.D. Shinn, J.F. Morar, and F.R. McFeely, *J. Vac. Sci. Tech. A* **2**, 1593 (1984).

[44] V.S. Aliev, V.N. Kruchinin, *Surf. Sci.* **442**, 206 (1999).

[45] C.W. Lo, P.R. Varekamp, D.K. Shuh, T.D. Durbin, V. Chakarian and J.A. Yarmoff, *Surf. Sci.* **292**, 171 (1993).

[46] W.C. Simpson, J.A. Yarmoff, *Surf. Sci.* **359**, 135 (1996).

[47] P.C. Weakliem, C.J. Wu, E.A. Carter, *Phys. Rev. Lett.* **69**, 200 (1992).

[48] C.T. Rettner and D.J. Auerbach, *Science* **263**, 365 (1994).

[49] M.G. Evans and M.C. Polanyi, *Trans. Faraday Soc.* **35**, 178 (1939).

[50] T.J. Chuang, *Phys. Rev. Lett.* **42**, 815 (1979).

Chapter 2: Comparison of the Interactions of XeF$_2$ and F$_2$ with Si(100)2×1

I. Introduction

The integration of conventional electronics with three-dimensional mechanical components within a Si microchip is known as microelectromechanical systems technology or MEMS. The fabrication of these three-dimensional mechanical structures involves many steps, which may include x-ray lithography, chemical vapor deposition, and anisotropic chemical etching, but it also requires an isotropic etching step. One isotropic etchant currently in use is XeF_2.[1-5] Xenon difluoride is a gas phase, plasmaless etchant that reacts rapidly and isotropically with Si at room temperature, neither leaving an adsorbed by-product on nor radiatively damaging the Si. Its etching rates are as high as 40 μ/min. Among other advantages offered by XeF_2 is compatibility with complementary metal oxide semiconductor technology processing.[6]

Of interest in the present work is the high reactivity of XeF_2 with Si as compared to the reactivity of F_2. Given the chemical similarities of XeF_2 and F_2, it is curious that the reaction rate of XeF_2 with Si to form volatile etch products such as SiF_4 is 10^3-10^4 times higher than that of F_2.[7-11] In short, XeF_2 etches Si while F_2 does not. Since the discovery that XeF_2 spontaneously etches Si under ambient conditions,[7] many investigators have sought to understand why XeF_2 is so reactive with Si.[12-20] The vast majority of these investigations have been carried out with sufficient XeF_2 exposure to produce high fluorine coverages that yield the volatile etch product. In contrast, this investigation compares the interactions of XeF_2 and F_2 as the fluorine coverage builds from zero. It aims to delineate the fluorine coverage at which the interactions of XeF_2 and F_2 diverge. This goal is now possible because of recent extensive and quantitative studies of the mechanism and dynamics of the dissociative chemisorption of F_2 on Si(100)2×1.[21-24] The results of these studies provide a means of calibrating the fluorine

coverage. The calibration in turn enables the absolute probability of the dissociative chemisorption of XeF_2 and the coverage at which etching begins to be determined.

This investigation also aims to test the notion that the release of the exothermicity to the Si upon XeF_2 dissociative chemisorption produces defects in and disorder of the surface structure. The surface defects and disorder are said to be responsible for the onset and subsequent high rates of XeF_2 etching.[25-28] This notion is curious, because our previous work has shown that F_2 incident at low translational energies (<3.8 kcal/mol) on Si(100) reacts only with the Si dangling bonds. No disorder of the surface is evident, even though the dissociative chemisorption of F_2 on Si can be exothermic by as much as 251 kcal/mol.[21,22] Indeed, the absence of disorder and defect formation upon the interaction of F_2 with Si and the absence of F_2 etching are consistent with the notion that disorder is a prerequisite for etching. However, consider the relative exothermicities of the interactions of F_2 and XeF_2 with Si. Although the dissociative chemisorption of XeF_2 is at least 28 kcal/mol *less* exothermic than the dissociative chemisorption of F_2, XeF_2 spontaneously etches Si whereas F_2 does not. It would be of interest to probe whether the dissociative chemisorption of XeF_2 induces disorder and surface defects in contrast to the behavior of the more exothermic interaction of F_2 on Si. The primary roadblock to an assessment of the structure of a fluorine overlayer is that the readily available technique, electron diffraction, is not suitable. The large electron stimulated desorption cross section of fluorine leads to destruction of the overlayer before the structure can be determined. In this study, He atom diffraction is employed to monitor the structure of the fluorine overlayer as a function of exposure to XeF_2 and F_2, thereby testing the notion that disorder and surface defects are necessary for the onset of etching.

II. Experimental

The apparatus has been described in detail elsewhere.[29] Briefly, the apparatus consists of two differentially pumped molecular beam sources coupled to an ultrahigh vacuum chamber (base pressure of 5×10^{-11} Torr) housing the Si crystal, a cylindrical mirror energy analyzer for Auger spectroscopy, an ion sputtering gun, a residual gas mass analyzer and a triply differentially pumped, line-of-sight, rotatable quadrupole mass spectrometer. The spectrometer is equipped with a pseudorandom chopper, allowing for time-of-flight measurements.

II.A. Molecular beams

The primary beam is a semi-effusive expansion of neat XeF_2 (99% pure by F ion titration, Lancaster Synthesis) or F_2 (97% pure, Air Products, without HF trap). To avoid decomposition of the XeF_2 upon exposure to atmospheric gases, the XeF_2 is stored under nitrogen and transferred to a stainless steel vessel in a pressurized nitrogen glove box. The stainless steel vessel is isolated and then attached to the gas-handling manifold leading to the beam source without exposing the XeF_2 to atmosphere. Prior to each day's experiments, the XeF_2 beam is allowed to flow for 15 min. The manifold is then evacuated and the process is repeated. This procedure serves to degas the XeF_2 sample and to passivate the walls of the stainless steel gas-handling manifold.[30] To achieve a constant stagnation pressure, the temperature of the stainless steel vessel containing the XeF_2 solid is held constant at 30($\pm$1) °C by submerging it in a water bath. The remainder of the gas-handling manifold including the nozzle is also warmed to eliminate "cold spots" that would condense the XeF_2 vapor and cause the stagnation pressure to fluctuate. Consequently, the stagnation pressure is constant at 6.40 ± 0.04 Torr as measured by a Baratron capacitance manometer. The neat F_2 is taken directly from

the gas cylinder and regulated at a stagnation pressure of 6.4 torr to match the XeF_2 stagnation pressure. The beams used in most of the experiments presented here are expanded from a $4.7(\pm 0.8) \times 10^{-9}$ m^2 orifice of a Ni nozzle and subsequently pass through a single differential pumping region, with collimating slits located at the entrance and exit of the differential stage. The average translational energy of the XeF_2 and F_2 beams formed in this fashion are 1.95 $\pm$ 0.07 and 1.63 $\pm$ 0.05 kcal/mol respectively, as measured by cross-correlation time-of-flight spectroscopy. The corresponding full energy widths at half maximum are 2.30 and 1.99 kcal/mol, respectively. Beams of XeF_2 and F_2 with average translational energies of 1.29 and 1.32 kcal/mol were also used in some experiments. The results are independent of these small changes in incident energy.

Determination of the absolute beam flux is detailed elsewhere.[22] Briefly, a beam of Ar at a stagnation pressure of 6.40 ± 0.04 Torr is directed into the chamber containing the crystal. The pressure rise in the chamber, P, is measured with a nude Bayard-Alpert ionization gauge and calibrated to the absolute pressure by accounting for the ionization efficiency, C, of Ar. The absolute flux of Ar impinging on an area, A, of the crystal is given by $I^{Ar} = PCS/kTA$ where S is the pumping speed of Ar and T is the temperature of the chamber. The flux of a beam of pure F_2 or XeF_2 at a stagnation pressure of 6.40 ± 0.04 Torr is given by $I = I^{Ar} v/v^{Ar}$ where v and v^{Ar} are the experimentally determined average speeds of F_2 or XeF_2 and Ar, respectively. Since there are two F atoms per molecule in both F_2 and XeF_2, the incident flux in terms of F atoms is I [F atoms/m^2 s] $= 2 I^{Ar} v/v^{Ar}$. This procedure yields values of 0.097(±0.005) and 0.16(±0.01) ML F atom/s for the flux of the incident XeF_2 and F_2 beams, respectively, where 1 ML is the surface density of Si atoms on a Si(100) surface, 6.78×10^{14} atoms/cm^2.

The secondary source is aimed at the crystal so that its beam is at a 20° angle from the primary beam. The secondary beam is a supersonic expansion of 300 torr of a mixture of 75% He (99.9999%, Spectra Gases) / 25% Ar (99.9995%, Spectra Gases) through a 0.002 in. diameter orifice held at 320±20 K. This expansion results in nearly monoenergetic He atoms with an average translational energy of 21.4 meV (FWHM = 13.3 meV) and a 0.93 Å de Broglie wavelength. This beam is used for He diffraction measurements.

II.B. Si(100) crystal

The lightly p-doped Si(100) crystal is mounted between two Ta clamps that are attached to the manipulator. The Ta clamps are flush with the crystal face, thereby eliminating the possibility of spurious shadowing effects of the crystal surface by the beams incident at glancing angles. The crystal can be cooled to 125 K and heated resistively to ~1100 K, as measured via a W-5%Re/W-26%Re thermocouple clamped to the back of the crystal. The temperature is held constant at 250 K during XeF_2 or F_2 exposure. The temperature is stabilized using a proportional-integral-differential (PID) feedback loop to control the resistive heating power supply.

The Si crystal is cut along the (100) plane, and cleaned by a wet etching procedure[31] prior to installation into the vacuum chamber. The crystal is mounted such that the scattering plane, defined by the beams, crystal normal and detector, is along the (10) direction of the crystal surface. Helium diffraction confirms the (2x1) periodicity of the reconstructed Si(100) surface. The crystal is cleaned by sputtering with 1.5 keV Ar^+ followed by a 30 minute anneal at 1100 K. This process is repeated until carbon and oxygen contamination are below the 1% sensitivity limit of Auger electron spectroscopy. No metal contamination, such as W, Ta, Cu, or Ni, is observed. In between experiments, a brief anneal at 1100 K is used to clean the surface and

restore the (2×1) surface periodicity. A heating rate of 2 K/s and a cooling rate of 0.7 K/s is used for all anneals. The crystal is replaced when an etch spot becomes visible, typically after several months of experiments. No difference in the reactivity or the diffraction spectra of the Si(100) crystal is observed over the lifetime of the crystal.

II.C. Detection scheme

Thermal desorption and scattering measurements employ a triply differentially pumped, rotatable quadrupole mass spectrometer with electron bombardment ionization as the detector. The detector rotates in the plane of the beams around their point of intersection at the crystal surface. The angular range of the detector is 35° to 180.5° with respect to the primary beam. Its angular resolution in the scattering plane is 3.52°. It has been shown that use of a properly differentially pumped detector is critical, in particular for the detection of radical species such as SiF_2. Spurious features due to secondary interactions of the radical species with the chamber walls can obfuscate the signal of the radical species scattered directly from the surface.[22]

III. Results

III.A. Dissociative chemisorption probability of XeF$_2$ on Si(100) at 250 K

Recent studies of the interaction of F_2 with Si(100)2×1 have shown that F_2 reacts via atom abstraction with the Si(100) surface dangling bonds. Once each dangling bond is bound to a F atom, the reaction ceases. The resulting saturation coverage is about 1 ML (0.94 ± 0.11).[22] The partial pressures of products desorbing from this layer that are monitored in a thermal desorption experiment and that are integrated over temperature are a measure of 1 ML of adsorbed fluorine. This value is used in the present study to calibrate the fluorine coverage resulting from a known exposure of Si(100) to XeF$_2$. Knowledge of this fluorine coverage

coupled with knowledge of the absolute flux of the incident XeF_2 beam enables the dissociative chemisorption probability of XeF_2 to be determined as a function of coverage, as follows.

The crystal is held at 250 K during exposure to a beam of F_2 or XeF_2. The beam is incident at 20° to the normal of the crystal surface. The crystal is subsequently rotated so that its normal is aligned with the axis of the differentially pumped mass spectrometer. The crystal temperature is then increased at a rate of 5 K/s and the masses at m/e = 66 (SiF_2^+) and m/e = 85 (SiF_3^+) are monitored. The SiF_2^+ and SiF_3^+ signals originate from the ionization or dissociative ionization of the SiF_2 and SiF_4 parent molecules, respectively, in agreement with previous results.[32] Figure 1 shows typical thermal desorption spectra measured after exposure to XeF_2 resulting in a variety of fluorine coverages measured in monolayers, where 1 ML is equivalent to one F atom per Si surface atom. The fluorine coverage determination is described below. The major product, SiF_2, is observed as a single feature around 800 K. The SiF_2 desorption rate exhibits second order kinetics as the coverage increases to 0.30 ML. Above 0.30 ML F atom coverage, the SiF_2 desorption rate is zero order. The minor product, SiF_4, desorbs as two broad features around 500 and 700 K as shown in Figure 1c. These desorption products and kinetics are essentially identical to those that have been previously reported for the interaction of F_2 with Si(100).[24] The thermal desorption traces for the F_2 system are not shown here. However, unlike the F_2 system, desorption of SiF_2 and SiF_4 are observed for coverages greater than 1 ML, as shown in Figures 1a and 1c, because, as explained below, the dissociative chemisorption probability of XeF_2 does not approach zero as the coverage increases to 1 ML.

The total thermal desorption yield at a given exposure or coverage is the sum of the SiF_2 and SiF_4 signals in Figure 1 integrated over temperature.[24] Briefly, the integrated yields of each

product are scaled for the relative detection sensitivities of SiF_2 and SiF_4, the factor of two more fluorine atoms that SiF_4 has relative to SiF_2, the different velocity and angular distributions of the desorbing SiF_2 and SiF_4 species, and their relative ionization cross sections and quadrupole transmissions. The SiF_4 thermal desorption yield as a result of exposure to XeF_2 is small, never exceeding 9% of the SiF_2 yield.

The total thermal desorption yield, in arbitrary units, is plotted on the right hand abscissa in Figure 2 as a function of exposure to XeF_2 and F_2. Both yields increase steadily as the exposure increases from zero to 1 ML F atoms, but beyond this exposure, the yield resulting from exposure to F_2 becomes constant while the yield resulting from exposure to XeF_2 continues to increase. Because the fluorine saturation coverage as a result of exposure to F_2 is known to be 0.94 ± 0.11 ML,[22] the abscissa on the left hand side has been calibrated such that the average of the total yields of the nine highest F_2 exposures (6.5 ML F atom exposure) is 0.94 ± 0.11 ML. With this calibration, it is clear that the fluorine coverage resulting from exposure to XeF_2 increases beyond the approximately 1 ML saturation coverage achieved by exposure to F_2. This observation implies that the dissociative chemisorption probability of XeF_2 on Si(100) covered by 1 ML of fluorine is not equal to zero.

There is a second important difference between the interaction of XeF_2 and F_2 with Si(100) at 250 K. For sufficiently long exposures to XeF_2, the fluorine that adsorbs does not have an infinitely long residence time at 250 K. Instead, the fluorine desorbs as the volatile etch product, SiF_4. This desorption is seen in Figure 3a which plots the signal at m/e = 85 (SiF_3^+), corresponding to SiF_4, as a function of exposure to XeF_2. The XeF_2 beam is incident at 20° from the normal while the mass spectrometer detector is positioned at 15° from the normal. The

ordinate in Figure 3a is converted from exposure to coverage by means of the calibration similar to that shown in Figure 2. The resulting plot of the etch product as a function of fluorine coverage is shown in Figure 3b. For coverages lower than 0.7 ML, negligible etch product is formed while between 0.8-1.0 ML, the amount of desorbing SiF_4 grows rapidly. Beyond 1.0 ML, the observed etch product remains essentially constant. Observation of this etch product is in striking contrast to the interaction of F_2 with Si(100), a system in which no etching is observed when F_2 is incident on Si(100) at 250 K.[22]

The dissociative chemisorption probability of XeF_2 and F_2 as a function of fluorine coverage is calculated from the derivatives of the plots in Figure 2. An exponential function given by

$$\text{coverage [ML]} = 0.950 - 0.970e^{-0.885\varepsilon} \quad \text{for } F_2 \tag{1}$$

$$\text{coverage [ML]} = 2.26 - 2.28e^{-0.362\varepsilon} \quad \text{for } XeF_2 \tag{2}$$

is fit to the measurements of coverage as a function of XeF_2 or F_2 exposure in ML F atoms, ε, in Figure 2. The derivative of these functions with respect to exposure yields the dissociative chemisorption probability as a function of exposure or coverage. The dissociative chemisorption probability as a function of coverage is plotted in Figure 4. Dissociative chemisorption probabilities for XeF_2 are calculated only for coverages below about 0.8 ML, because probabilities determined by this thermal desorption method are only valid when the residence time of the adsorbate is effectively infinite. As discussed above with reference to Figure 3, during exposure to XeF_2, the fluorine begins to desorb as SiF_4 as the fluorine coverage builds to 0.8 ML. More precisely, the probability plotted in Figure 4 represents the sum $0.5P_1 + P_2$, where P_1 is the probability for single atom abstraction and P_2 is the probability for two-atom

adsorption. Single atom abstraction refers to the abstraction of a single F atom from an incoming F_2 or XeF_2 molecule by a Si dangling bond, yielding the complementary fragments F or XeF, respectively, scattered into the gas phase. Two atom adsorption refers to the abstraction of one F atom from the incident F_2 or XeF_2 followed by the adsorption of the complementary F atom in the case of F_2 or the abstraction of the second F atom from the complementary XeF fragment in the case of XeF_2. A more detailed explanation of the definition of the dissociative chemisorption probability is given in the discussion of eq IV.11 in reference 22. The definition of the dissociative chemisorption probability is not of consequence in the present work. It is only of consequence when comparing its value to literature measurements of this quantity.[33,34]

Our previous determination of the quantity $0.5P_1 + P_2$ by a scattering method[22] for the interaction of F_2 with Si(100) has been included for comparison in Figure 4. There is good agreement between the F_2 adsorption probability measured as described here and the measurements made by a scattering method. The F_2 adsorption probability decreases rapidly with increasing coverage, approaching zero at 0.94 ± 0.11 ML, the saturation coverage. In contrast, the XeF_2 adsorption probability is weakly dependent on coverage, decreasing to only about 0.6 at 0.8 ML coverage, the coverage at which etching begins to occur.
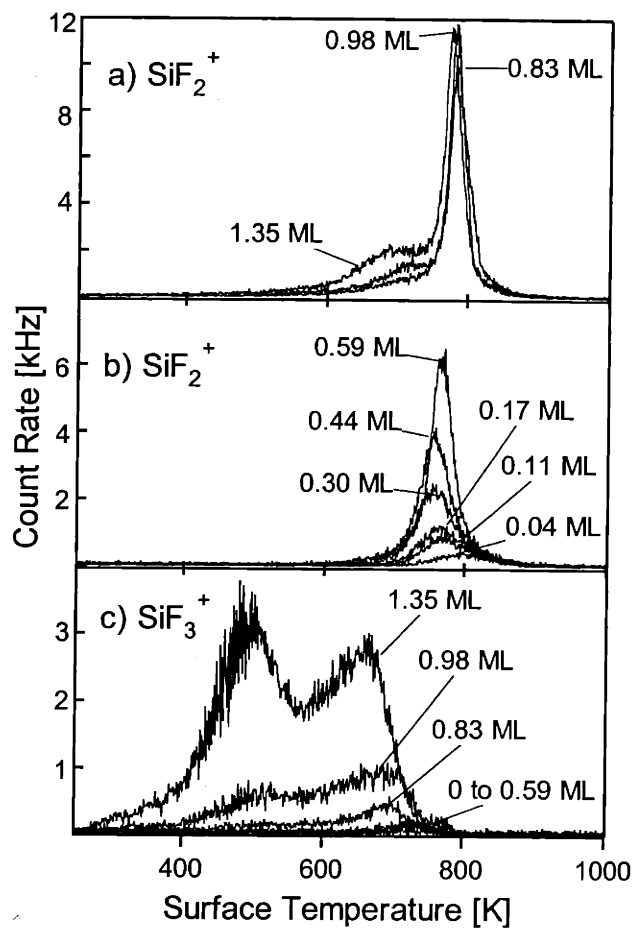
Figure 1 Thermal desorption spectra

Thermal desorption spectra measured at m/e = 66 (a,b) and m/e = 85 (c) after XeF_2 exposure at T_s = 250 K to yield the fluorine coverages in ML F atom that are shown for each trace. Temperature ramp rate is 5 K/s.
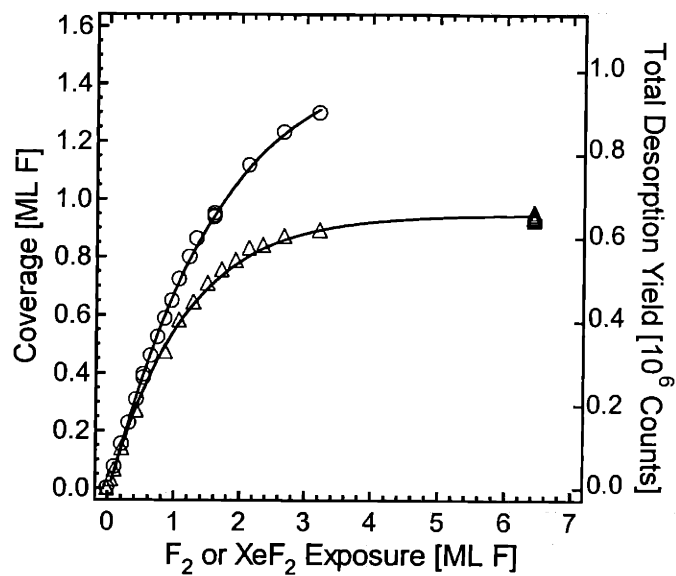
Figure 2 Total thermal desorption yield
Total thermal desorption yield (right axis) and fluorine coverage in ML F atoms (left axis) as a function of exposure to F_2 (triangles) and XeF_2 (circles) in ML F atoms. See text for explanation of axes. Solid lines are exponential fits to the data.
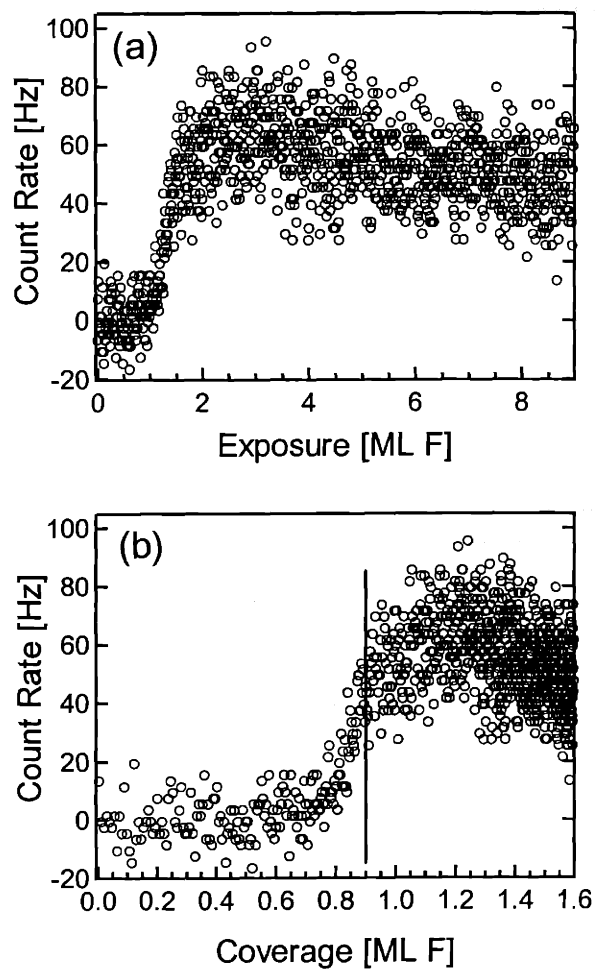
Figure 3 Etch product
SiF_3^+ (m/e = 85) signal as a function of a) exposure and b) coverage during exposure to XeF_2. Average of five experiments. The XeF_2 beam is incident at θ_i = 20°, and the detector is at θ_d = 15° from the normal. The line marks the onset of etching.
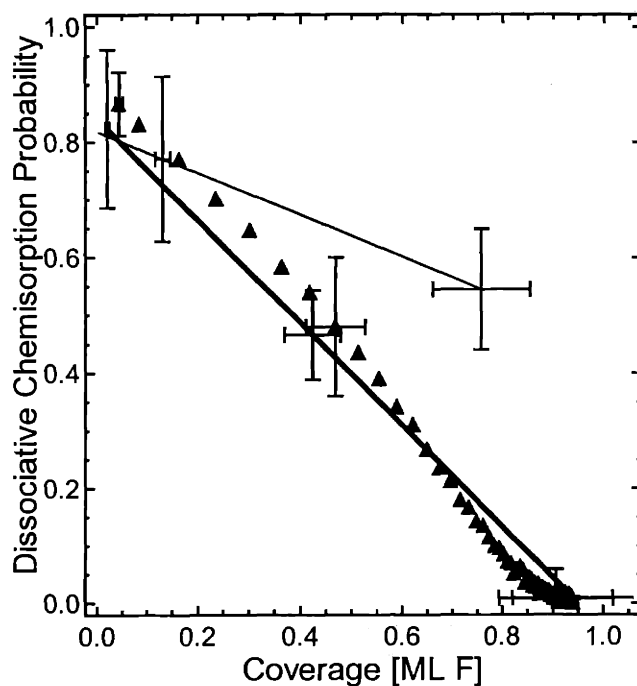
Figure 4 Dissociative chemisorption probability
Dissociative chemisorption probability $(0.5P_1 + P_2)$ calculated from the derivative of the exponential fits in Fig. 2. The thick and thin lines show the derivative of the exponential fits with respect to F_2 and XeF_2 exposure respectively, plotted vs. coverage. The closed triangles show $0.5P_1 + P_2$ adapted from Reference 22. Note that above ~0.8 ML, XeF_2 exposure produces SiF_4 etch product, so the probability cannot be determined by this method. Error bars are 95% confidence limits and are the propagated errors resulting from the uncertainties of the fit in Figure 2, of the beam flux and of the saturation coverage given in reference 22.

III.B. Surface structure determination by He atom diffraction

Previous reports have detailed the He atom diffraction technique with regards to the reconstructed Si(100) surface[35] and specifically its application to the fluorinated surface.[24] Si(100) reconstructs forming rows of surface Si dimers resulting in one partially-filled molecular orbital or dangling bond projecting into the vacuum for each surface Si atom. The distance between equivalent Si atoms in adjacent dimers in the same row is the same as the lattice spacing, while the distance between equivalent Si atoms in dimers from adjacent rows is twice the lattice spacing, resulting in a (2×1) surface unit cell that is observable by He diffraction.

The characteristic He diffraction spectrum arising from this reconstructed surface is shown in Figure 5a as a function of angle from the surface normal. All He diffraction spectra are measured from a surface at 250 K and with the He beam incident at 40° from the surface normal. The scattered He signal is presented in Figure 5a with no background subtraction. The resulting spectrum consists of specular, half-order and first-order diffraction features, as indicated in Figure 5a. The broad width of the diffraction features is a consequence of the large acceptance angle of the detector, which was chosen to optimize the intensity of the reactively scattered signal rather than the angular resolution of the elastically scattered signal. The widths of these features can be reproduced well in a simulation that convolutes the finite size of the incident beam and the detector chamber entrance slits with the distribution of velocities of the incident beam.[36] The intensity of the specular feature is quite sensitive to disorder, and is used in this study as a measure of the overall surface order. The half-order diffraction feature arises from the periodic doubling of the lattice spacing in the direction perpendicular to the dimer rows. It is therefore a signature for the presence of the Si dimers, and is used in this study as an indicator

for cleavage of Si-Si σ dimer bonds upon the adsorption of fluorine. The first order feature arises from diffraction parallel to the dimer rows.

The Si dangling bonds, which are effectively radical sites and hence very reactive species, are the logical sites for F atom reaction. It has been reported earlier that F_2 reacts solely at the dangling bonds on the Si(100) surface, and that no Si-Si lattice bonds or σ dimer bonds are broken.[24] Shown in Figure 5b is a He diffraction spectrum of the Si surface after sufficient exposure to F_2 to saturate the dangling bonds. Although the intensities of the features are changed upon fluorination from that of a clean surface, the (2×1) periodicity persists. The reaction produces a fully fluorinated and well ordered Si(100)2×1 surface where no Si-Si bonds have been broken, the Si dimers remain intact, and each surface Si atom is decorated with a single fluorine atom. The F_2 does not etch the Si surface.[22]

A He diffraction spectrum measured after exposure of Si(100) to 1.5 ML F atom of XeF_2, which yields a coverage of 0.9 ML, is shown in Figure 5c. The diffraction spectrum measured after this exposure to XeF_2 is nearly identical to the spectrum measured after F_2 exposure in Figure 5b! The dimer rows are intact as indicated by the persistence of the (2×1) periodicity, and at 0.9 ML coverage, almost every surface Si atom is decorated with a single fluorine atom. Despite its superior etching ability and large reaction exothermicity, XeF_2 has not induced any significant disorder of the surface, even though XeF_2 has reacted sufficiently to cover the surface with 0.9 ML F atoms.

While this experiment provides a snapshot of the fluorine overlayer at a single coverage, it is informative to probe the surface periodicity as the fluorine overlayer evolves. To do so, the intensities of the He diffraction features are monitored as a function of F_2 or XeF_2 exposure.

The He probe beam is incident at 40° with respect to the surface normal, while the F_2 or XeF_2 reactant beam is simultaneously incident at 20° with respect to the normal. The differentially pumped mass spectrometer is positioned at 40° from the normal angle in the forward scattering direction. The intensity of the specular feature is then monitored by the mass spectrometer as a function of exposure. Figure 6a shows the evolution of the specular feature with respect to exposure of Si(100) to both F_2 and XeF_2. The maximum intensities of both traces have been normalized. Figure 6b shows the same evolution of the intensity of the specular feature plotted with respect to coverage. The coverage at a given exposure is calculated from expressions such as shown in eqs 1 and 2. The intensity of the specular feature decays rapidly during the initial exposure of the surface to both F_2 and XeF_2. This initial loss of intensity can be understood in terms of fluorination of the surface at random sites. The presence of a F atom bonded to a dangling bond changes the interaction potential of the He atom with that surface unit cell, thereby making it different from the surrounding unit cells that do not yet include a F atom. The surface order is disrupted, thus resulting in a loss of coherency of the diffracted He beam.[24,37] The specular intensity reaches a minimum at about 0.35 ML and then begins to recover. This recovery signals the transition to a new order as the periodicity of the fluorinated surface unit cells begins to predominate over the unfluorinated unit cells. Eventually the original (2×1) periodicity is recovered, indicating that most dangling bonds are fluorinated and that most unit cells are fluorinated identically as their neighbors. The intensity of the specular feature fully recovers at 0.9±0.1 ML coverage, corresponding to F_2 and XeF_2 exposures of 3-5 ML and 1.3 ML F atoms, respectively. The uncertainty in the coverage arises from the propagated uncertainty in the fit of the thermal desorption signal and the uncertainty of the previously reported determination of the saturation coverage.[22]

The recovery of the specular feature at a coverage that is slightly below the coverage of 1 ML where the surface is more fully ordered can be understood in terms of the limited transfer width of the apparatus. As discussed elsewhere in detail,[24] the transfer width of the apparatus is estimated as 35 Å, which means that ordered regions of the surface greater than 35 Å in length will not contribute to the intensity of the diffracted beams.[38] That is, once the ordered regions of the surface have increased past this size, the intensity of the diffracted beam will remain constant as the coverage increases. However, for microscopic two-dimensional ordering below the transfer width of the apparatus, the He diffracted intensities are extremely sensitive to surface disorder. As apparent in Figure 6b, the He diffraction technique is sensitive to the surface disorder produced by a change in coverage of as little as 0.01 ML.

Figure 6 shows that in the sub-monolayer coverage regime, there is a striking similarity between F_2 and XeF_2. In fact, up to 0.9 ML coverage, it would be extremely difficult to distinguish between the two reactants based solely on the evolution of the surface order. However, beyond 0.9 ML, the reactivities differ greatly. The intensity of the specular feature remains essentially constant upon further exposure to F_2, because the F_2 dissociative chemisorption probability becomes effectively zero, as shown in Figure 4. In contrast, the intensity of the specular feature decreases rapidly upon further exposure to XeF_2, indicating that the periodicity is rapidly destroyed.

The half-order and first-order diffraction features were also monitored as a function of coverage during exposure to XeF_2. The half-order feature is of interest because it is arises from the periodicity of the dimer rows, and hence is only visible when the dimer bonds are intact. It is used in this study as an indicator for the cleavage of Si-Si σ dimer bonds upon the adsorption of fluorine. The He probe beam is incident at 40° with respect to the surface normal, while the F_2

or XeF$_2$ reactant beam is simultaneously incident at 20° with respect to the normal. The intensity of the first and half order features are monitored by the differentially pumped mass spectrometer positioned at 21.5° and 51.25°, respectively, from the normal in the forward scattering direction. The evolution of these features, whose intensities are normalized, as a function of coverage resulting from XeF$_2$ exposure is shown in Figure 7. Both features show the characteristic initial decrease caused by random fluorination, recovery at 0.9 ML, and subsequent decay. The decay of the both features beyond 0.9 ML is evidence for the destruction of the (2×1) periodicity and hence the cleavage of the Si-Si σ dimer and Si-Si lattice bonds due to continued reaction with XeF$_2$. Indeed, the dissociative chemisorption probability of XeF$_2$ remains high at 0.9 ML, as shown in Figure 4. In addition, the onset of desorption of the etch product, SiF$_4$, is observed at this coverage, as shown in Figure 3. Clearly, in contrast to the interaction of F$_2$ with 1 ML of F adsorbed on Si(100), the XeF$_2$ reacts at this coverage, depositing additional fluorine while cleaving Si-Si bonds. The additional fluorine and the desorption of the etch product lead to disordering of the surface, as evident by He atom diffraction.
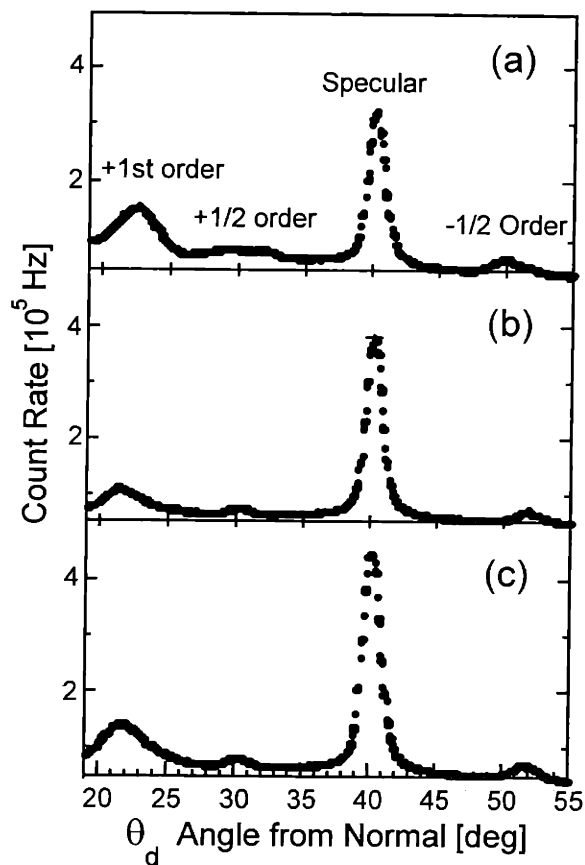
Figure 5 Helium diffraction spectra

Helium signal scattered from Si(100) at 250 K and at $\theta_i = 40°$ as a function of detector angle θ_d: (a) clean surface; (b) 0.9 ML coverage resulting from F_2 exposure; (c) 0.9 ML coverage resulting from XeF_2 exposure. Each point represents a measurement made with a dwell time of 2 s and at angular intervals of 0.25°. Error bars on the He atom count rate are smaller than the width of each point.
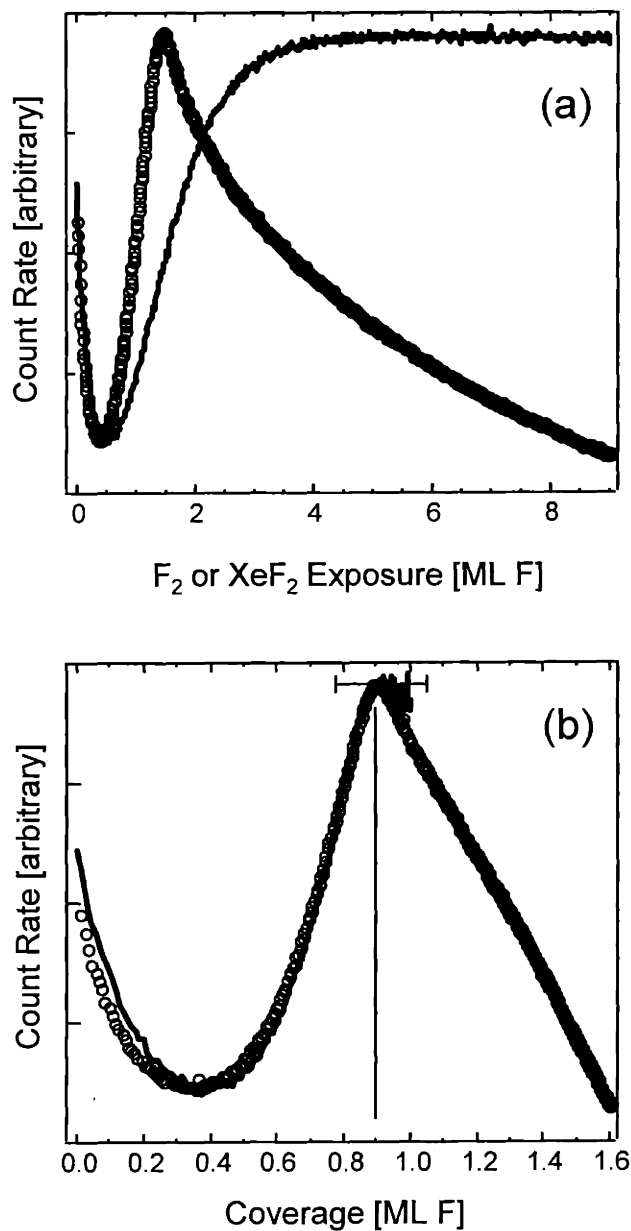
Figure 6 Helium diffraction specular feature intensity
Intensity of the specular He diffraction feature as a function of a) exposure; b) coverage during exposure to F_2 (solid line) and XeF_2 (open circles). The He beam is incident at $\theta_i = 40°$; the F_2 or XeF_2 beam is incident at $\theta_i = 20°$; the detector is positioned at $\theta_d = 40°$. Signals have been normalized at the maximum intensity of each trace. Error bars on the He atom count rate are smaller than the width of each point. The line marks the coverage at which the scattered He signal is a maximum.
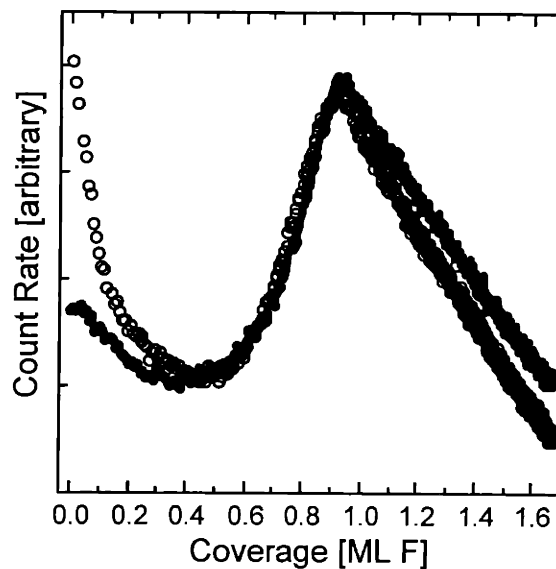
Figure 7 Helium diffraction half and first order features intensity

Intensity of the +1 order (solid line) and -1/2 order (open circles) He diffraction features as a function of coverage during exposure to XeF_2. The He beam is incident at $\theta_i = 40°$; the F_2 or XeF_2 beam is incident at $\theta_i = 20°$; the detector is positioned at $\theta_d = 21.5°$ (+1 order) or $\theta_d = 51.25°$ (-1/2 order). Signals have been normalized at the maximum intensity of each trace. Error bars on the He atom count rate are smaller than the width of each point.

IV. Discussion

This study has shown that dissociative chemisorption of XeF_2 proceeds in the manner identical to that of F_2 as the coverage increases from zero to about 1 ML on Si(100)2×1. Figure 6b shows that the intensity of the specular He diffraction feature as a function of fluorine coverage produced by the dissociative chemisorption of XeF_2 is indistinguishable in this coverage regime from that produced by the dissociative chemisorption of F_2. Both XeF_2 and F_2 dissociatively chemisorb initially by reacting solely with dangling bonds at random sites, leading to a loss of coherence of the zero order diffraction beam. As the coverage increases and more unit cells are fluorinated, the coherence of the specular beam recovers and its intensity becomes a maximum at about 0.9 ML for both systems, XeF_2 and F_2. Diffraction spectra measured from a fluorinated surface at 0.9 ML coverage over a wide angular range are shown in Figures 5b and 5c for the F_2 and XeF_2 systems, respectively. They reveal that the fluorinated surface is well-ordered with a (2×1) periodicity. The dimer rows remain intact with each surface Si atom decorated with a fluorine atom. The only difference between XeF_2 and F_2 in this coverage regime is that the chemisorption probability of XeF_2 decreases only slowly as the coverage approaches 1 ML while that of F_2 decreases rapidly and is effectively zero at 1 ML, as shown in Figure 4. The relative constancy of a chemisorption probability with coverage is usually interpreted in terms of a long lifetime of an extrinsic precursor, which is a species physisorbed on top of filled sites.[39] An extrinsic precursor diffuses on top of the filled sites until it encounters an empty site, such as a dangling bond, and reacts or desorbs without dissociating. In short, the extrinsic precursor makes it more likely that a XeF_2 molecule will encounter an unoccupied dangling bond and hence, increases the dissociation probability. The substantially greater

polarizability of XeF_2 as compared to F_2 suggests that a XeF_2 extrinsic precursor would have a longer lifetime than that of F_2. A second explanation for the relative constancy of the dissociative chemisorption probability is the longer collision time of XeF_2 as compared to F_2. Because it is four times more massive than F_2, XeF_2 spends twice as long as F_2 in the near surface region where it may encounter an unoccupied dangling bond. It is not clear from the present study if both effects or either of them are operative.

Once the dangling bonds are saturated at about 1 ML coverage, the interactions of XeF_2 and F_2 differ dramatically. While the reaction of F_2 with Si(100) essentially ceases, XeF_2 continues to dissociatively chemisorb, as indicated by the increase in fluorine coverage beyond 1 ML in Figure 2. Chemisorption of fluorine beyond 1 ML requires cleavage of the Si-Si σ dimer bonds, the Si-Si lattice bonds or both. The simultaneous decay of both the first and half order diffraction features provides evidence that the cleavage of both types of Si-Si bonds is occurring. The concomitant cleavage of Si-Si bonds and formation of Si-F bonds leads to disorder of the surface periodicity, as indicated by the decay of the specular, first and second order diffraction features as the coverage increases beyond 1 ML. The increased fluorine coverage results in the formation of higher fluorinated species such as SiF_2 and SiF_3. These species have been identified in XPS measurements of Si(100) at approximately 1.5 ML coverage.[40-42] They eventually form the SiF_4 that desorbs. In short, XeF_2 etches the Si surface while F_2 does not.

Clearly, the dangling bond sites on the Si(100) surface are by far the dominant sites for the dissociative chemisorption of XeF_2, just as they are for F_2.[27,43,44] Previous work has demonstrated that the mechanism for dissociative chemisorption of F_2 is atom abstraction. The cross section for F atom abstraction from F_2 by the dangling bonds is measured to be large

compared to the cross sectional area of a surface site.[23] The large cross sections suggest the presence of an attractive interaction potential that is consistent with the notion of molecular steering.[45,46] Recent work has also provided direct evidence for atom abstraction in the $XeF_2/Si(100)$ system.[47] Upon saturation of the dangling bonds, the only sites available for reaction are ones that involve cleavage of Si-Si bonds. An F_2 molecule incident at thermal energies does not react with them. In fact, it has been shown that a barrier to that reaction of 3.8 kcal/mol exists.[24] This barrier can be surmounted by translational activation of F_2. In contrast, it is apparent that no such barrier exists in the case of XeF_2. The XeF_2 molecule incident at thermal energies reacts readily with these sites.

An important point demonstrated by this study is that the exothermicity released to the surface upon dissociative chemisorption of XeF_2 or F_2 below about 1 ML coverage does not destroy the surface order, in contrast to the conclusions of previous work.[25-28] It is also clear that the presence of disorder is not a precondition for etching to begin. Clearly, XeF_2 begins to react with the Si-Si bonds in the presence of an ordered overlayer of fluorine. It is the reaction of XeF_2 with these Si-Si bonds that leads to the disorder of the surface periodicity rather than the disorder induced by the exothermicity release that leads to the reaction of XeF_2 with the Si-Si bonds.

We have shown that the reaction of low energy XeF_2 with the Si(100)(2×1) reconstructed surface occurs solely at the Si dangling bonds up to a fluorine coverage of 0.9 ML. No Si-Si bonds are broken, and the ordered (2×1) reconstruction is preserved. The presence of the half-order feature at 0.9 ML coverage provides evidence that even the Si-Si σ dimer bonds are undisturbed, preserving the original dimer rows. Up until 0.9 ML, the reaction of XeF_2 with Si

is remarkably similar to the reaction of F_2, especially considering the fact that their steady-state etch rates differ by four orders of magnitude. However, after saturation of the dangling bonds, F_2 ceases reacting with the surface while XeF_2 continues to deposit fluorine on the surface by reaction with the Si-Si bonds. The surface order is destroyed as a result of the continued fluorine deposition and ultimately etching occurs by the formation of volatile SiF_4.

V. Supplemental Information

V.A. XeF$_2$ handling procedure

Xenon difluoride is a stable crystalline solid at room temperature with a vapor pressure of ~5 torr. However, it is also strong oxidizer and extremely reactive. In the presence of atmospheric water, XeF$_2$ hydrolyzes to form Xe and HF. The HF is corrosive around the edges of the nozzle orifice and can therefore produce volatile fluorinated metal species, which could potentially result in unacceptable metal contamination on the crystal surface. The HF can also directly interfere with the experimental results as it can cause an unintended side reaction with the Si crystal. The other contaminant produced as a result of the hydrolysis is Xe, which can be unreactively scattered from the crystal surface and contribute to the observed signal at m/e=129. This complicating contribution must be eliminated, as described in Chapter 3. A handling protocol was therefore developed to avoid exposure of the XeF$_2$ sample to atmosphere.

Xenon difluoride (99% pure by F ion titration, Lancaster Synthesis) is synthesized and packaged into PTFE bottles under an inert nitrogen environment. The PTFE bottles are stored in a sealed, desiccated bell jar until needed. The solid XeF$_2$ is transferred from the PTFE bottle to a stainless steel "transport" in a dry nitrogen glove box. The XeF$_2$ transport is shown in Figure 8 and consists of a valve that is connected by a gasket seal to a larger storage vessel. Prior to the transfer procedure the transport is attached to the manifold and baked out under vacuum to insure that no atmospheric water is adsorbed on the stainless steel surface before it comes in contact with the XeF$_2$. After the bakeout the valve seal is closed, and the transport is removed from the gas manifold at the 1/4" VCR connection. The transport is then put into a nitrogen glove box along with the sealed XeF$_2$ PTFE bottle. The 1/2" VCR connection between the valve and the storage vessel is broken, and the XeF$_2$ is transferred to the storage vessel from the PTFE bottle.

The 1/2" VCR connection is then re-sealed, and the transport is re-attached to the gas handling manifold. This procedure insures that at no point does the XeF_2 sample come in contact with atmospheric water.

However, even after this exhaustive procedure is followed, XeF_2 is still observed to react with the manifold and nozzle. A mass spectrum of the initial XeF_2 beam shows that most of the beam is Xe, with little signal from XeF_2.[48] If the beam is left on and the Xe^+ and XeF_2^+ signals are monitored, it is observed that the ratio of XeF_2^+ signal to Xe^+ signal monotonically increases until a steady-state level is reached after approximately five minutes at a stagnation pressure of 6.4 torr. This phenomenon is referred to as "passivation" of the nozzle. The XeF_2 reacts with the metal of the manifold or nozzle, releasing free Xe atoms and forming a thin fluorinated surface layer in a self-limiting reaction.[49] It was found that if the XeF_2 is evacuated from the manifold and the XeF_2 beam is restarted then the XeF_2^+:Xe^+ ratio would increase by approximately 25% to a higher steady-state level. If the beam was pumped out and restarted once more, then the XeF_2^+:Xe^+ ratio did not change significantly, and further pump out/restart cycles did not affect the XeF_2^+:Xe^+ ratio. This observation led to the following "passivation procedure" which was performed at the beginning of each day prior to performing any experiments. The XeF_2 beam is started and allowed to run for 15 minutes. Then the XeF_2 beam is stopped, the manifold evacuated, and the beam restarted. The beam is allowed to run for another 15 minutes, then pumped out and restarted. At this point, the nozzle and manifold are considered "fully passivated" and experiments are begun.

Although the ratio XeF_2^+:Xe^+ is constant after the passivation procedure, it is possible that the XeF_2 continues to react with the nozzle at a constant rate, producing free Xe contamination in the beam. Concern about this possible free Xe contamination motivated the

construction of a manifold and nozzle made entirely of PTFE and Teflon, described fully in chapter 3.

Stainless steel
bellows-sealed
packless valve

1/2" SS tube
containment vessel

Re-sealable
1/4" VCR fitting
to gas manifold

Re-sealable
1/2" VCR connection

1/2" VCR plug
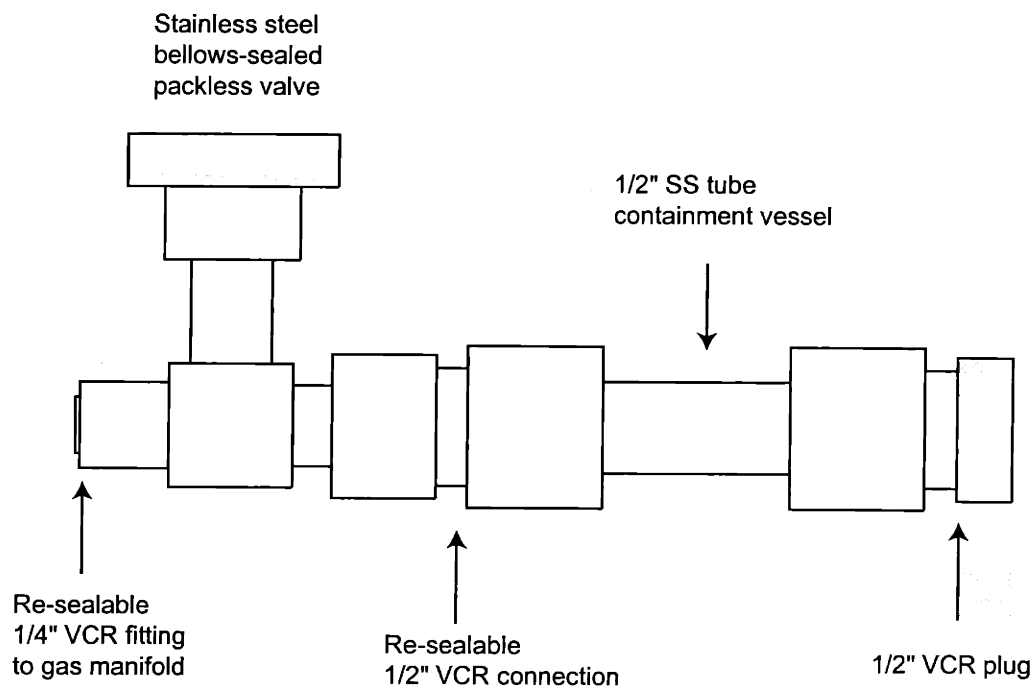
Figure 8 Schematic picture of XeF$_2$ transport and containment vessel

V.B. Stainless steel gas handling manifold

During one of the transfer procedures an incident occurred that highlights the high reactivity of XeF_2 and the need to keep it isolated from atmospheric water. While tightening the gasket seals on the transport vessel in the glove box, a fragment of XeF_2 lodged in the gasket, which led to an improperly tightened seal. When the vessel was subsequently submerged in the constant-temperature bath, water leaked through this seal, forming a concentrated aqueous HF/XeF_2 slurry. This mixture then reacted with the stainless steel walls of the gas handling manifold, producing a greenish oxide residue. This oxide residue resulted in a persistent contamination problem, manifested in the observation of a substantial signal (about 50% of the signal at $m/e=38$) at $m/e=32$, presumably due to O_2, in the mass spectrum of the incident F_2 beam. The signal at $m/e=32$ could not be eliminated by heating, high pressure F_2 treatment, or cleaning by various organic solvents of the gas manifold. Since it was impossible to physically scrub the interior surfaces, it was necessary to entirely rebuild the manifold. Figure 9 shows a schematic of the design of the replacement manifold. The replacement manifold was designed along similar lines as the original design.[50] However, there are some notable differences. The original manifold was copper brazed in a vacuum oven, while the replacement manifold is made entirely from welded stainless steel. This minimizes any potential contamination from the copper braze. The original manifold was constructed as one piece, while the replacement manifold was designed as a three-piece modular construction. This will allow for greater flexibility if further modifications are necessary. The original manifold utilized several different connectors, including VCR metal gasket face-seal fittings, VCO viton face-seal fittings, and Swagelok ferrule-seal fittings. However, our experience has shown us that most Swagelok connections will eventually develop small leaks over the course of years. This could lead to

unacceptable contamination by atmospheric gases. Therefore, all connections were standardized to VCR metal gasket face-seal fittings. A final change in the design of the manifold is that the leak valve has replaced the pressure regulator as the primary method of controlling the beam stagnation pressure, a method that has proved effective in regulating stagnation pressures up to 700 torr. Since the molecular beams used for the present experiments are regulated at a stagnation pressure of 300 torr or less, the pressure regulator has been removed, although the connection ports have been preserved. Using the new manifold, the m/e=32 signal is reduced to less than 0.05% of the m/e=38 signal in the incident F_2 beam.
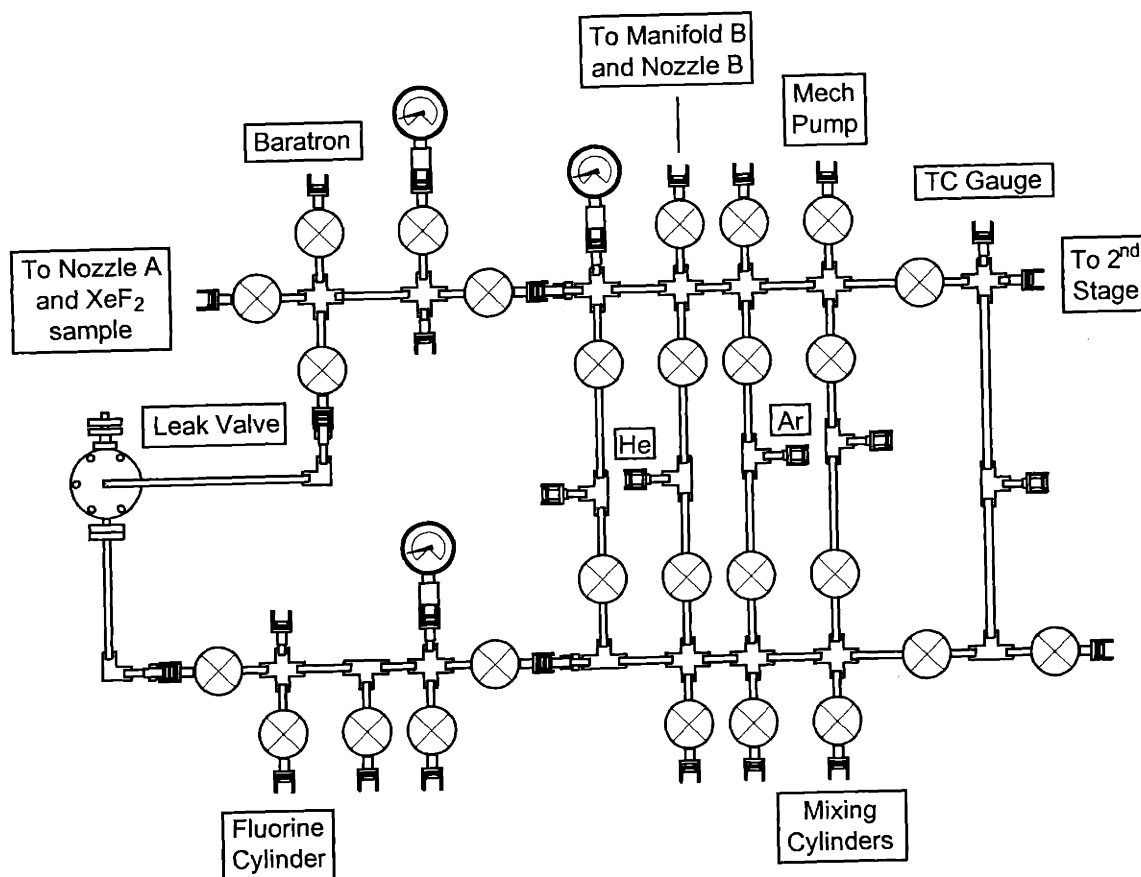
Figure 9 Schematic picture of new primary gas handling manifold
Fittings that are not labeled have been blanked off.

V.C. Effusive molecular beams

Ideally, the presence of a skimmer in between the nozzle beam source and the collimating slits should not affect the effusive beam flux. However, it was found that removal of the skimmer resulted in an increase of approximately a factor of two in the incident beam flux of the quasi-effusive beam, as determined by the pressure rise from a pure Ar beam. From this result it is clear that the presence of the skimmer was reducing the intensity of the beam more than that expected from geometrical constrictions. Therefore, the skimmer was removed for the duration of the present experiments. It is unclear as to the exact cause of the intensity reduction. One possible cause is that there was a slight misalignment of the nozzle and skimmer, which then resulted in an attenuation of the beam at lower beam fluxes. The removal of the skimmer results in a loss of differential pumping between the source and 1st stage pumping stages. Thus, the effusive beam without the skimmer has only two stages of differential pumping on the source, compared to the supersonic beam studies, which had three stages of differential pumping on the source.

The primary beam is a semi-effusive expansion of neat XeF_2 (99% pure by F ion titration, Lancaster Synthesis) or F_2 (97% pure, Air Products). Two separate nozzles are used in the present experiments. The measurement of the etch product and the helium diffraction results presented in Figures 3, 5, 6, and 7 are performed using a Nickel nozzle and a stagnation pressure of 6.40±0.04 torr as measured by a Baratron capacitance manometer. The thermal desorption results shown in Figures 1 and 2 are performed using a Teflon nozzle, which is described in detail in Chapter 3, and a stagnation pressure of 0.62±0.02 torr. To achieve a constant stagnation pressure of 6.40 torr, the temperature of the stainless steel vessel containing the XeF_2 solid is held constant at 30°±1° C by submerging it in a heated water bath. To achieve a constant

stagnation pressure of 0.62 torr, the temperature of the XeF_2 sample is held constant by immersion in an ice bath. The remainder of the gas-handling manifold including the nozzle is warmed in either case to eliminate "cold spots" that would condense the XeF_2 vapor and cause the stagnation pressure to fluctuate. The neat F_2 is taken directly from the gas cylinder and regulated at a stagnation pressure of 0.62 torr or 6.40 torr to match the XeF_2 stagnation pressure. The orifice of the Nickel nozzle has been measured using a comparator to have a cross-sectional area of $4.7\pm0.8x10^{-9}$ m^2. The cross-sectional area has also been estimated using the beam flux of an effusive expansion of pure Ar to be $2.0x10^{-9}$ m^2, more than a factor of two lower. The source of this discrepancy is unclear, but may be the result of an hourglass-shaped cross-section for the aperture. The area of the aperture of the Teflon nozzle has not been measured using a comparator, but an estimate based on the beam flux of an effusive expansion of pure Ar yields a value of $5.6x10^{-9}$ m^2, which is larger than the value found for the Nickel nozzle. In the case of the experiments performed with the Nickel nozzle, the effusive beams are expanded from the nozzle orifice, and subsequently pass through two differentially pumped regions, with collimating slits located at the exit of the second differential stage. In the case of the experiments performed with the Teflon nozzle, the effusive beams pass through only one differentially pumped region, with collimating slits located at the exit of the differential stage. The geometry of the Teflon nozzle is fully described in Chapter 3.

The time-of-flight (TOF) spectra of the incident F_2 and XeF_2 expanded from the Nickel nozzle at a stagnation pressure of 6.40 torr are shown in Figure 10a and Figure 10b respectively, and the resulting energy distributions of both beams are shown in Figure 10c. The average translational energy of the XeF_2 and F_2 beams formed in this fashion are 1.95 ± 0.07 kcal/mol and 1.63 ± 0.05 kcal/mol respectively. The corresponding full widths at half maximum are 2.30

kcal/mol and 1.99 kcal/mol, respectively. Also shown for comparison is the energy distribution of a purely effusive expansion at 300 K, which has an average energy of 1.19 kcal/mol, and a FWHM of 1.44 kcal/mol. It can be seen that the energy distribution of the quasi-effusive beams are somewhat more energetic than a purely effusive expansion. The measurement of the absolute beam flux for a quasi-effusive expansion is detailed above. The absolute flux of the XeF_2 and F_2 beams formed in this way is 0.097±0.005 and 0.16±0.01 ML F atom/s respectively.

The TOF spectra of the incident F_2 and XeF_2 expanded from the Teflon nozzle at a stagnation pressure of 0.62 torr are shown in Figure 11a and Figure 11b respectively and the resulting energy distributions of both beams are shown in Figure 11c. The average translational energy of the XeF_2 and F_2 beams formed in this fashion are 1.28±0.01 kcal/mol and 1.31±0.01 kcal/mol respectively. The corresponding full widths at half maximum are 1.52 kcal/mol and 1.59 kcal/mol, respectively. It is evident that the energy distributions of these beams are much closer to the energy distribution of a purely effusive distribution. The absolute flux of the XeF_2 and F_2 beams formed in this way is 0.053±0.003 and 0.11±0.01 ML F atom/s respectively, as calculated in Appendix B.
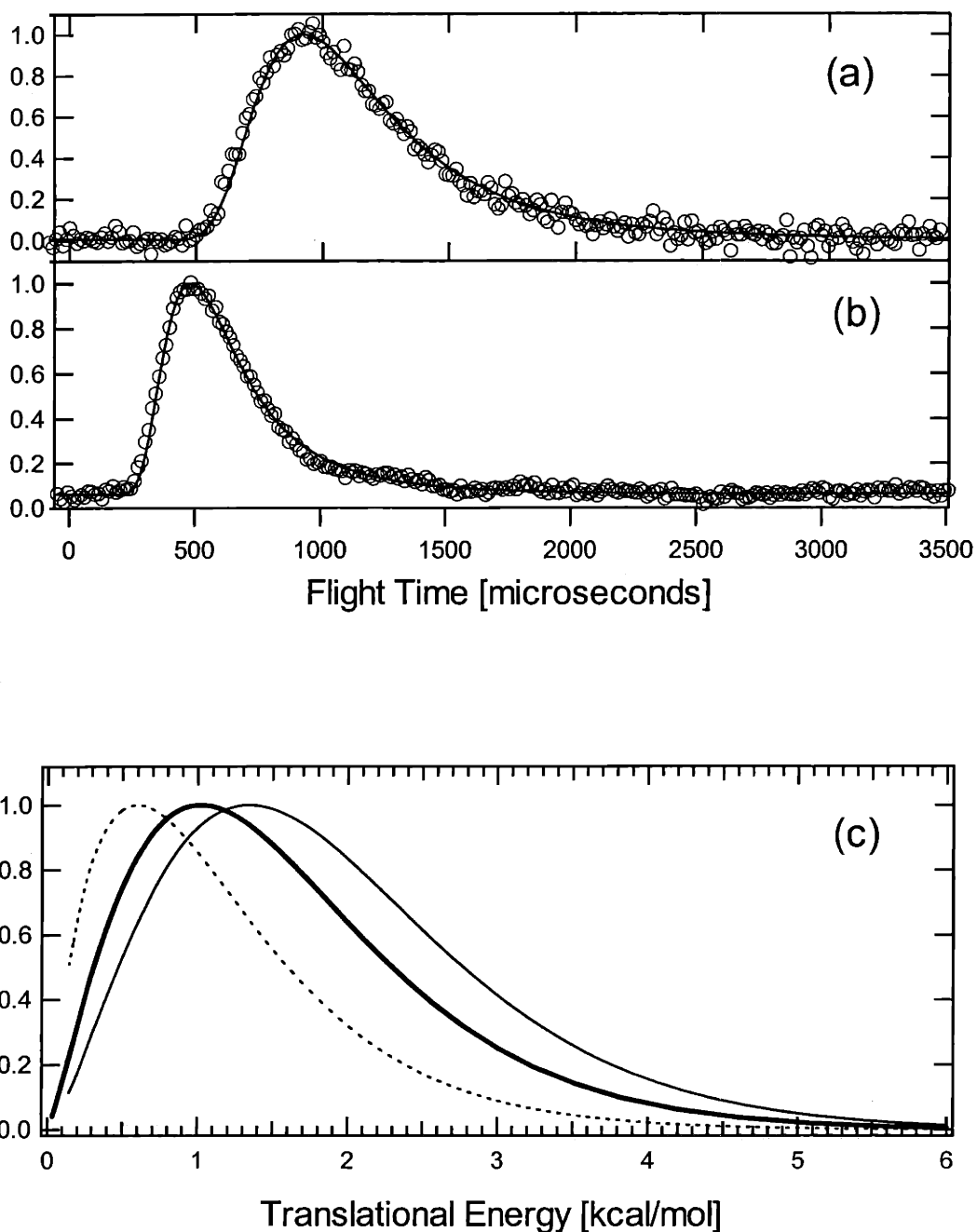
Figure 10 TOF distributions of F_2 and XeF_2 molecular beams from the Nickel nozzle
(a) TOF spectrum of quasi-effusive molecular beam expansion of 6.40 torr neat XeF_2. Solid line shows fit to the data of the Maxwell-Boltzmann function. (b) TOF spectrum of quasi-effusive molecular beam expansion of 6.40 torr neat F_2. Solid line shows fit to the data of the Maxwell-Boltzman function. (c) Kinetic energy distribution of quasi-effusive molecular beam of neat XeF_2 (thin line) and quasi-effusive molecular beam of neat F_2 (thick line). The translational energy distribution for a purely effusive molecular beam at 300 K is shown as a dashed line for comparison.
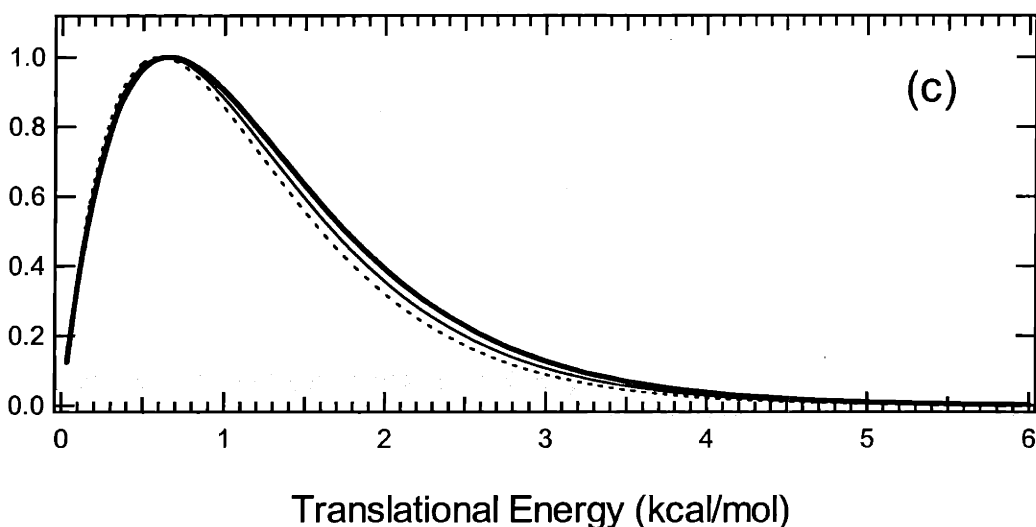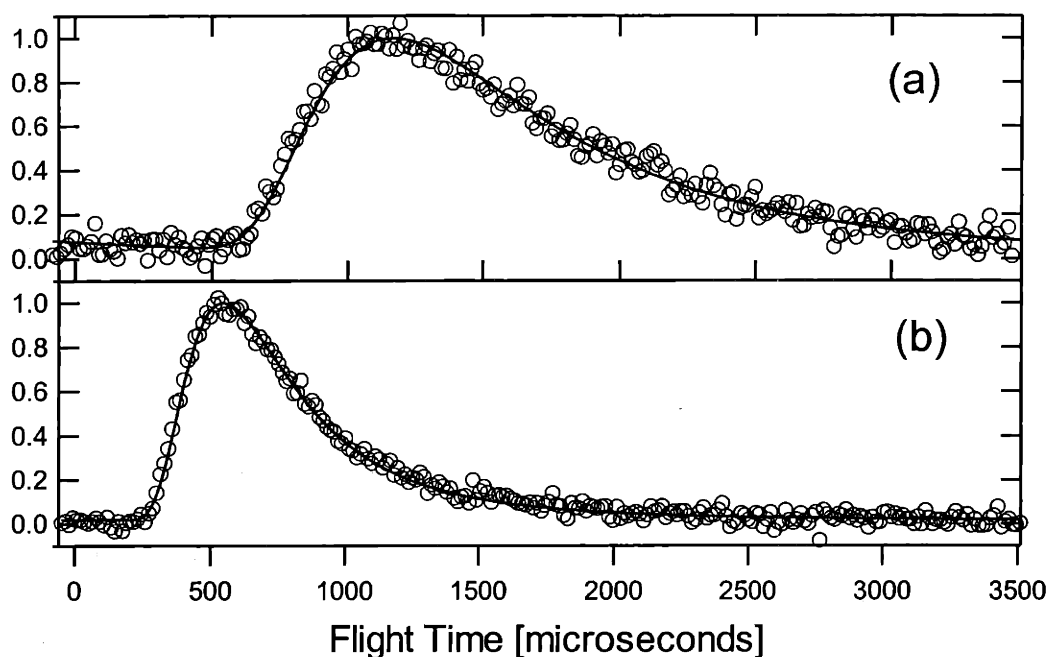
Figure 11   TOF distributions of F_2 and XeF_2 molecular beams from the Teflon nozzle
(a) TOF spectrum of quasi-effusive molecular beam expansion of 0.62 torr neat XeF_2. Solid line shows fit to the data of the Maxwell-Boltzmann function. (b) TOF spectrum of quasi-effusive molecular beam expansion of 0.62 torr neat F_2. Solid line shows fit to the data of the Maxwell-Boltzman function. (c) Kinetic energy distribution of quasi-effusive molecular beam of neat XeF_2 (thin line) and quasi-effusive molecular beam of neat F_2 (thick line). The translational energy distribution for a purely effusive molecular beam at 300 K is shown as a dashed line for comparison.

V.D. Helium diffraction probe beam

The secondary source is aimed at the crystal so that its beam is at a 20° angle from the primary beam. The secondary beam is a supersonic expansion of 300 torr of a mixture of 75% He (99.9999%, Spectra Gases) / 25% Ar (99.9995%, Spectra Gases) through a 0.002 in. diameter orifice held at 300±20 K. The TOF spectrum of the resulting beam is shown in Figure 12a, and the energy distribution is shown in Figure 12b. This expansion results in nearly monoenergetic He atoms with an average velocity of 1003±37 m/s and an average energy of 0.49±0.04 kcal/mol, or 21±2 meV (FWHM = 13 meV) and a 0.93 Å de Broglie wavelength. This beam is used for He diffraction measurements. The fit is slightly poorer than those reported earlier.[51] The small peaks at longer flight time could be caused by harmonics of the main peak, or by slight imperfections in the machining of the chopper slits, or by slight variations in the speed of the chopper during the experiment.[52]
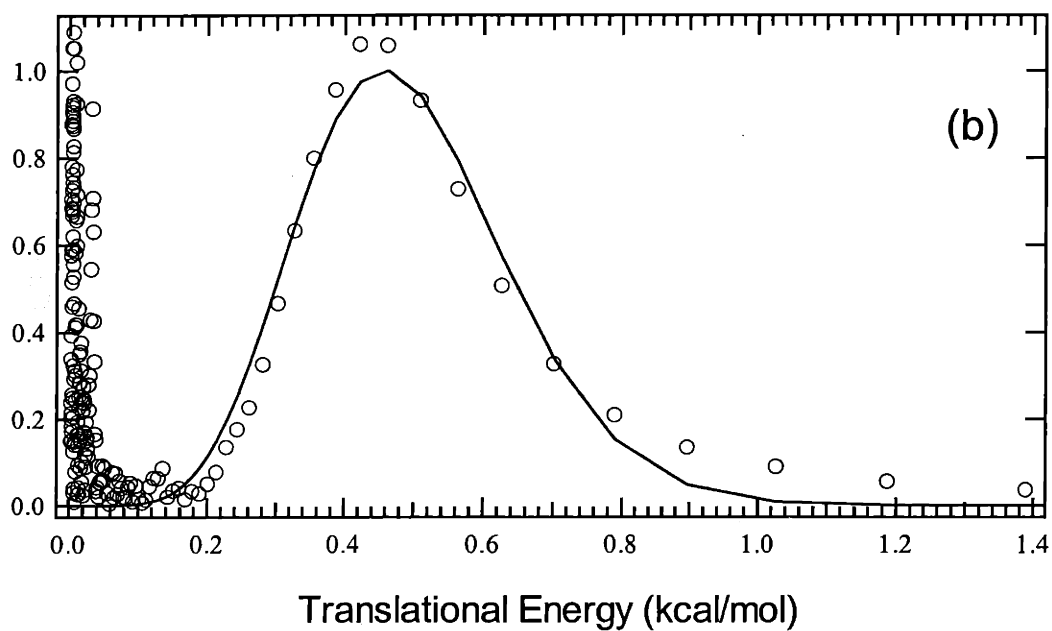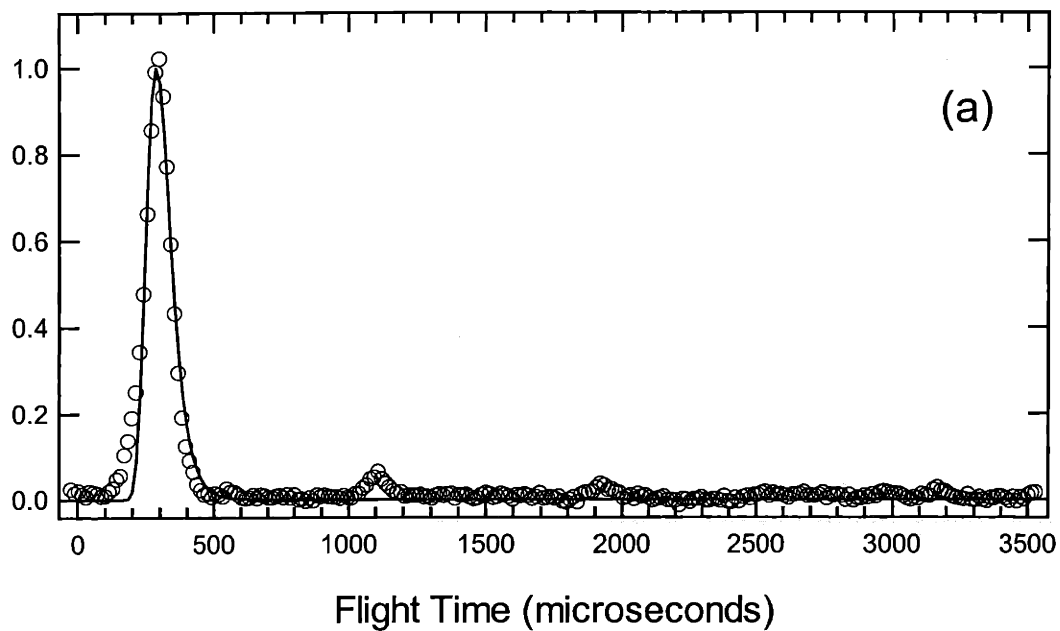
Figure 12 TOF distributions of supersonic 75% He/Ar molecular beam
(a) TOF spectrum of a supersonic molecular beam expansion of 300 torr 75% He/Ar. Solid line shows fit to the data of the Maxwell-Boltzmann function. (b) Translational energy distribution of the supersonic 75% He/Ar molecular beam (circles) and the fit to the data (solid line).

V.E. Broadening of He diffraction features

Due to the fact that the incident helium beam is not truly monoenergetic, the helium diffraction features can be artificially broadened.[53] Since the diffraction condition is given by $n\lambda_{He} = d(\sin\theta_f - \sin\theta_i)$, the feature broadening can be predicted using the incident wavelengths that correspond to the high and low energy values given by the energy distribution FWHM. Shown in Figure 13 is an expanded view of the helium diffraction spectra shown in Figure 5 of the clean and XeF_2 fluorinated Si(100) surfaces. Also shown are the predicted feature widths based on the FWHM of the energy distribution of the incident helium beam. It can be seen that the observed broadening of the helium diffraction features is consistent with the non-monoenergetic nature of the incident helium beam. Although the features are also observed to shift slightly upon fluorination of the surface, the shifted features still fall within their respective predicted angular ranges. This shifting is likely due to the sensitivity of the structure factor to the incident energy.
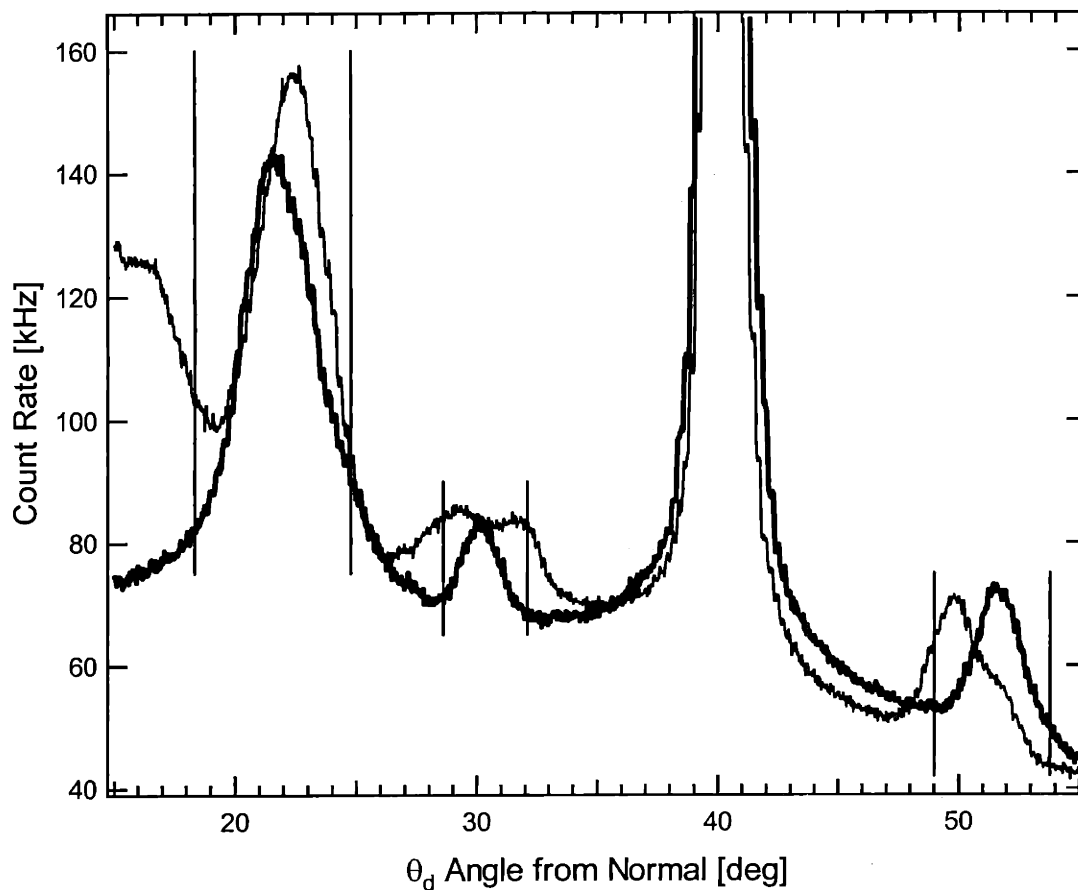
Figure 13 Helium diffraction feature broadening

Helium signal scattered from clean (thin solid line) and XeF_2 fluorinated (thick solid line) Si(100) at 250 K and at $\theta_i=40°$ as a function of detector angle, θ_d. Data from Figure 5. Also shown are the predicted peak widths based on the energy FWHM of the incident beam.

V.F. Impact of cooling rate on the He diffraction spectrum

Previous STM studies of the Si(111) surface have shown that the cooling rate after an anneal can affect the quality of the surface reconstruction.[54] During the course of the present experiments, it was found that the quality of the helium diffraction spectra was influenced by the rate at which the crystal was cooled after an anneal. Shown in Figure 14 are two diffraction spectra of the clean Si(100) surface. The thin solid line shows a helium diffraction spectrum taken after an anneal with a cooling rate of 4 K/s, and the thick solid line shows a helium diffraction spectrum taken after an anneal with a cooling rate of 0.7 K/s. These spectra were recorded using a helium beam with a de Broglie wavelength of λ_{He}=1.31 Å. It is evident that the quality of the helium diffraction spectrum is significantly increased by using the slower cooling rate. Therefore, an anneal with a cooling rate of 0.7 K/s was used prior to all subsequent helium diffraction experiments.
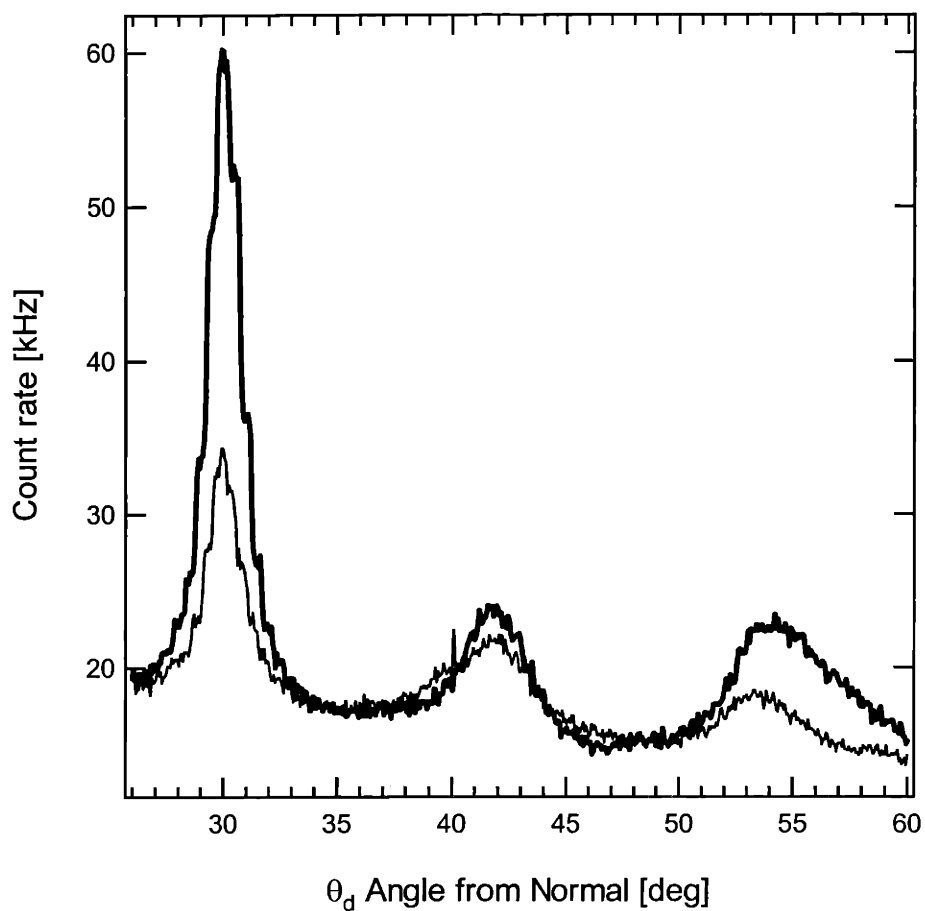
Figure 14 Helium diffraction spectra vs cooling rate
Helium diffraction spectra of a clean Si(100) surface measured with the helium beam incident at $\theta_i=30°$, after cooling the crystal at a rate of 4 K/s (thin solid line) and 0.7 K/s (thick solid line). The helium beam used in this experiment has a de Broglie wavelength of $\lambda_{He}=1.31$ Å.

REFERENCES

[1] I.C. Ressejac, L.M. Landsberger, and J.F. Currie, *J. Vac. Sci. Technol. A* **18**, 746 (2000).

[2] N.H. Tea, V. Milanović, C.A. Zincke, J.S. Suehle, M. Gaitan, M.E. Zaghloul, and J. Geist, *J. Microelec. Sys.* **6**, 363 (1997).

[3] F.I. Chang, R. Yeh, G. Lin, P.B. Chu, E. Hoffman, E.J.J. Kruglick, K.S.J. Pister, and M.H. Hecht, *SPIE* **117**, 2641 (1995).

[4] P.B. Chu, J.T. Chen, R. Yeh, G. Lin, J.C.P. Huang, B.A. Warneke, and K.S.J. Pister, *Transducers* **97**, 665 (1997).

[5] R. Toda, K. Minami, and M. Esashi, *Transducers* **97**, 671 (1997). *Sensors and Actuators A* **66**, 268 (1998).

[6] G.T.A. Kovacs, N.I. Maluf, and K.E. Petersen, *Proc. IEEE* **86**, 1536 (1998).

[7] H.F. Winters and J.W. Coburn, *Appl. Phys. Lett.* **34**, 70 (1979).

[8] J.A. Mucha, V.M. Donnelly, D.L. Flamm, and L.M. Webb, *J. Phys. Chem.* **85**, 3529 (1981).

[9] D.L. Flamm, V.M. Donnelly, and J.A. Mucha, *J. Appl. Phys.* **52**, 3633 (1981).

[10] M.J. Vasile, *J. Appl. Phys.* **54**, 6697 (1983).

[11] D.E. Ibbotson, D.L. Flamm, J.A. Mucha, and V.M. Donnelly, *Appl. Phys. Lett.* **44**, 1129 (1984).

[12] H.F. Winters and J.W. Coburn, *Surf. Sci. Rep.* **14**, 165 (1992).

[13] Y.Y. Tu, T.J. Chuang, and H.F. Winters, *Phys. Rev. B.* **23**, 823 (1981).

[14] R.A. Haring, A. Haring, F.W. Saris, and A.E. de Vries, *Appl. Phys. Lett.* **41**, 174 (1982).

[15] M.J.M. Vugts, L.J.F. Hermans, and H.C.W. Beijerinck, *J. Vac. Sci. Tech. A* **14**, 2138 (1996). *J. Vac. Sci. Tech. A* **14**, 2820 (1996).

[16] T.J. Chuang, *J. Chem. Phys.* **74**, 1461 (1981).

[17] F.A. Houle, *J. Chem. Phys.* **79**, 4237 (1983). *J. Chem. Phys.* **80**, 4851 (1984).

[18] F.A. Houle, *Appl. Phys. Lett.* **50**, 1838 (1987). *Phys. Rev. Lett.* **61**, 1871 (1988). *Phys. Rev. B* **39**, 10120 (1989).

[19] B. Li, U. Streller, H.P. Krause, I. Twesten, and N. Schwentner, *J. Appl. Phys.* **77**, 350 (1995).

[20] V.S. Aliev and V.N. Kruchinin, *Surf. Sci.* **442**, 206 (1999).

[21] Y.L. Li, D.P. Pullman, J.J. Yang, A.A. Tsekouras, D.B. Gosalvez, K.B. Laughlin, Z. Zhang, M.T. Schulberg, D.J. Gladstone, and S.T. Ceyer, *Phys. Rev. Lett.* **74**, 2603 (1995). S.T. Ceyer, *Proc. R. A. Welch Found. Conf. Chem. Res. XXXVIII: Chemical Dynamics of Transient Species*; Welch Foundation: Houston, p. 156-172 (1994). D.P. Pullman and S.T. Ceyer, *Abstracts of the ACS* **207**, 168 (1994).

[22] M.R. Tate, D. Gosalvez-Blanco, D.P. Pullman, A.A. Tsekouras, Y.L. Li, J.J. Yang, K.B. Laughlin, S.C. Eckman, M.F. Bertino, and S.T. Ceyer, *J. Chem. Phys.* **111**, 3679 (1999).

[23] M.R. Tate, D.P. Pullman, D. Gosalvez-Blanco, A.A. Tsekouras, Y.L. Li, and S.T. Ceyer, *J. Chem. Phys.* **112**, 5190 (2000).

[24] D.P. Pullman, A.A. Tsekouras, Y.L. Li, J.J. Yang, M.R. Tate, D. Gosalvez-Blanco, K.B. Laughlin, M.T. Schulberg, and S.T. Ceyer, *J. Phys. Chem. B* **105**, 486 (2001).

[25] C.W. Lo, P.R. Varekamp, D.K. Shuh, T.D. Durbin, V. Chakarian, and J.A. Yarmoff, *Surf. Sci.* **292**, 171 (1993).

[26] W.C. Simpson and J.A. Yarmoff, *Surf. Sci.* **359**, 135 (1996).

[27] P.C. Weakliem and E.A. Carter, *J. Chem. Phys.* **98**, 737 (1993).

[28] L.E. Carter, S. Khodabandeh, P.C. Weakliem, and E.A. Carter, *J. Chem. Phys.* **100**, 2277 (1994).

[29] S.T. Ceyer, D.J. Gladstone, M. McGonigal, and M.T. Schulberg, In *Physical Methods of Chemistry*, 2nd ed.; B.W. Rossiter, R.C. Baetzold, Eds., Wiley: New York, 1993; Vol. IXA, p. 383.

[30] S.R. Qiu, and J.A. Yarmoff, *Phys. Rev. B* **63**, 115409 (2001).

[31] A. Ishizaka, and Y. Shiraki, *J. Electrochem. Soc.* **133**, 666 (1986).

[32] H.F. Winters and F.A. Houle, *J. Appl. Phys.* **54**, 1218 (1983).

[33] J.R. Engstrom, M.M. Nelson, and T. Engel, *Surf. Sci.* **215**, 437 (1989).

[34] E.R. Behringer, H.C. Flaum, D.J. Sullivan, D.P. Masson, E.J. Lanzendorf, and A.C. Kummel, *J. Phys. Chem.* **99**, 12863 (1995).

[35] M.J. Cardillo and G.E. Becker, *Phys. Rev. B* **21**, 1497 (1980).

[36] Yang, J. J. Ph.D. Thesis, Massachusetts Institute of Technology, Cambridge, MA, 1997.

[37] B. Poelsema and G. Comsa, *Scattering of Thermal Energy Atoms from Disordered Surfaces*; Springer-Verlag: Berlin, 1989.

[38] G. Comsa, *Surf. Sci.* **81**, 57 (1979).

[39] P. Kisliuk, *J. Phys. Chem. Solids* **3**, 95 (1957).

[40] T.J. Chuang, *J. Appl. Phys.* **51**, 2614 (1980).

[41] F.R. McFeely, J.F. Morar, N.D. Shinn, G. Landgren, and F.J. Himpsel, *Phys. Rev. B* **30**, 764 (1984).

[42] N.D. Shinn, J.F. Morar, and F.R. McFeely, *J. Vac. Sci. Tech. A* **2**, 1593 (1984).

[43] F.H. Stillinger and T.A. Weber, *Phys. Rev. Lett.* **62**, 2144 (1989). *J. Chem. Phys.* **92**, 6239 (1990).

[44] T.A. Schoolcraft and B.J. Garrison, *J. Vac. Sci. Tech. A* **8**, 3496 (1990).

[45] M. Gostein and G.O. Sitz, *J. Chem. Phys.* **106**, 7378 (1997).

[46] G.R. Darling, M. Kay, and S. Holloway, *Surf. Sci.* **400**, 314 (1998).

[47] S.T. Ceyer, To be published.

[48] D. Gozalvez-Blanco, Ph. D. Thesis, Massachusetts Institute of Technology, 1997.

[49] S.R. Qiu and J.A. Yarmoff, *Phys. Rev. B* **63**, 115409 (2001)

[50] D.J. Gladstone, Ph.D. Thesis, Massachusetts Institute of Technology, 1989.

[51] J.J. Yang, Ph.D. Thesis, Massachusetts Institute of Technology, 1993.

[52] G. Comsa, R. David, and B.J. Schumacher, *Rev. Sci. Inst.* **52**, 789 (1981).

[53] W. Allison, R.F. Willis, and M. Cardillo, *Phys. Rev. B* **23**, 6824 (1981).

[54] M.D. Pashley, K.W. Haberern and W. Friday, *J. Vac. Sci. Tech. A* **6**, 488 (1988).

Chapter 3: Reactive Scattering of XeF$_2$ from Si(100)

I. Introduction

The results presented in Chapter 2 give a description of the interaction of XeF_2 and F_2 with Si(100) in terms of the evolution of the surface order and the reaction probability with respect to the coverage. It is found that up to 1 ML coverage the evolution of the surface order with exposure to both XeF_2 and F_2 is strikingly similar, in that both reactions proceed solely at the Si dangling bonds, and both reactions produce an ordered surface at 1 ML coverage. After 1 ML coverage, however, the reactivities of XeF_2 and F_2 diverge markedly. While F_2 ceases to react with the surface, XeF_2 continues to deposit fluorine, reacting with the Si-Si σ bonds and etching the surface by the formation of volatile SiF_4. The present Chapter is the logical continuation of the results presented in Chapter 2, in that the experiments presented in Chapter 2 give a description of the reaction based on observations of the surface-bound products of the reaction using the thermal desorption and helium diffraction techniques, while the gas-phase products of the reaction, other than the SiF_4 etch product, are not considered. In the present Chapter the gas-phase products of the reaction are investigated in detail, using the time-of-flight technique.

The gas phase products of the reaction of XeF_2 with Si(100) can be enumerated by a description of the various reaction channels that are available to an incident XeF_2 molecule. The incident XeF_2 molecule can either undergo an unreactive collision with the surface, resulting in a gas-phase XeF_2 particle, or it can react with a Si dangling bond via single atom abstraction, fluorinating the dangling bond and liberating a XeF fragment. The XeF fragment can 1) survive to become gas-phase XeF, or 2) dissociate in the gas phase, resulting in a gas-phase Xe atom and a F atom, or 3) react with the surface, resulting in two-atom adsorption and a gas-phase Xe atom.

A previous study of the interaction of XeF_2 with Si(100),[1] as summarized in Chapter 1, illustrates these four reaction pathways.

The present study is focused on two fundamental problems that remain unresolved by the previous studies, as well as the studies described in Chapter 2: 1) understanding the nature of gas-phase dissociation of XeF, and 2) using that understanding to unravel the multiple contributions to the Xe signal.

Knowledge of the exothermicity of the dissociative chemisorption of XeF_2 on Si(100) is important for the analysis of the results presented in this Chapter, because the exothermicity of the reaction determines the nature of the gas-phase dissociation of XeF. However, the exothermicity of the reaction depends on what, if any, Si-Si bonds are broken. Specifically, adsorption on a dangling bond on a half-filled dimer does not break any Si-Si bonds, while adsorption on an empty dimer results in the disruption of the weak π dimer bond, which has an estimated bond strength of 7 kcal/mol.[2,3] It is also possible that the reaction can result in the breakage of a Si-Si σ bond, which has an estimated bond strength of about 54 kcal/mol.[4] Spectroscopic studies[5] have found the Xe-F bond dissociation energy to be 3.04±0.03 kcal/mol, and the total XeF_2 dissociation energy to be 63.4±0.5 kcal/mol, which yields a value of 60.4±0.5 kcal/mol for the first bond dissociation energy. This bond energy can be used along with the value of 148 kcal/mol for the Si-F bond energy[6] to yield an exothermicity of about 87.6 kcal/mol for single atom abstraction on a half-filled dimer, 80.6 kcal/mol for single atom abstraction on an empty dimer, and 33.6 kcal/mol for single atom abstraction that results in the cleavage of a Si-Si σ bond.

There are a number of ways that the exothermicity of the reaction can be channeled into internal energy of the XeF fragment. Shown in Figure 1 are the electronic energy states relevant

to the gas phase dissociation of XeF[5,7]. Dissociation could result from electronic excitation to the bound charge-transfer excimer B, C and D states, from electronic excitation to the repulsive A state, or from direct excitation to a rovibrational state that is above the dissociation limit in the ground electronic state. Excitation to the charge-transfer excimer B state is investigated using the parameters given in Reference 5, which yield an energy difference between the ground vibrational states of the X and B states of 82.5 kcal/mol. If excitation to the B state were to occur, close to 100% of the exothermicity of the atom abstraction reaction on a half-filled dimer would have to be channeled into electronic excitation of the XeF fragment. If the observed translational excitation of the XeF, which is ≥ 6 kcal/mol, is taken into account, fully 100% of the reaction exothermicity must be channeled into the XeF fragment in order to achieve excitation to the B state. However, prior results for the interaction of F_2 with $Si(100)$[8] have shown that channeling of the reaction exothermicity to the surface bath is quite effective upon F atom abstraction. Therefore, given the similarity of the abstraction reactions, X→B electronic excitation by channeling of the exothermicity to the electronic degrees of freedom is extremely unlikely. Excitation to the C and D states would require similar or greater energy input, and may likewise be ruled out. However, direct excitation to the repulsive A state is easily accessible given the large exothermicity of the atom abstraction reaction. Another possible dissociation pathway is excitation into a rovibrational state in the ground electronic state that is above the dissociation threshold. In either case, dissociation is expected to occur with a time scale that is on the order of a vibrational period.

The gas-phase dissociation of XeF is strongly suggested by a previous investigation in this laboratory,[1] which reported scattered TOF spectra at m/e=19 upon exposure of Si(100) to XeF_2. However, only a rudimentary one-dimensional model of the XeF dissociation was

proposed. In the current study, a comprehensive model for XeF dissociation is proposed using conservation of energy and momentum. That is, the final velocity and direction of the F and Xe atoms are uniquely determined by the velocity, direction, orientation, and internal energy of the XeF prior to the dissociation. Since the initial conditions of the XeF prior to the dissociation are characterized by distributions instead of singular values, it is necessary to perform a calculation that convolutes the effect of each distribution in order to find the final velocity and direction distributions of the Xe and F atoms. The ability of this simple momentum-matching model to correctly predict the observed F atom velocity and angular distributions gives confidence to the conclusion that the scattered F atoms arise from XeF dissociation. The predicted Xe atom velocity and angular distributions are used to identify what part of the m/e=129 signal is due to Xe from XeF dissociation.

Previous investigations[1] of the scattered TOF spectra at m/e=129 have been hampered by the multiple sources of signal that give rise to the observed m/e=129 TOF spectra. The five possible contributions to the signal at m/e=129 are: dissociative ionization of XeF_2 and XeF in the electron bombardment ionizer of the mass spectrometer detector, Xe from dissociation of gas-phase XeF, unreactively scattered Xe from free Xe contamination of the incident beam, and Xe from two-atom adsorption. The only one of these five sources that is known is the dissociative ionization of XeF_2, which can be accounted for by subtracting the observed XeF_2 signal multiplied by the $Xe^+:XeF_2^+$ cracking ratio from the observed m/e=129 signal. The second contribution is cracking from XeF. Due to the fact that a source of pure XeF is unavailable, the $Xe^+:XeF^+$ cracking ratio cannot be measured. The third possible contribution is Xe arising from dissociation of XeF prior to reaching the detector, which is the signal of interest. The fourth possible signal source is unreactively scattered Xe present as contamination in the

incident beam, produced from the reaction of XeF_2 with the stainless steel manifold or Ni nozzle. The last signal source is Xe arising from two-atom adsorption. The results presented in this chapter will show how the multiple contributions to the observed m/e=129 signal are disentangled by a combination of experimental modifications and the results of the momentum matching calculation described above.

The modifications to the experimental procedure are summarized as follows. First, the possibility of free Xe contamination in the incident beam is eliminated by the construction of a Teflon® manifold and nozzle. Second, the ionizer settings are altered so as to minimize the contribution due to cracking from XeF_2. Third, the temperature of the crystal was decreased from 250 K to 150 K. This decrease in the temperature has the effect of slowing down the velocity of the thermal feature, where the thermal feature is due to Xe that equilibrates with the surface and subsequently desorbs at the surface temperature. A slower thermal feature results in a greater separation between the thermal feature and the non-thermal features in the observed TOF spectra. Fourth, the chopper used for the time-of-flight measurements is spun at a higher frequency, 392 Hz vs. 280 Hz previously. The higher frequency results in a greater time-of-flight resolution for the features of interest. Fifth, the average energy of the incident XeF_2 beam is decreased to 1.4 kcal/mol, resulting in a slower unreactively scattered XeF_2 signal, which has the effect of separating the cracking from unreactively scattered XeF_2 from the non-thermal features of the m/e=129 TOF spectra. Last, greater signal averaging is performed at m/e=129, increasing the signal to noise ratio of those TOF spectra.

With the elimination of the unreactively scattered free Xe in the incident beam, the net m/e=129 spectra, with the known XeF_2 cracking subtracted, consists of three unknown signal sources – cracking from XeF, Xe from XeF dissociation, and Xe from two-atom adsorption. In

the present study the unknown Xe^+:XeF^+ cracking ratio is taken into account by analyzing the spectra using a maximum, intermediate, and minimum Xe^+:XeF^+ cracking ratio, and showing that the conclusions of the analysis are unaffected by the Xe^+:XeF^+ cracking ratio used. The Xe from XeF dissociation is identified using the predicted Xe velocity and angular distributions given by the momentum-matching calculation described above. The Xe from two-atom adsorption is then the remainder of the m/e=129 signal.

An overview of the current Chapter is given as follows. The experimental considerations are described in detail in Section II. The experimental results are given in Section III. Due to the fact that the surface temperature has been reduced for the time-of-flight studies, thermal desorption and helium diffraction experiments similar to those in Chapter 2 are reproduced at a surface temperature of 150 K. The main result is the observed TOF spectra and angular distributions of the scattered products of the reaction. In particular, it is shown that the net m/e=129 TOF spectra are composed of three distinct features, corresponding to fast, medium and slow scattered Xe atoms, at all coverages and detection angles. Section IV describes the momentum matching calculation that has been performed to predict the F and Xe atom TOF distributions resulting from the gas-phase dissociation of XeF. The predicted F atom TOF and angular distributions match the observed m/e=19 distributions at virtually all coverages and scattering angles. The predicted Xe atom TOF and angular distributions unambiguously identify the fast feature of the m/e=129 TOF spectra as consistent with Xe atoms resulting from the gas-phase dissociation of XeF. Section V is a discussion of the experimental results and the results of the momentum matching calculation, which show that the atom abstraction reaction can be described by an "early barrier" potential energy surface, and that XeF dissociation occurs primarily by excitation to an excited rovibrational state in the ground electronic state.

Additionally, the results of the momentum matching calculation suggest that the reaction geometry of the XeF in the transition state has the F atom pointing into the vacuum. Section VI offers some concluding remarks on the experiment and its implications for our understanding of the reaction of XeF_2 with Si(100).
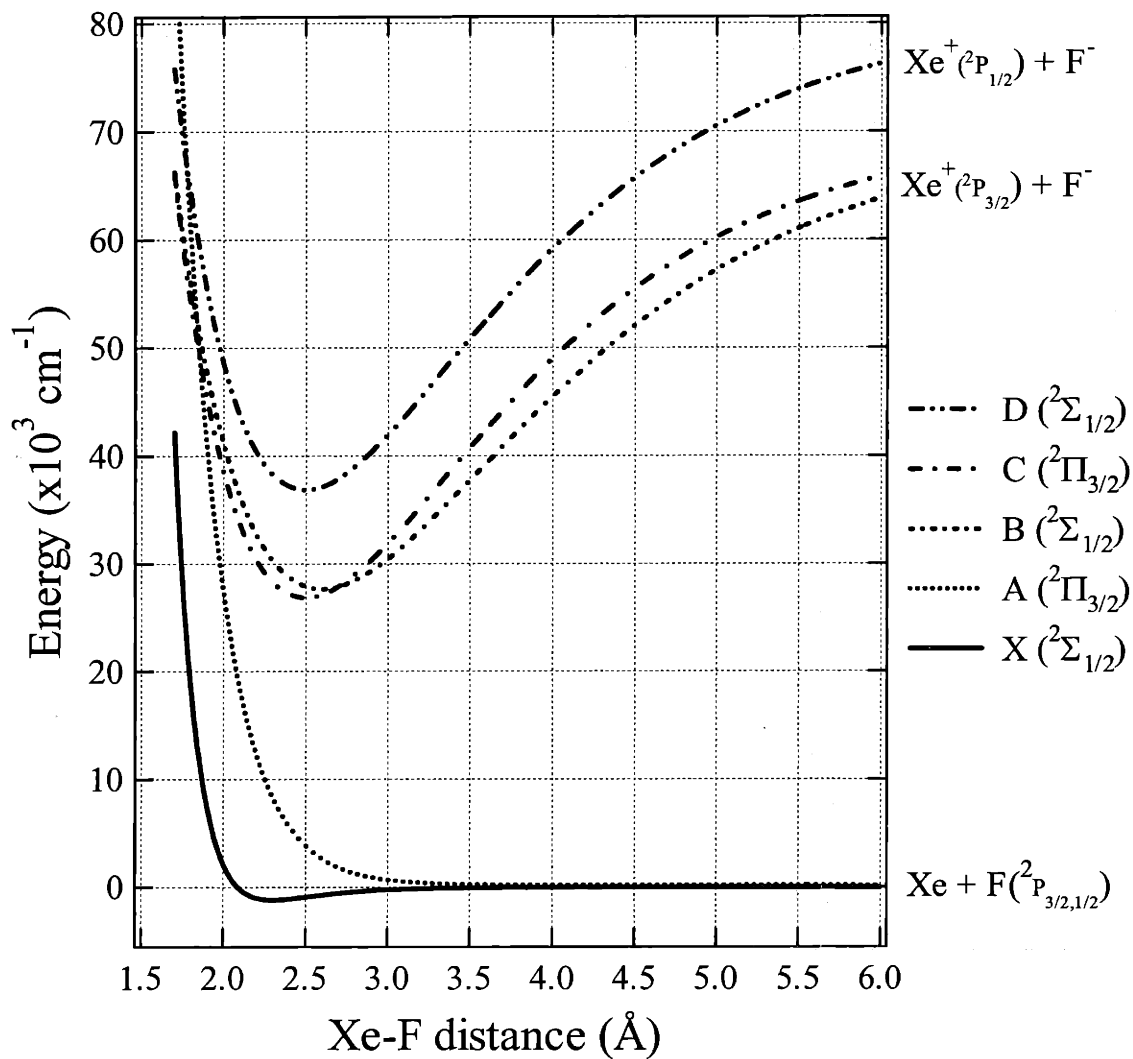
Figure 1 Potential energy diagram of the electronic states of XeF
Morse potentials based on parameters from References 5 and 7.

II. Experimental

II.A. XeF$_2$ molecular beam

II.A.1. Free Xe contamination

Chapter 2 of this thesis detailed a new XeF$_2$ transfer protocol that eliminated contact between the solid sample and atmospheric gases. The purpose of this procedure was to eliminate any possible free Xe contamination that may have resulted from the reaction of XeF$_2$ with the atmosphere. However, this procedure did not eliminate reactions of XeF$_2$ with the stainless steel walls of the gas-handling manifold. Although it was believed that the passivation procedure resulted in a beam that did not have significant free Xe contamination, this possible contamination could not be completely ruled out. The only way to completely rule out free Xe contamination is to effectively remove any contact between the XeF$_2$ and any material that could possibly react with it prior to the reaction with the crystal surface. This goal led to the design and construction of a manifold made completely from Teflon® (also known as Polytetrafluoroethylene or PTFE).

II.A.2. Teflon manifold

Although in principle, the design of an PTFE manifold is straightforward, it is severely complicated by the fact that the PTFE tubing and fittings used are permeable to helium. This permeability means that it is impossible to verify that the manifold is leak-free using a helium leak detector. The inability to determine the vacuum integrity of the manifold led to the design of a stainless steel vacuum jacket that surrounds the entire PTFE manifold. The vacuum jacket ensures that even if leaks are present in the manifold there are no complicating reactions with atmospheric gasses. A further consideration is the need for reliable temperature control of the XeF$_2$ reservoir. The same constant temperature bath that was used with the stainless steel vessel

is used to surround the XeF_2 reservoir. Finally, an all-Teflon® nozzle was designed and built specifically for the effusive beam experiments.

A schematic of the design of the manifold is shown in Figure 2. All PTFE fittings, tubing and valves are manufactured by Swagelok. The XeF_2 reservoir is constructed from a ¾" diameter Teflon® dowel with a ½" hole drilled down the middle of the dowel but not completely through the dowel. This reservoir is connected to a PTFE valve via a NPT to swagelok adapter and a ¼" PTFE tube. The reservoir is loaded with XeF_2 in a nitrogen glove box, and isolated from atmosphere by attaching the closed PTFE valve to the reservoir via the NPT fitting. The reservoir is then installed into the stainless steel vacuum jacket and the vacuum jacket is evacuated. The PTFE valves are controlled from outside the vacuum jacket via two stainless steel rods, which are connected to the PTFE valve stems. Each control rod passes through the vacuum jacket at an Ultra-Torr vacuum feedthrough, which allows for rotary motion of the rod in order to open and close the valves without compromising the vacuum.

The PTFE valve that is immediately attached to the XeF_2 reservoir is connected via a PTFE tube through a flexible formed metal bellows to a tee fitting on the inside of the primary source chamber as shown in Figure 2. This arrangement allows the source chamber to serve as the pump for the vacuum jacket. This tee connects to both the Teflon nozzle and also to a second PTFE valve. This second PTFE valve is connected to the primary stainless steel gas handling manifold described in Chapter 2. This connection is necessary both in order to evacuate the PTFE manifold, and also to supply gasses for beams other than neat XeF_2. For instance, in order to determine the flux of the beam it is necessary to run a pure Ar beam from the primary manifold.
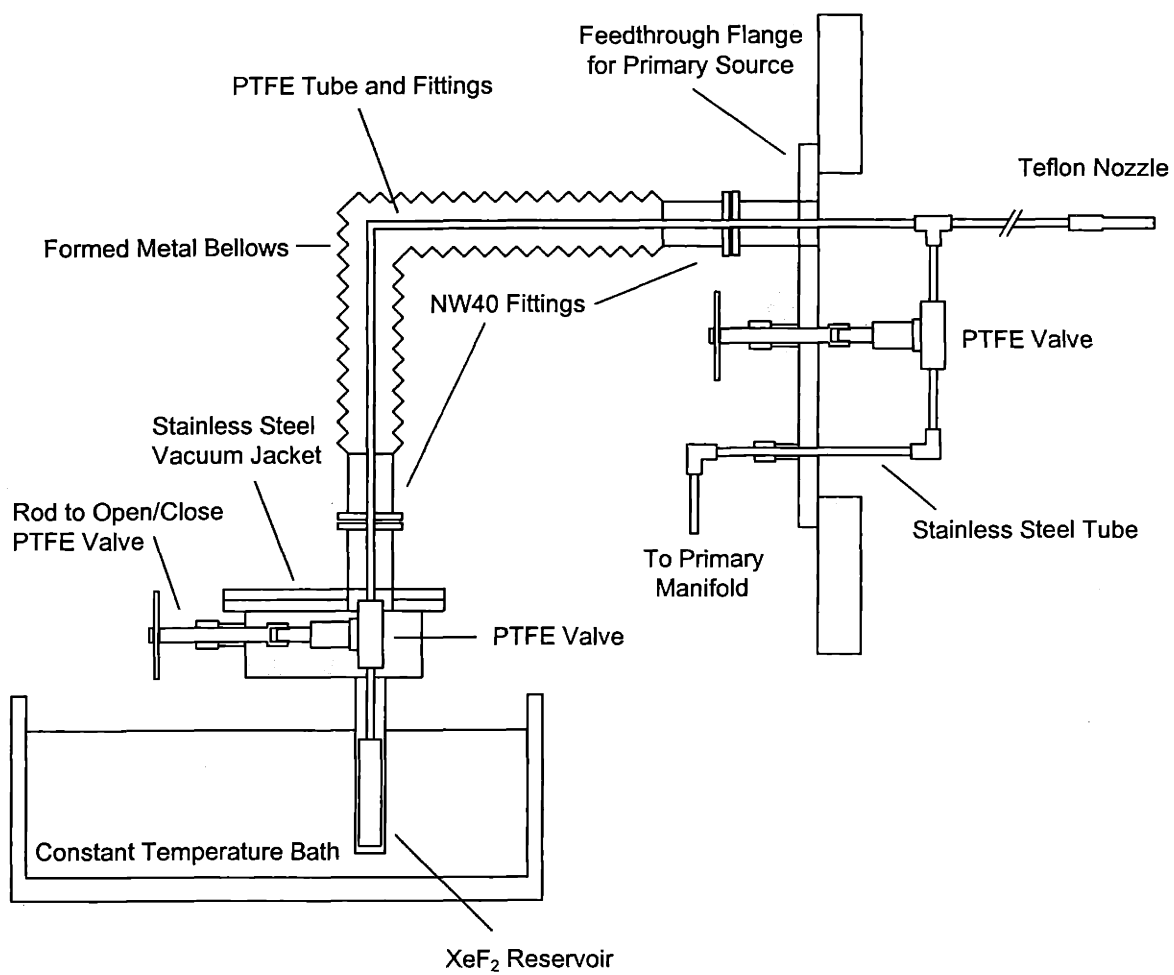
Figure 2 Schematic of Teflon manifold and vacuum jacket assembly

II.A.3. Teflon nozzle

The Teflon® nozzle was constructed from a solid ½" dowel. A long hole was drilled almost entirely through the dowel from the rear of the nozzle. The aperture was then drilled from the front of the nozzle using a 0.002" diameter spade drill. A small groove was cut towards the front end of the nozzle to allow for the installation of a wire clamp after the nozzle is installed in its mounting bracket. Finally, a ½" PTFE Swagelok fitting is attached directly to the rear of the nozzle, connecting it to the rest of the manifold.

The configuration of the effusive Teflon® nozzle with respect to the collimating slits and the crystal is shown in Figure 3. The first feature that should be emphasized is that the effusive nozzle aperture is positioned 1.460" closer to the crystal than the supersonic nozzle. The decreased distance between the nozzle and the crystal, as well as the fact that the Teflon® nozzle aperture is slightly larger than the Ni nozzle aperture, has the effect of significantly increasing the beam flux at the crystal, allowing the use of lower stagnation pressure for the XeF_2 beam. However, the removal of the skimmer has decreased the number of stages of differential pumping between the source aperture and the crystal from three differential stages down to two differential stages. Given that the total flux out of the nozzle is much lower for an effusive expansion than for a supersonic expansion, removal of the skimmer does not result in any significant beam attenuation. Note that the new nozzle configuration results in a larger cross sectional area of the beam image on the crystal. The larger area must be taken into account when calculating the beam flux, as detailed in the Appendix 2.
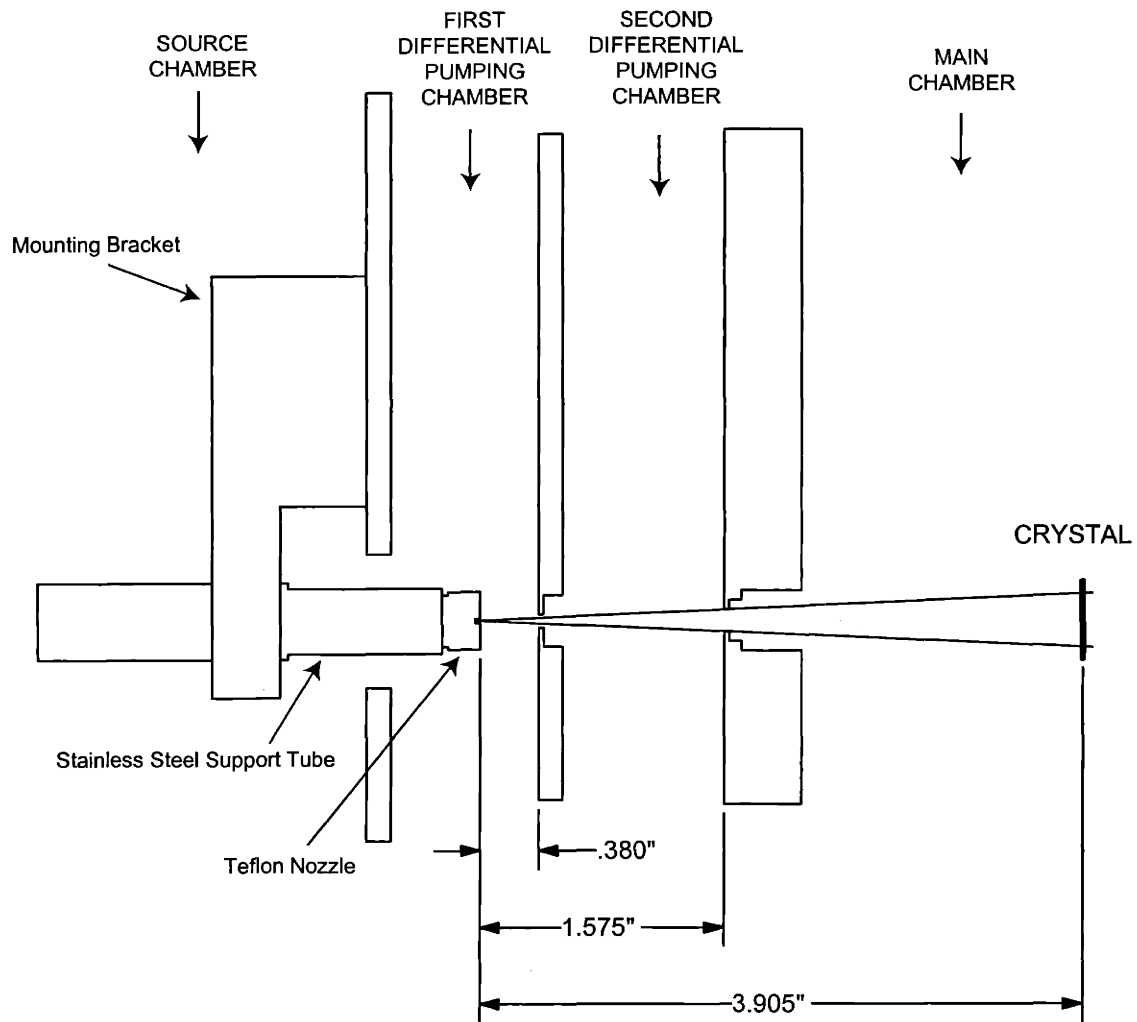
Figure 3 Mounting configuration for the effusive Teflon nozzle.

II.A.4. Incident XeF$_2$ Beam

The time-of-flight (TOF) spectrum of the incident XeF$_2$ beam is shown in Figure 4(a) for a beam of 0.7 torr neat XeF$_2$ expanded from the Teflon nozzle. This stagnation pressure was chosen because it was easily reproduced by filling the constant temperature bath with a water/ice mixture, and also because it gave a convenient experimental time frame for the reaction. The time-of-flight distribution of the beam formed under these conditions is only slightly supersonic. A truly effusive expansion would have a flow velocity of zero, but the distribution shown in Figure 4(a) is well defined by a Maxwell-Boltzmann distribution with a flow velocity of 46.5±5.8 m/s and a beam temperature of 289±8 K. The beam has an average velocity of 250.9±4.4 m/s and an average energy of 1.40±0.05 kcal/mol. The uncertainties in the fit parameters are the standard deviation, given by the square root of the diagonal elements of the covariance matrix, and the uncertainties of the average velocity and energy are given by the propagated uncertainty in the fit parameters and the uncertainty due to the finite length of the ionizer region. For a detailed discussion of the error analysis, see Appendix 2. The observed TOF spectrum transformed into a flux energy distribution and the corresponding Maxwell-Boltzmann fit are shown in Figure 4(b), from which a value of 1.70 kcal/mol for the energy full width at half maximum (FWHM) can be determined. A detailed description of the measurement and analysis of time-of-flight spectra is given in Section II.D.2, including the functional form of the Maxwell-Boltzmann distribution and the transformation between a number density TOF distribution and a flux energy distribution.

Determination of the absolute beam flux is detailed elsewhere.[8] Briefly, a beam of Ar at a stagnation pressure of 0.70 ± 0.04 Torr is directed into the chamber containing the crystal. The pressure rise in the chamber, P, is measured with a nude Bayard-Alpert ionization gauge and

calibrated to the absolute pressure by accounting for the ionization efficiency, C, of Ar. The absolute flux of Ar impinging on an area, A, of the crystal is given by $I^{Ar} = PCS/kTA$ where S is the pumping speed of Ar and T is the temperature of the chamber. The flux of a beam of pure XeF_2 at a stagnation pressure of 0.70 ± 0.04 Torr is given by $I = I^{Ar} v/v^{Ar}$ where v and v^{Ar} are the experimentally determined average speeds of XeF_2 and Ar, respectively. Since there are two F atoms per molecule in XeF_2, the incident flux in terms of F atoms is I [F atoms/m^2 s] = 2 I^{Ar} v/v^{Ar}. This procedure yields a value of 0.066($\pm$0.004) ML F atom/s for the flux of the incident XeF_2 beam, where 1 ML is the surface density of Si atoms on a Si(100) surface, 6.78×10^{14} atoms/cm^2.

A mass spectrum of the incident beam from the Teflon nozzle is shown in Figure 5, superimposed on data taken previously for a 5 torr expansion of neat XeF_2 with the Ni nozzle.[1] It can be seen that for spectra taken at similar resolution settings the cracking ratio $XeF_2^+:Xe^+$ is virtually unchanged, suggesting that after the initial passivation period there is minimal free Xe produced by the reaction of XeF_2 with the stainless manifold and Ni nozzle.

Although the PTFE manifold and nozzle have eliminated the possibility that XeF_2 is reacting with either that atmospheric gases or the stainless steel walls of the manifold, the possibility exists that there is free Xe trapped in the XeF_2 solid prior to its expansion in the manifold and nozzle. However, it is found using nuclear magnetic resonance spectroscopy that the concentration of Xe in the solid XeF_2 sample is less than 1% of the concentration of XeF_2. This result will be detailed in a future work.[9]
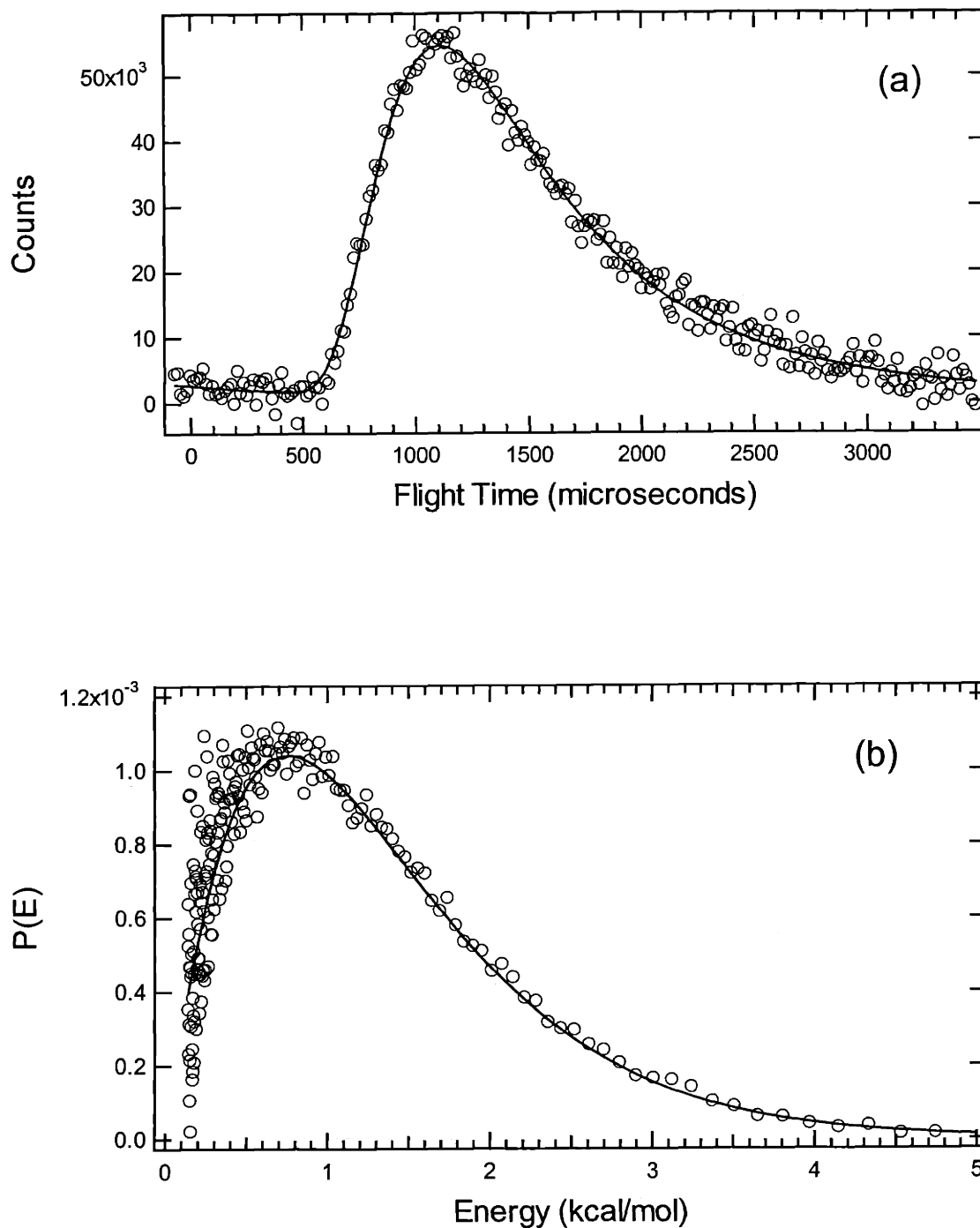
Figure 4 TOF distribution of the effusive XeF₂ beam

(a) TOF spectrum of quasi-effusive molecular beam expansion of 0.7 torr neat XeF₂ expanded from the Teflon nozzle. The solid line shows a Maxwell-Boltzmann distribution fit to the data with a flow velocity of 46.5±5.8 m/s and a beam temperature of 289±8 K. The beam has an average velocity of 250.9±4.4 m/s and an average energy of 1.40±0.05 kcal/mol. (b) TOF data and Maxwell-Boltzmann fit shown in (a) transformed into flux energy distributions. Energy FWHM is 1.70 kcal/mol.
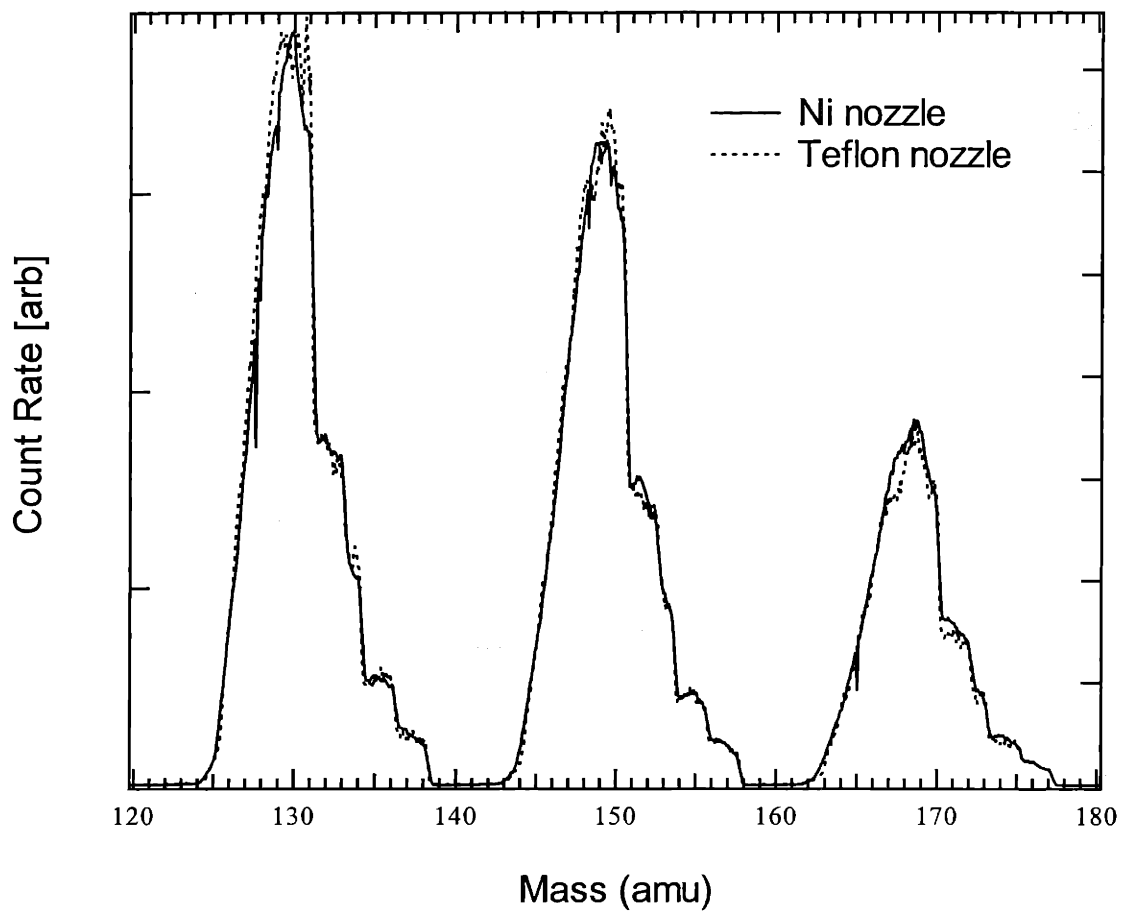
Figure 5 Mass spectra of XeF₂ molecular beam

The solid line is data reported previously[1] for a quasi-effusive expansion of XeF_2 from the Ni nozzle. The dotted line is the mass spectrum of a quasi-effusive expansion of XeF_2 from the Teflon nozzle. Signal intensities have been normalized to match the peak signal at m/e = 167.

II.B. Si(100) crystal

The crystal is mounted between two Ta clamps that are attached to the manipulator. The crystal is mounted such that the crystal face is flush with the Ta brackets to preclude its shadowing by the brackets. The crystal normal can be rotated in the scattering plane defined by the axes of the two molecular beams and the detector. The axis of crystal rotation is perpendicular to and intercepts the intersection of these three axes. The crystal can be cooled to 125 K with liquid N_2 and heated resistively to ~1100 K. Its temperature is measured via a W-5%Re/W-26%Re thermocouple spot welded to a thin Ta tab in thermal contact with the back of the crystal. As with the experiments described in Chapter 1, the surface temperature is held constant at 150 K during XeF_2 exposure.

The lightly p-doped Si crystal is cut along the (100) plane and cleaned by a wet etching procedure[10] prior to installation into the vacuum chamber. The crystal is sputtered with 1.5 keV Ar^+ and subsequently annealed to ~1100 K. This process is repeated until C and O contamination are below the 1% sensitivity limit of Auger electron spectroscopy. No metal contaminants, such as W, Ta, Cu, or Ni, are observed. The crystal is typically mounted such that the scattering plane, defined by the beams, crystal normal and detector, is along the (10) direction of the crystal surface. Helium diffraction confirms the (2x1) periodicity of the reconstructed Si(100) surface. A brief anneal of the crystal to about 1100 K after each XeF_2 exposure removes all the fluorine and results in recovery of the 2x1 periodicity of the surface. The crystal is sputtered and annealed after about ten exposures to XeF_2 to ensure surface cleanliness and order. The crystal is replaced when an etch spot becomes visible, typically after several months of experiments. No difference in reactivity is observed over the lifetime of the crystal.

II.C. Detection scheme

All measurements described in this chapter were made with the triply differentially pumped quadrupole mass spectrometer detector. The detected species are ionized via electron impact bombardment, and ions of a given mass to charge ratio are selected by a quadrupole mass filter. The ions that survive the journey through the quadrupole field are detected using a channeltron electron multiplier. The functioning of the channeltron electron multiplier and the associated pulse counting electronics are described in detail in the Appendix.

The behavior of the electron impact ionizer is governed by six different parameters, which subsequently determine the detection efficiency. The electron impact energy, E_{e^-}, determines the kinetic energy of the incident ionizing electron. The cracking ratio can be changed dramatically by changing this value, as will be shown below. The extractor voltage V_{ext} attracts the positive ions out of the electron bombardment region. The ion energy E_{ion} defines the energy of the ion going into the quadrupole mass selection region. Finally, a set of three lenses L_1, L_2, and L_3 focus the ions into the entrance to the quadrupole. Optimal ionizer settings have been reported previously[1] following a procedure that treats the set of three lenses as an einzel lens ($L_1 = L_3$) with the outer lenses grounded ($L_1 = L_3 = 0$ V). However, for the current experiment these ionizer settings have been re-optimized using a more exhaustive phase space search where the focusing lenses were not constrained as an einzel lens.

The electron energy has a dramatic effect on the cracking ratio. Shown in Figure 6 are two mass spectra of the incident XeF_2 beam. For these spectra, in order to avoid overloading the detector, the XeF_2 stagnation pressure was decreased to ~0.05 torr by immersing the XeF_2 reservoir in a dry ice/acetone slurry. It can be seen that by decreasing the electron energy from 75 eV to 26.5 eV, the Xe^+:XeF_2^+ cracking ratio can be decreased from 2:1 to 0.25:1. Lowering

the electron energy effectively reduces the relative Xe^+ signal from cracking of XeF_2^+ by a factor of eight, but it comes at the cost of a factor of five reduction in the overall detection efficiency. The other ionizer settings remained the same at 26.5 eV as at 75 eV. The optimized settings are given in Table 1.

Table 1 Optimized ionizer settings

Parameter	Value
Electron energy (E_{e^-})	75 eV (normal) 26.5 eV (low cracking)
Extractor voltage (V_{ext})	-250 V
Ion energy (E_{ion})	45 V
Lens 1 (L_1)	145 V
Lens 2 (L_2)	- 307 V
Lens 3 (L_3)	- 307 V

The detector rotates in the plane of the beams around their point of intersection at the crystal surface. The angular range is 35° to 180.5° with respect to the primary beam. The angular resolution in the scattering plane as determined by the acceptance angle of the detector is 3.52°. It has been shown that use of a properly differentially pumped detector is critical, in particular for the detection of the radical species SiF_2.
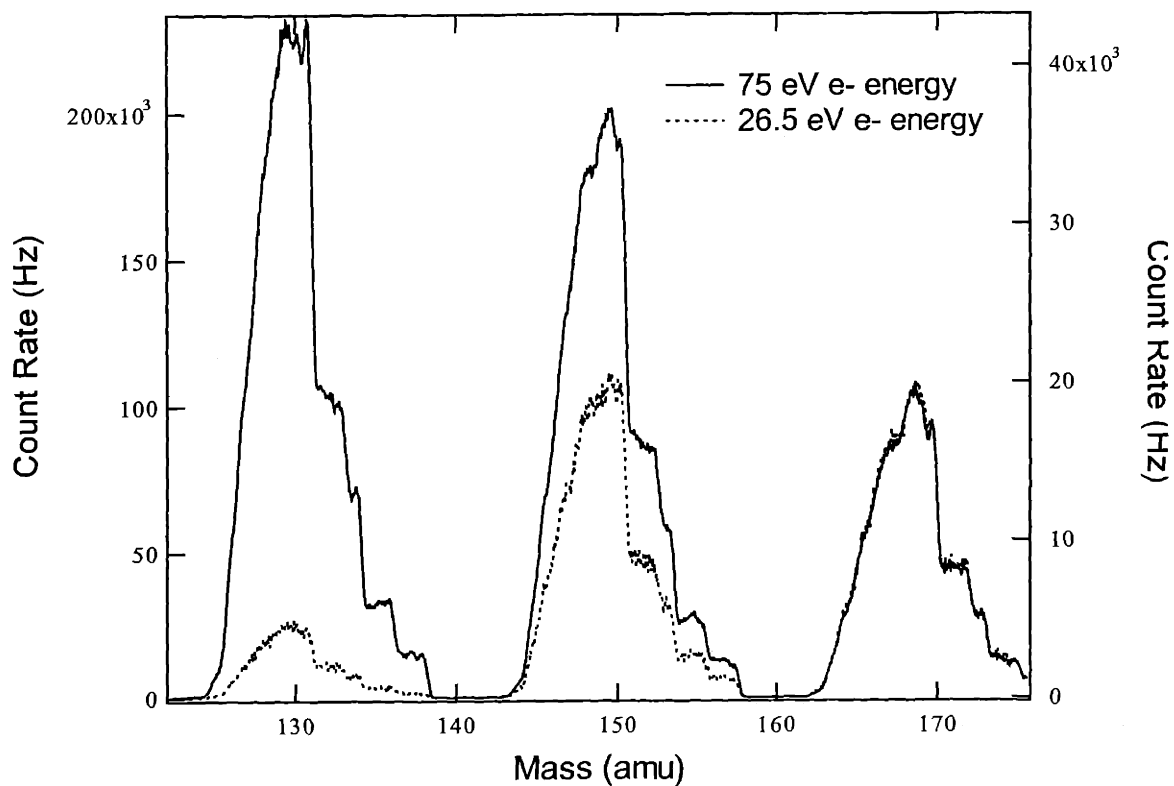
Figure 6 Mass spectra of the XeF$_2$ molecular beam at 75 eV and 26.5 eV electron impact energy
Mass spectra of quasi-effusive molecular beams XeF$_2$. The solid line is data taken at an electron energy of 75 eV and is plotted as the left axis. The dotted line is data taken at an electron energy of 26.5 eV and is plotted as the right axis.

II.D. Time-of-flight technique

II.D.1. Chopper design modifications and balancing procedure

The original chopper design is described elsewhere.[11] Briefly, a 115V, 400 Hz hysteresis synchronous motor[12] has been modified to be UHV compatible by replacing all brass parts with equivalent stainless steel parts. Additionally, dry lubricant stainless steel ball bearings are used.[13] The entire chopper motor assembly is shown in Figure 7. The chopper is mounted on the rotor shaft with an aluminum sleeve and cap shown in detail in Figure 8. The inside diameter of the sleeve is a precision fit to the motor shaft.

Three main changes have been made. First, a spacer has been added between the sleeve and the first set of bearings. This spacer was proven to be necessary after the inadvertent destruction of a chopper wheel that ran too close to the photodiode mount.

The second change is to the design of the cap and screw combination that secures the assembly together. The previous chopper mounting design utilized a flathead screw that matched a conical depression in the cap. This design served well for many years. However, one of the problems with a conical mating surface is that unless both surfaces are perfect, each time the surfaces are re-tightened against one another a different mating configuration is reached. This variability in the screw/cap mating configuration proved to be incompatible with the improved balancing procedure described below. The cap and screw were therefore redesigned to insure a reproducible balance, and to allow for greater precision in the balancing procedure. Instead of a flathead screw, a cap head machine screw is used. Instead of a conical mating surface, a flat mating surface is provided between the side of the screw and the inner surface of the cap. The screw top is machined down to the correct diameter to ensure a tight fit at this

surface. As before, a vacuum relief hole is drilled through the center of the screw. After these modifications, it was found that a reliable and reproducible fit could be obtained.

The third change involves the dynamic balancing procedure. The chopper balancing procedure was modified in several ways. Previously, the chopper was dynamically balanced using a belt assembly attached to the sleeve to drive the rotor shaft. Although this method provided satisfactory results, a better method is to reproduce the experimental setup as closely as possible during the balancing procedure. It has been shown that driving the motor at 60 Hz using common line voltage and a simple circuit design is sufficient for the purposes of dynamic balancing. The motor circuit wiring diagram is shown in Figure 9. The 60 Hz and 400 Hz configurations differ only in the value of the capacitor. The sinusoidal driving voltage (supplied by either a 60 Hz waveform from line voltage or a 280 Hz or 400 Hz waveform from the synchronous chopper motor drive frequency generator[14]) is connected as shown to the wires coming from the chopper motor, which are color-coded. In order to switch the direction of rotation, the black and brown wires are interchanged.

Previously, the sleeve, cap and wheel were assembled as a unit and then balanced as a unit. This procedure allowed for the possibility that intrinsic imbalance in the chopper wheel could be accounted for by removal of material from the cap and sleeve. If imbalance in the wheel was corrected by removing material from the cap or sleeve, and their orientations were subsequently changed upon reassembly, then the resulting imbalance could be greater than the initial imbalance, which is an unacceptable situation. Two changes were made to ensure that this did not happen. First, the rotor was balanced separately from the cap and sleeve, which were in turn balanced separately from the chopper wheel, resulting in a reproducible balance regardless of the orientation of the components. Second, alignment marks were scribed on the surface of

each of the components, so that even if alignment issues were to be a problem, the original alignment can always be reproduced.

Explicitly, the balancing procedure consisted of the following steps. First, the bearings are installed on the rotor shaft and the rotor shaft is installed into the chopper motor. The motor is then attached to a Variac transformer using the circuit diagram given in Figure 9. The rotor shaft is balanced by drilling dimples into the shaft away from the bearing surfaces. At this point a single groove is cut radially on the front and back surfaces of the rotor shaft. These grooves serve as alignment marks for the rest of the chopper fittings. Next the spacer, sleeve and cap are installed without the chopper wheel and balanced as a unit by removal of material from the cap and sleeve. Alignment grooves are then cut radially on the outside surface of both the cap and the sleeve in the same position as the alignment groove on the rotor shaft. Finally the chopper wheel is installed and balanced by drilling holes into the inner surface of the wheel, and an alignment mark is made in the same position as the alignment grooves on the rotor shaft, sleeve and cap. By balancing the sleeve and cap as a unit prior to balancing the chopper wheel, the possibility of using the cap and sleeve to accommodate intrinsic imbalance of the chopper wheel is eliminated. Aligning the pieces to each other during installation produces a reliable, reproducible, balanced assembly. All balancing was performed by Lindskog Balancing Corporation.[15]

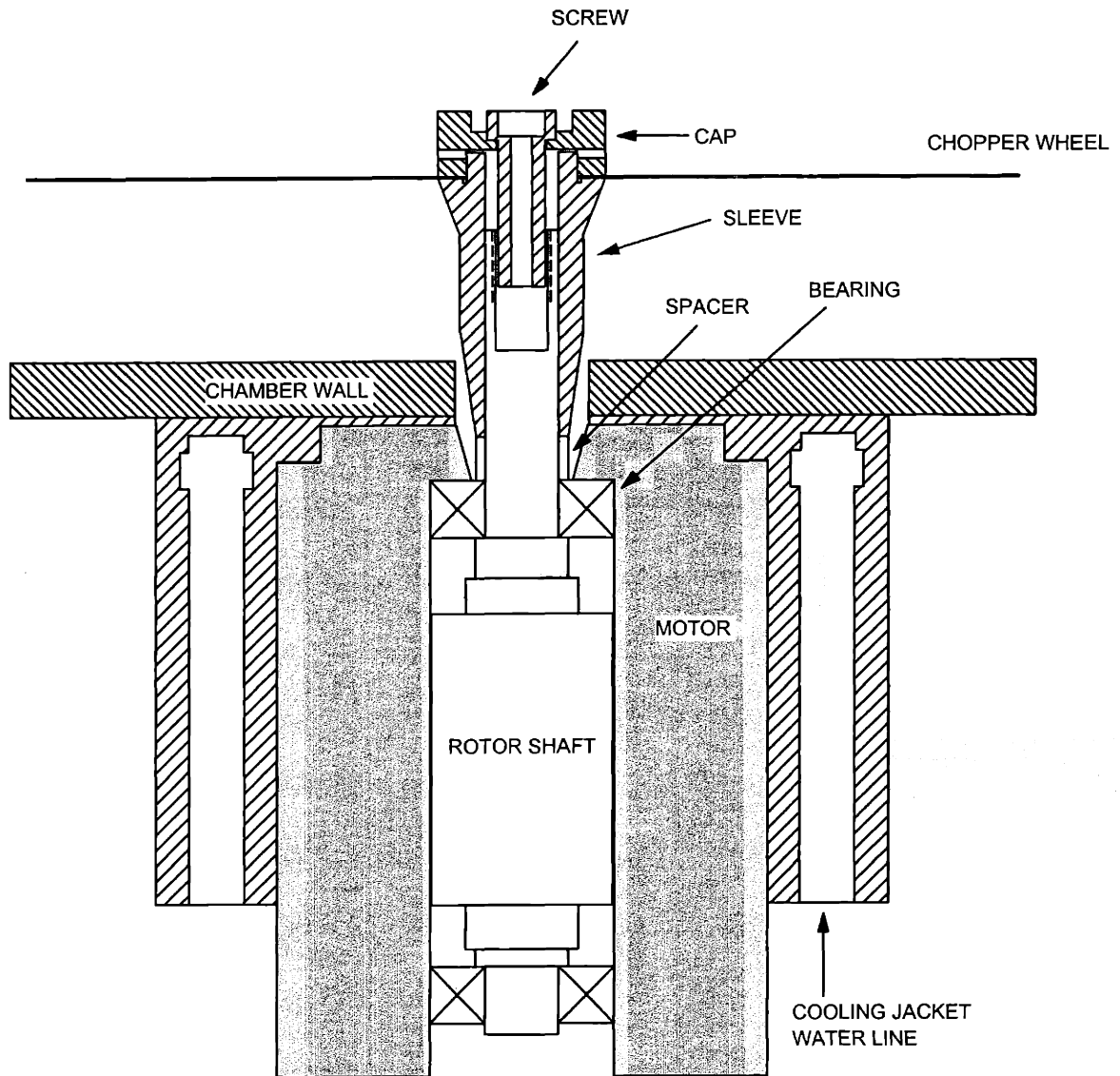**Figure 7 Chopper motor assembly**

112
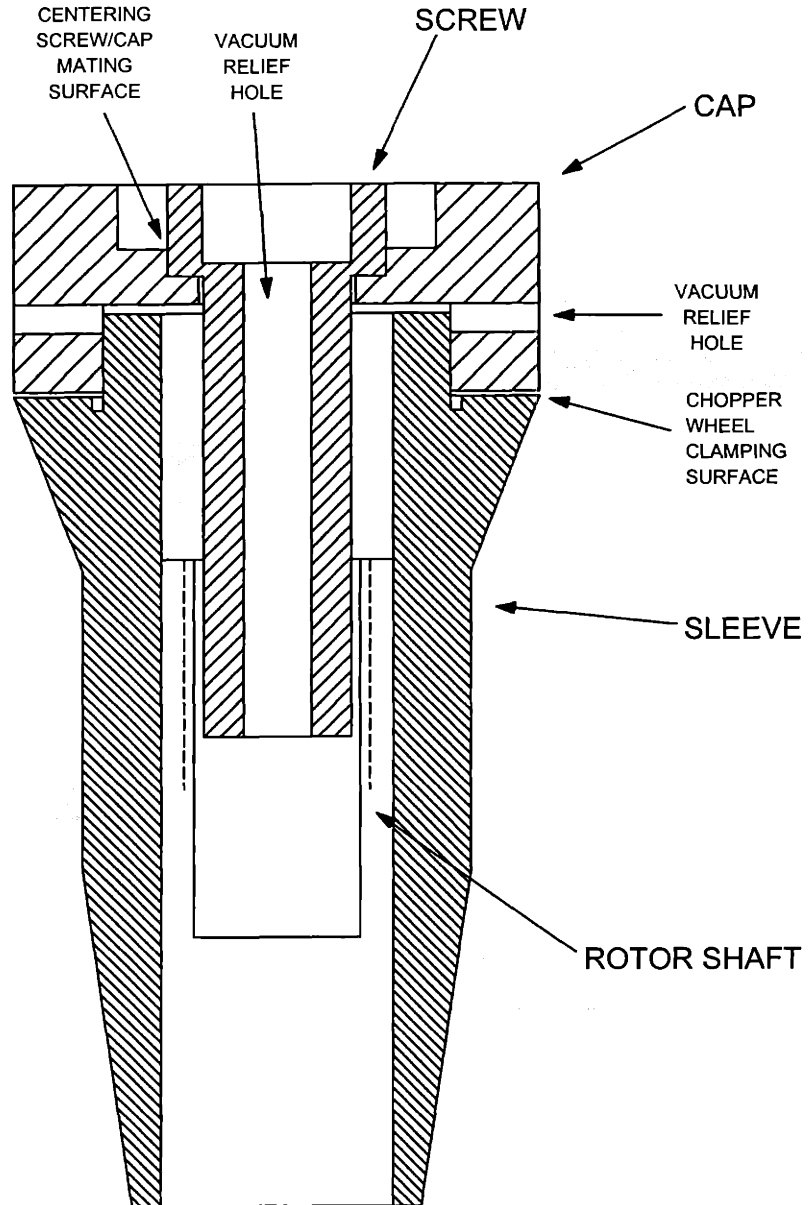
Figure 8 Chopper sleeve and cap detail

CAPACITOR
2 μF (60 Hz)
0.22 μF (400 Hz)

RED

BLACK

DRIVING
SINUSOIDAL

MOTOR
WINDING

MOTOR
WINDING

WHITE/BLUE

BROWN
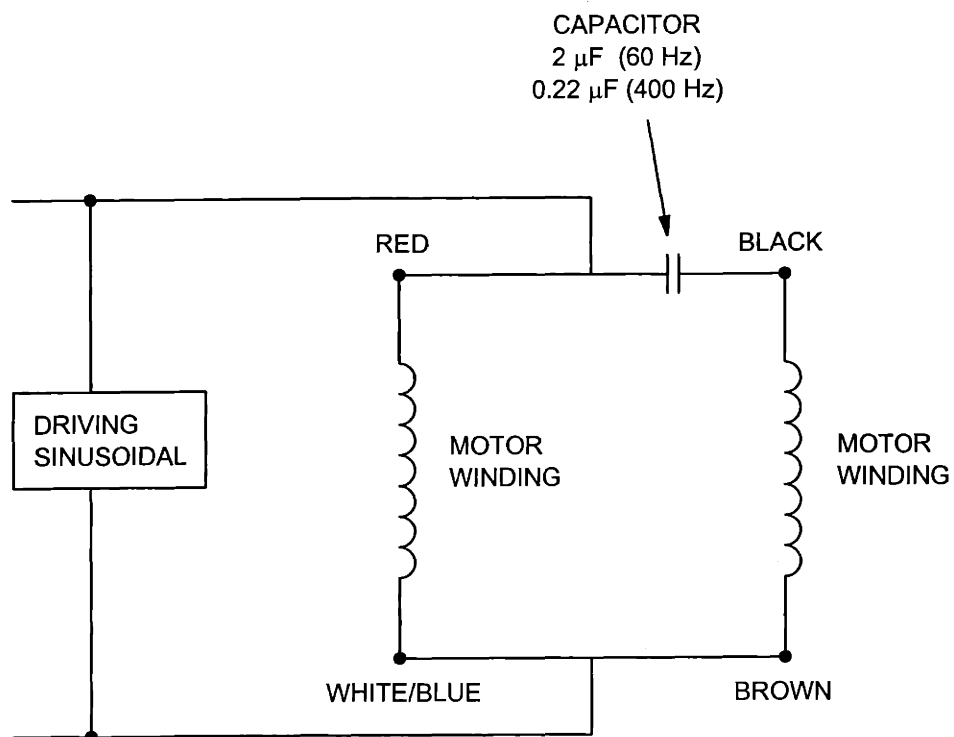
Figure 9 Motor wiring diagram schematic

II.D.2. Measurement and analysis of TOF spectra

A pseudorandom cross-correlation chopper wheel with 255 slots is spun at a frequency of 280 Hz or 392 Hz, corresponding to a dwell time of 14 μs or 10 μs respectively. The chopper wheel is located at the entrance to the detector, allowing line-of-sight time-of-flight (TOF) measurements to be made of the incident beam or of species scattered from the crystal surface. The deconvolution of the raw data is described in detail elsewhere.[11] The neutral flight path is L=0.293±0.013 m, where the uncertainty in the flight path is due to the finite length of the ionizer region.

The TOF measurements presented in Section III of this chapter are the result of extensive signal averaging. TOF spectra were measured at four separate masses, m/e = 167, 148, 129 and 19, corresponding to XeF_2^+, XeF^+, Xe^+ and F^+, and at three detection angles, θ_d = 15°, 30° and 60°. For the TOF spectra measured at m/e=167, 148 and 19 the ionizer was set at the normal setting, with an electron energy of 75 eV. For the TOF spectra measured at m/e=129 the ionizer was set at the low cracking setting, with an electron energy of 26.5 eV. The number of experiments performed at each mass and at each angle is given in the following table:

m/e	15°	30°	60°
167	40	81	40
148	40	81	40
129	80	160	160
19	40	81	40

For each experiment, the signal is collected at a single mass over the entire coverage range. Since the velocity distributions of the detected species in general are not constant with respect to exposure, it is desirable to have the TOF spectra recorded in different 'bins' with respect to exposure. Acquisition of the TOF spectra is controlled by the data acquisition software as described below. First the molecular beam shutter is opened for a brief period of

time, referred to as a bin, and the TOF spectrum is recorded. The molecular beam flag is subsequently closed for 0.25s while the TOF signal is stored on the computer. The response time of the shutter, shown in Figure 10, was measured by monitoring the signal as a function of time of a beam of neat Ar at a stagnation pressure of 0.8 torr upon opening and closing the beam shutter. The response time is less than 0.01s for both opening and closing, and the difference between the opening and closing times is less than 0.01s. The uncertainty in the dose time due to the shutter opening and closing is less than 0.7%, and is therefore negligible. The process repeats for the next exposure interval and continues until the entire exposure is complete. After the experiment is over, the crystal is briefly annealed to ~1100 K to desorb the fluorine and restore order to the surface.

In the present experiment, the total exposure time of 35.0 s was divided into twenty-four separate bins of 1.46 s each. The XeF_2 incident beam flux is 0.0663 ML F atoms/s, so each bin corresponds to an exposure range of 0.0968 ML F atoms. Due to signal to noise constraints, however, it was desirable to combine sets of three bins together to form eight time "slices." Each time slice therefore corresponds to an exposure range of 0.290 ML F atoms.

The TOF distribution for the *detected* particles is given by a number-density Maxwell-Boltzmann (MB) distribution transformed into time coordinates.[16]

$$F^{\# dens}(t)dt = A\frac{L^3}{t^4}\exp\left[-\left(\frac{mL^2}{2kT}\right)\left(\frac{1}{t}-\frac{1}{t_f}\right)^2\right]dt \qquad \text{[Eq. II. 1]}$$

where the flight time, t is the independent variable, L is the flight path length and is fixed, and the four fit parameters are the normalization constant A; the mass of the particle that gives rise to the signal, m; the temperature of the distribution, T; and the flow velocity, v_f, which is related to

the flow time, t_f, by the formula $v_f = \dfrac{L}{t_f}$. For a detailed discussion of the flow velocity and flow time, see Appendix 2.

The number density MB distribution can be transformed into a flux distribution by multiplying by the velocity, $v = \dfrac{L}{t}$. The total flux is then obtained by integrating the flux distribution over the entire time domain.

$$F^{flux}(t)dt = vF^{\#dens}(t)dt = A\frac{L^4}{t^5}\exp\left[-\left(\frac{mL^2}{2kT}\right)\left(\frac{1}{t}-\frac{1}{t_f}\right)^2\right]dt$$

$$I_{tot} = \int_0^\infty F^{flux}(t)dt = \int_0^\infty A\frac{L^4}{t^5}\exp\left[-\left(\frac{mL^2}{2kT}\right)\left(\frac{1}{t}-\frac{1}{t_f}\right)^2\right]dt \qquad \text{[Eq. II. 2]}$$

The other two quantities of interest are the average velocity and the average energy of the distribution. These are given by the formulae:

$$V_{avg} = \frac{\int_0^\infty vF^{flux}(t)dt}{I_{tot}} = \frac{\int_0^\infty A\frac{L^5}{t^6}\exp\left[-\left(\frac{mL^2}{2kT}\right)\left(\frac{1}{t}-\frac{1}{t_f}\right)^2\right]dt}{I_{tot}} \qquad \text{[Eq. II. 3]}$$

$$E_{avg} = \frac{\int_0^\infty \frac{1}{2}mv^2 F^{flux}(t)dt}{I_{tot}} = \frac{\int_0^\infty A\frac{1}{2}m\frac{L^6}{t^7}\exp\left[-\left(\frac{mL^2}{2kT}\right)\left(\frac{1}{t}-\frac{1}{t_f}\right)^2\right]dt}{I_{tot}} \qquad \text{[Eq. II. 4]}$$

A detailed discussion of the propagation of error for these equations is given in the Appendix.

Occasionally, it is necessary to transform a number density TOF distribution into a flux energy distribution. To do so, one must first find the Jacobian to transform between energy and flight time:

$$E = \frac{1}{2}mv^2 = \frac{1}{2}m\left(\frac{L}{t}\right)^2$$

<div align="right">[Eq. II. 5]</div>

$$dE = (mv)dv = -m\left(\frac{L^2}{t^3}\right)dt$$

Resulting in the following transformation:

$$F^{flux}(E) = \frac{1}{m\left(\frac{L^2}{t^3}\right)} F^{flux}(t(E)) = \frac{t^3}{mL^2}\left(\frac{L}{t} F^{\#dens}(t(E))\right) = \frac{t^2}{mL} F^{\#dens}(t(E)) \qquad \text{[Eq. II. 6]}$$
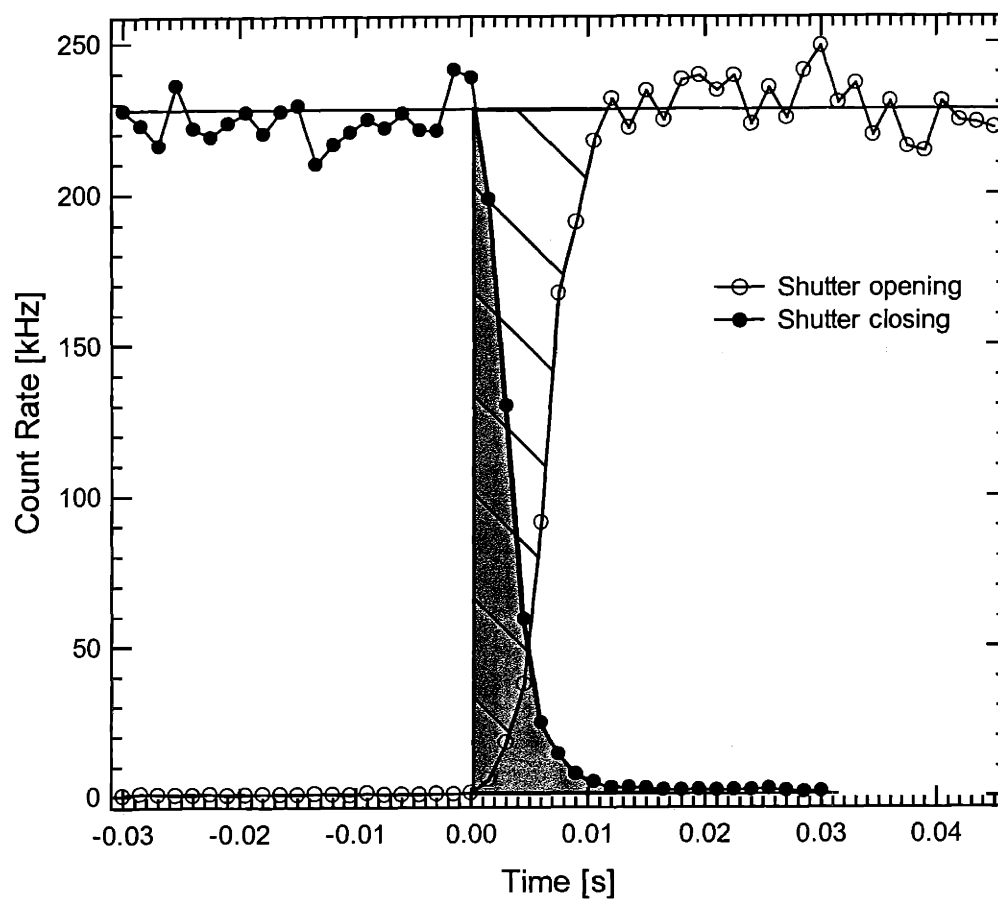
where $t(E) = \sqrt{\dfrac{mL^2}{2E}}$.

Figure 10 Molecular beam shutter response time

II.D.3. Ionizer fragmentation

The nature of the electron impact bombardment ionizer used in the quadrupole mass spectrometer detector is such that significant amounts of fragmentation can occur in the ionizer region. This fragmentation complicates the interpretation of the TOF spectra, since the ionization of the parent XeF_2 molecule gives rise to species that can be detected as XeF^+, Xe^+ or F^+. Similarly, ionization of XeF gives rise to species that can be detected as Xe^+ or F^+. If the fragmentation patterns, or cracking ratios, of the parent molecules are known, then the net signal at each mass can be determined by subtracting the signal of any parent molecule multiplied by its respective cracking ratios. In order to measure the fragmentation pattern of XeF_2, the incident beam is directed into the mass spectrometer detector. Since the incident beam contains only XeF_2 molecules, any signal at the other masses must be due to ionizer fragmentation of XeF_2. The TOF spectra are measured at each mass using the ionizer settings that were used to collect the TOF spectra shown in Section III. That is, the TOF spectra at m/e=167, 148 and 19 are measured using the "normal" setting with an electron energy of 75 eV, and the signal at m/e=129 is measured using the "low cracking" setting with an electron energy of 26.5 eV. The XeF_2 cracking ratios are given by the flux, as determined in Eq. (II.2), at masses 148, 19 and 129 each divided by the flux at m/e=167. Using these cracking ratios, the contribution from the dissociative ionization of XeF_2 can be subtracted from the measured XeF^+, Xe^+ and F^+ TOF spectra.

Since a source of pure XeF is unavailable, the fragmentation pattern of XeF to form Xe^+ or F^+ is not known. The maximum cracking ratios are determined to be that which results in a non-negative TOF signal after cracking has been subtracted at all detection angles and at all coverage ranges. That is, the F^+:XeF^+ or Xe^+:XeF^+ cracking ratios are increased until the net F^+

or Xe^+ signals respectively are observed to become zero at any flight times of any of the individual TOF spectra. The limiting spectra for m/e=19 were the spectra at θ_d=15° and 0.88 ML – 1.25 ML coverage, while the limiting spectra for m/e=129 were the spectra at θ_d=60° and 1.01 ML – 1.25 ML. The maximum F^+:XeF^+ and Xe^+:XeF^+ cracking ratios found in this way are 0.4:1 and 1.0:1 respectively. However, there is no a priori way to know that the maximum possible cracking ratio is the true cracking ratio. Therefore, the m/e=129 TOF spectra are analyzed using three different values for the Xe^+:XeF^+ cracking ratio – the maximum cracking ratio determined as stated above, an intermediate cracking ratio arbitrarily set to be half of the maximum cracking ratio, and a minimum cracking ratio, which is set to zero. The effect of changing the Xe^+:XeF^+ cracking ratio is discussed in the subsection below describing the observed m/e=129 TOF spectra.

III. Results

The TOF spectra of the scattered products of the reaction have been measured as a function of exposure to XeF_2 with the detector positioned at $\theta_d=15°$, $30°$ and $60°$ from the surface normal in the forward scattering direction. The TOF measurements are the most important results of the current experiment because knowledge of the velocity distributions of XeF, F and Xe allows for the momentum matching calculation that not only demonstrates that gas-phase XeF dissociation is responsible for the observed F atom signal, but also distinguishes the Xe atoms due to XeF dissociation from the rest of the Xe TOF signal. The results span the coverage range from 0 ML to 1.25 ML as calibrated by thermal desorption spectroscopy. Four distinct species are investigated: 1. unreactively scattered XeF_2, 2. XeF arising from single atom abstraction, 3. F atoms arising from the dissociation of XeF prior to detection in the mass spectrometer, and 4. Xe arising from both two atom adsorption and XeF gas phase dissociation.

The presentation of the experimental results is divided into five sections. The first section briefly describes the results of thermal desorption measurements and describes how the dissociative chemisorption probability of XeF_2 as a function of coverage can be determined from them. The second section describes the observation of the SiF_4 etch product as a function of coverage. The third section gives the evolution of the He diffraction specular feature with respect to coverage. The results described in the first three sections mirror the results described in Chapter 2. However, they are measured again at the lower surface temperature used for the time-of-flight study that is the main result of the present chapter. The last four sections present the TOF distributions for each of the scattered reaction products as a function of coverage and scattering angle.

III.A. Thermal desorption spectroscopy

Recent studies of the interaction of F_2 with Si(100)2×1 have shown that F_2 reacts via atom abstraction with the Si(100) surface dangling bonds. Once each dangling bond is bound to a F atom, the reaction ceases. The resulting saturation coverage is about 1 ML (0.94 ± 0.11).[8] The partial pressures of products desorbing from this layer that are monitored in a thermal desorption experiment and are integrated over temperature are a measure of 1 ML of adsorbed fluorine. This value is used in the present study to calibrate the fluorine coverage resulting from a known exposure of Si(100) at 150 K to XeF_2. Knowledge of the fluorine coverage coupled with knowledge of the absolute flux of the incident XeF_2 beam also enables the dissociative chemisorption probability of XeF_2 to be determined as a function of coverage on Si(100) at 150 K, as was carried out in the experiment at 250 K described in Chapter 2.

The crystal is held at 150 K during exposure to a beam of F_2 or XeF_2. The beam is incident at 20° to the normal of the crystal surface. The crystal is subsequently rotated so that its normal is aligned with the axis of the differentially pumped mass spectrometer. The crystal is heated from 150 K to a maximum temperature of 1000 K at a constant rate of 5 K/s and the masses at m/e = 66 (SiF_2^+) and m/e = 85 (SiF_3^+) are monitored essentially simultaneously by switching between masses at a rate of 10 Hz. The SiF_2^+ and SiF_3^+ signals originate from the ionization or dissociative ionization of the SiF_2 and SiF_4 parent molecules, respectively, in agreement with previous results.[17] The resulting thermal desorption spectra are shown in Figure 11 and are similar to those shown in Chapter 2, Figure 1. Note that the temperature scale in Figure 11 has been adjusted so that the main SiF_2^+ feature occurs at 800 K. The total thermal desorption yield at a given exposure or coverage is proportional to the fluorine coverage and is given by the sum of the SiF_2 and SiF_4 signals integrated over temperature. The integrated yields

of each product are scaled for the relative detection sensitivities of SiF_2 and SiF_4, the factor of two more fluorine atoms that SiF_4 has relative to SiF_2, the different velocity and angular distributions of the desorbing SiF_2 and SiF_4 species, and their relative ionization cross sections and quadrupole transmissions.[18] More detailed information about this procedure is given in Appendix B. The SiF_4 thermal desorption yield as a result of exposure to XeF_2 is small, never exceeding 9% of the SiF_2 yield.

In Figure 12, the total thermal desorption yield is plotted on the right axis as a function of XeF_2 exposure to Si(100) at 150 K, where the exposure is measured in ML F. This total thermal desorption yield is converted into coverage using the value of the total thermal desorption yield after a long-time exposure to F_2, which is known to represent the saturation coverage of about 1 ML (0.94 ± 0.11),[8] as the calibration. The coverage is plotted on the left hand abscissa so that it corresponds to the calibrated thermal desorption yield on the right hand abscissa in Figure 12. The results are similar to those shown in Chapter 2, Figure 2 for XeF_2 incident on Si(100) at 250 K. The coverage at a given exposure is calculated from the fit to the data shown in Figure 12. To do so, an exponential function given by

$$\text{coverage [ML]} = 3.71 - 3.71e^{-0.202\varepsilon} \tag{III. 1}$$

is fit to the measurements of coverage as a function of XeF_2 exposure in ML F atoms, ε, in Figure 12. Eq. (III.1) is used to calibrate the coverage from a known exposure of XeF_2 for all the ensuing results presented in this chapter.

Knowledge of the fluorine coverage coupled with knowledge of the absolute flux of the incident XeF_2 beam enables the dissociative chemisorption probability of XeF_2 reacting with Si(100) at 150 K to be determined as a function of coverage. The derivative of Eq. (III.1) with respect to exposure yields the dissociative chemisorption probability as explained in Chapter 2.

The dissociative chemisorption probability as a function of coverage is plotted in Figure 13. Probabilities for XeF_2 are calculated only for coverages below about 0.8 ML, because probabilities determined by this thermal desorption method are only valid when the residence time of the adsorbate is effectively infinite. The results presented in Section III.B below show that fluorine begins to desorb as SiF_4 as the fluorine coverage builds to 0.8 ML as a result of exposure to XeF_2. The dissociative chemisorption probability starts at around 0.73±0.26 on a clean surface and decreases to around 0.40±0.16 just prior to the onset of etching, where the error bars are calculated as described in Appendix B. These probabilities are similar to those presented in Chapter 2 for a surface temperature of 250 K, which showed a dissociative chemisorption probability of about 0.82±0.14 on a clean surface, decreasing to about 0.54±0.10 just prior to the onset of etching. It should be noted that the dissociative chemisorption probability is equal to $0.5P_1 + P_2$, where P_1 and P_2 are the probabilities of single atom abstraction and two atom adsorption respectively, as given in the discussion of Eq. (IV.11) in reference 26 and in Chapter 2.

It is noted here for reference that the TOF results described in Section III.D span an exposure range from 0 ML to 2.32 ML F. Each experiment records TOF spectra at eight equally divided exposure ranges of 0.29 ML each, spanning the entire exposure range. Each exposure range can be calibrated to a coverage range using the results shown in Figure 12 and Eq. (III.1), yielding the following coverage ranges: 0-0.22 ML; 0.22-0.40 ML; 0.40-0.57 ML; 0.57-0.73 ML; 0.73-0.88 ML; 0.88-1.01 ML; 1.01-1.14 ML; and 1.14-1.25 ML.
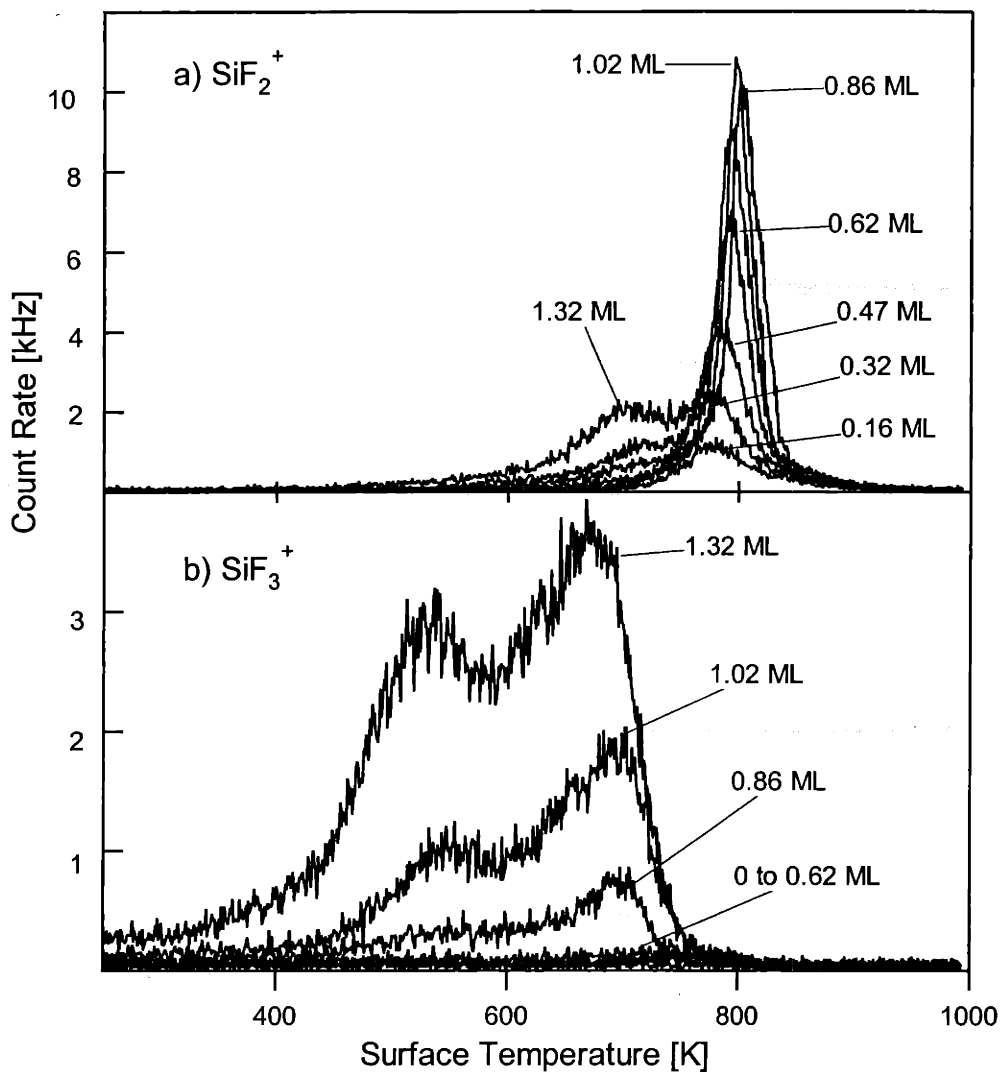
Figure 11 Thermal desorption spectra

Thermal desorption spectra measured at (a) m/e=66 and (b) m/e=85 after XeF$_2$ exposure at θ_i=20° and T$_s$=150 K to yield the fluorine coverages in ML F atom that are shown for each trace. Temperature ramp rate is 5 K/s. Temperature scale is calibrated so that the main feature in (a) occurs at 800 K.
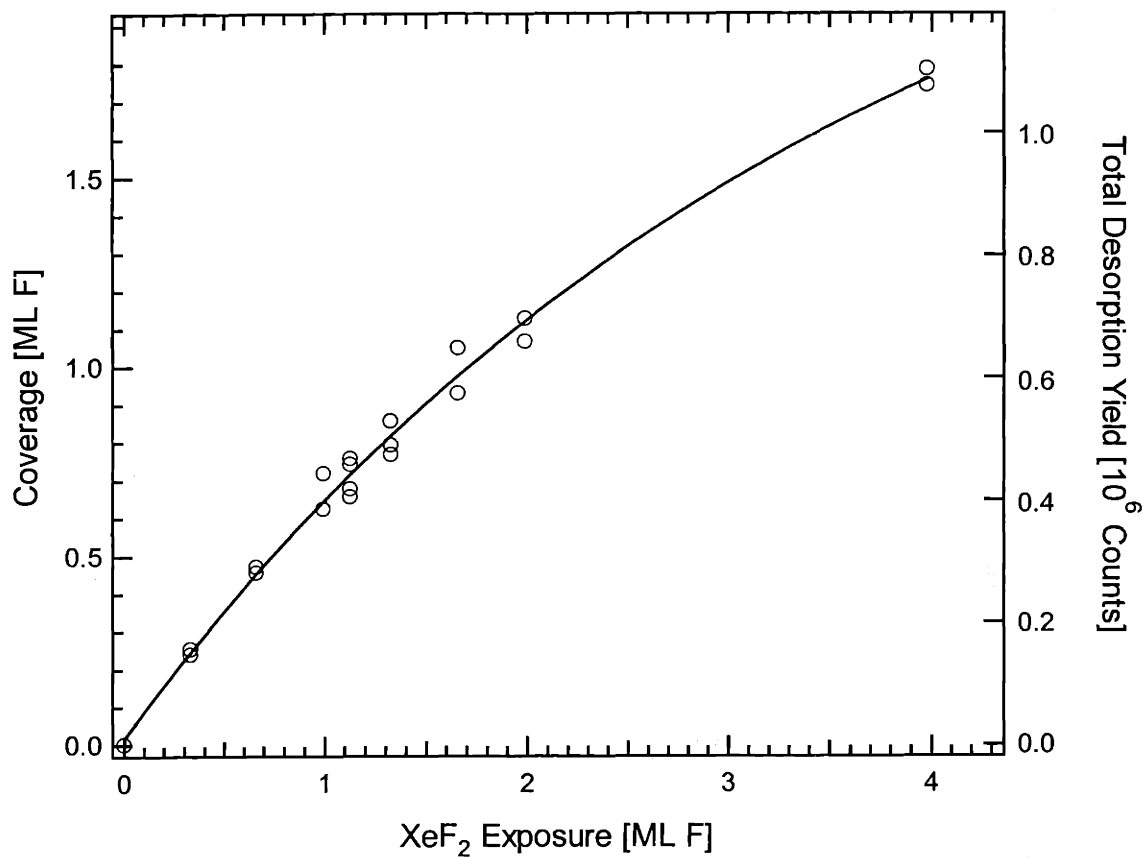
Figure 12 Fluorine coverage as a function of XeF₂ exposure at 150 K surface temperature
Fluorine coverage in ML F atoms as a function of XeF₂ exposure at a surface temperature of 150 K. Solid line is an exponential fit to the data.
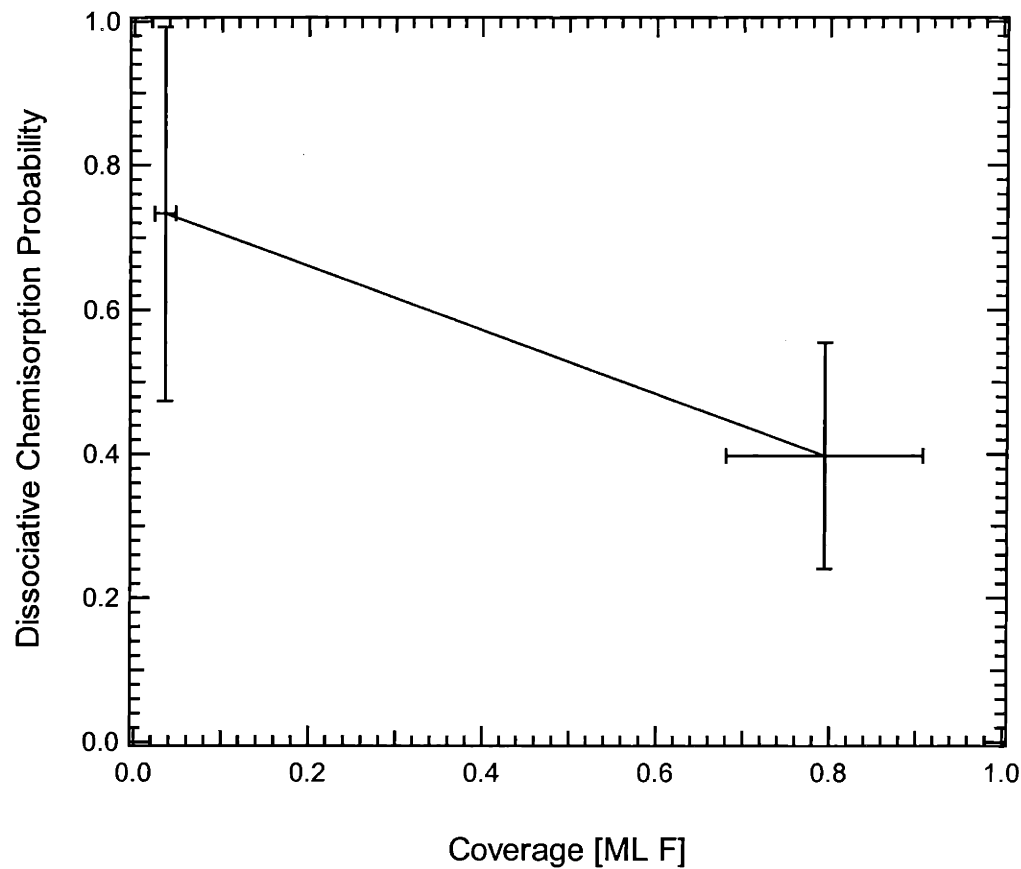
Figure 13 Dissociative chemisorption probability at 150 K surface temperature
Dissociative chemisorption probability (0.5 P_1 + P_2) calculated from the derivative of the exponential fit in Figure 12. Note that above ~0.8 ML coverage XeF_2 exposure produces SiF_4 etch product, so the dissociative chemisorption probability cannot be determined by this method. Error bars are 95% confidence limits.

III.B. Etch product

Similar to the results presented in Chapter 2, Figure 3, the etch product is monitored during the course of the reaction in order to determine at what coverage XeF_2 begins to etch the Si surface. Figure 14 shows a plot of the signal intensity at m/e=85, corresponding to SiF_3^+ arising from the etch product SiF_4, as a function of coverage during exposure of XeF_2 to Si(100) at 150 K. The measurement is for a scattering geometry in which the XeF_2 beam is incident at 20° from the surface normal, $\theta_i=20°$, and the detector is positioned at a forward scattering angle of 15°, $\theta_d=15°$. The signal intensity remains zero or near zero below 0.8 ML coverage. Above 0.8 ML coverage, there is a slight increase in the intensity of the signal, and after about 1.2 ML coverage the signal increases dramatically. The initial increase at about 0.8 ML is consistent with the results presented in Chapter 2, Figure 3, at a surface temperature of 250 K. However, the dramatic increase in signal after about 1.2 ML coverage is in contrast to the 250 K results, which reached a steady-state value. A direct comparison between Chapter 2, Figure 3, and Figure 14 in the present chapter is complicated by the fact that the two experiments were performed at different incident energies, with different incident fluxes, and with different detector settings. An increase in the XeF_2 etch rate with decreasing temperature has been observed previously[19,20] and has been taken as evidence for an extrinsic precursor mechanism.
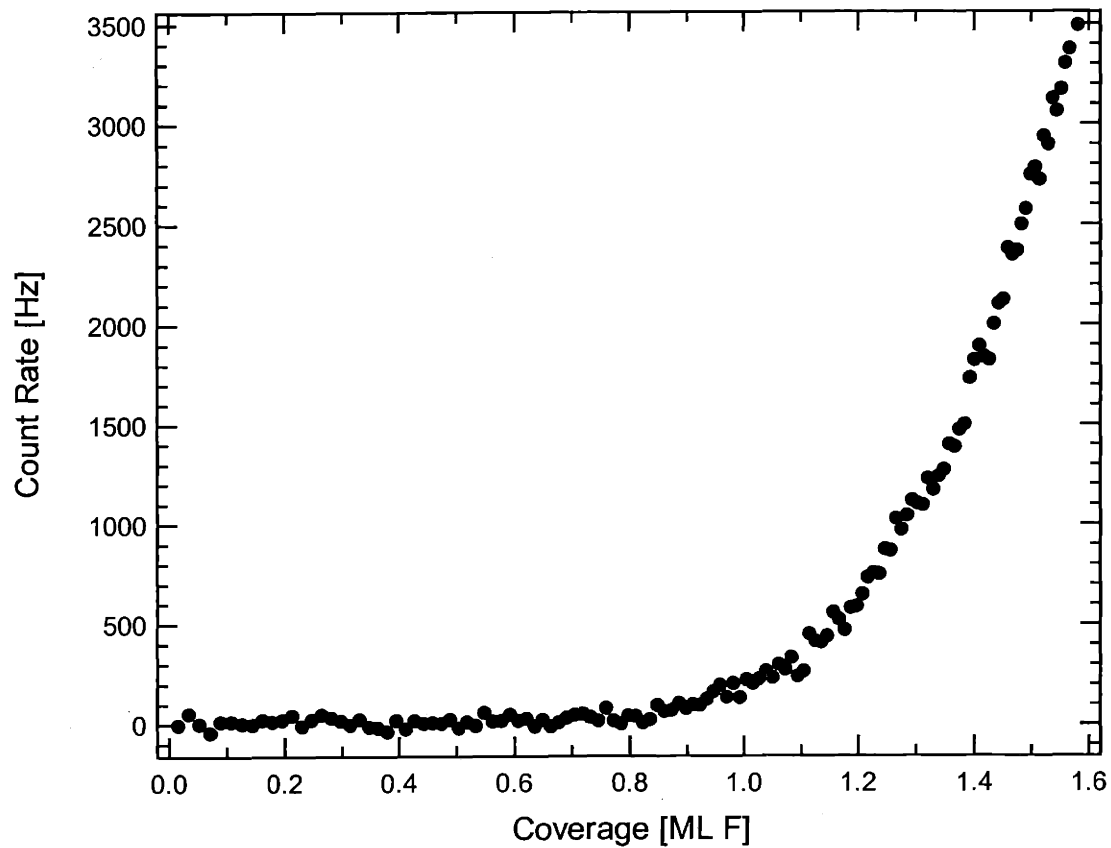
Figure 14 Coverage dependence of scattered SiF$_3^+$ signal

Signal at m/e=85 resulting from exposure of low energy XeF$_2$ exposure at θ_i=20°, θ_d=15° and T$_s$=150 K. Coverage is calculated using the calibration curve shown in Figure 12 and Eq. (III.1). Electron impact energy is 75 eV.

III.C. Helium diffraction

Similar to the results presented in Chapter 2, Figure 6, the intensity of the He diffraction specular feature is monitored as a function of XeF_2 exposure at a surface temperature of 150 K in order to determine the evolution of the surface order as the reaction progresses. The He probe beam is incident at 40° with respect to the surface normal, while the XeF_2 reactant beam is simultaneously incident at 20° with respect to the normal. The differentially pumped mass spectrometer is positioned at 40° from the normal angle in the forward scattering direction. The intensity of the specular feature is then monitored by the mass spectrometer as a function of exposure.

Figure 15a shows the evolution of the specular feature with respect to exposure of Si(100) at 150 K to XeF_2. Figure 15b shows the same evolution of the intensity of the specular feature plotted with respect to coverage. The coverage at a given exposure is calculated from Eq. (III. 1). The intensity of the specular feature decays rapidly during the initial exposure of the surface to XeF_2. This initial loss of intensity can be understood in terms of fluorination of the surface at random sites. The presence of a F atom bonded to a dangling bond changes the interaction potential of the He atom with that surface unit cell, thereby making it different from the surrounding unit cells that do not yet include a F atom. The surface order is disrupted, thus resulting in a loss of coherency of the diffracted He beam[21]. The specular intensity reaches a minimum at about 0.3 ML and then begins to recover. The specular intensity fully recovers around 0.7-0.8 ML, and then begins to decay rapidly between 0.8 − 1.0 ML, and reaching a minimum value at 1.1 ML. The 0.7-0.8 ML recovery at 150 K is lower than the 0.9 ML recovery reported in Chapter 2 for a surface temperature of 250 K. The fact that the 150 K recovery occurs at a lower coverage than the 250 K recovery is likely due to the presence of physisorbed

XeF$_2$ on the surface at 150 K. Physisorbed XeF$_2$ disrupts the periodicity of the fluorinated surface unit cell, resulting in a loss of specular intensity.
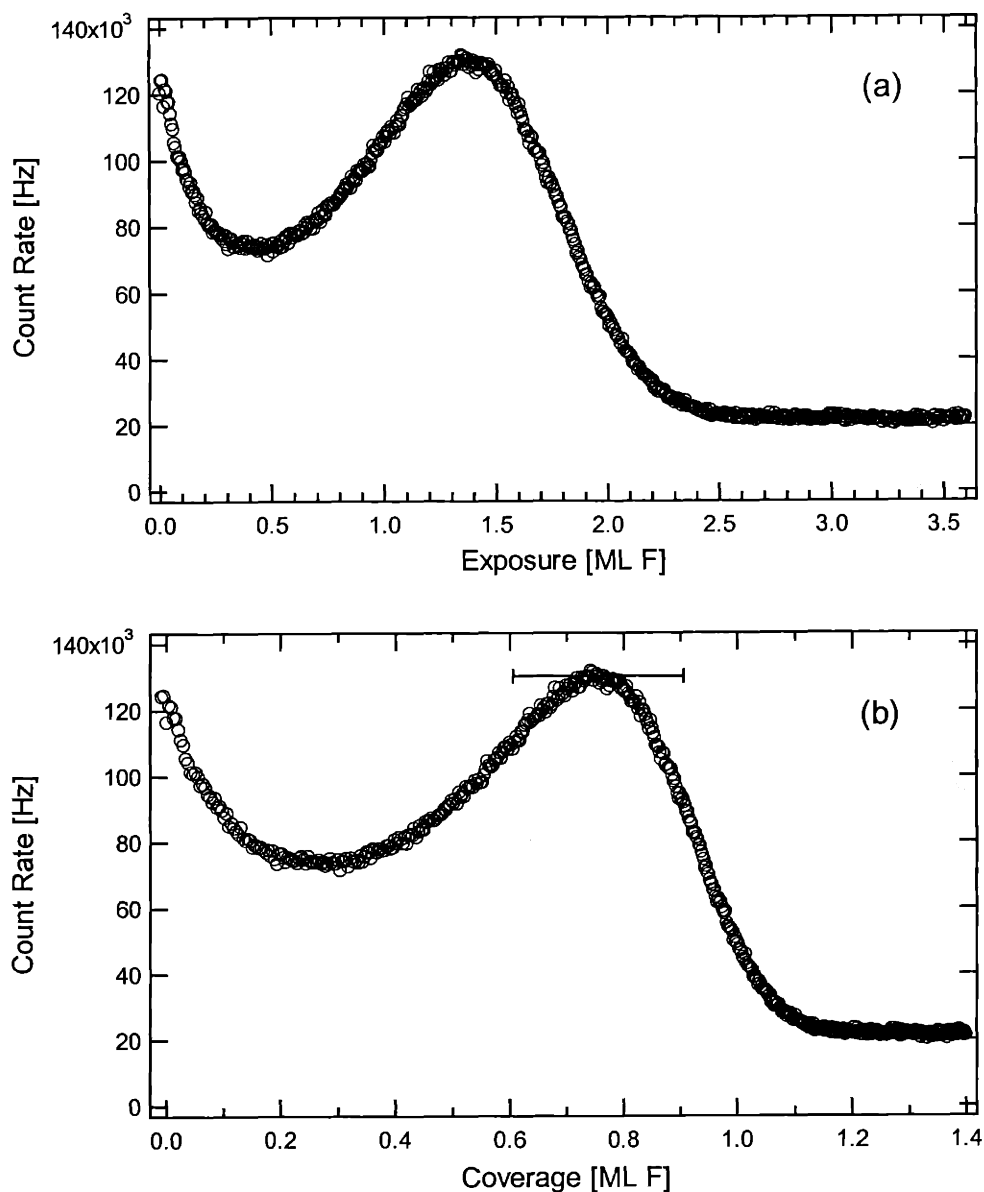
Figure 15 He diffraction specular feature intensity
Intensity of the specular He diffraction feature as a function of a) exposure or b) coverage during exposure to XeF$_2$ at 150 K surface temperature. The He beam is incident at $\theta_i = 40°$; the XeF$_2$ beam is incident at $\theta_i = 20°$; the detector is positioned at $\theta_d = 40°$. Coverage is calculated using the calibration curve shown in Figure 12 and Eq. (III.1). Error bars reflect a 95% confidence limit.

III.D. Scattered TOF spectra at m/e = 167

The scattered TOF distributions at m/e=167 resulting from the interaction of XeF_2 with

Si(100) at an incident energy E_i=1.4 kcal/mol, an incident angle of θ_i = 20°, and a surface

temperature of 150 K are measured at three detection angles, θ_d = 15°, 30°, and 60° in the

forward scattering direction. The signal at m/e=167 corresponds to XeF_2^+ which arises solely

from unreactively scattered XeF_2. As described in Section II.D.2, the TOF spectra are recorded

at eight different coverage ranges: 0-0.22 ML; 0.22-0.40 ML; 0.40-0.57 ML; 0.57-0.73 ML;

0.73-0.88 ML; 0.88-1.01 ML; 1.01-1.14 ML; and 1.14-1.25 ML.

Each of the individual TOF spectra are shown in Figures 16, 17, and 18 for the detection

angles θ_d = 15°, 30°, and 60° respectively. All experiments were taken with an electron energy

of 75 eV and a mass resolution that corresponds to the spectra shown in Figure 6 of the

experimental section. Each spectrum at θ_d = 15°, and 60° are the average of 175s total collection

time, while each spectrum at θ_d = 30° is the average of 354s total collection time. These spectra

exhibit an extremely low signal to noise ratio because very little XeF_2 scatters unreactively from

the surface. While it is possible to fit each of these spectra to Eq. (II. 1) independently, these fits

can be unduly influenced by noise, resulting in fit parameters that vary widely from one coverage

range to the next.

In order to obtain a more consistent fit, the fit parameters for each spectrum are held at

those parameters that best fit the average of all the TOF spectra shown in Figures 16, 17, and 18,

where the contribution of each spectrum to the average is weighted by the number of

experiments taken at that detection angle. The average TOF spectrum is shown in Figure 19, and

spans the entire coverage range 0-1.25 ML, and is comprised of the average of 40 experiments

taken at θ_d = 15°, 81 experiments taken at θ_d = 30°, and 40 experiments taken at θ_d = 60°. The

TOF distribution is fit with a Maxwell-Boltzmann distribution with a flow velocity of 132±44 m/s, a temperature of 194±60 K, and a baseline that was allowed to freely fit the data. This distribution has an average velocity of 263±6 m/s and an average energy of 1.49±0.07 kcal/mol, similar to the average energy of the incident beam.

The individual m/e=167 TOF spectra were fit by fixing the flow velocity and temperature of the Maxwell-Boltzmann distribution at the values for the averaged TOF spectra shown in Figure 19. The baseline of each individual spectrum was fit with the baseline determined from the TOF spectra averaged over a single detection angle. That is, the TOF spectra at θ_d=15°, θ_d=30°, and θ_d=60° were averaged. These three averaged spectra are not shown. The averaged spectra at each scattering angle were then fit with the flow velocity and temperature fixed at those given above for the averaged TOF spectra shown in Figure 19, but the baseline was allowed to vary. The baseline of each of the individual TOF spectra was then fixed at the baseline determined by the fit to the averaged TOF spectrum at that scattering angle.

The flux of each individual TOF distribution is determined by integrating the flux TOF distribution over the flight time as described by Eq. (II. 2) in the experimental section. The angular distribution of the flux is shown in Figure 20, normalized by the number of experiments taken at each angle. The angular distribution of the flux is reasonably well described by a cosine distribution at all coverages. The general trend is that the flux of XeF_2 decreases as the coverage increases. An alternative way of plotting the fluxes, as a function of coverage, is shown in Figure 21.

It should be noted that for the TOF distribution shown in Figure 19 a small amount of signal is evident at flight times around zero. Strictly speaking, the Maxwell-Boltzmann distribution described by Eq. (II.1) goes to zero at these low flight times, which correspond to

very high velocity. However, due of the cyclic nature of the time axis in TOF measurements modulated with a mechanical chopper wheel, when the period of one chopper cycle (2550 µs) is shorter than the flight time of the slowest particles (v<115 m/s), these slow particles are detected at the beginning of the subsequent cycle of the chopper wheel, corresponding to very short flight times, and hence artificially fast velocities, in the TOF measurement. This "wrap-around" component of the observed TOF signal is taken into account during the fitting procedure. The TOF spectrum is fit to a one component Maxwell-Boltzmann function F(t) (Eq. (II.1)) where the flow velocity and temperature are free parameters. The total TOF distribution is calculated as the sum of the TOF distribution at each flight time, plus the signal from the "wrap-around" component. Explicitly, $F^{tot}(t) = F(t) + F(t+2550 \text{ µs})$. Strictly speaking, this sum should include more terms corresponding to wrap-around from multiple cycles of the chopper wheel. However, the contributions due to these terms are found to contribute less than 0.5% to the total signal, and so they are not included.
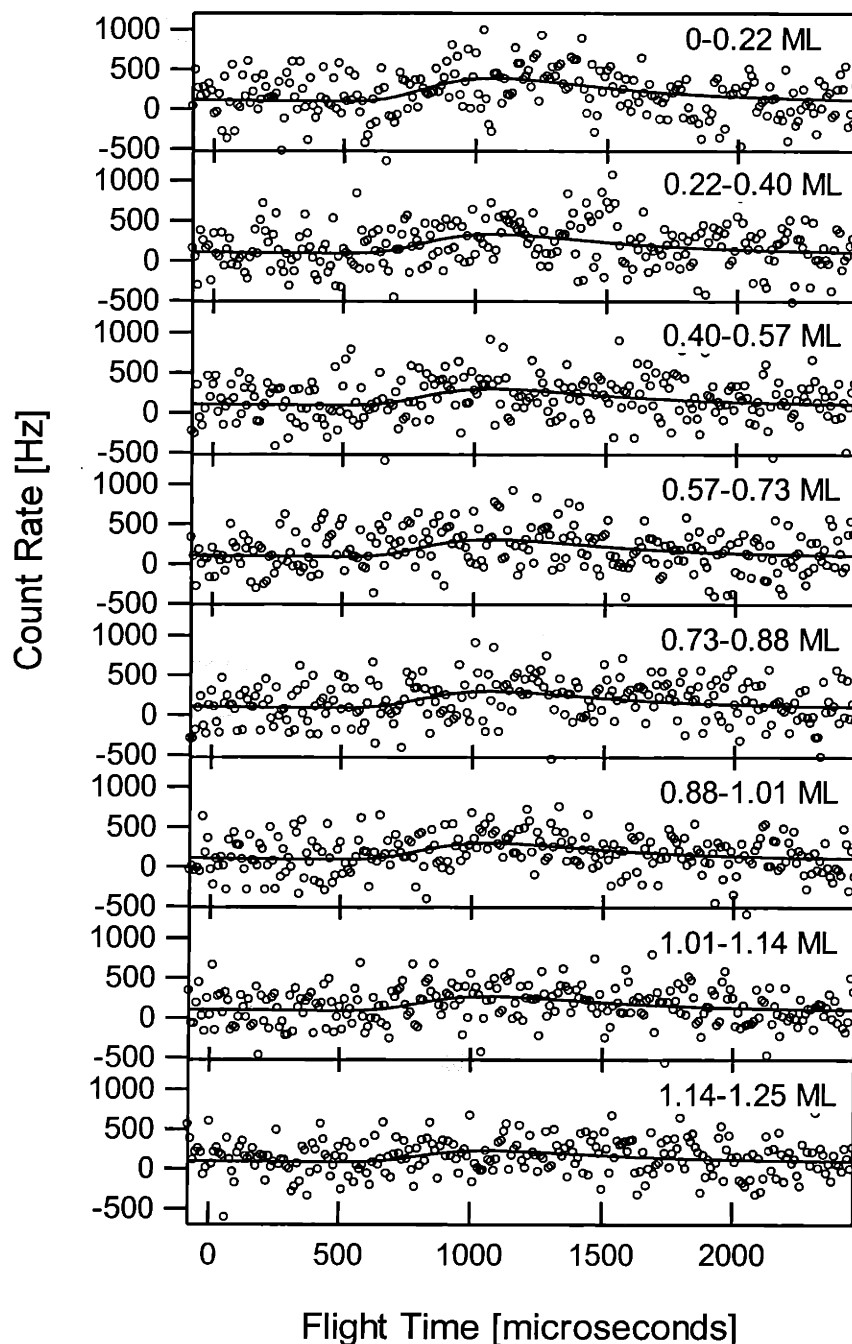
Figure 16 TOF spectra at m/e=167 and $\theta_d = 15°$

TOF spectra at m/e = 167 and a detector angle θ_d = 15° for 8 coverage ranges upon exposure to XeF_2 at θ_i=20° and T_s = 150 K. Thick solid lines shows a least squares fit to a Maxwell-Boltzmann distribution with a flow velocity fixed at 132 m/s and a temperature fixed at 194 K given by the TOF distribution shown in Figure 19. Each TOF spectrum is the average of 40 separate experiments. Electron impact energy is set to 75 eV.

Figure 17 TOF spectra at m/e=167 and $\theta_d = 30°$

TOF spectra at $m/e = 167$ and a detector angle $\theta_d = 30°$ for 8 coverage ranges upon exposure to XeF_2 at $\theta_i=20°$ and $T_s = 150$ K. Thick solid lines shows a least squares fit to a Maxwell-Boltzmann distribution with a flow velocity fixed at 132 m/s and a temperature fixed at 194 K given by the TOF distribution shown in Figure 19. Each TOF spectrum is the average of 81 separate experiments. Electron impact energy is set to 75 eV.
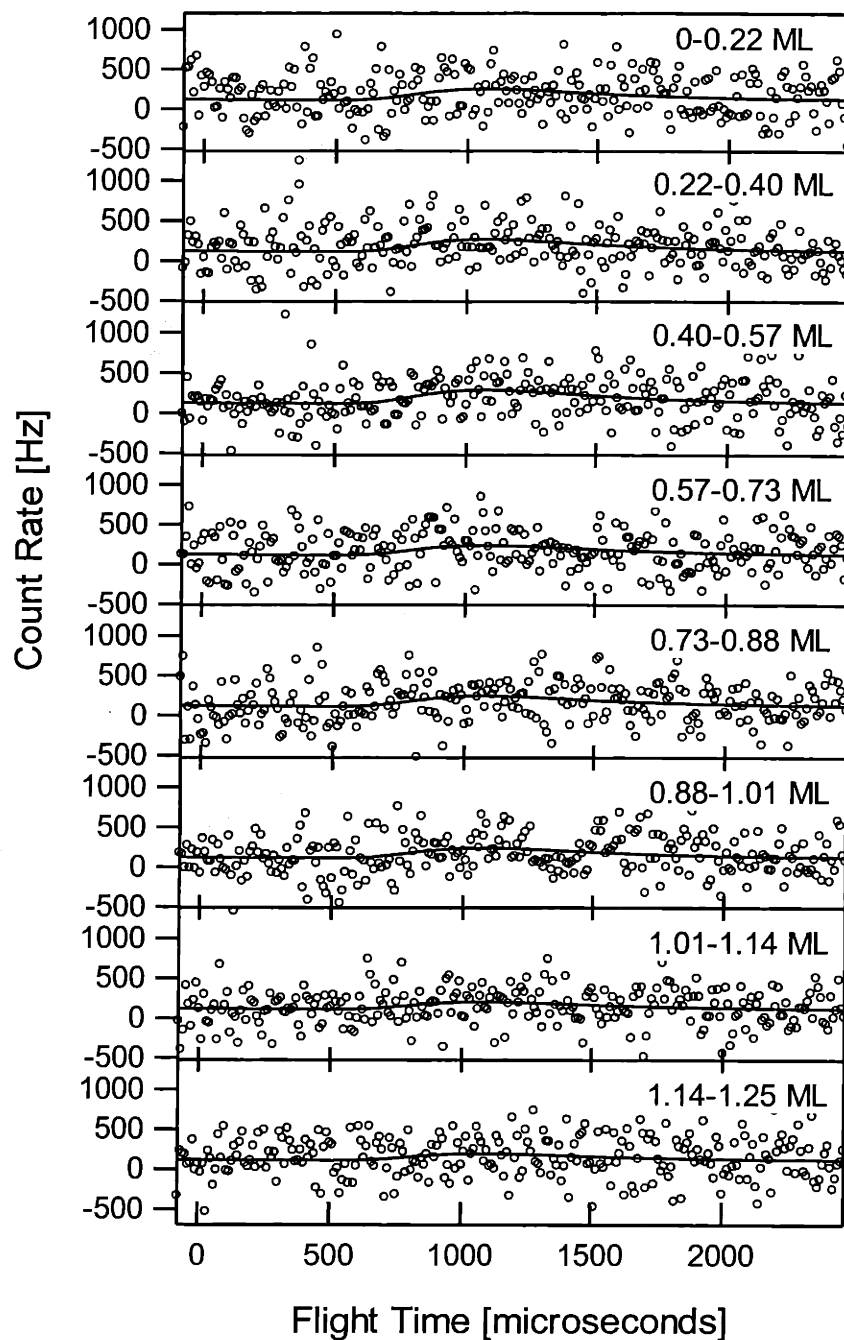
Figure 18 TOF spectra at m/e=167 and θd = 60°

TOF spectra at m/e = 167 and a detector angle θd = 60° for 8 coverage ranges upon exposure to XeF$_2$ at θi=20° and T$_s$ = 150 K. Thick solid lines shows a least squares fit to a Maxwell-Boltzmann distribution with a flow velocity fixed at 132 m/s and a temperature fixed at 194 K given by the TOF distribution shown in Figure 19. Each TOF spectrum is the average of 40 separate experiments. Electron impact energy is set to 75 eV.
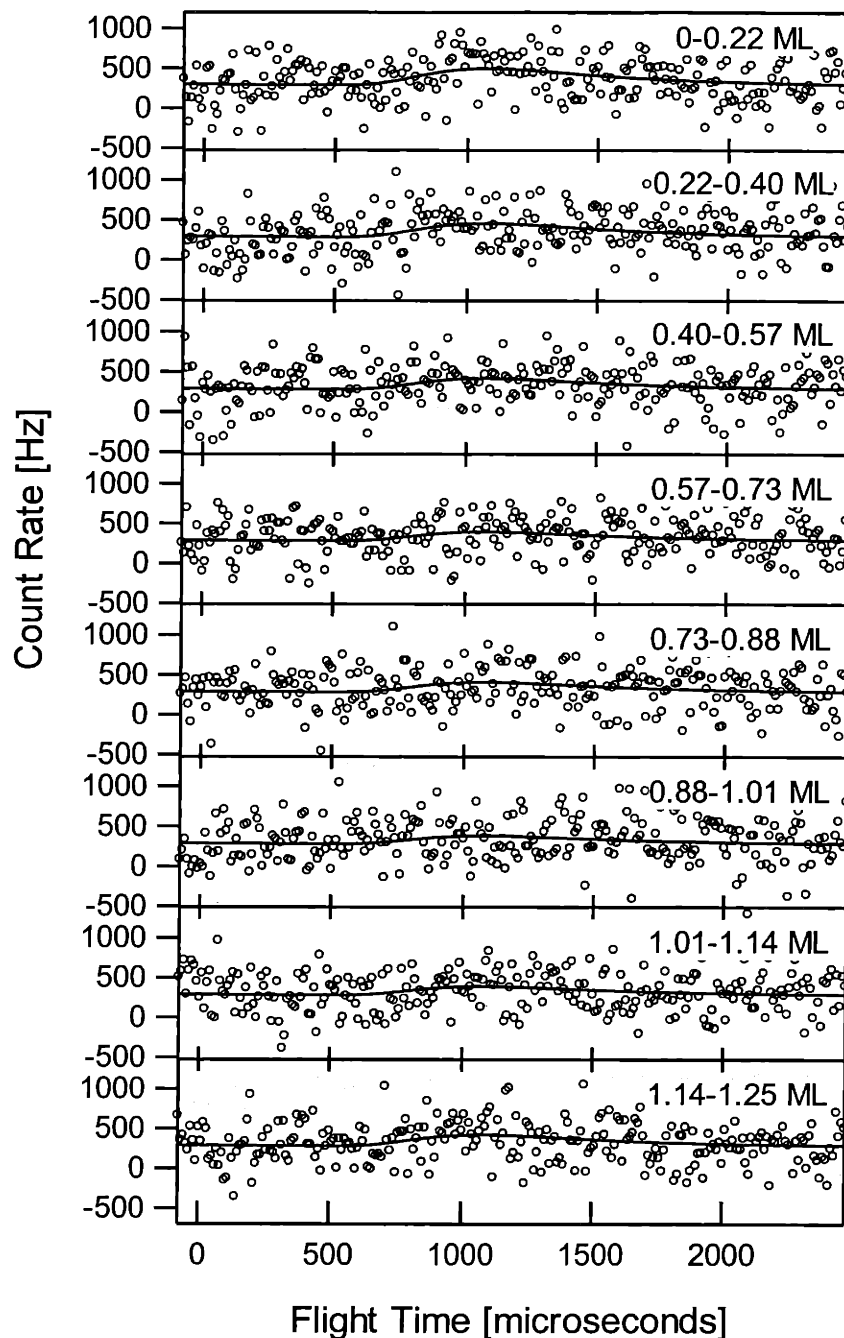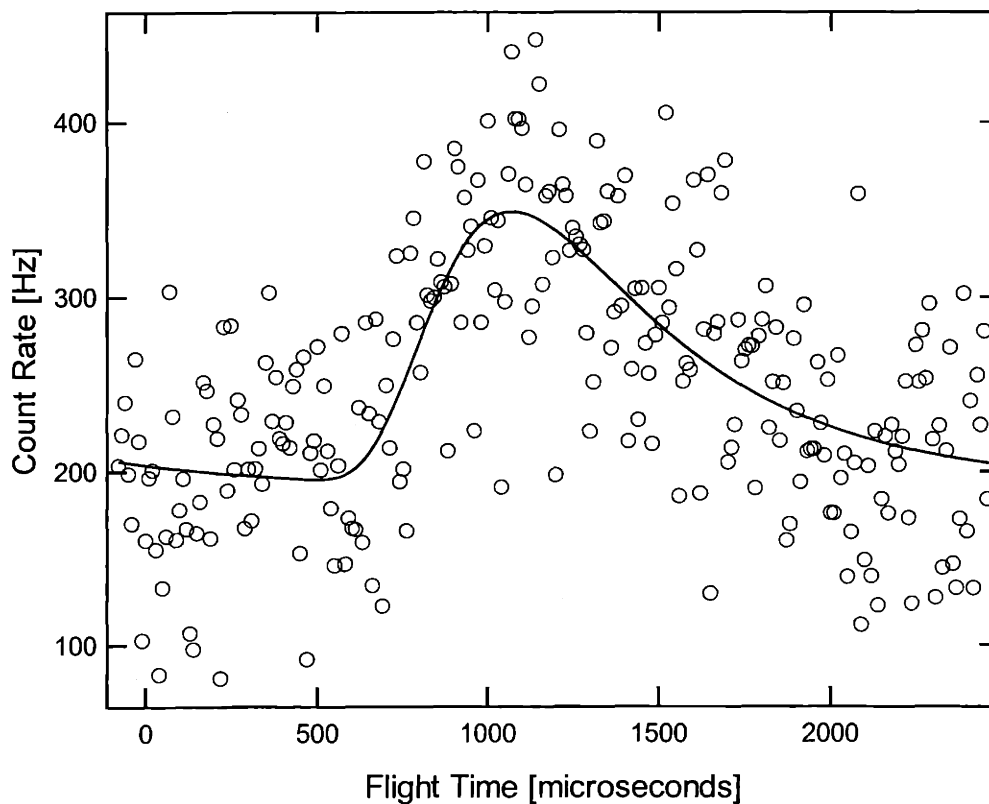
Figure 19 Average TOF distribution at m/e=167

Average TOF spectra at m/e = 167 for the coverage range 0-1.25 ML upon exposure to XeF_2 at $\theta_i=20°$ and T_s = 150 K. Thick solid line shows a least squares fit of a Maxwell-Boltzmann distribution with a flow velocity of 132 m/s and a temperature of 194 K. The signal at short flight times (high velocity) is due to "wrap-around" from the slow part of the distribution. The average velocity and energy of the distribution are 263±37 m/s and 1.49±0.42 kcal/mol respectively. Electron impact energy is set to 75 eV. Average of all TOF spectra shown in Figures 16, 17, and 18 weighted by the number of experiments taken at each detection angle.
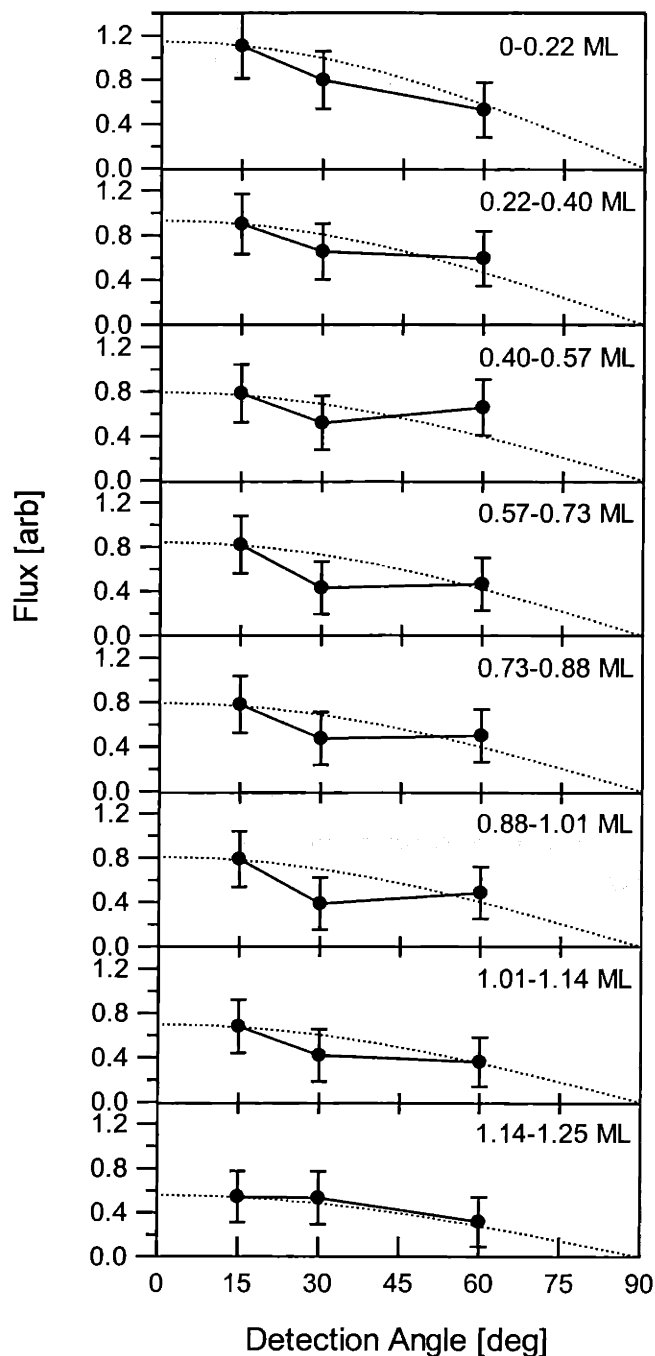
Figure 20 Coverage dependence of the flux of XeF₂ scattered from Si(100)
Scattered flux of XeF_2 determined from the Maxwell-Boltzmann fit to the data in Figures 16, 17, and 18, using Eq. (II.2). Flux at each point is normalized to the number of experiments at that detection angle. Dotted line shows a cosine distribution normalized to match the flux at $\theta_d=15°$. Error bars reflect a 95% confidence limit.
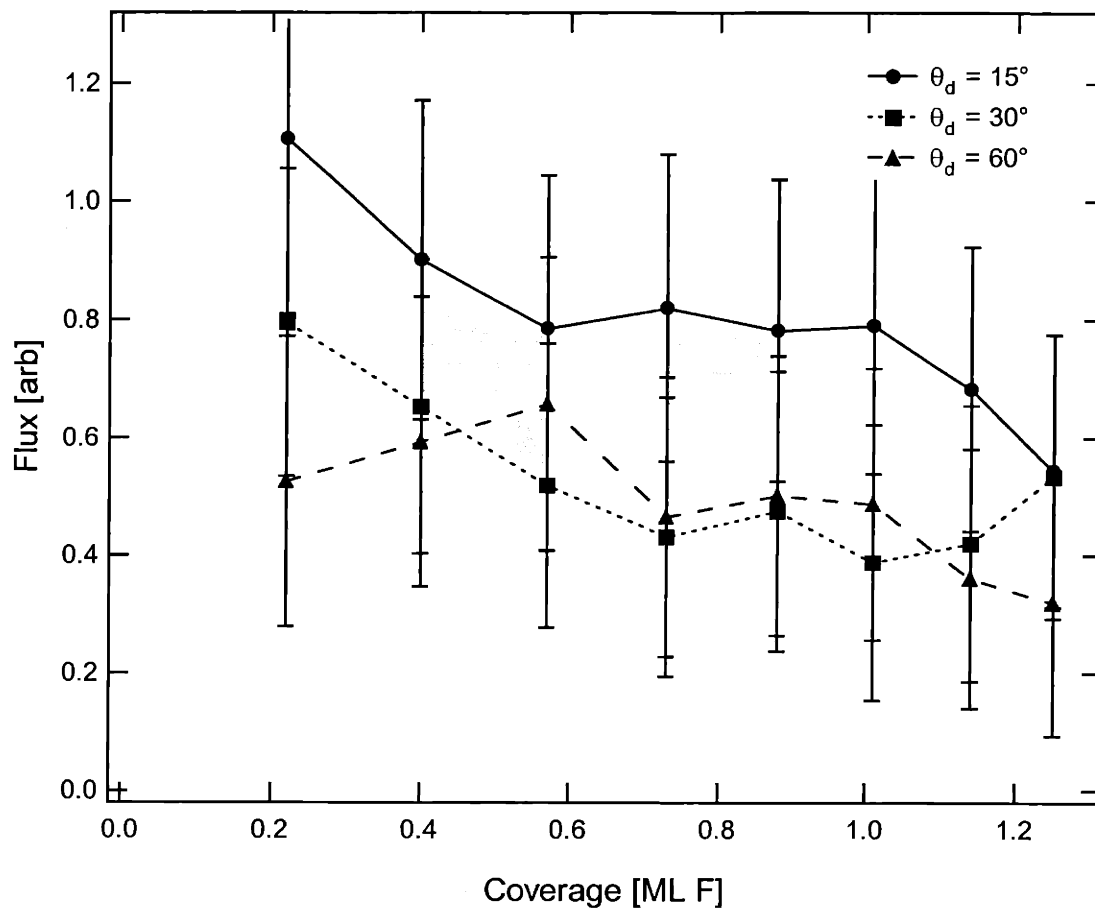
Figure 21 Coverage dependence of the flux of XeF$_2$ scattered from Si(100)

Scattered flux of XeF$_2$ determined from the Maxwell-Boltzmann fit to the data in Figures 16, 17, and 18 at $\theta_d = 15°$ (circles), $\theta_d = 30°$ (squares), and $\theta_d = 60°$ (triangles), using Eq. (II.2). Flux at each point is normalized to the number of experiments at that detection angle. Error bars reflect a 95% confidence limit.

III.E. Scattered TOF spectra at m/e = 148

Analogous to the TOF measurements at m/e=167 presented in Sec. III.D, TOF distributions at m/e=148 have been measured at three detection angles and eight coverage ranges. All spectra were taken with an electron energy of 75 eV and a mass resolution that corresponds to the spectra shown in Figure 6 of the experimental section. The signal at m/e=148 corresponds to both XeF arising from atom abstraction as well as cracking from ionizer fragmentation of unreactively scattered XeF_2. The measured $XeF^+:XeF_2^+$ cracking ratio is 1.9:1. This cracking ratio can nominally be used to perform a point-by-point subtraction of the observed XeF_2 TOF spectra at m/e=167 multiplied by the $XeF^+:XeF_2^+$ cracking ratio from the observed signal at m/e=148, leaving the net signal due to XeF. However, because the XeF_2 spectra have low signal-to-noise ratios, a point-by-point subtraction of the data increases the noise of the net spectra to the point where they are quite difficult to fit. This problem can be avoided by subtracting the fit to the m/e=167 data, multiplied by the $XeF^+:XeF_2^+$ cracking ratio, from the m/e=148 spectra instead of subtracting the individual data points to obtain the net m/e=148 spectra that corresponds to the XeF arising from atom abstraction. Figure 22 illustrates the subtraction of cracking from XeF_2. Figure 22(a) shows the TOF signal at m/e=148 at θ_d=15° over the coverage range 0-0.22 ML resulting from the reaction of XeF_2 with Si(100) at 150 K, along with the fit to the average m/e=167 TOF data multiplied by the $XeF^+:XeF_2^+$ cracking ratio, 1.9:1. Figure 22(b) shows the net XeF TOF distribution after the cracking from XeF_2 is subtracted.

The net XeF TOF spectra are shown in Figures 23, 24, and 25 for the detection angles θ_d = 15°, 30°, and 60° respectively. Each net TOF spectrum is fit to a Maxwell-Boltzmann distribution where the flow velocity and temperature are allowed to vary, but the baseline values are fixed. In order to find the baseline values, the spectra at each detection angle are averaged

and fit with flow velocity, temperature and baseline which are all allowed to vary. These spectra are not shown. The baseline value for each individual TOF spectrum is then fixed at the baseline value found for the average spectrum at that detector angle.

The flux of each net TOF distribution is determined by integrating the flux distribution as described by Eq. (II.2) in the experimental section. The angular distribution of the flux at each coverage range is shown in Figure 26, where the flux at each angle is normalized by the number of experiments at that angle. The general trend is that the angular distribution becomes more peaked towards normal as the coverage increases. That is, the flux of XeF increases over the observed coverage range for θ_d=15° and 30°, but remains fairly constant for θ_d=60°. An alternative way of plotting the flux is shown in Figure 27.

The average energy is calculated by integrating the energy-weighted flux distribution as described in Eq. (II.4) in the experimental section. The average energy as a function of angle is shown in Figure 28. In general, the average energy of the XeF decreases with increasing scattering angle and also decreases with increasing coverage. The trend of decreasing energy is clearly shown in Figure 29, which shows the average energy as a function of coverage for the three detection angles. The trend of decreasing average energy at θ_d=15° from ~10 kcal/mol on a clean surface to ~7 kcal/mol on a fluorinated surface is similar to that observed previously for the interaction of XeF_2 with Si(100) at 250 K.[1] However, the trend of decreasing energy with increasing scattering angle is in contrast to the 250 K results, which showed no perceptible trend with respect to scattering angle.

The strong coverage dependence of the translational energy of the reactively scattered XeF abstraction product is in stark contrast to the translational energy of the scattered F atoms in the interaction of F_2 with Si, which is independent of coverage.
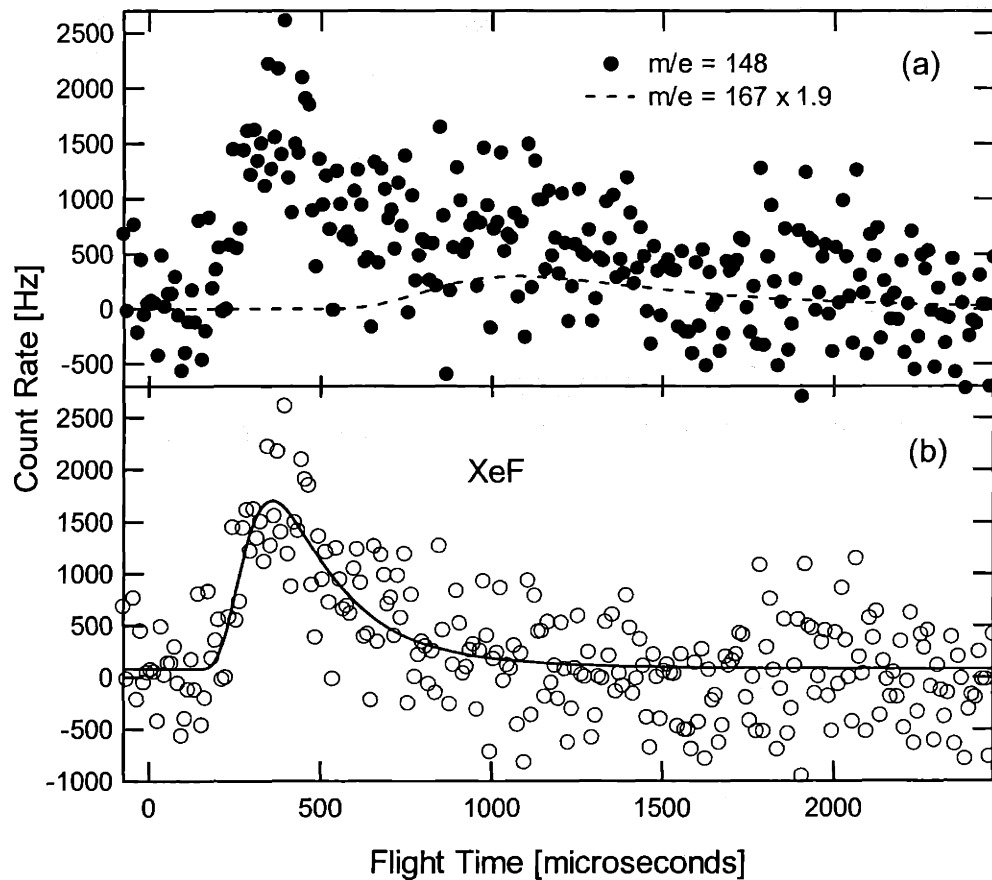
Figure 22 TOF distribution at m/e=148 illustrating cracking subtraction

(a) TOF spectrum taken at m/e=148 and $\theta_d=15°$ for the coverage range 0-0.22 ML upon exposure to XeF_2 at 150 K and $\theta_i=20°$. The dashed line in (a) shows the fit to the TOF distribution at m/e=167 multiplied by the $XeF^+:XeF_2^+$ cracking ratio. (b) Net scattered XeF signal obtained after cracking has been subtracted.
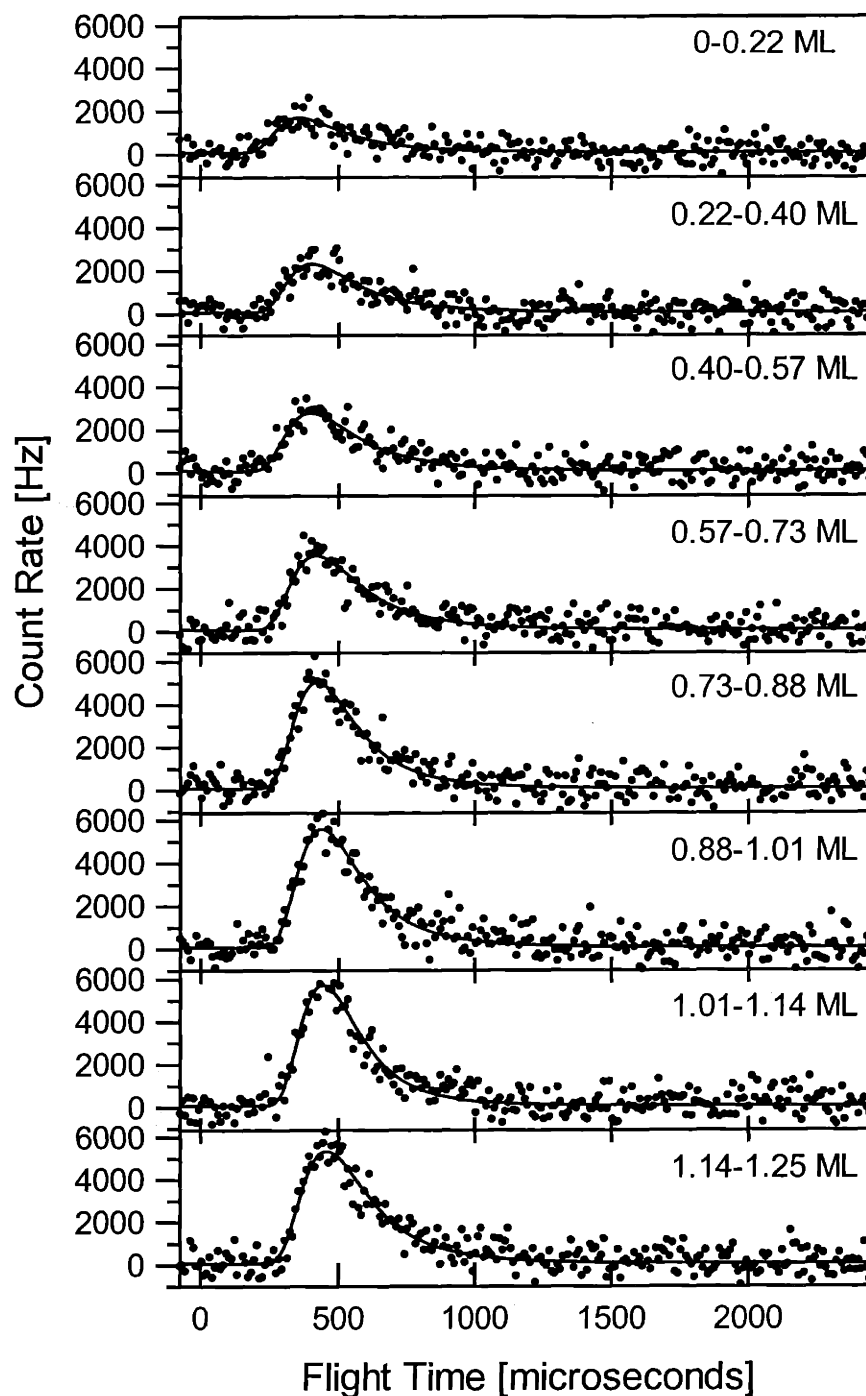
Figure 23 Net TOF spectra at m/e=148 and θ_d=15°

Net TOF spectra at m/e=148 and a detector angle θ_d=15° for 8 coverage ranges upon exposure to XeF_2 at θ_i=20° and T_s=150 K. Solid lines show the least squares fits to a Maxwell-Boltzmann distribution. Each TOF spectrum is the average of 40 separate experiments. Electron impact energy is set to 75 eV.
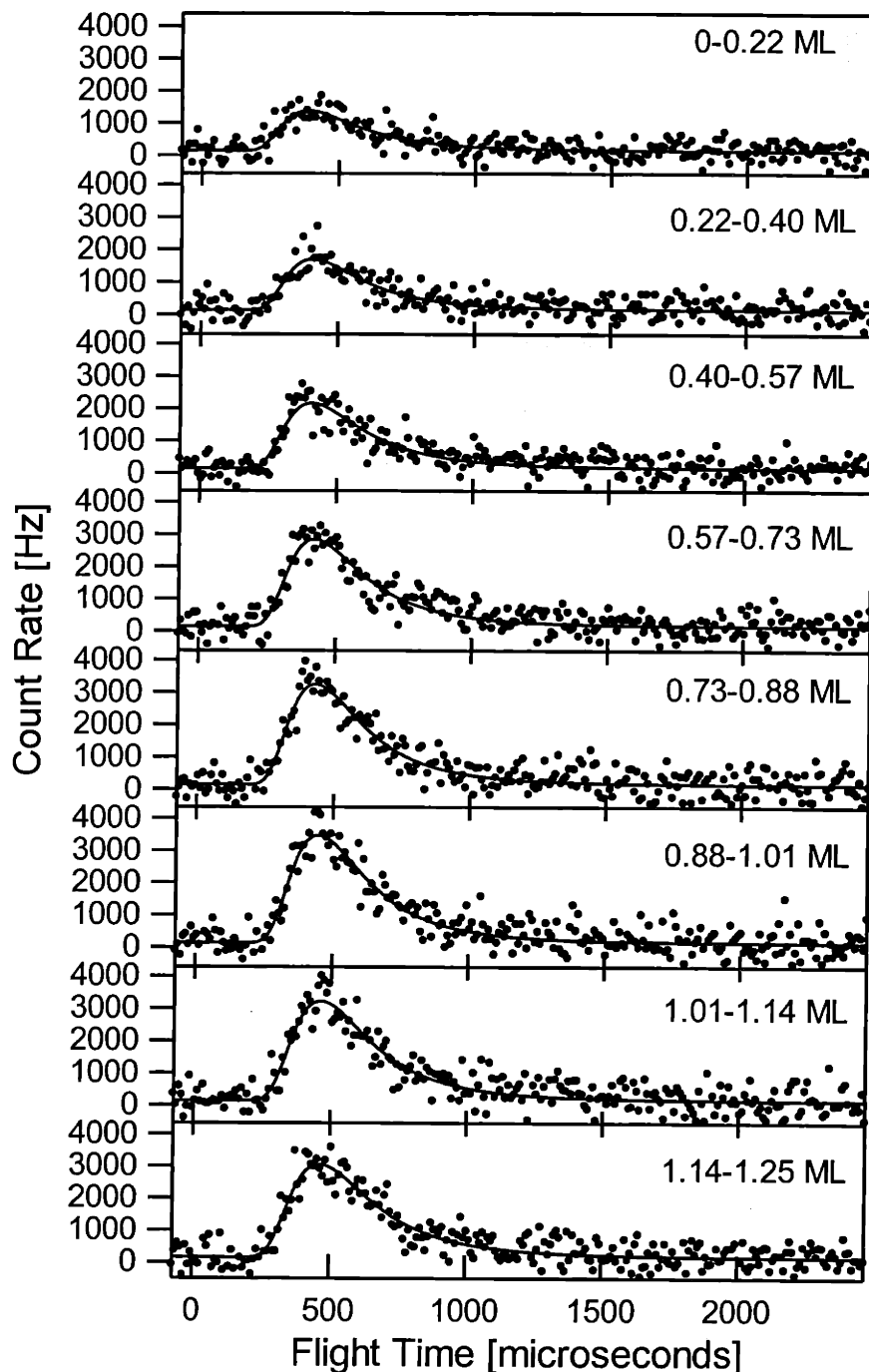
Figure 24 Net TOF spectra at m/e=148 and θ_d=30°

Net TOF spectra at m/e=148 and a detector angle θ_d=30° for 8 coverage ranges upon exposure to XeF_2 at θ_i=20° and T_s=150 K. Solid lines show the least squares fits to a Maxwell-Boltzmann distribution. Each TOF spectrum is the average of 40 separate experiments. Electron impact energy is set to 75 eV.
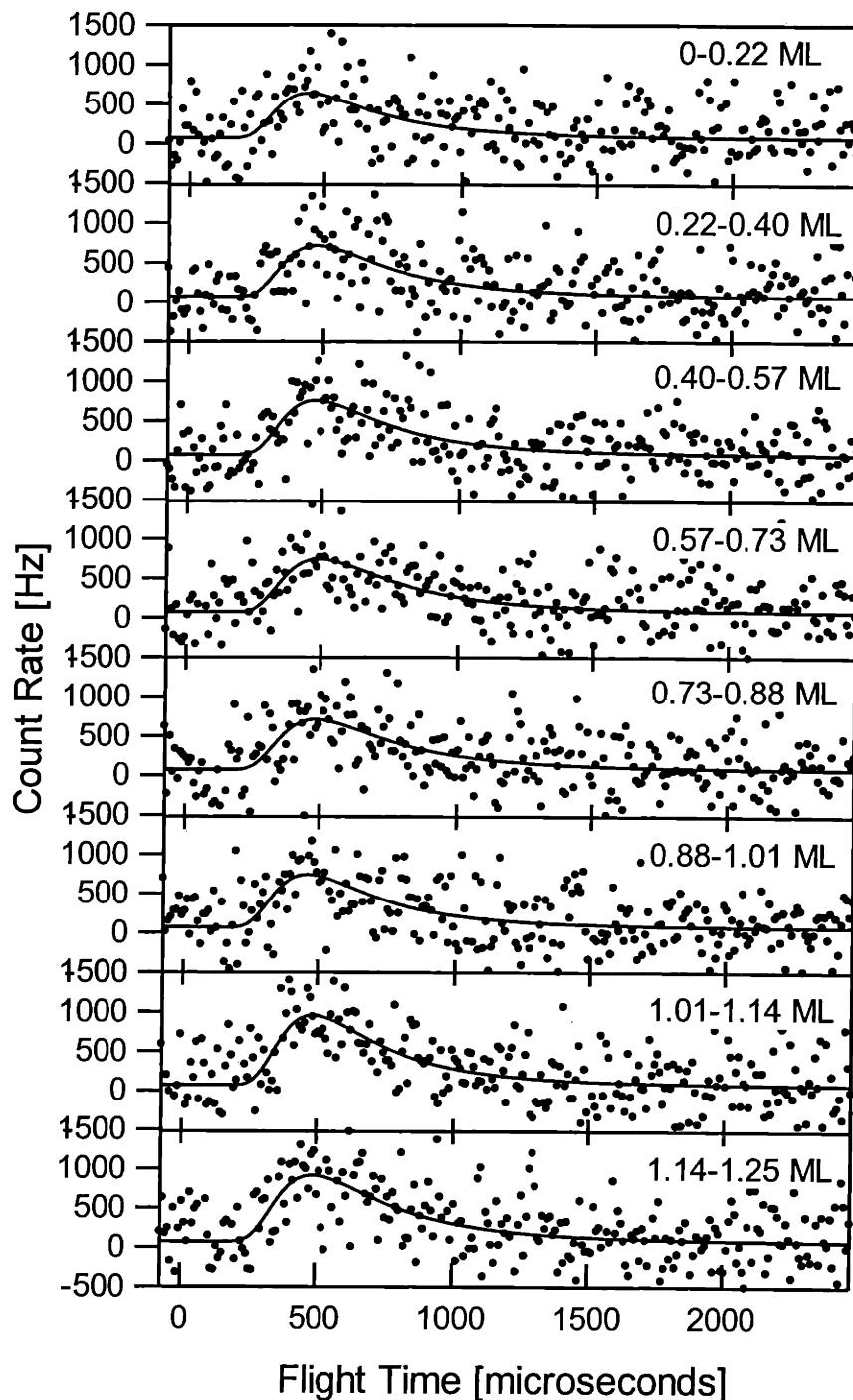
Figure 25 Net TOF spectra at m/e=148 and θ_d=60°

Net TOF spectra at m/e=148 and a detector angle θ_d=60° for 8 coverage ranges upon exposure to XeF_2 at θ_i=20° and T_s=150 K. Solid lines show the least squares fits to a Maxwell-Boltzmann distribution. Each TOF spectrum is the average of 40 separate experiments. Electron impact energy is set to 75 eV.

Figure 26 Angular dependence of the flux of XeF scattered from Si(100)

Scattered flux of XeF determined from the Maxwell-Boltzmann fit to the data in Figures 23, 24, and 25, using Eq. (II.2). Flux at each point is normalized to the number of experiments at that detection angle. Dotted line shows a cosine distribution normalized to match the flux at $\theta_d=15°$. Error bars reflect a 95% confidence limit.
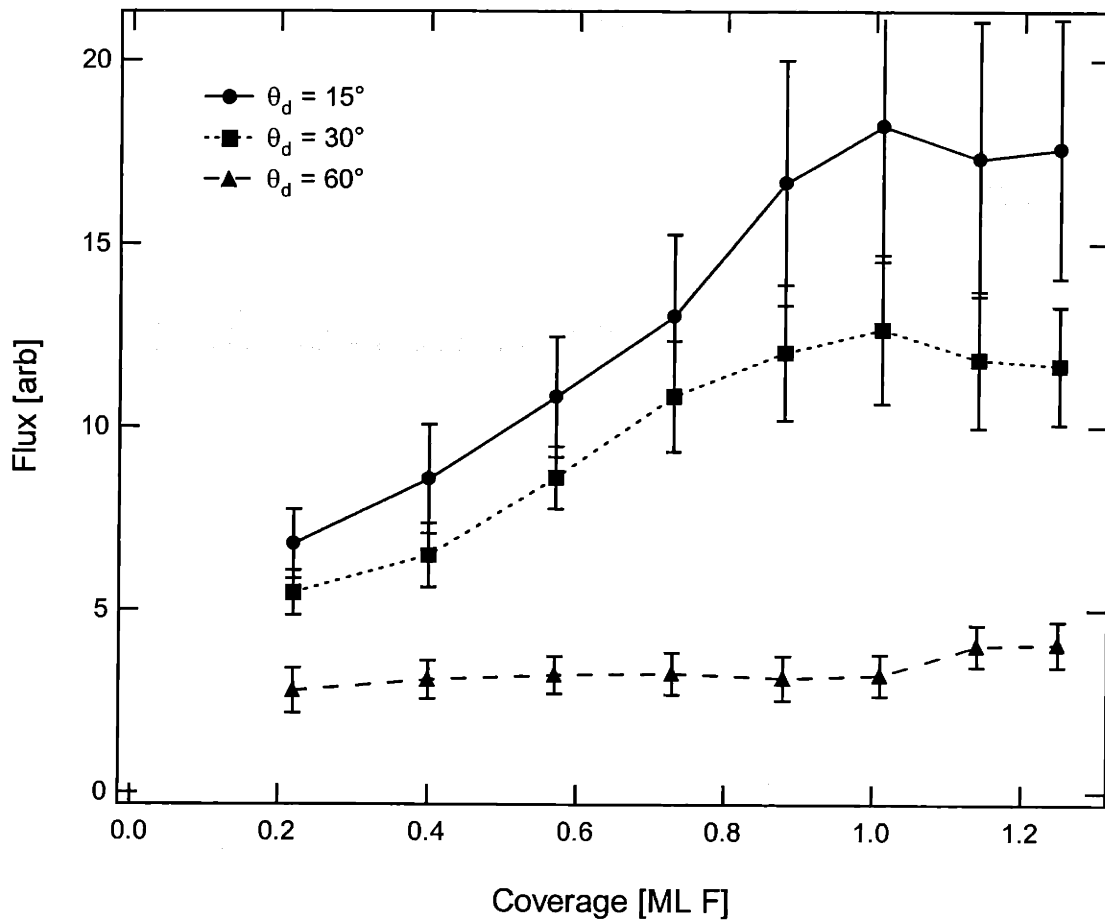
Figure 27 Coverage dependence of the flux of XeF scattered from Si(100)

Scattered flux of XeF determined from the Maxwell-Boltzmann fit to the data in Figures 23, 24, and 25 at $\theta_d = 15°$ (circles), $\theta_d = 30°$ (squares), and $\theta_d = 60°$ (triangles), using Eq. (II.2). Flux at each point is normalized to the number of experiments at that detection angle. Dotted line shows a cosine distribution normalized to match the flux at $\theta_d = 15°$. Error bars reflect a 95% confidence limit.
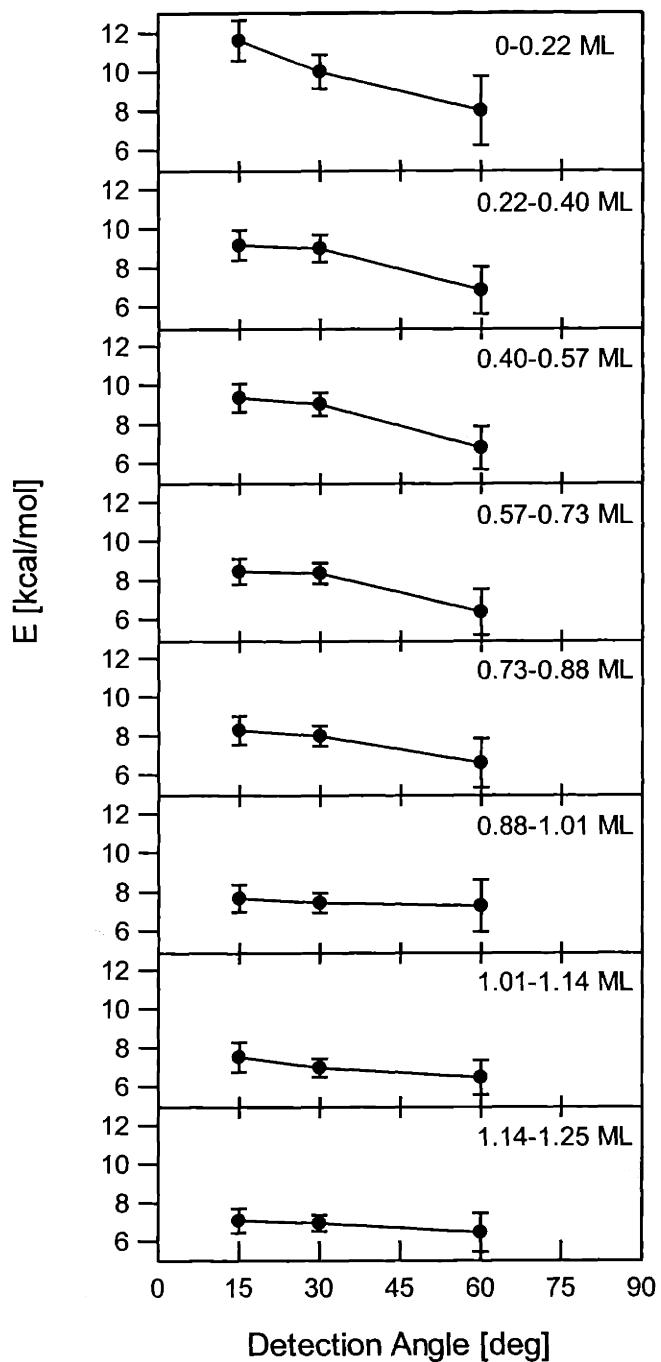
Figure 28 Angular dependence of the average energy of XeF scattered from Si(100)
Average energy determined from the Maxwell-Boltzmann fit to the data shown in Figures 23, 24, and 25, using Eq. (II.4). Error bars reflect a 95% confidence limit.
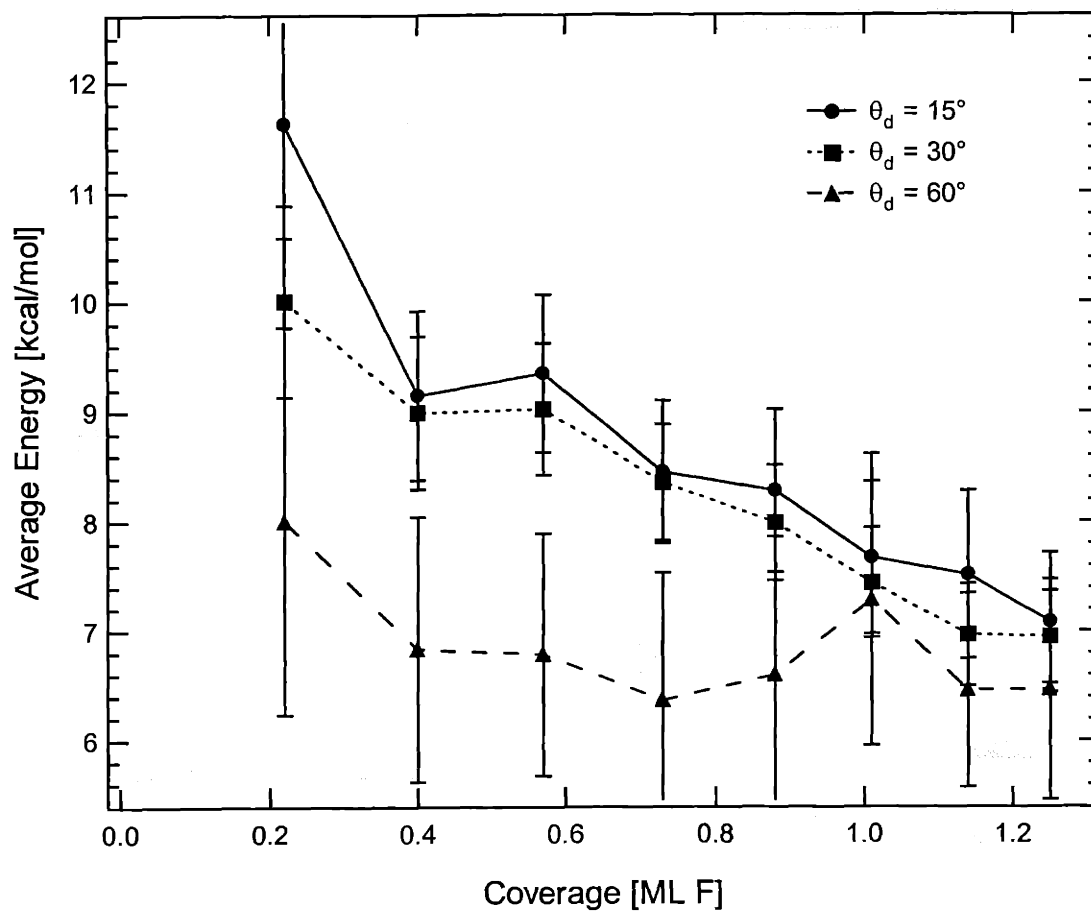
Figure 29 Coverage dependence of the average energy of XeF scattered from Si(100)
Average energy determined from the Maxwell-Boltzmann fit to the data shown in Figures 23, 24, and 25, at $\theta_d = 15°$ (circles), $\theta_d = 30°$ (squares), and $\theta_d = 60°$ (triangles), using Eq. (II.4). Error bars reflect a 95% confidence limit.

III.F. Scattered TOF spectra at m/e = 19

Analogous to the TOF measurements at m/e=167 and m/e=148, presented in Sec. III.D and Sec. III.E respectively, TOF distributions at m/e=19 have been measured at three detection angles and eight coverage ranges. The signal at m/e=19 corresponds to scattered F atoms from XeF dissociation, F^+ from ionizer fragmentation of unreactively scattered XeF_2, and F^+ from ionizer fragmentation of XeF from single atom abstraction. The F^+:XeF_2^+ cracking ratio is measured to be 0.33:1. The maximum F^+:XeF^+ cracking ratio is determined to be 0.40:1 as discussed in Section II.D.3. Figure 30 illustrates the subtraction of cracking from XeF_2 and XeF. Figure 30(a) shows the TOF signal at m/e=19 at θ_d=15° for the coverage range 0-0.22 ML resulting from the reaction of XeF_2 with Si(100) at 150 K, along with the fit to the average m/e=167 TOF data multiplied by the F^+:XeF_2^+ cracking ratio, and the fit to the net m/e=148 TOF data multiplied by the maximum F^+:XeF^+ cracking ratio. Figure 30(b) shows the net F atom TOF distribution after the cracking from XeF_2 and XeF is subtracted.

Each of the net m/e=19 TOF spectra are shown in Figures 31, 32, and 33. The net m/e=19 spectra are due solely to the scattered F atom signal. All experiments were taken with an electron energy of 75 eV and a mass resolution that corresponds to the spectra shown in Figure 6 of the experimental section. Although it is not known that this maximum F^+:XeF^+ cracking ratio is the true cracking ratio, it results in reasonable F atom TOF spectra that are well described by the forward convolution calculation described in Sec. IV. Each net TOF spectrum is fit to a Maxwell-Boltzmann distribution with the flow velocity and temperature allowed to vary, but the baseline values are fixed. In order to find the baseline values, the spectra at each detection angle are averaged and fit with all parameters allowed to vary. These spectra are not shown. The

baseline value for each individual TOF spectrum is then fixed at the baseline value found for the average spectrum at that detector angle.

The flux of each net TOF distribution is determined by integrating the flux distribution as described by Eq. (II.2) in the experimental section. The angular distribution of the flux at each coverage range is shown in Figure 34, normalized by the number of experiments taken at each angle. The general trend is that the angular distribution becomes slightly more peaked towards normal at higher coverages. An alternative way of plotting the flux is shown in Figure 35.

The average energy is calculated by integrating the energy-weighted flux distribution as described in Eq. (II.4) in the experimental section. The average energy as a function of coverage is shown in Figure 36. In general the average energy of the F atoms remains relatively constant with coverage. The exception to this is the anomalously high results at a scattering angle $\theta_d =$ 60° and a coverage of 0.73-1.01 ML. These anomalously high energies may be due to the low signal to noise ratios of the TOF spectra shown in Figure 33.
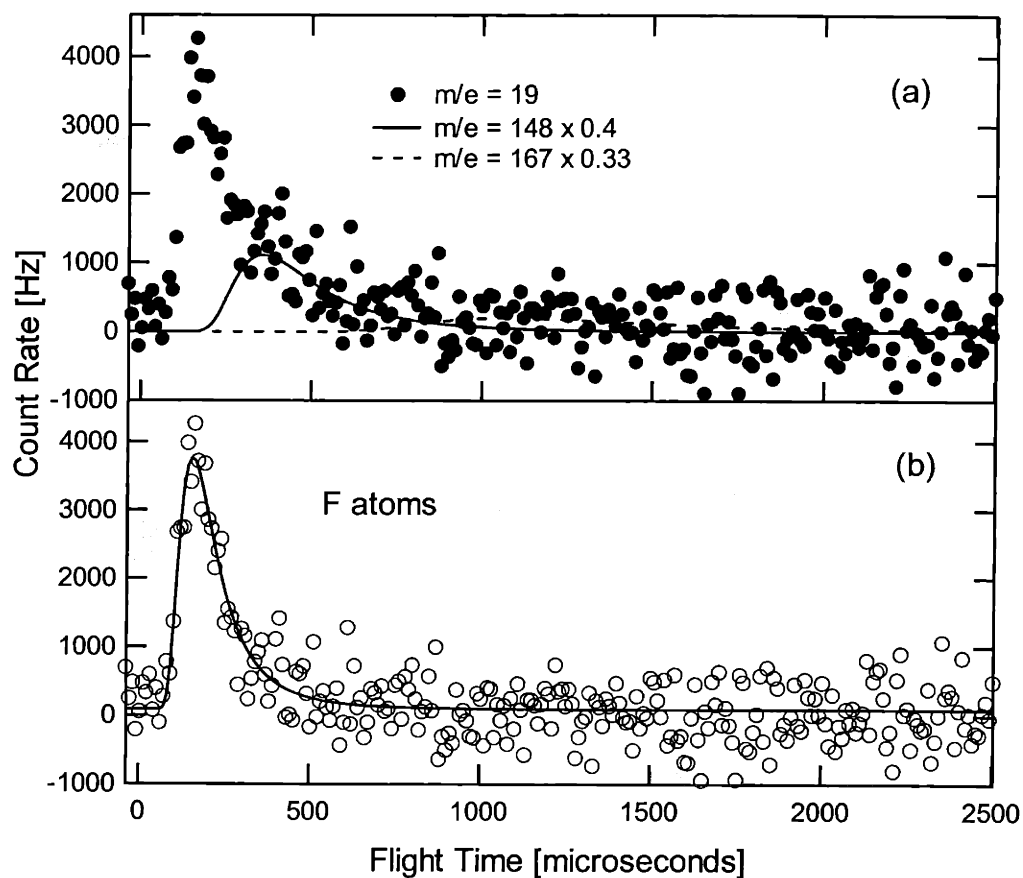
Figure 30 Average TOF distribution at m/e=19 illustrating cracking subtraction

(a) TOF spectrum taken at m/e=19 at θ_d=15° for the coverage range 0-0.22 ML upon exposure to XeF_2 at 150 K and θ_i=20°. The dotted line in (a) shows the fit to the TOF distribution at m/e=167 multiplied by the F^+:XeF_2^+ cracking ratio. The solid line in (a) shows the fit to the TOF distribution at m/e=148 multiplied by the maximum F^+:XeF^+ cracking ratio. (b) Net scattered F atom signal obtained after cracking has been subtracted.
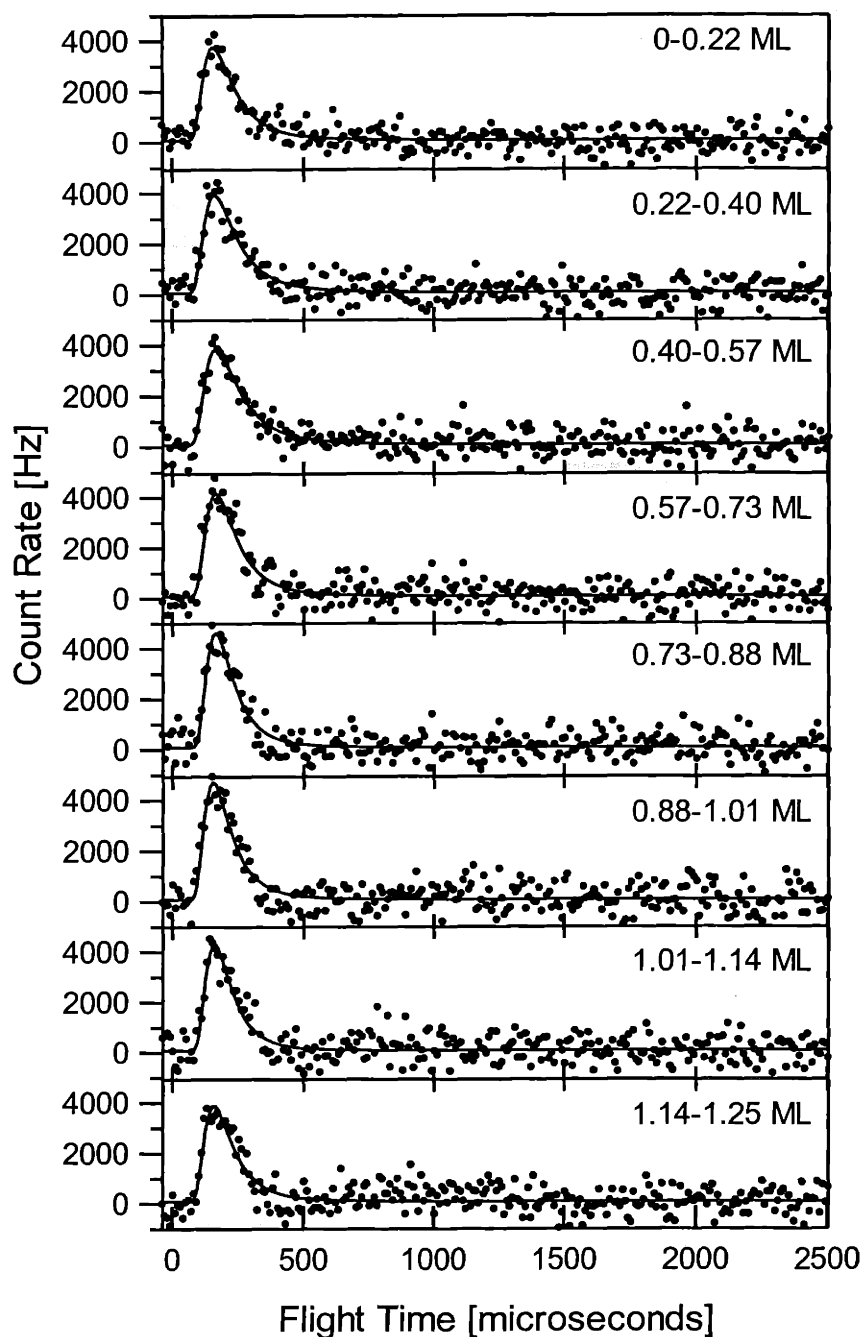
Figure 31 Net TOF spectra at m/e=19 and θ_d=15°

Net TOF spectra at m/e=19 and a detector angle θ_d=15° for 8 coverage ranges upon exposure to XeF_2 at θ_i=20° and T_s=150 K. Solid lines show the least squares fits to a Maxwell-Boltzmann distribution. Each TOF spectrum is the average of 40 separate experiments. Electron impact energy is set to 75 eV.
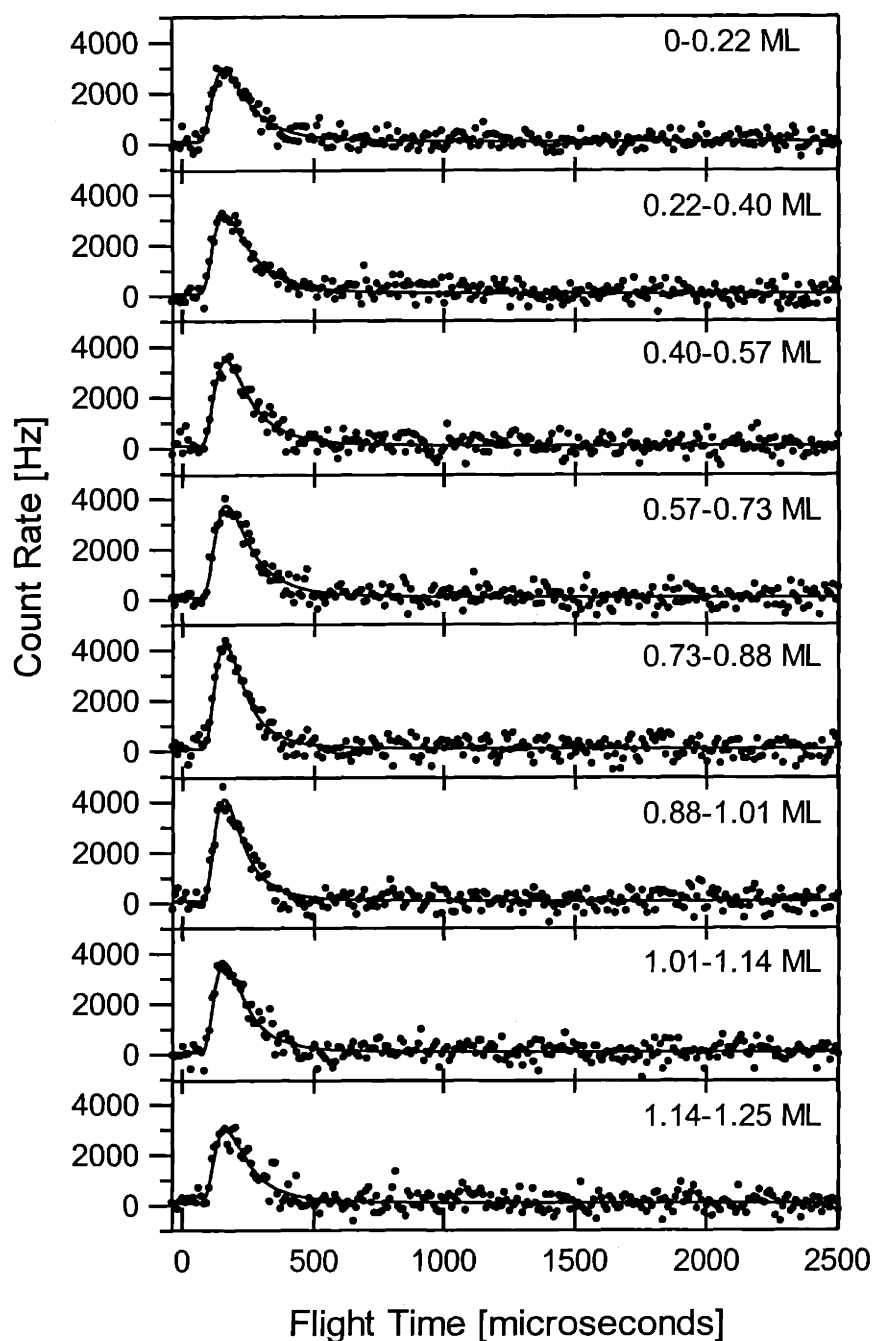
Figure 32 Net TOF spectra at m/e=19 and θ_d=30°

Net TOF spectra at m/e=19 and a detector angle θ_d=30° for 8 coverage ranges upon exposure to XeF_2 at θ_i=20° and T_s=150 K. Solid lines show the least squares fits to a Maxwell-Boltzmann distribution. Each TOF spectrum is the average of 40 separate experiments. Electron impact energy is set to 75 eV.
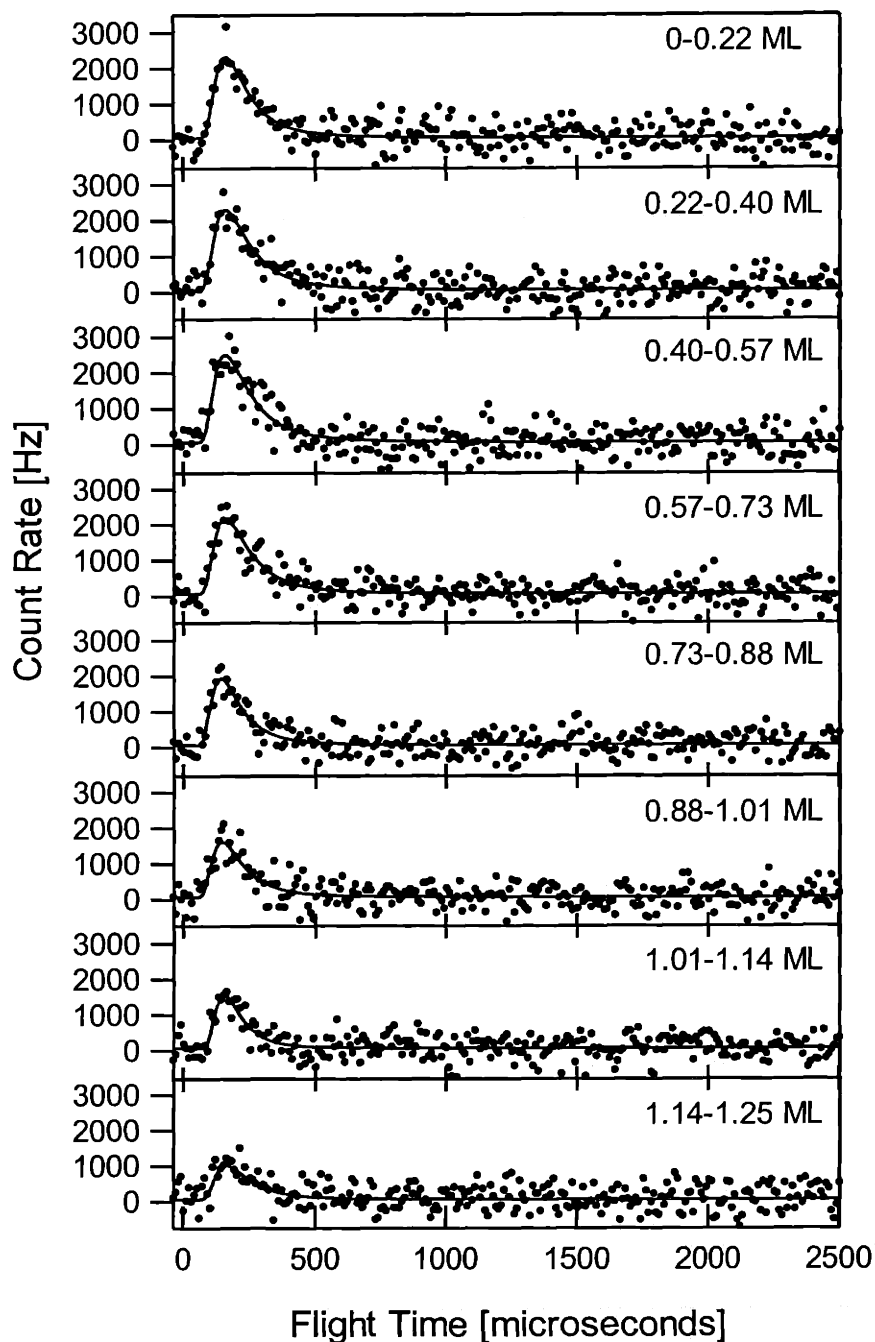
Figure 33 Net TOF spectra at m/e=19 and θ_d=60°

Net TOF spectra at m/e=19 and a detector angle θ_d=60° for 8 coverage ranges upon exposure to XeF_2 at θ_i=20° and T_s=150 K. Solid lines show the least squares fits to a Maxwell-Boltzmann distribution. Each TOF spectrum is the average of 40 separate experiments. Electron impact energy is set to 75 eV.

Figure 34 Angular dependence of the flux of F scattered from Si(100)

Scattered flux of F determined from the Maxwell-Boltzmann fit to the data shown in Figures 31, 32, and 33 using Eq. (II.2). Flux at each point is normalized to the number of experiments at that detection angle. Dotted line shows a cosine distribution normalized to match the flux at $\theta_d=15°$. Error bars reflect a 95% confidence limit.
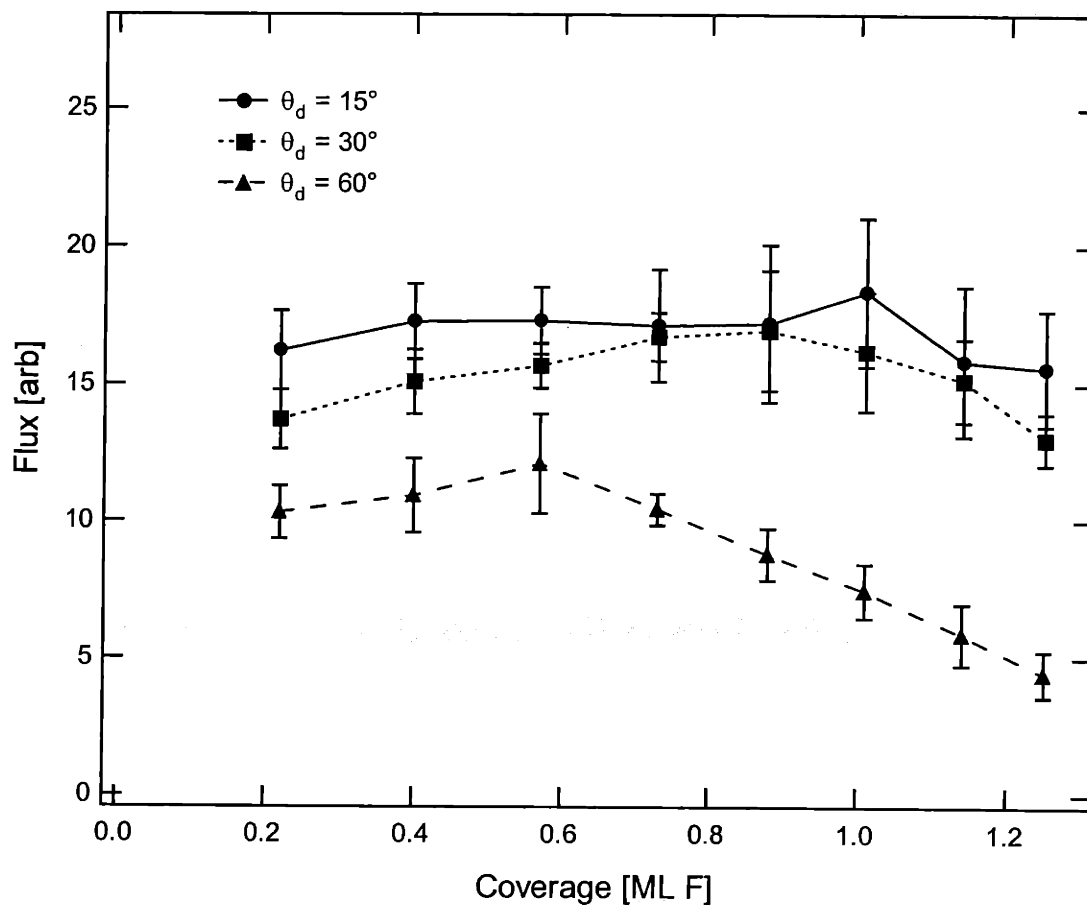
Figure 35 Coverage dependence of the flux of F scattered from Si(100)

Scattered flux of F determined from the Maxwell-Boltzmann fit to the data shown in Figures 31, 32, and 33 at $\theta_d = 15°$ (circles), $\theta_d = 30°$ (squares), and $\theta_d = 60°$ (triangles), using Eq. (II.2). Flux at each point is normalized to the number of experiments at that detection angle. Dotted line shows a cosine distribution normalized to match the flux at $\theta_d=15°$. Error bars reflect a 95% confidence limit.
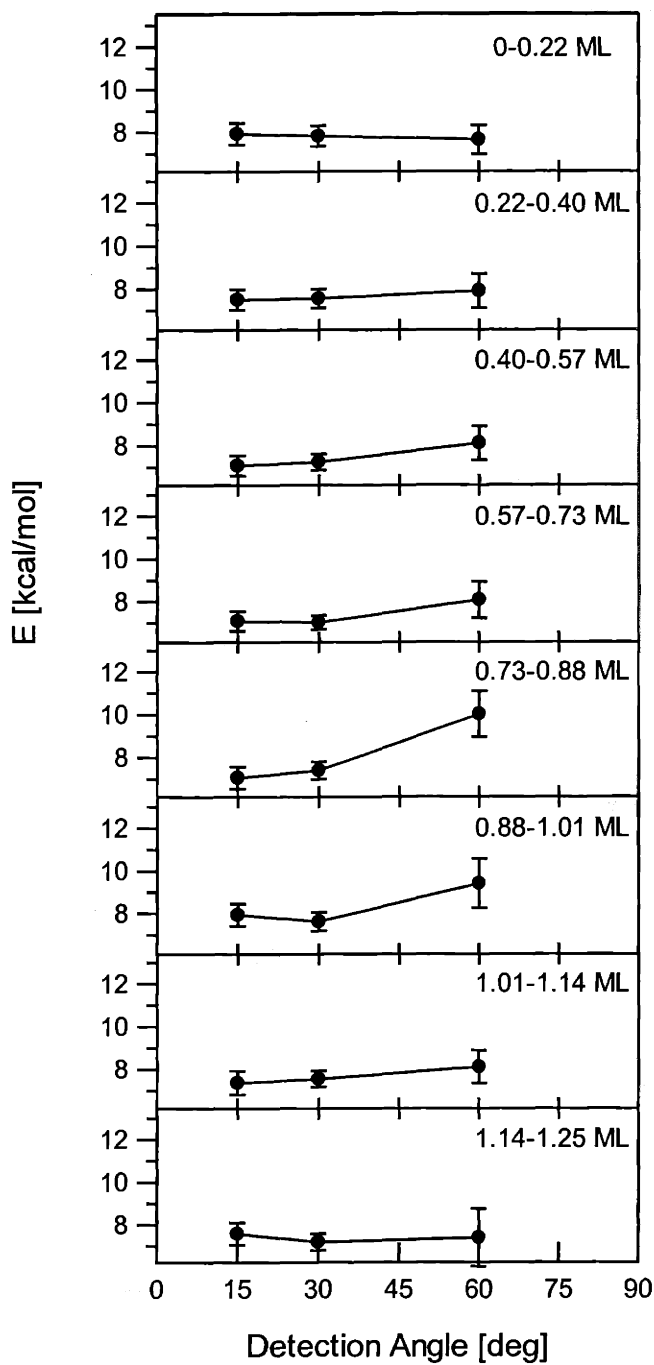
Figure 36 Angular dependence of the average energy of F scattered from Si(100)
Average energy determined from the Maxwell-Boltzmann fit to the data shown in Figures 31, 32, and 33, using Eq. (II.4). Error bars reflect a 95% confidence limit.
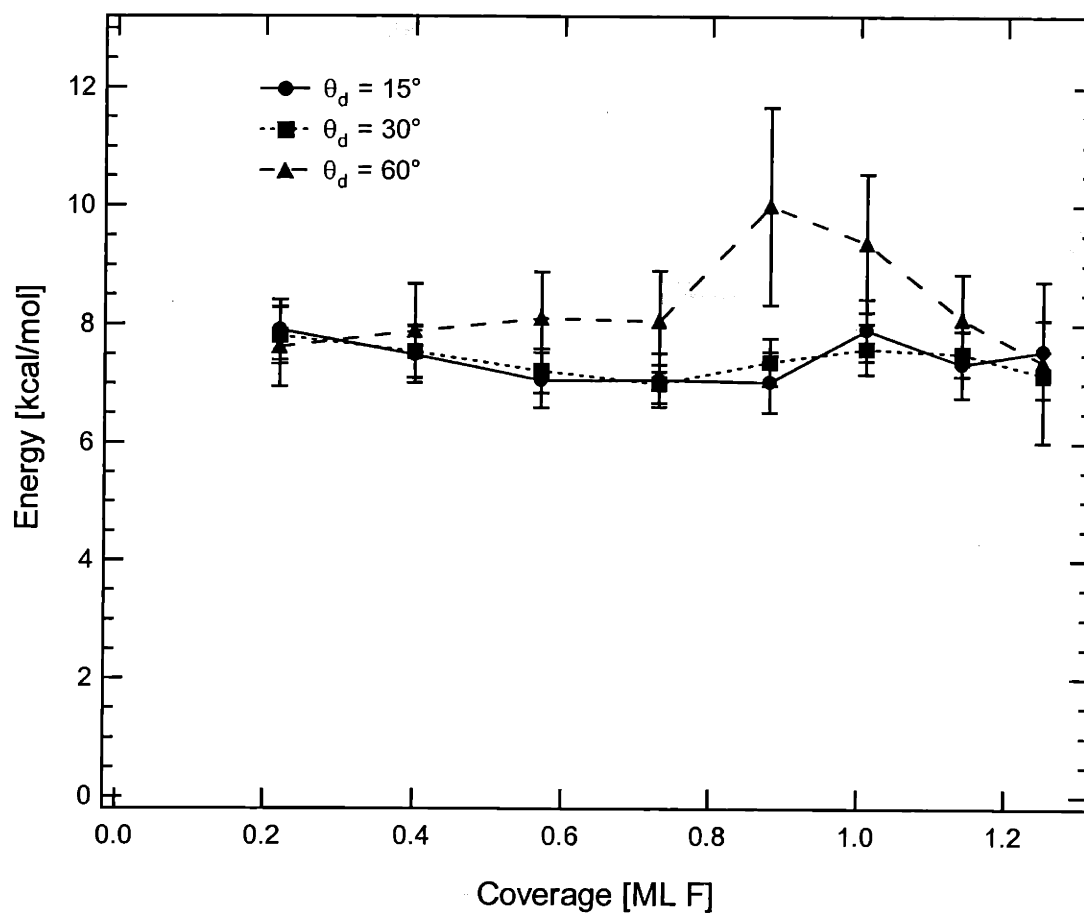
Figure 37 Coverage dependence of the average energy of F scattered from Si(100)

Average energy of F determined from the Maxwell-Boltzmann fit to the data in Figures 31, 32, and 33 at $\theta_d = 15°$ (circles), $\theta_d = 30°$ (squares), and $\theta_d = 60°$ (triangles). Error bars reflect a 95% confidence limit.

III.G. Scattered TOF spectra at m/e = 129

Analogous to the TOF measurements at m/e=167 presented in Sec. III.D, TOF distributions at m/e=129 have been measured at three detection angles and eight coverage ranges. All experiments were measured with an electron energy of 26.5 eV and a mass resolution that corresponds to the spectra shown in Figure 6 of the experimental section. The signal at m/e=129 corresponds to scattered Xe atoms from XeF dissociation and 2-atom adsorption, as well as Xe^+ from fragmentation of unreactively scattered XeF_2 in the ionizer, and Xe^+ from fragmentation of XeF produced by single atom abstraction. The contribution to the m/e=129 signal from the ionizer fragmentation of XeF_2 can be eliminated by subtracting the fit to the m/e=167 TOF spectra multiplied the $Xe^+:XeF_2^+$ cracking ratio, which is determined from Figure 6 to be 0.045:1. However, eliminating the contribution to the m/e=129 signal from the ionizer fragmentation of XeF is more difficult. As described in section II.D.3, because a source of pure XeF is unavailable, the cracking ratio $Xe^+:XeF^+$ cannot be measured. The maximum $Xe^+:XeF^+$ cracking ratio was found by examining the high coverage, $\theta_d=60°$ TOF spectra. If the $Xe^+:XeF^+$ cracking ratio is assigned a value that is greater than 1.0:1, the net m/e=129 TOF signal becomes negative, which is an unphysical result. Figure 38 illustrates the subtraction of cracking from XeF_2 and XeF. Figure 38(a) shows the TOF signal at m/e=129 at $\theta_d=15°$ for the coverage range 0-0.22 ML resulting from the reaction of XeF_2 with Si(100) at 150 K, along with the fit to the average m/e=167 TOF data multiplied by the $Xe^+:XeF_2^+$ cracking ratio, and the fit to the net m/e=148 TOF data at $\theta_d=15°$ and 0-0.22 ML multiplied by the maximum $Xe^+:XeF^+$ cracking ratio. Figure 38(b) shows the net F atom TOF distribution after the cracking from XeF_2 and XeF is subtracted, along with a three-component fit to the net Xe signal, which is described in detail

below. The net m/e=129 TOF distributions after subtraction of the cracking from XeF_2 and the maximum cracking from XeF at each scattering angle are shown in Figures 39, 40, and 41.

Although subtraction of the XeF cracking using the maximum possible $Xe^+:XeF^+$ cracking ratio results in physically reasonable net m/e=129 spectra, there is no a priori reason to believe that the maximum $Xe^+:XeF^+$ cracking ratio is the true cracking ratio. With this in mind, the TOF data at m/e=129 are also analyzed using an intermediate $Xe^+:XeF^+$ cracking ratio of 0.5:1, and a minimal $Xe^+:XeF^+$ cracking ratio of zero. Figures 42, 43, and 44 show the net m/e=129 TOF distributions after subtraction of an intermediate XeF cracking contribution. Figures 45, 46, and 47 show the net m/e=129 TOF distributions after subtraction of cracking from XeF_2, but with no cracking from XeF subtracted.

It should be emphasized that there is no way of determining which of the maximum, intermediate or minimum $Xe^+:XeF^+$ cracking ratios is closest to the true cracking ratio. The goal of the analysis presented in the next section is to determine what part of the observed net Xe TOF distribution can be attributed to XeF dissociation, regardless of the $Xe^+:XeF^+$ cracking ratio used. In order to show that the results of the analysis are independent of the $Xe^+:XeF^+$ cracking ratio, the analysis will be performed for the maximum, intermediate and minimum $Xe^+:XeF^+$ cracking ratios, and it will be shown that the results of the analysis are unaffected by the cracking ratio used.

Each net Xe TOF spectrum is fit to three Maxwell-Boltzmann distributions – a fast feature, a medium feature, and a slow feature. These fits are also shown in Figures 39-47. The sum of the fits to each feature is also shown. The temperature of the slow feature is fixed at the surface temperature of 150 K, and the flow velocity of the slow feature is fixed at zero. This feature corresponds to Xe that desorbs in thermal equilibrium with the surface. The parameters

of the fast feature and the medium feature are allowed to vary, but the baseline values are fixed. In order to find the baseline values, the spectra at each detection angle are averaged and fit with the baseline allowed to vary. These spectra are not shown. The baseline value for each individual TOF spectrum is then fixed at the baseline value found for the average spectrum at that detector angle. The angular distributions of the flux and energy of each MB feature will be presented in the Discussion.
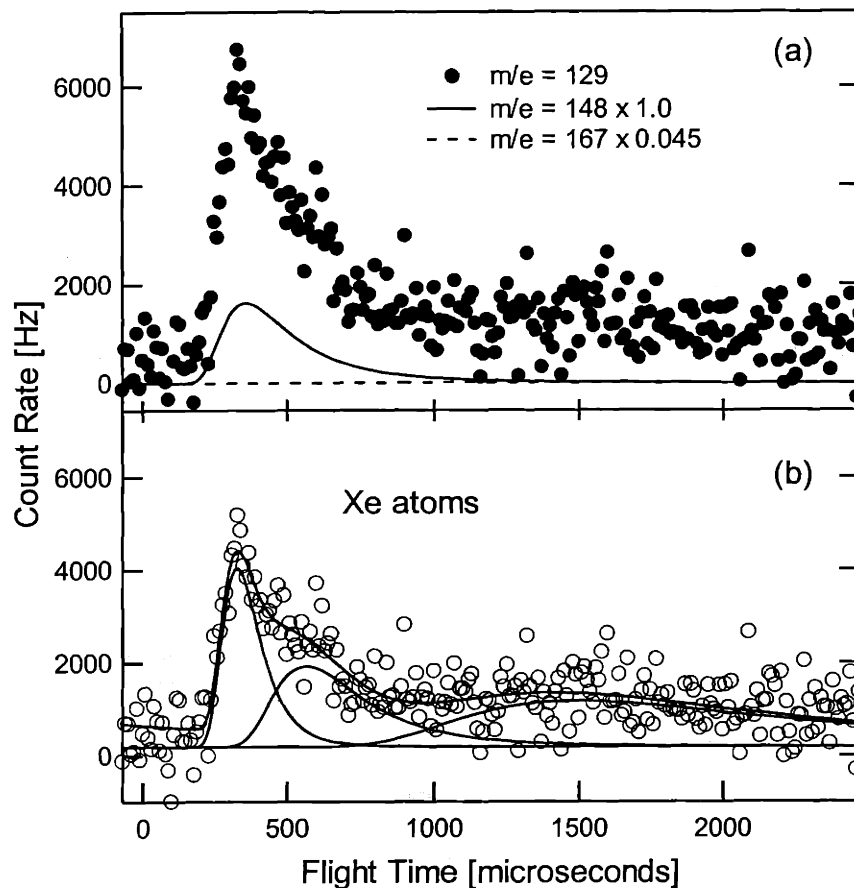
Figure 38 Average TOF distribution at m/e=129 illustrating cracking subtraction

(a) TOF spectrum taken at m/e=129 at θ_d=15° for the coverage range 0-0.22 ML upon exposure to XeF_2 at 150 K and θ_i=20°. The dotted line in (a) shows the fit to the TOF distribution at m/e=167 shown in Figure 16 at 0-0.22 ML multiplied by the Xe^+:XeF_2^+ cracking ratio. The solid line in (a) shows the fit to the TOF distribution at m/e=148 shown in Figure 22b multiplied by the maximum Xe^+:XeF^+ cracking ratio. (b) Net scattered Xe atom signal obtained after cracking has been subtracted, along with the fast, medium and slow features and the sum of the three features.

Figure 39   Net TOF spectra at m/e=129 and θ_d=15° after maximum XeF cracking is subtracted

Net TOF spectra at m/e=129 and a detector angle θ_d=15° for 8 coverage ranges upon exposure to XeF_2 at θ_i=20° and T_s=150 K.   Solid lines show the least squares fit to three Maxwell-Boltzmann distributions and the sum of the fits to each feature.   Each TOF spectrum is the average of 80 separate experiments.   Electron impact energy is set to 26.5 eV.
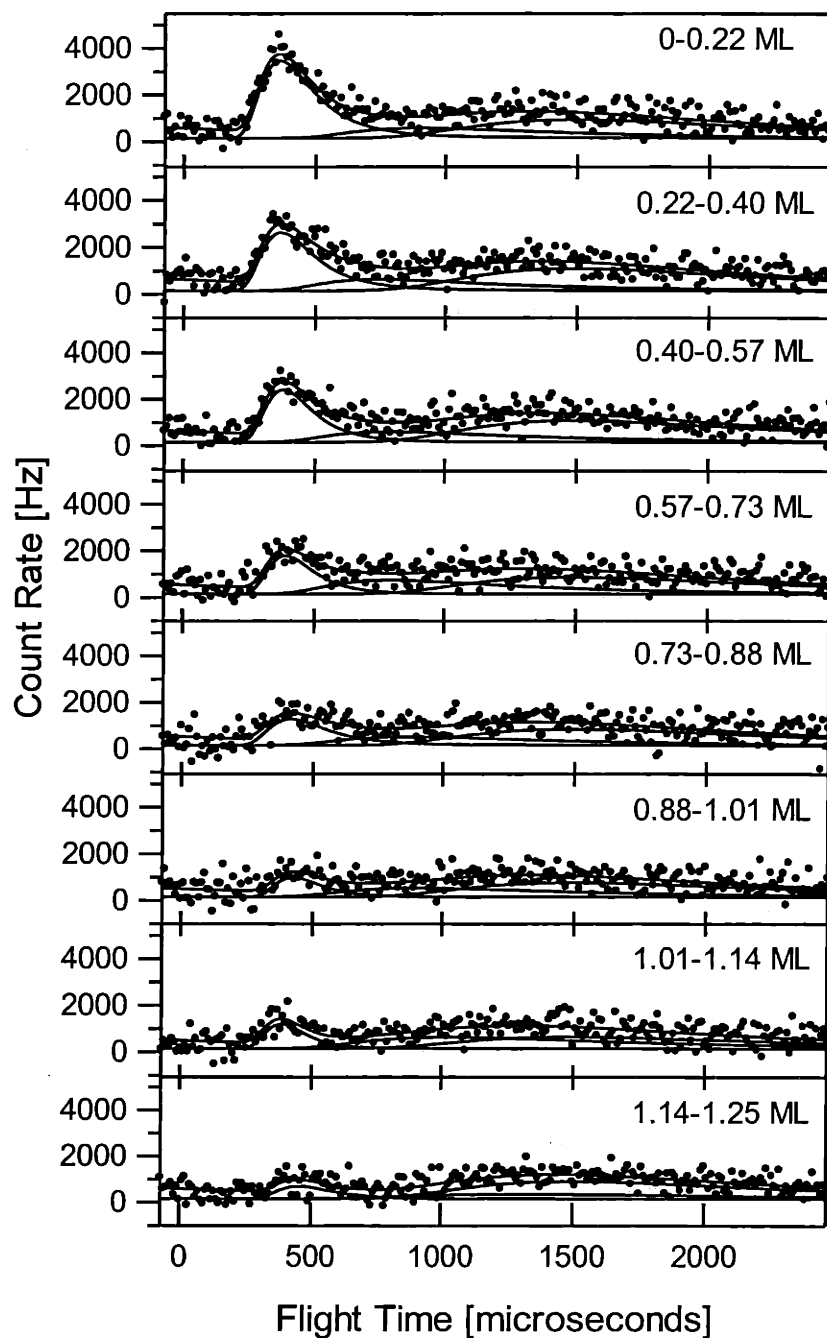
Figure 40 **Net TOF spectra at m/e=129 and θ_d=30° after maximum XeF cracking is subtracted**

Net TOF spectra at m/e=129 and a detector angle θ_d=30° for 8 coverage ranges upon exposure to XeF_2 at θ_i=20° and T_s=150 K. Solid lines show the least squares fit to three Maxwell-Boltzmann distributions and the sum of the fits to each feature. Each TOF spectrum is the average of 160 separate experiments. Electron impact energy is set to 26.5 eV.
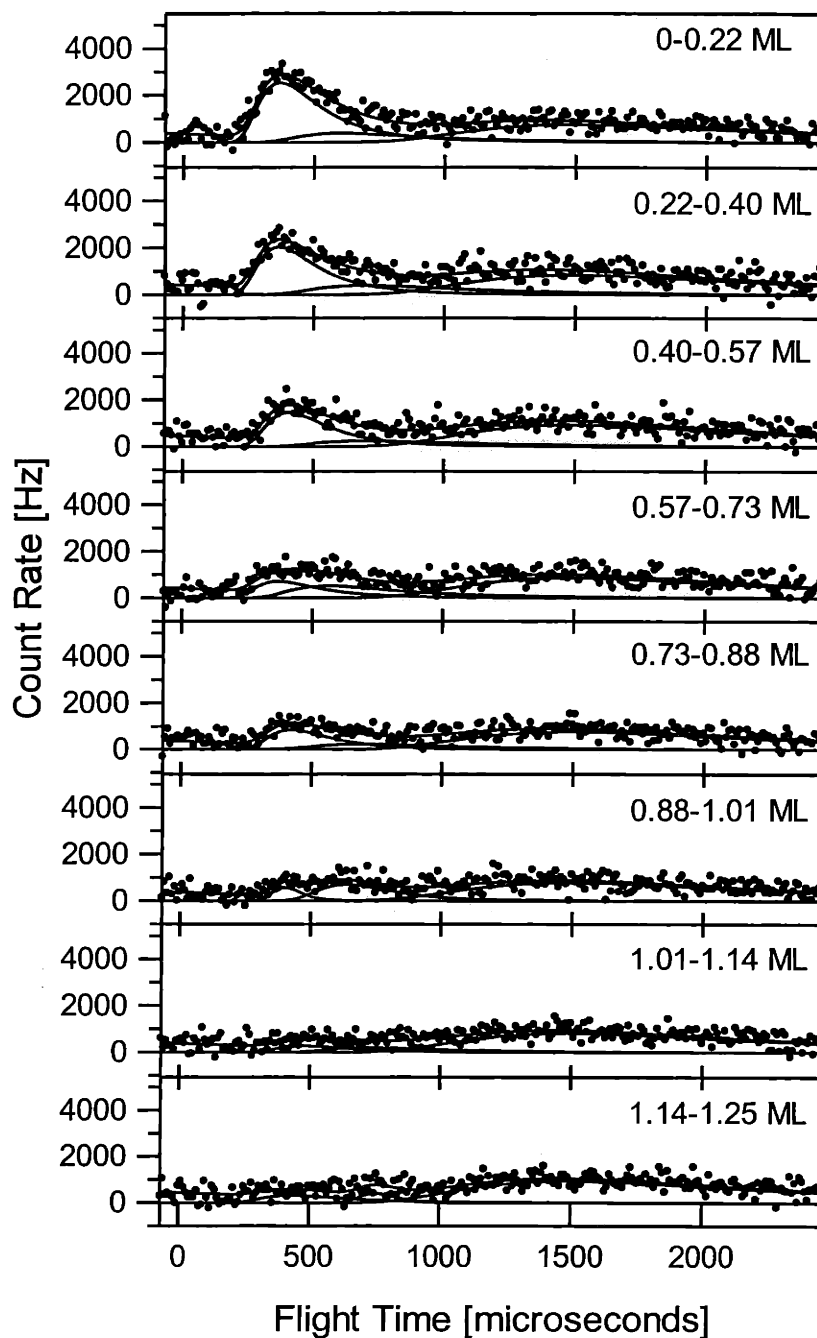
Figure 41   Net TOF spectra at m/e=129 and θ_d=60° after maximum XeF cracking is subtracted

Net TOF spectra at m/e=129 and a detector angle θ_d=60° for 8 coverage ranges upon exposure to XeF$_2$ at θ_i=20° and T$_s$=150 K. Solid lines show the least squares fit to three Maxwell-Boltzmann distributions and the sum of the fits to each feature. Each TOF spectrum is the average of 160 separate experiments. Electron impact energy is set to 26.5 eV.

Figure 42 Net TOF spectra at m/e=129 and θ_d=15° after intermediate XeF cracking is subtracted

Net TOF spectra at m/e=129 and a detector angle θ_d=15° for 8 coverage ranges upon exposure to XeF$_2$ at θ_i=20° and T$_s$=150 K and the sum of the fits to each feature. Solid lines show the least squares fit to three Maxwell-Boltzmann distributions. Each TOF spectrum is the average of 80 separate experiments. Electron impact energy is set to 26.5 eV.
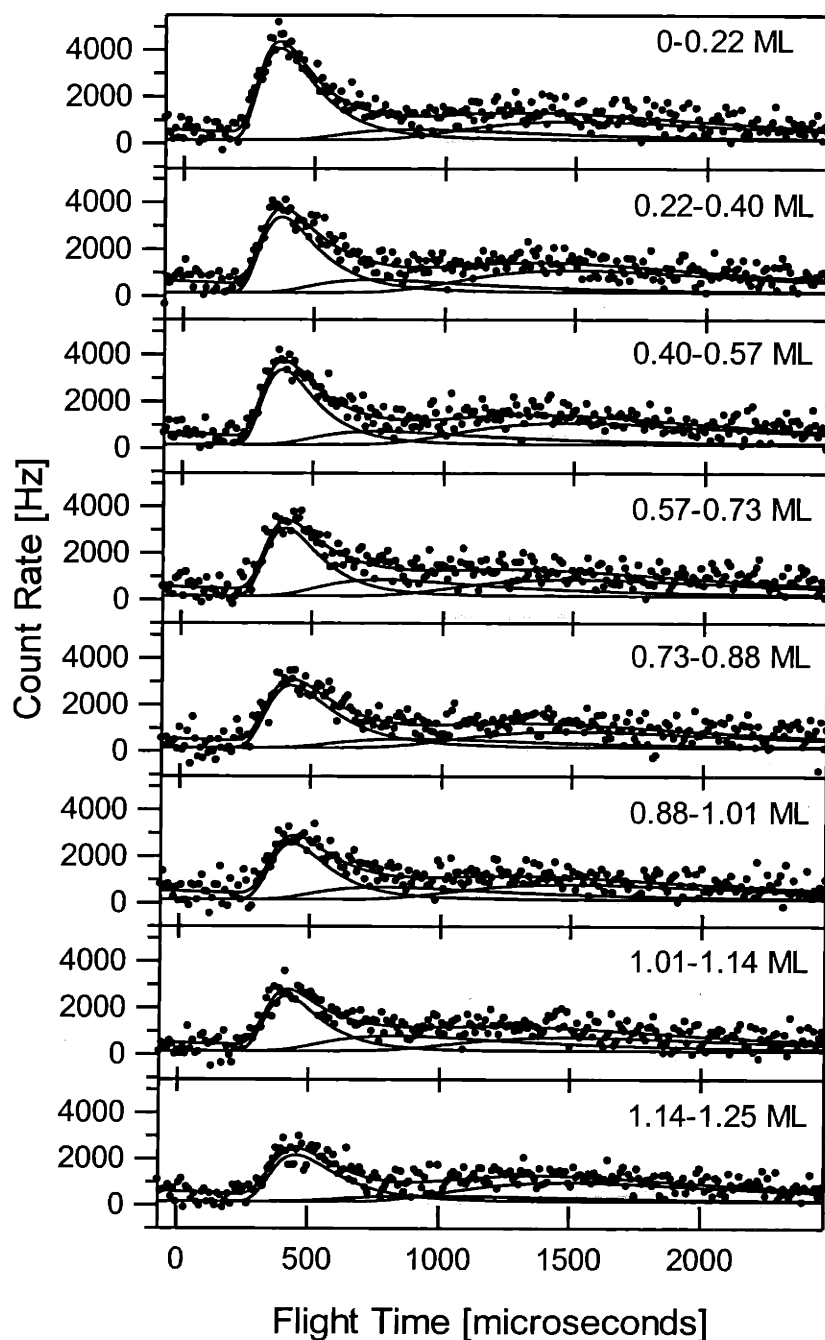
Figure 43 Net TOF spectra at m/e=129 and θ_d=30° after intermediate XeF cracking is subtracted

Net TOF spectra at m/e=129 and a detector angle θ_d=30° for 8 coverage ranges upon exposure to XeF$_2$ at θ_i=20° and T$_s$=150 K. Solid lines show the least squares fit to three Maxwell-Boltzmann distributions and the sum of the fits to each feature. Each TOF spectrum is the average of 160 separate experiments. Electron impact energy is set to 26.5 eV.
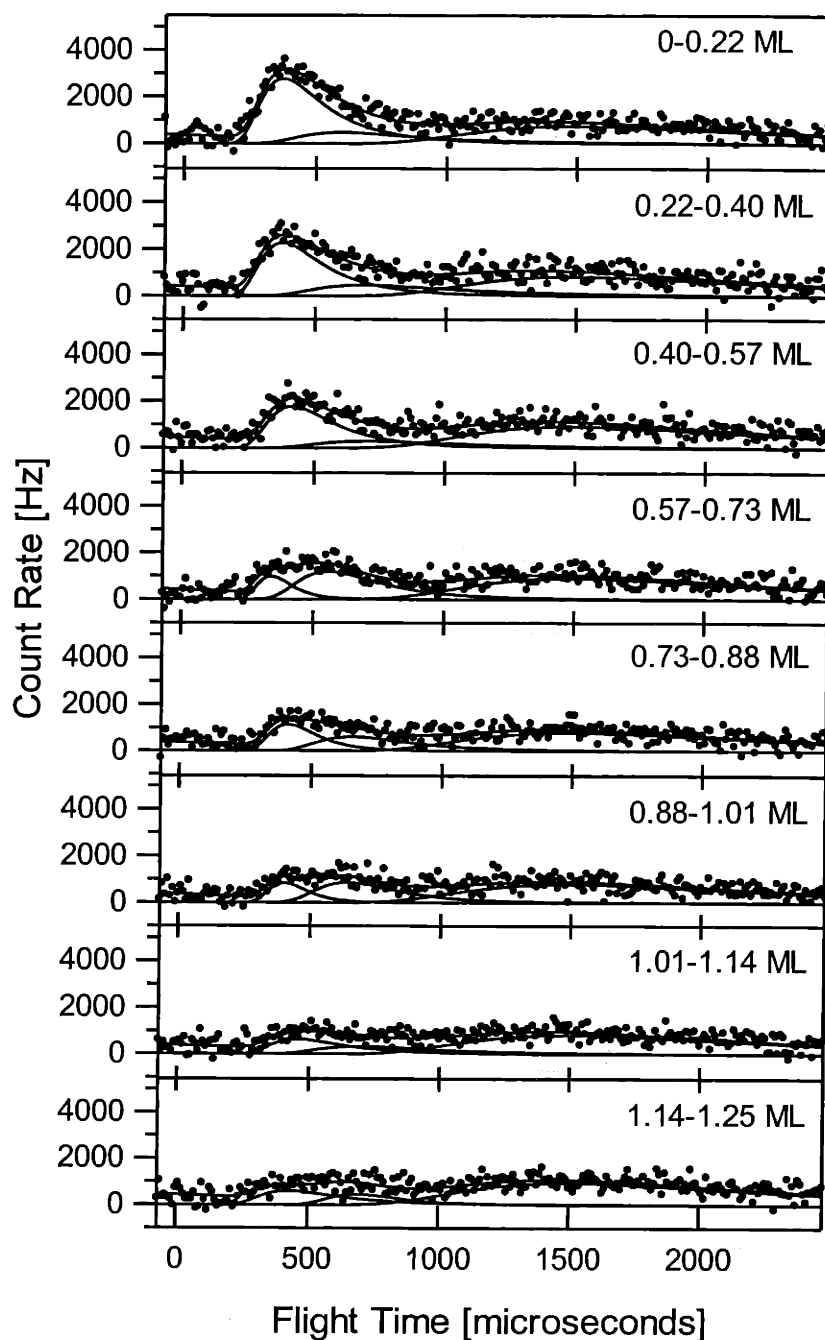
Figure 44 Net TOF spectra at m/e=129 and θ_d=60° after intermediate XeF cracking is subtracted

Net TOF spectra at m/e=129 and a detector angle $\theta_d=60°$ for 8 coverage ranges upon exposure to XeF_2 at $\theta_i=20°$ and $T_s=150$ K. Solid lines show the least squares fit to three Maxwell-Boltzmann distributions and the sum of the fits to each feature. Each TOF spectrum is the average of 160 separate experiments. Electron impact energy is set to 26.5 eV.
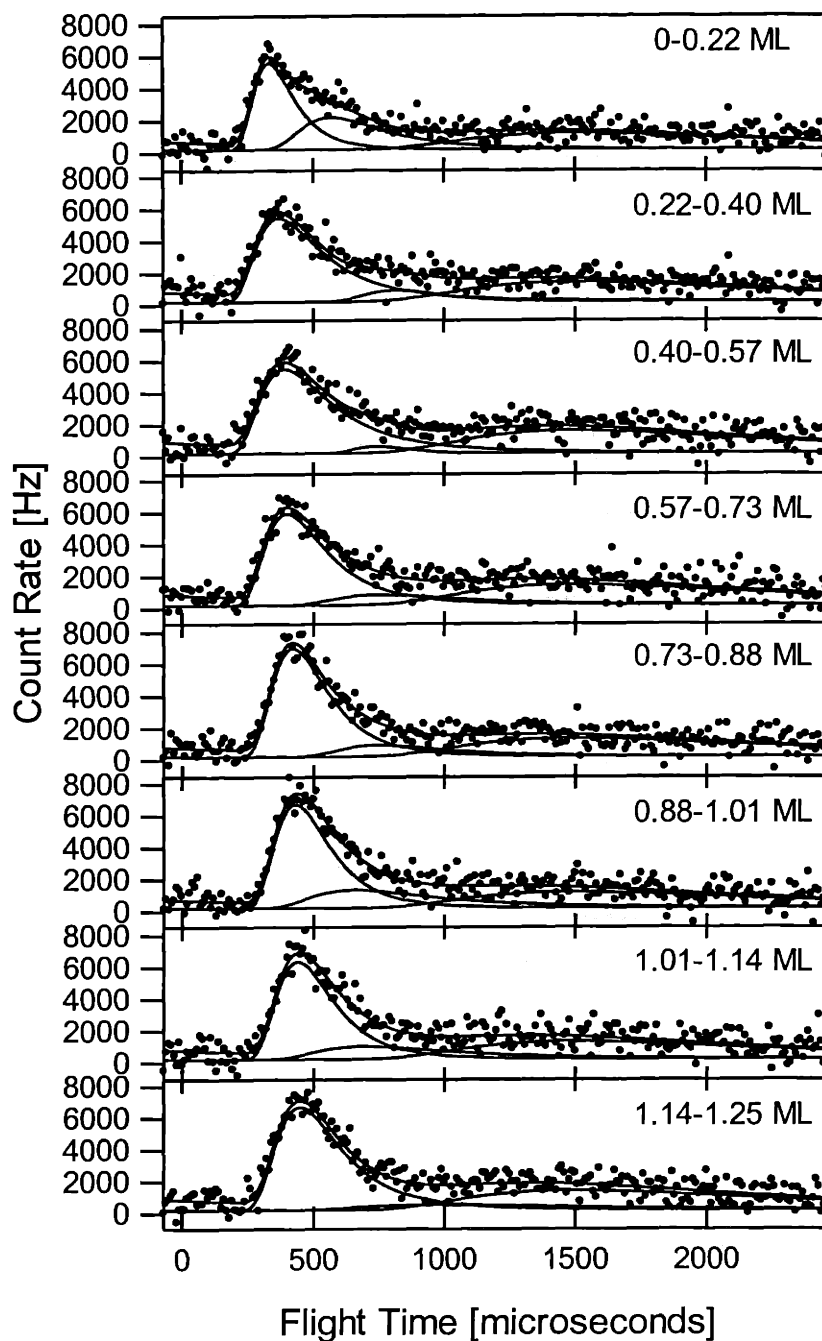
Figure 45 Net TOF spectra at m/e=129 and θ_d=15° with no XeF cracking subtracted

Net TOF spectra at m/e=129 and a detector angle θ_d=15° for 8 coverage ranges upon exposure to XeF_2 at θ_i=20° and T_s=150 K. Solid lines show the least squares fit to three Maxwell-Boltzmann distributions and the sum of the fits to each feature. Each TOF spectrum is the average of 80 separate experiments. Electron impact energy is set to 26.5 eV.
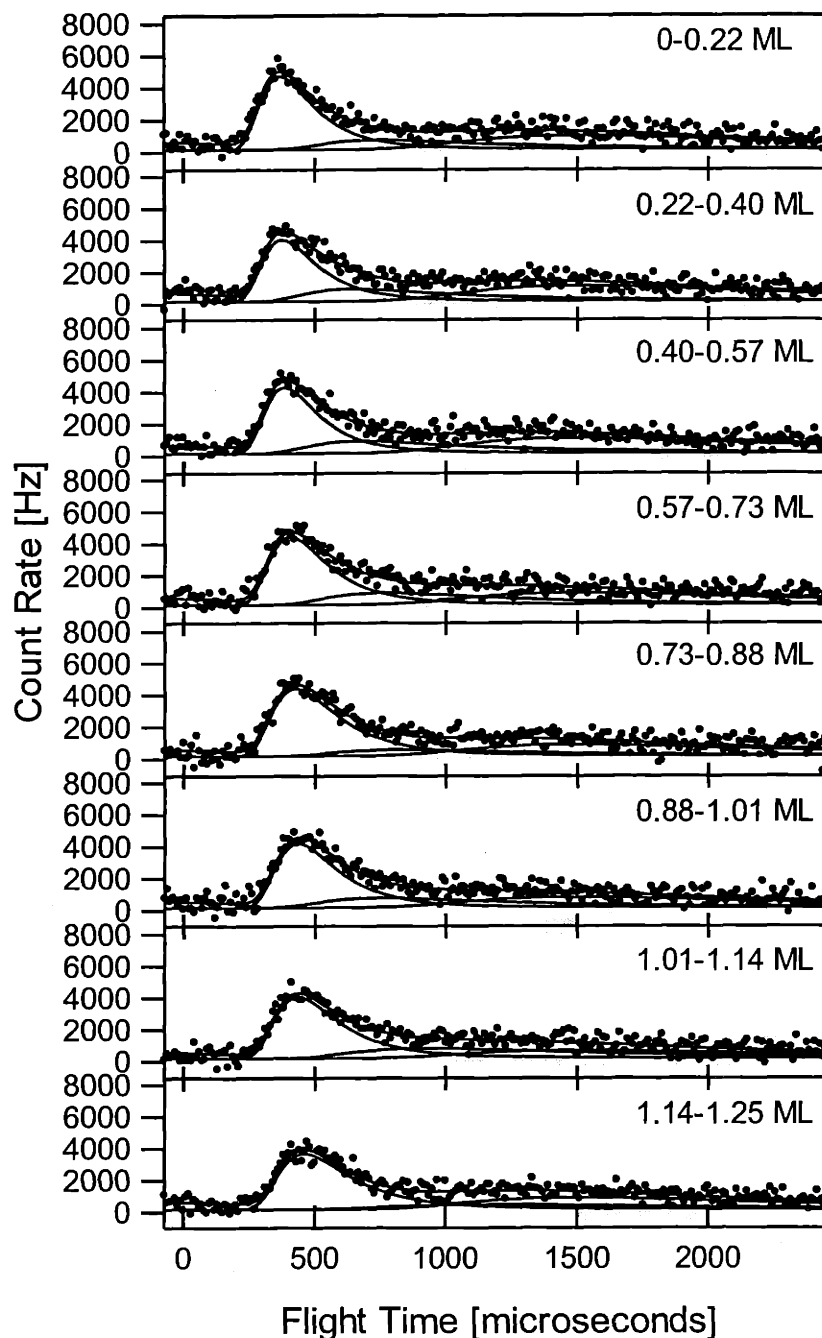
Figure 46 Net TOF spectra at m/e=129 and θ_d=30° with no XeF cracking subtracted

Net TOF spectra at m/e=129 and a detector angle θ_d=30° for 8 coverage ranges upon exposure to XeF_2 at θ_i=20° and T_s=150 K. Solid lines show the least squares fit to three Maxwell-Boltzmann distributions and the sum of the fits to each feature. Each TOF spectrum is the average of 160 separate experiments. Electron impact energy is set to 26.5 eV.
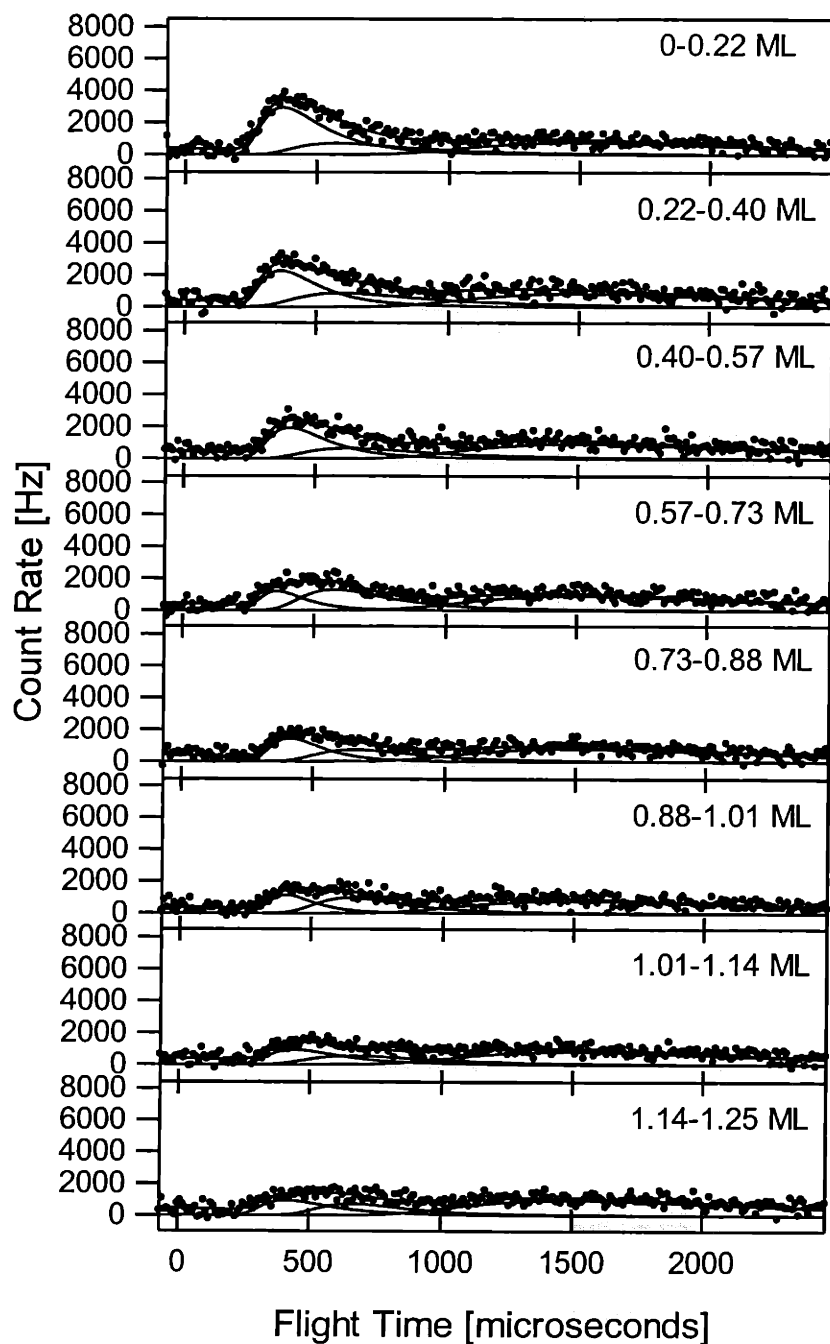
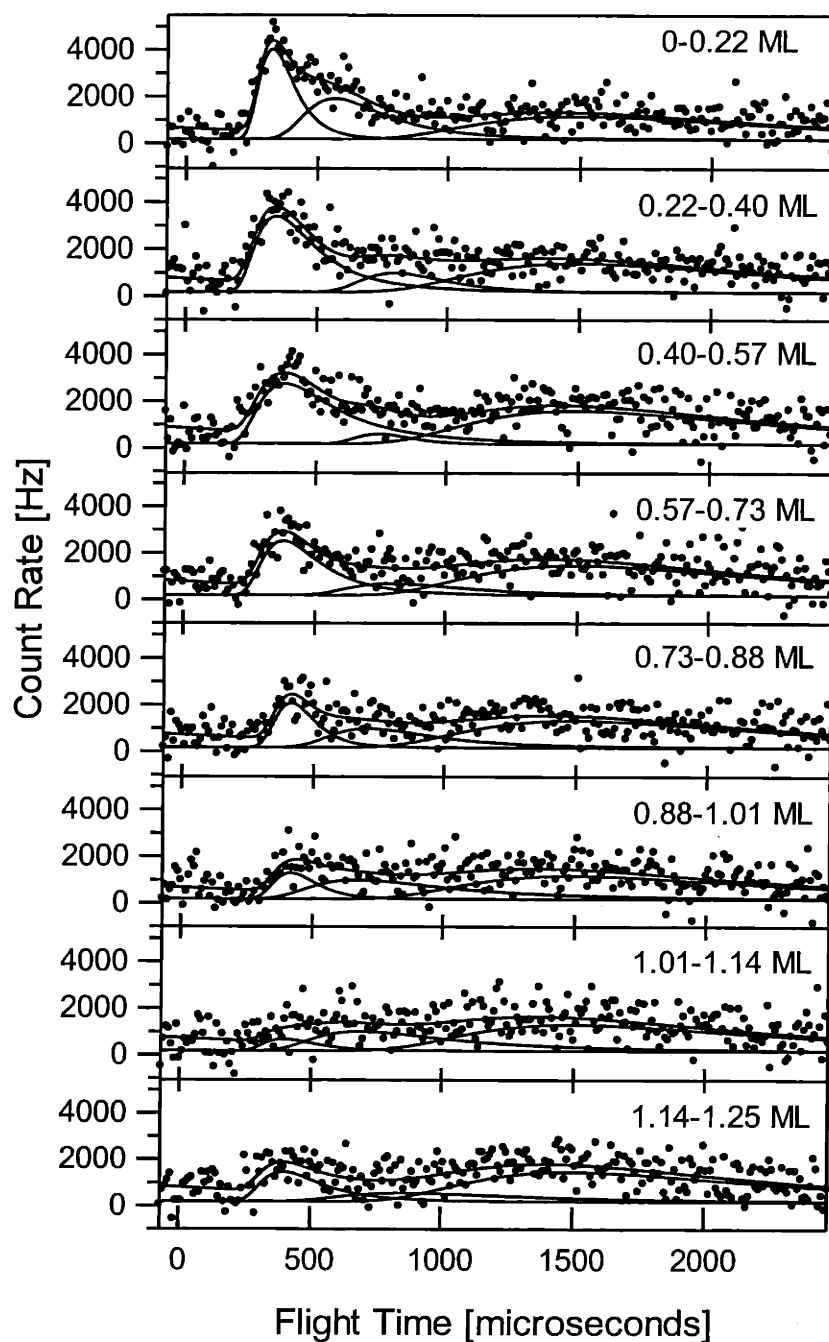**Figure 47 Net TOF spectra at m/e=129 and θ_d=60° with no XeF cracking subtracted**

Net TOF spectra at m/e=129 and a detector angle θ_d=60° for 8 coverage ranges upon exposure to XeF$_2$ at θ_i=20° and T$_s$=150 K. Solid lines show the least squares fit to three Maxwell-Boltzmann distributions and the sum of the fits to each feature. Each TOF spectrum is the average of 160 separate experiments. Electron impact energy is set to 26.5 eV.
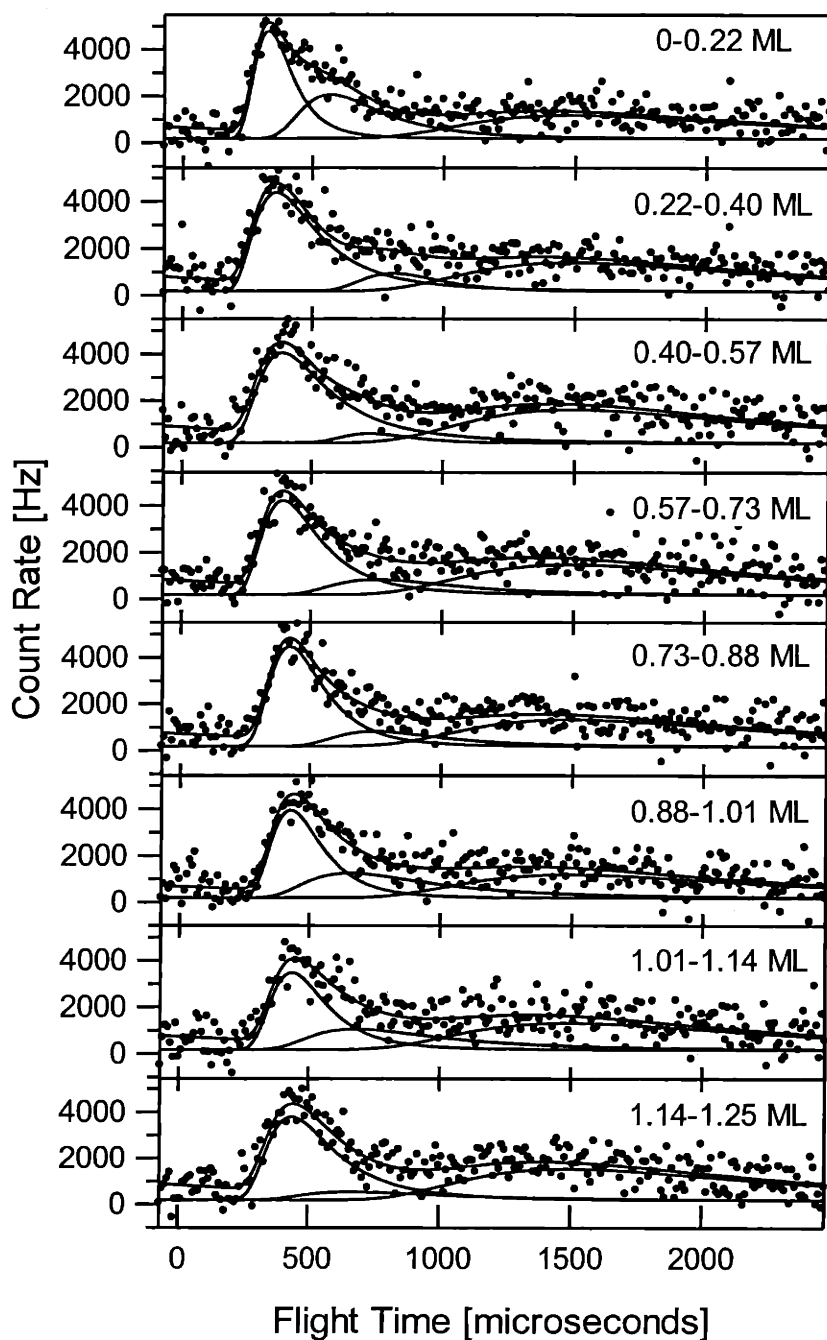
IV. Analysis

The observation of F atoms as a product of the dissociative chemisorption of XeF_2 on Si(100) provides evidence for the gas-phase dissociation of internally excited XeF prior to reaching the detector. Because the exothermicity of single atom abstraction is extremely large with respect to the bond strength of XeF, if only a small fraction of the energy liberated in the reaction is coupled into the internal energy of the XeF molecule, the XeF molecule will dissociate into a Xe atom and an F atom. The goal of the current analysis is to show that the observed F atom and Xe atom TOF distributions are consistent with the gas phase dissociation of XeF, and furthermore to identify which of the three Xe features observed in the TOF distribution is due to XeF dissociation.

IV.A Forward convolution momentum matching calculation

The dissociation of gas-phase XeF into Xe and F atoms is strongly suggested by the observation of the TOF spectra of F atoms arising from the reaction of XeF_2 with Si(100). The identification of the complementary Xe atom in the observed Xe atom TOF spectra is complicated by the fact that both XeF dissociation and 2-atom adsorption contribute to the m/e = 129 signal. In order to determine which of the three features in the Xe atom TOF distribution can be attributed to XeF dissociation, it is necessary to model the XeF dissociation and then predict the expected Xe atom TOF distribution. Since the XeF dissociation occurs in the gas phase it can be considered as an isolated system. Therefore, any momentum gained by the F atom as a result of the dissociation must be balanced by an equal and opposite momentum of the Xe atom, as dictated by the conservation of momentum. Similarly, all translational energy and the internal energy over the dissociation limit of the XeF prior to its dissociation will be

converted to translational energy of the F and Xe atoms, as dictated by the conservation of energy. The equations for conservation of momentum and energy are given in the lab frame by:

$$m_{XeF}\vec{v}_{XeF}^{LAB} = m_{Xe}\vec{v}_{Xe}^{LAB} + m_F\vec{v}_F^{LAB} \qquad (IV.1)$$

$$E_{trans}^{LAB}(XeF) + E_{int}(XeF) = E_{trans}^{LAB}(Xe) + E_{trans}^{LAB}(F) + E_{diss}(XeF) \qquad (IV.2)$$

where m_i, $\vec{v}_i^{LAB}$ and $E_{trans}^{LAB}(i)$ (i = XeF, Xe and F) are the mass, lab-frame velocity, and lab-frame translational energy of each particle respectively, $E_{int}(XeF)$ is the internal energy of XeF prior to the dissociation, and $E_{diss}(XeF)$ is the XeF dissociation energy.

A schematic of the relevant velocity vectors involved in the momentum matching analysis are shown in Figure 48. The initial lab-frame velocity vector of the XeF fragment is shown in Figure 48(a). The XeF velocity vector is defined by a magnitude $|v_{XeF}|$, and an angle θ defined from the surface of the Si crystal. The orientation of the XeF molecular axis is given by ϕ, defined relative to the XeF velocity vector. Also shown in Figure 48(a) are the x and y components of the XeF velocity vector, which will be used in subsequent steps. For purposes of this analysis, it is useful to introduce the center of mass coordinate system, defined by the velocity vector of the XeF. That is to say, in the center of mass frame the velocity of the XeF fragment prior to dissociation is zero. The velocity vectors of the Xe and F atoms in the center of mass coordinate frame are shown in Figure 48(b). The final lab frame Xe and F velocity vectors are given by simple vector addition, as shown in Figure 48(c). The Xe and F velocity vectors are defined by the magnitudes $|v_{Xe}^{LAB}|$ and $|v_F^{LAB}|$ and the angles χ_{Xe} and χ_F, defined from the Si surface.

In the center of mass frame shown in Figure 48(b), Eqs. (IV. 1) and (IV. 2) become:

$$m_{Xe}\vec{v}_{Xe}^{CM} = -m_F\vec{v}_F^{CM} \qquad (IV.3)$$

$$E_{CM} = \frac{1}{2} m_{Xe} \left| \vec{v}_{Xe}^{CM} \right|^2 + \frac{1}{2} m_F \left| \vec{v}_F^{CM} \right|^2$$

(IV.4)

where Eq. (IV.4) has been simplified by introducing the center of mass energy, $E_{CM}=E_{int}(XeF)-E_{diss}(XeF)$, which is the internal energy over the dissociation limit. That is, the center of mass energy E_{CM} is the amount of internal energy of the XeF that is converted to translational energy of the Xe and F atoms once the dissociation occurs. By substituting Eq. (IV.3) into Eq. (IV.4), the CM velocity of the F and Xe atoms after dissociation can be determined as a function of the center of mass energy, E_{CM}:

$$\left| \vec{v}_F^{CM} \right| = \sqrt{\frac{2E_{CM}}{m_F \left(1 + \frac{m_F}{m_{Xe}} \right)}} \qquad \left| \vec{v}_{Xe}^{CM} \right| = \sqrt{\frac{2E_{CM}}{m_{Xe} \left(1 + \frac{m_{Xe}}{m_F} \right)}} \qquad \text{(IV.5)}$$

The x and y components of the lab-frame velocities of Xe and F can be found by vector addition as shown in Figure 48(c):

$$v_{F,x}^{LAB} = \left| \vec{v}_F^{CM} \right| \cos(\theta + \phi) + \left| \vec{v}_{XeF} \right| \cos\theta$$

$$v_{F,y}^{LAB} = \left| \vec{v}_F^{CM} \right| \sin(\theta + \phi) + \left| \vec{v}_{XeF} \right| \sin\theta$$

(IV.6)

$$v_{Xe,x}^{LAB} = \left| \vec{v}_{Xe}^{CM} \right| \cos(\theta + \phi + \pi) + \left| \vec{v}_{XeF} \right| \cos\theta$$

$$v_{Xe,y}^{LAB} = \left| \vec{v}_{Xe}^{CM} \right| \sin(\theta + \phi + \pi) + \left| \vec{v}_{XeF} \right| \sin\theta$$

The expressions for the F and Xe CM velocities differ by a factor of π because the Xe atom is pointing 180° away from the F atom. Once the x and y components of the lab-frame F and Xe velocities are known, the magnitude and direction of the velocities can be calculated:

$$\left| \vec{v}_F^{LAB} \right| = \sqrt{v_{F,x}^{LAB2} + v_{F,y}^{LAB2}} \qquad \chi_F = \cos^{-1} \left(\frac{v_{F,x}^{LAB}}{\left| \vec{v}_F^{LAB} \right|} \right)$$

$$\left|\vec{v}_{Xe}^{LAB}\right| = \sqrt{v_{Xe,x}^{LAB^2} + v_{Xe,y}^{LAB^2}} \qquad \chi_{Xe} = \cos^{-1}\left(\frac{v_{Xe,x}^{LAB}}{\left|\vec{v}_{Xe}^{LAB}\right|}\right) \qquad \text{(IV.7)}$$

Thus, the lab-frame velocity and the lab scattering angle χ of the F and Xe are determined by the initial lab-frame XeF velocity, v_{XeF}, the initial lab angle of the XeF velocity, θ, the orientation of the XeF molecular axis with respect to the XeF velocity during dissociation, ϕ, and the center of mass velocities, $\vec{v}_F^{CM}$ and $\vec{v}_{Xe}^{CM}$. The CM velocities are determined by the center of mass energy, E_{CM}, and the relative Xe and F masses as given by Eq. (IV.5). Note that θ in this case is defined from the surface. This definition is different from the convention used previously for reporting the scattering angles, which are defined from the surface normal. This definition of θ from the surface simplifies the momentum matching equations, but for all subsequent discussions the scattering angle will be defined from the surface normal, as before.

Using Eqs. (IV. 5-7) shown above, the final velocity and scattering angle of the F and Xe atom can be determined given any set of initial parameters $\{\theta, \phi, v_{XeF}, E_{CM}\}$. However, each of these parameters actually has a distribution of values, $P(\phi)$, $P(\theta, v_{XeF})$, and $P(E_{CM})$, where $P(x)$ is the probability distribution with respect to the variable x. Although in principle these distributions may be mutually dependent, they are assumed to be independent, without additional constraints. The validity of this assumption is borne out by the results presented below. The center of mass flux for a given set of initial parameters is given by:

$$I_{CM}(\theta, \phi, v_{XeF}, E_{CM}) = P(\phi) \cdot P(\theta, v_{XeF}) \cdot P(E_{CM})$$

It will be shown in Section IV.B. that this assumption results in predicted F atom TOF spectra that match the observed F atom TOF spectra.

To convert the center of mass frame flux into detected lab-frame flux, it is necessary to take into account the fact that the solid angle sustained by the detector is inversely proportional

to the square of the velocity of the detected particle[23]. The transformation Jacobian between the center of mass flux and the lab frame flux is therefore $(v^{LAB} / v^{CM})^2$:

$$I_F^{LAB}\left(v_F^{LAB},\chi_F\right)=\left(\frac{v_F^{LAB}}{v_F^{CM}}\right)^2 I_{CM}\left(\theta,\phi,v_{XeF},E_{CM}\right)=\left(\frac{v_F^{LAB}}{v_F^{CM}}\right)^2 P(\phi)\cdot P\left(\theta,v_{XeF}\right)\cdot P\left(E_{CM}\right)$$

$$\text{(IV.8)}$$

$$I_{Xe}^{LAB}\left(v_{Xe}^{LAB},\chi_{Xe}\right)=\left(\frac{v_{Xe}^{LAB}}{v_{Xe}^{CM}}\right)^2 I_{CM}\left(\theta,\phi,v_{XeF},E_{CM}\right)=\left(\frac{v_{Xe}^{LAB}}{v_{Xe}^{CM}}\right)^2 P(\phi)\cdot P\left(\theta,v_{XeF}\right)\cdot P\left(E_{CM}\right)$$

In order to use Eqs. (IV.7) and (IV.8) to predict the F and Xe atom TOF distributions a forward convolution calculation is performed. This calculation has been used previously in gas-phase photodissociation studies[22,23] to fit the observed TOF spectra of the gas-phase unimolecular photodissociation products. The forward convolution method uses an initial velocity distribution prior to the dissociation event, a distribution of molecular orientations of the dissociating XeF molecule, and a distribution of internal energies to predict the observed product TOF distribution. This method is implemented via a MATLAB program that calculates the final flux of F and Xe with respect to velocity and detection angle given the initial distributions $P(\phi)$, $P(\theta,v_{XeF})$, and $P(E_{CM})$. This calculation takes a range of values for each of the four initial variables $\{\theta,\phi,v_{XeF},E_{CM}\}$, calculates the corresponding $\{v_F^{LAB},\chi_F\}$ and $\{v_{Xe}^{LAB},\chi_{Xe}\}$ using Eq. (IV.7), then calculates the flux using Eq. (IV.8). The program then stores the results of the calculation in a matrix that includes v_F^{LAB}, χ_F, I_F^{LAB}, v_{Xe}^{LAB}, χ_{Xe}, and I_F^{LAB}. The F and Xe flux velocity distributions at a particular detection angle are obtained from the flux of all the trajectories that result in χ_F or χ_{Xe} that match that detection angle. In order to take into account the finite angular resolution of the detector, all trajectories falling within $\pm 3°$ of each detection angle are included. Increasing or decreasing this acceptance angle to $\pm 10°$ and $\pm 1°$ does not have a significant effect on the results of the calculation.

Since the XeF which dissociates cannot be detected, the distribution $P(\theta, v_{XeF})$ in Eq. (IV. 8) is not known. A good first approximation is to use the distributions of the detected XeF for $P(\theta, v_{XeF})$. That is, for each $\{\theta, v_{XeF}\}$, $P(\theta, v_{XeF})$ is determined from the XeF velocity distribution that is observed for the scattering angle closest to θ and the observed angular distribution of the XeF flux, as described in greater detail below. This approximation will be shown in Section IV.B. to result in predicted F atom distributions that match the observed F atom TOF spectra.

The XeF velocity distributions for $P(\theta, v_{XeF})$ are taken from the experimental velocity distributions measured at the three scattering angles, $\theta_d=75°$, $60°$ and $30°$, corresponding to the detection angles $\theta_d=15°$, $30°$ and $60°$ respectively. These results are extrapolated by assuming that any angle in the range $0 \leq \theta < 45°$ can be described by the observed XeF velocity distribution at $\theta_d=60°$; any angle in the range $45° \leq \theta < 67.5°$ can be described by the observed velocity distribution at $\theta_d=30°$; and any angle in the range $67.5° \leq \theta < 90°$ can be described by the observed velocity distribution at $\theta_d=15°$. Recall that $\theta=90°-\theta_d$. Again, the distributions were assumed to be symmetric about the surface normal. The calculation was performed using 19 different values of θ and 60 different values of v_{XeF} at each θ.

The XeF angular distributions for $P(\theta, v_{XeF})$ are taken from an earlier study[1] performed at 250 K, which gave the XeF angular distribution over the range $\theta_d = 0° - 80°$ at the four coverage ranges 0-0.4 ML, 0.4-0.7 ML, 0.7-0.9 ML and 0.9-1.1 ML. The reported angular distributions can be fit to $\cos^n(\theta)$, which gives the values n = 0.485, 1.23, 3.53 and 5.26 at the four coverage ranges. These values are used to give $P(\theta)$ in the calculation. The distributions are assumed to be symmetric about the surface normal.

The distribution of molecular orientations, $P(\phi)$, is not known but is assumed to be isotropic. That is, any orientation with the F atom pointing away from the surface is equally likely. Specifically, $P(\phi)=1$ for $-\theta<\phi<(\pi-\theta)$ and $P(\phi)=0$ for $(\pi-\theta)\leq\phi\leq(2\pi-\theta)$. This assumption is based on the fact that the XeF dissociation is expected to occur with a time scale that is on the order of a vibrational period, which is much shorter than a rotational time period. Therefore, the XeF is not expected to rotate from its transition state orientation prior to the dissociation. Although it is possible that the transition state orientation of the XeF has the fluorine atom pointing towards the surface, this orientation is expected to be less likely due to the large distortion in the F-Xe-F bond angle. The validity of this assumption will be tested later. The calculation was performed using 19 different values of ϕ at each of the 19 different values of θ and 60 different values of v_{XeF}. Typical distributions used in the calculation are shown in figure Figure 49.

In order to compare the F and Xe atom flux velocity distributions predicted by Eq. (IV.8) with the observed TOF spectra, they are transformed into number density time-of-flight distributions at each detection angle χ using the transformations:

$$t = \frac{L}{v}$$

$$F^{\#dens}(t,\chi) = \frac{1}{v} \cdot I(t,\chi) = \frac{1}{v}\left(\frac{v^2}{L}I(v)\right) = \frac{v}{L}I(v,\chi) \qquad (IV.9)$$

Given these initial distributions, trial and error is used determine a functional form for the distribution of center of mass energy $P(E_{CM})$ used in Eq. (IV. 8) that reproduces the observed F atom distribution. Although multiple different functional forms for the energy distribution were tried, the F atom TOF spectra were best reproduced using:

$$P(E_{CM}) \propto E_{CM}^{\frac{1}{2}} \exp\left(-\frac{E_{CM}}{RT}\right) \qquad\qquad (IV.10)$$

The calculation was performed using 120 different values of E_{CM} at each of the 19 different values of ϕ, the 19 different values of θ, and 60 different values of v_{XeF} at each θ. Thus, the total number of trajectories calculated is $120*19*19*60 = 2,599,200$ trajectories.

For the final calculation, the effect of the spin states of the F atom was taken into account. As shown in Figure 1, the F atom can be in one of two spin states, $^2P_{3/2}$ or $^2P_{1/2}$, which differ in energy by 404 cm^{-1}. All else being equal, if the dissociation produces a F atom in the higher energy spin state, $^2P_{1/2}$, less energy will go to the translational energy of the F and Xe. Therefore, the final energy distribution was constructed by taking the sum of two distributions that differed in average energy by 404 cm^{-1}. Because the product distribution should favor the lower energy spin state, a weighting of 80%/20% was applied to the sum of the two energy distributions. This relative population was chosen arbitrarily. The energy distributions used are shown in Figure 50. The lower energy spin state, $^2P_{3/2}$ corresponds to the center of mass energy distribution shown with the long dashed line. This distribution is characterized by an effective temperature of 2187 K, and has an average energy of 6.46 kcal/mol. The center of mass energy distribution shown with the short dashed line corresponds to the higher energy spin state, $^2P_{1/2}$, and is characterized by an effective temperature of 1769 K, with an average energy of 5.31 kcal/mol. The overall distribution has an average energy of 6.23 kcal/mol.

At these temperatures, it should be noted that the relative population of the two spin states would be 72%/28%, if the F atoms were produced with an equilibrium distribution of electronic energy. However, it is not known whether the F atoms are produced in electronic equilibrium. If they are not, it is most likely that the F atoms are produced in the $^2P_{3/2}$ state, because this state correlates with a stable, ground X state of the XeF molecule. In this case, the

population distribution is 100%/0%. Changing the relative population to either 72%/28% or 100%/0% has a negligible effect on the results of the calculation, so the original population distribution of 80%/20% was used for all calculations. Thus, the average internal energy prior to dissociation, which is simply the average energy of the center-of-mass energy distribution plus the dissociation energy, is approximately 9 kcal/mol.
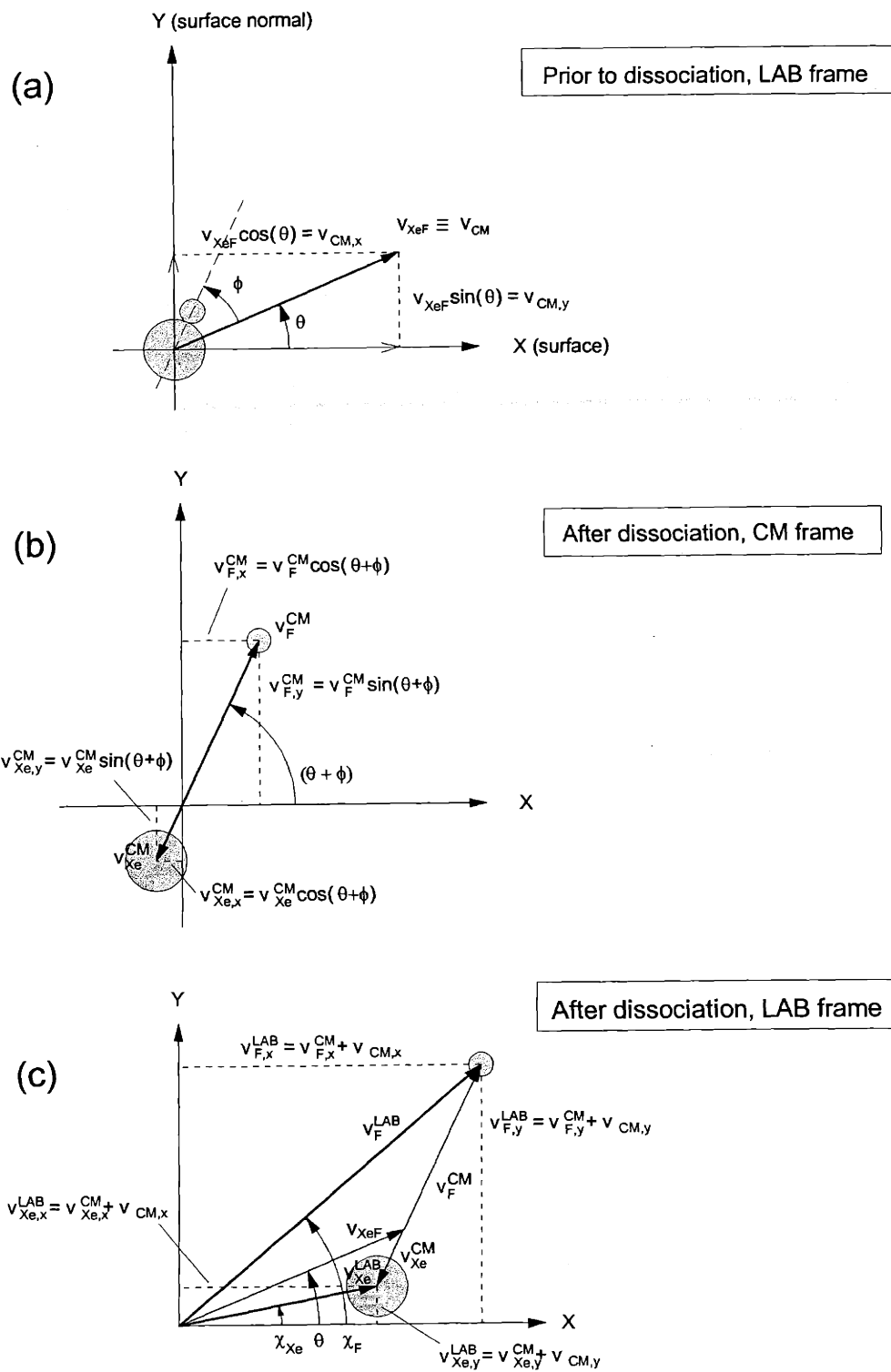
Figure 48 Coordinate system for momentum matching calculations
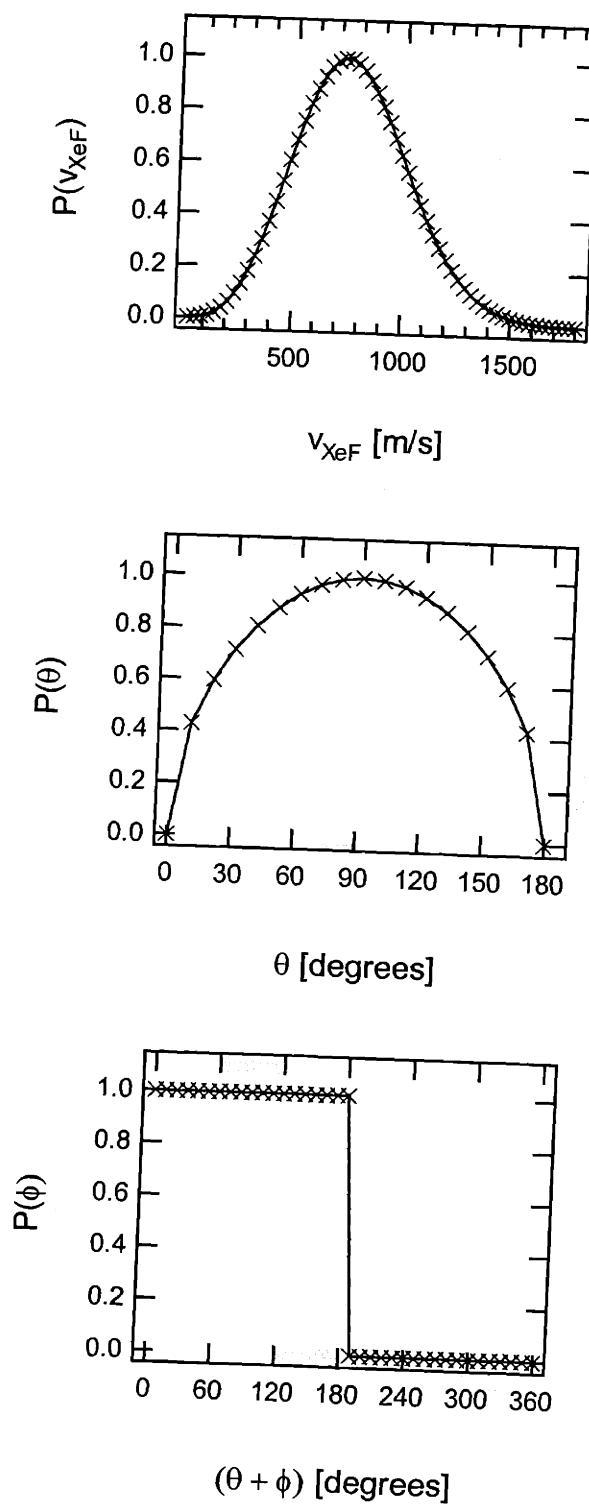
Figure 49 **Typical distributions for** v_{XeF}, θ, **and** ϕ
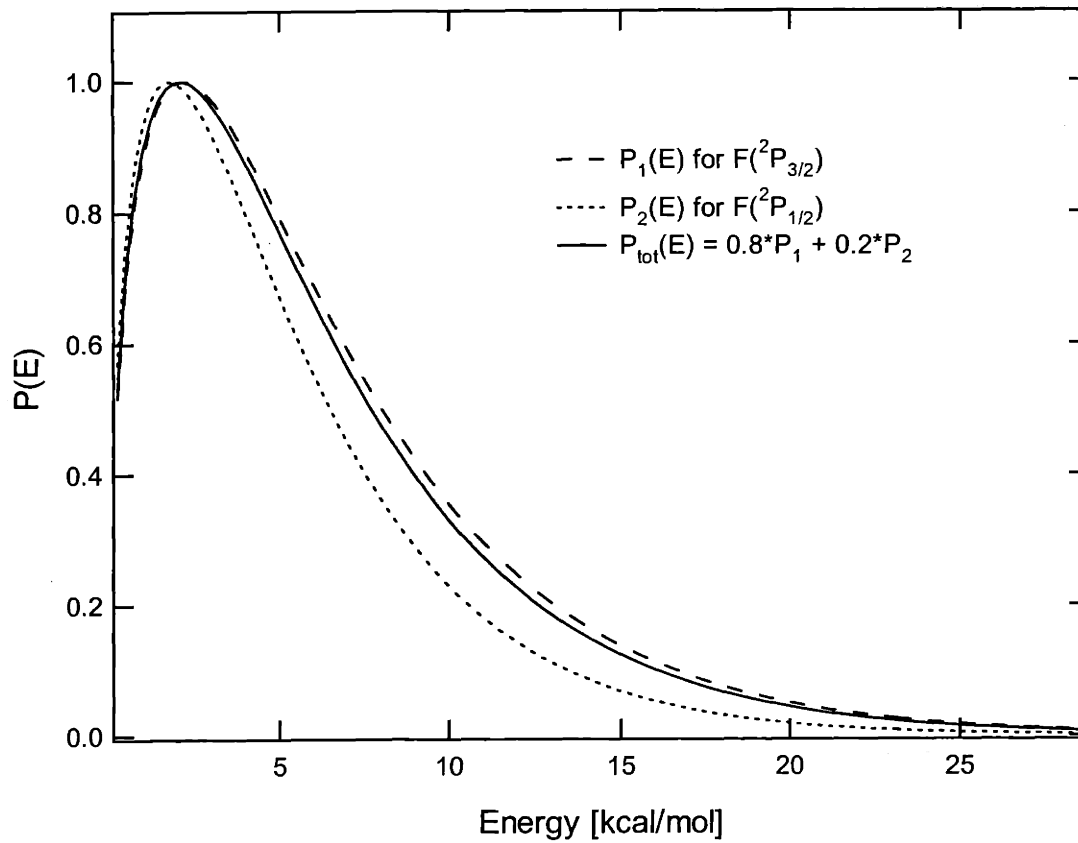
Figure 50 Center of mass energy distribution P(E$_{CM}$)

IV.B Predicted F and Xe distributions

In order to arrive at the center of mass energy distribution $P(E_{CM})$ shown in Figure 50, multiple calculations were performed and the energy distribution was adjusted by trial and error until the observed F atom TOF distribution scattered from a clean surface was correctly reproduced. The trial and error procedure is as follows. A center of mass energy distribution is assumed, and the forward convolution calculation is performed, solving Eq. (IV.8) to yield the predicted F atom flux velocity distribution. The predicted F atom flux velocity distribution is then converted to a number density TOF distribution using Eq. (IV.9), and compared with the observed F atom TOF distribution. If the predicted F atom distribution is slower than the observed F atom TOF distribution, then the average energy of $P(E_{CM})$ is incrementally increased, and vice versa. If the TOF distribution is too narrow, then the functional form for $P(E_{CM})$ is adjusted so that the energy distribution is more broad, and vice versa. Through a succession of these iterations the energy distribution $P(E_{CM})$ is found that best reproduces the observed F atom TOF distribution. The F atom TOF distribution was fit instead of the Xe atom distribution because the F atom signal is observed to be a single feature due solely to XeF dissociation, while the Xe atom signal is observed to be three features, any of which could be due either to XeF dissociation or to two-atom adsorption.

The predicted F atom TOF distributions calculated from the forward convolution calculation are shown in Figures 51, 52, and 53 along with the data and the Maxwell-Boltzmann fit to the data at all angles and coverage ranges. The agreement between the predicted distributions and the data is quite good. A single energy distribution correctly accounts for the observed F atom distributions across the entire coverage range and at all angles, despite the large variation in the observed XeF velocity distributions as shown in Figures 23, 24, and 25. The

implication of a single center of mass energy distribution applying to all coverages and scattering angles is explored in greater detail in the discussion section. The predicted F atom angular distribution is shown in Figures 54 along with the experimentally observed angular distribution, where the predicted flux distribution is normalized to the value of the flux at $\theta_d=15°$ for each coverage range. The forward convolution calculation successfully predicts the observed F atom angular distribution at all coverages.

Once the center of mass energy distribution, $P(E_{CM})$, is found that correctly predicts the observed F atom TOF spectra, the same center of mass energy distribution is used in the forward convolution calculation to predict the Xe atom TOF distributions from XeF dissociation. Figure 55 shows the observed Xe atom TOF spectra after subtraction of the maximum XeF cracking for the coverage range 0.22 – 0.40 ML at the three detection angles. The predicted Xe atom distribution from XeF dissociation is shown as a thick solid line. In section III.E. it was shown that the observed Xe atom TOF signal can be fit by three Maxwell-Boltzmann features, fast, medium and slow. These Maxwell-Boltzmann features are shown as a thin solid line (fast feature), short dashed line (medium feature), and long dashed line (slow feature). Note that the predicted Xe atom distributions are normalized so that the maximum intensity of the predicted Xe distribution matches the maximum intensity of the fit to the fast feature. For this coverage range and with the maximum XeF cracking subtracted, the predicted Xe atom distribution matches the fast feature at all detection angles. Figures 56 and 57 show the observed Xe atom TOF spectra after subtraction of the intermediate and minimum XeF cracking respectively for the coverage range 0.22 – 0.40 ML at the three detection angles. Again, the predicted Xe atom distributions are normalized so that the intensity of the predicted Xe distribution matches the maximum intensity of the fit to the fast feature. The predicted Xe atom TOF distributions match

the fast feature of the observed Xe atom TOF spectra. The agreement between the predicted Xe atom distribution and the fast feature is unaffected by the value chosen for the XeF cracking ratio.

The predicted Xe atom distributions at all angles and coverage ranges are shown in Figures 58, 59, and 60 compared to the observed m/e = 129 TOF spectra with the intermediate XeF cracking subtracted. The agreement between the predicted Xe atom distribution and the fast feature is quite good at virtually all angles and coverages. As with the predicted F atom distributions, the same center of mass energy distribution, $P(E_{CM})$, is used for all coverages, and the predicted Xe atom TOF distribution from XeF dissociation is consistent with the fast feature of the observed Xe TOF spectra at all coverages and detection angles. The identification of the fast feature of the Xe TOF signal as consistent with Xe from XeF dissociation will be explored further in the discussion section.

Recall that the definition of $P(\phi)$ for the above results was defined so that the F atom was always pointing into the vacuum. In order to gain physical insight into the possibility that other XeF molecular orientations contribute to the dissociation, the forward convolution calculation was re-calculated with the range of molecular orientations increased to include all possible XeF orientations. Explicitly this means $P(\phi)=1$ for $0 \leq \phi < 2\pi$. The predicted F atom distributions for this definition of $P(\phi)$ are identical to those shown in Figures 51, 52, and 53, and are not reproduced. The predicted Xe atom distributions are shown in Figures 61, 62, and 63 at all angles and coverage ranges compared to the observed m/e=129 TOF spectra with the intermediate XeF cracking subtracted. It can be seen that the agreement between the predicted and observed Xe atom distributions is markedly poorer. In fact, at several coverage ranges, most notably 0.73 ML – 1.01 ML at $\theta_d=15°$ and 0 ML – 0.73 ML at $\theta_d=30°$, the predicted Xe atom

distribution is faster than the observed Xe atom TOF signal. Thus, if all possible XeF orientations are included in the forward convolution calculations, the predicted Xe TOF distribution does not match the observed Xe TOF distribution. Therefore, the results of the forward convolution calculation strongly suggest that the dissociation event occurs with a XeF orientation where the F atom is pointing into the vacuum. A priori, one might expect the rotational excitation of the XeF to scramble the XeF molecular orientations. The fact that this does not occur implies that the dissociation occurs more quickly than a rotational period, consistent with the expectation that the dissociation occurs on the time scale of a few vibrational periods.
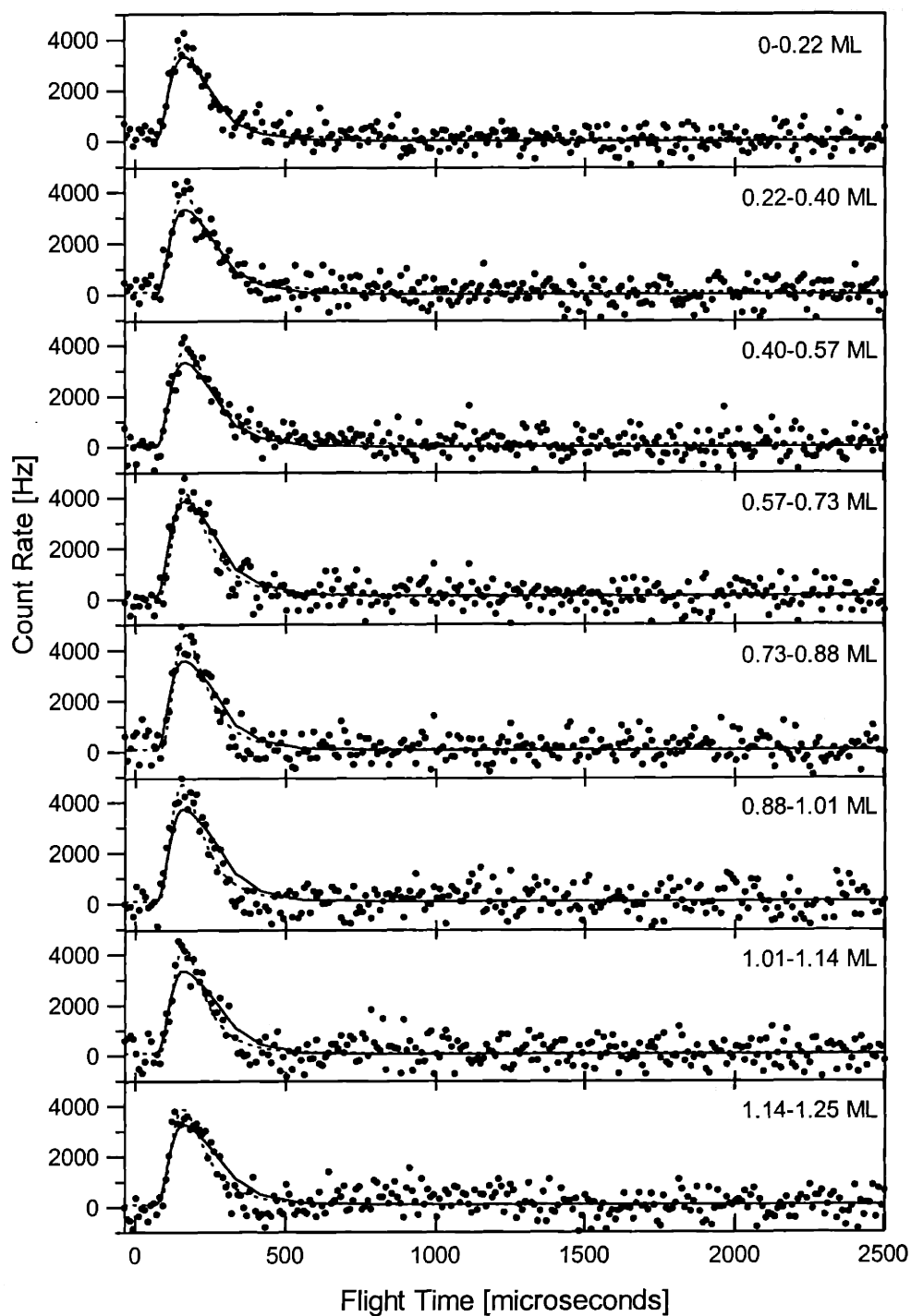
Figure 51 Predicted F atom TOF at $\theta_d = 15°$

Net TOF spectra at m/e=19 and a detector angle θ_d=15°. Solid lines show the predicted F atom distribution given by the forward convolution calculation. Dotted lines show the Maxwell-Boltzmann fit to the data. Data taken from Figure 31.
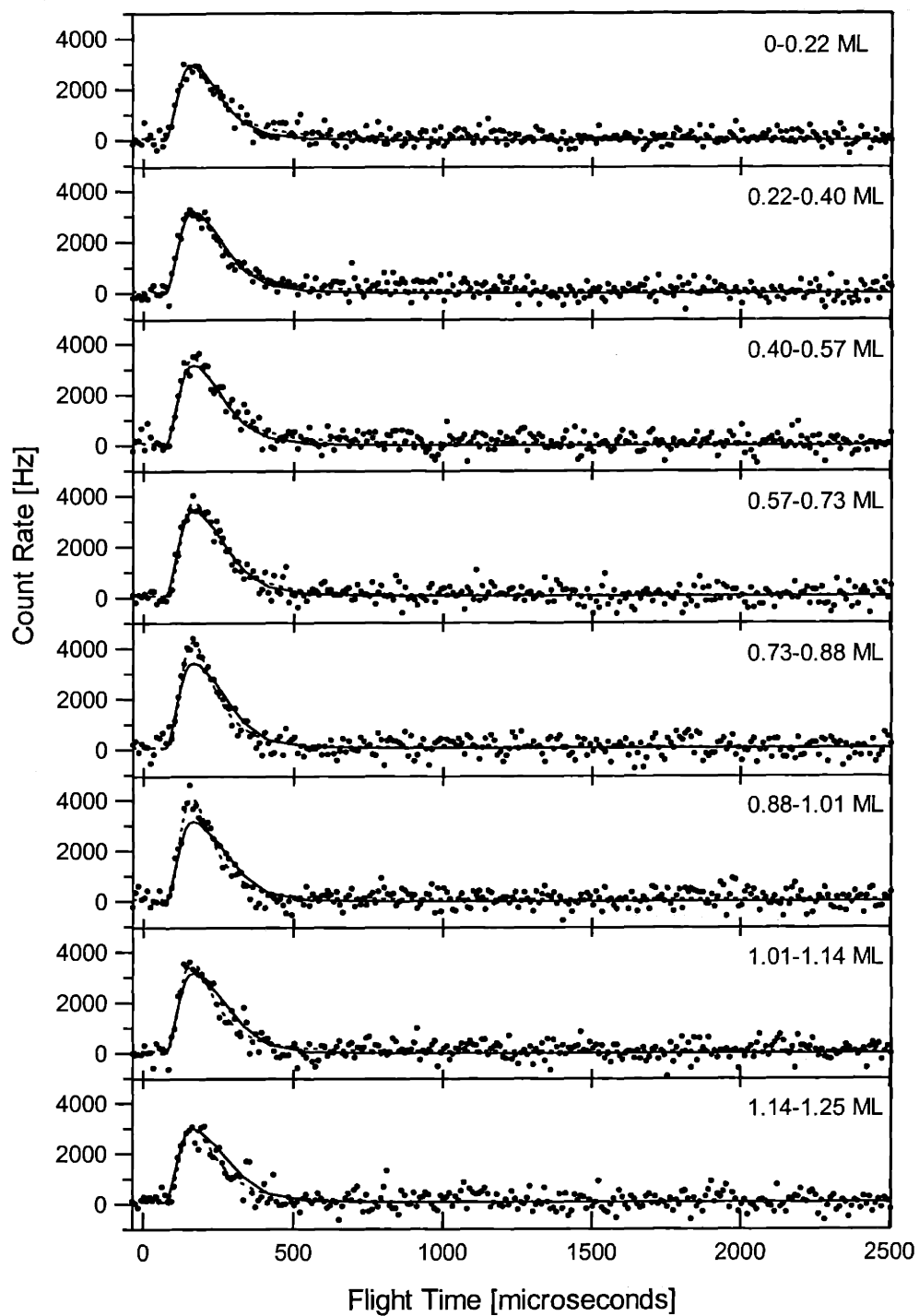
Figure 52 Predicted F atom TOF at $\theta_d = 30°$

Net TOF spectra at m/e=19 and a detector angle θ_d=30°. Solid lines show the predicted F atom distribution given by the forward convolution calculation. Dotted lines show the Maxwell-Boltzmann fit to the data. Data taken from Figure 32.
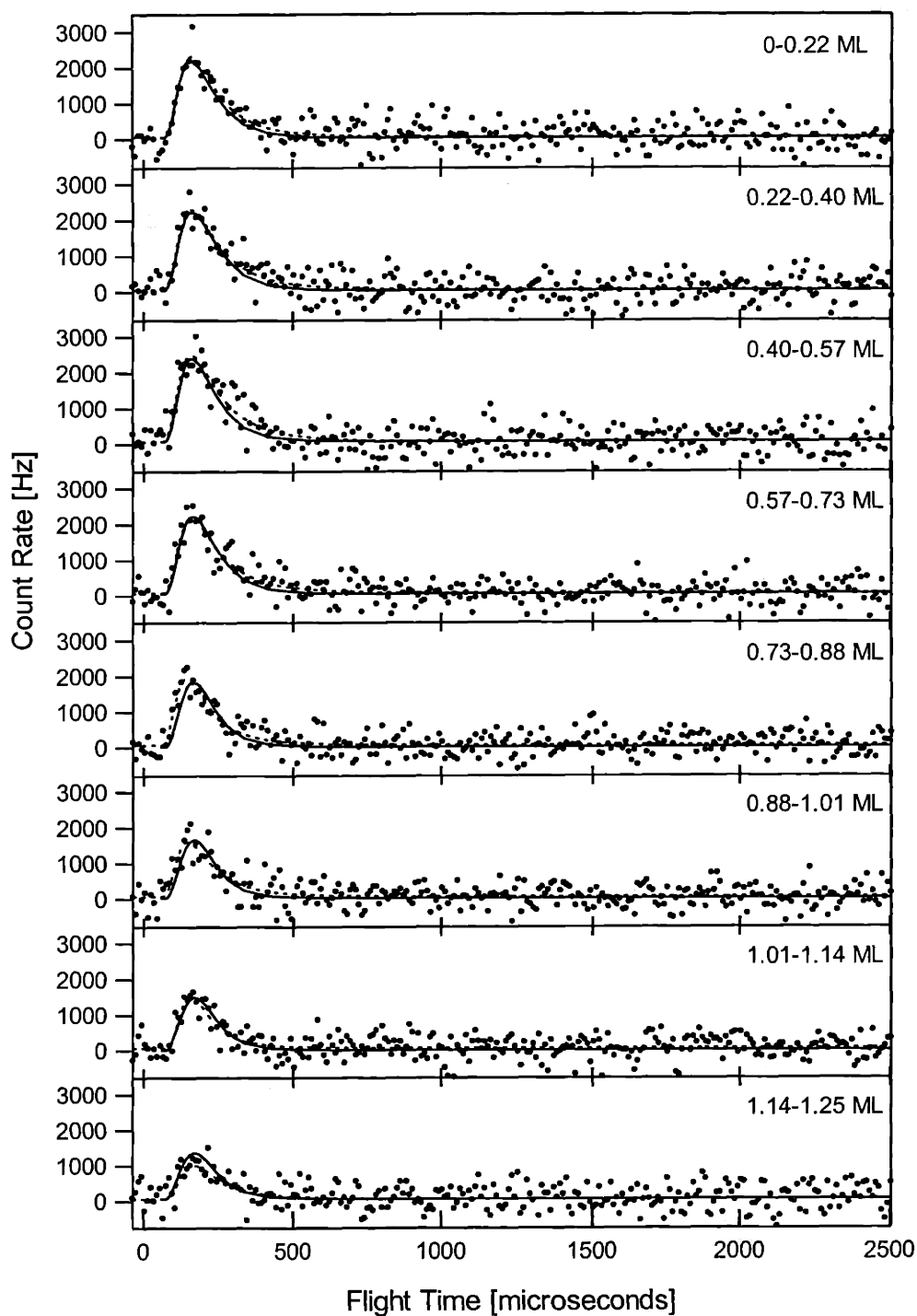
Figure 53 Predicted F atom TOF at $\theta_d = 60°$

Net TOF spectra at m/e=19 and a detector angle θ_d=60°. Solid lines show the predicted F atom distribution given by the forward convolution calculation. Dotted lines show the Maxwell-Boltzmann fit to the data. Data taken from Figure 33.
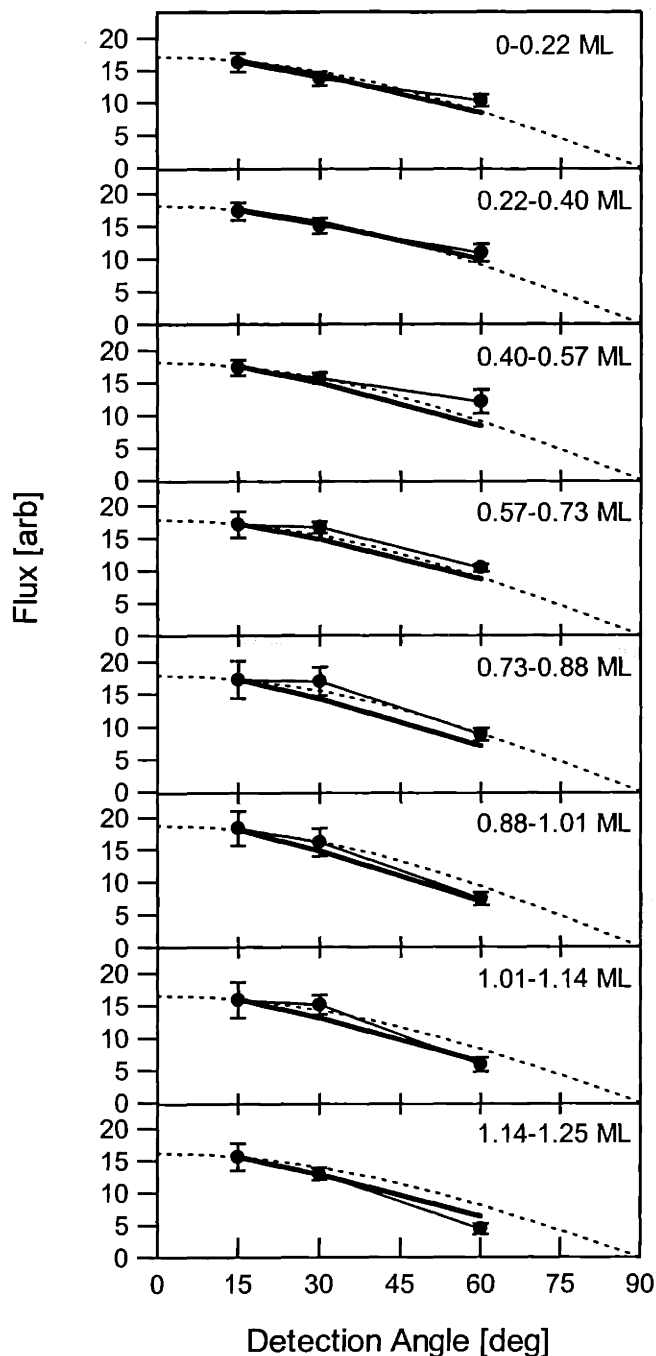
Figure 54 Angular dependence of the flux of F scattered from Si(100)

Scattered flux of F determined from the Maxwell-Boltzmann fit to the data shown in Figures 31, 32, using Eq. (II.2). Flux at each point is normalized to the number of experiments at that detection angle. Dotted line shows a cosine distribution normalized to match the flux at θ_d=15°. Predicted F from XeF dissociation angular distribution shown as a thick solid line, normalized to the observed flux at θ_d=15°. Error bars reflect a 95% confidence limit.
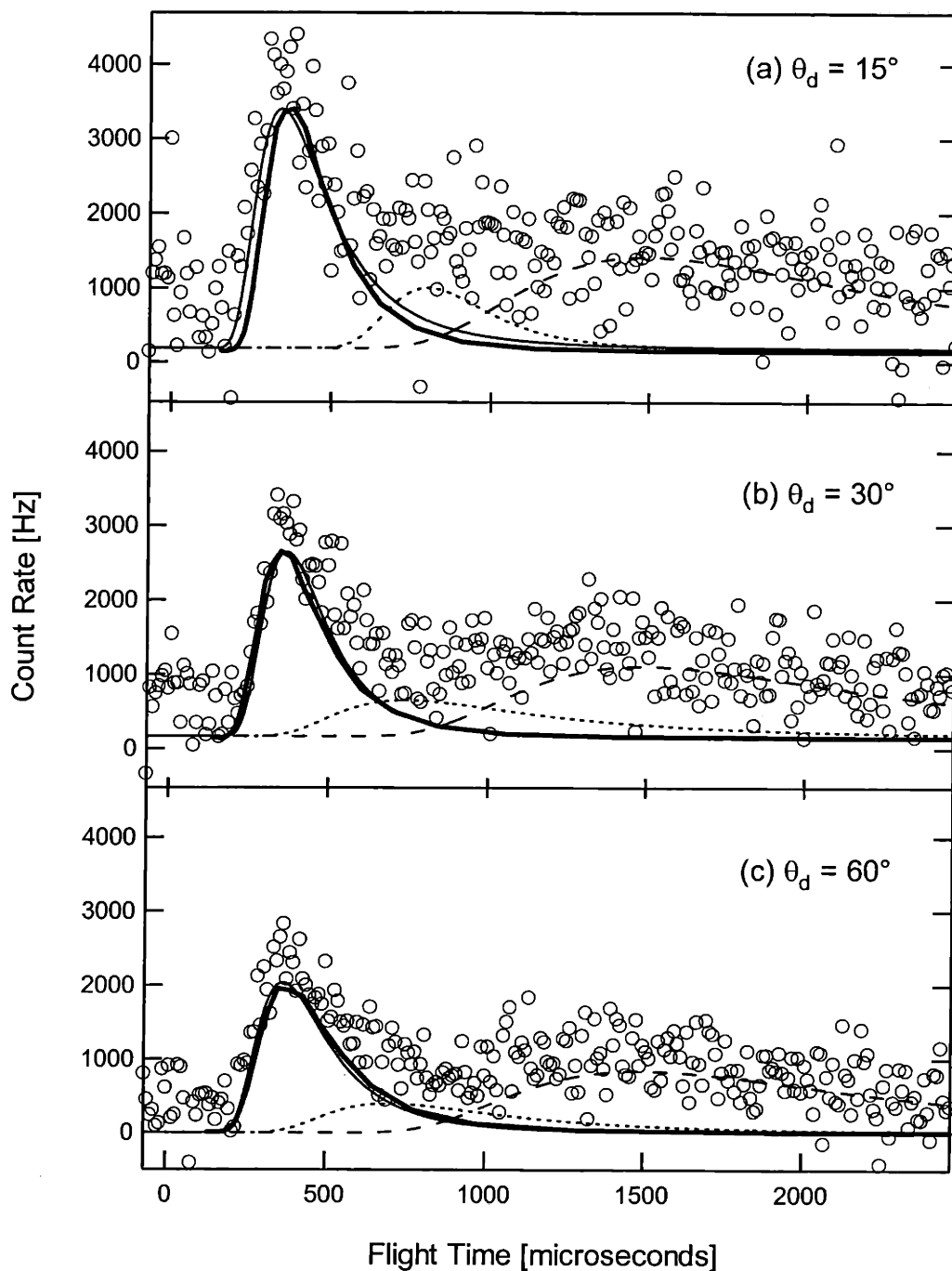
Figure 55 **Predicted Xe atom TOF at 0.22–0.44 ML coverage with maximum XeF cracking subtracted**

Net TOF spectra at m/e=129 for the coverage range 0.22-0.40 ML. The cracking from XeF_2 has been subtracted, as well as the maximum XeF cracking. Thick solid lines show the predicted Xe atom distribution. The Maxwell-Boltzmann fits to the data are shown for the fast feature (thin solid line), medium feature (short dashed line) and slow feature (long dashed line). Data taken from Figures 39, 40, and 41.
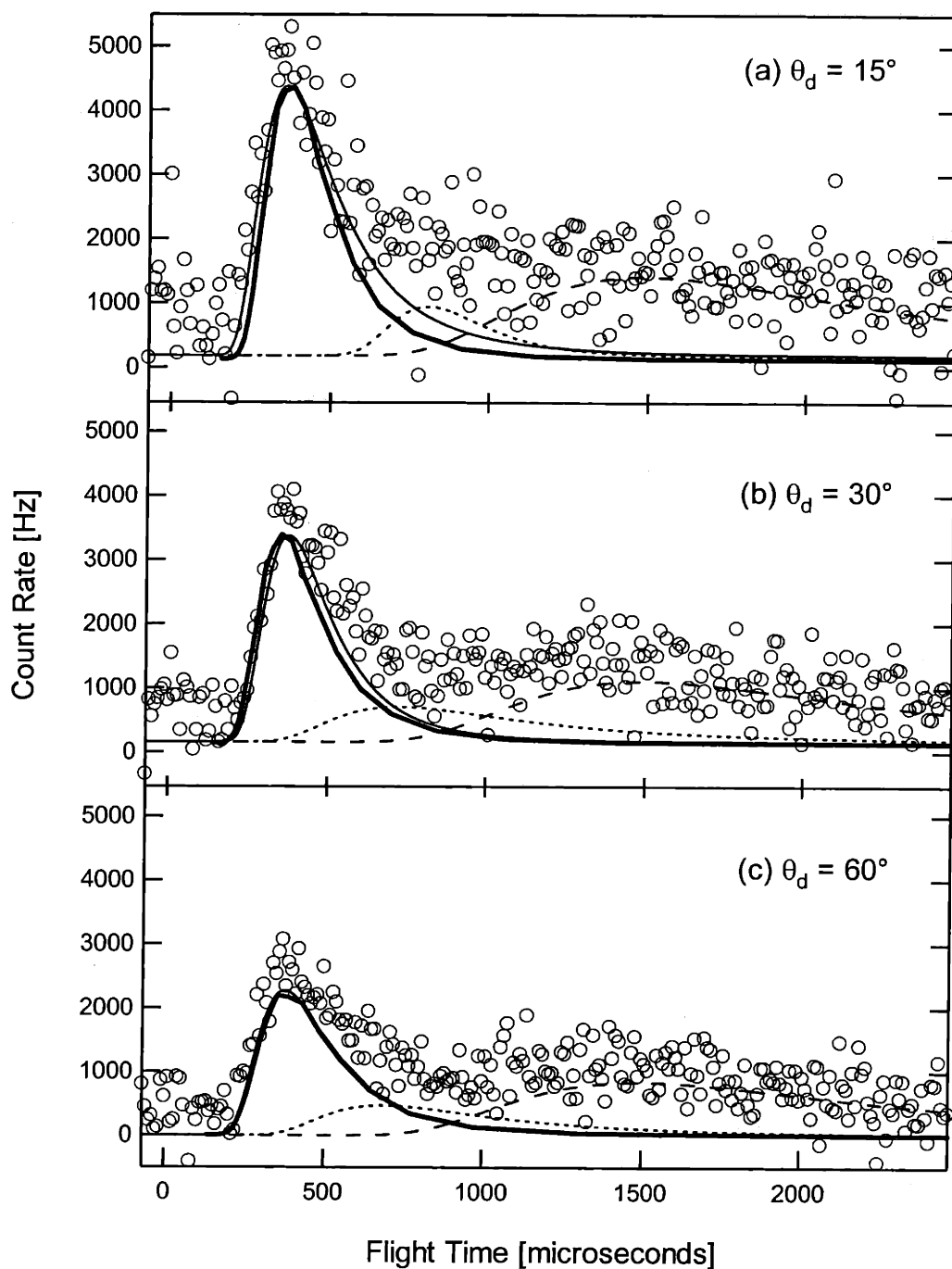
Figure 56 Predicted Xe atom TOF at 0.22 – 0.44 ML coverage with intermediate XeF cracking subtracted

Net TOF spectra at m/e=129 for the coverage range 0.22-0.40 ML. The cracking from XeF_2 has been subtracted, as well as the intermediate XeF cracking. Thick solid lines show the predicted Xe atom distribution. The Maxwell-Boltzmann fits to the data are shown for the fast feature (thin solid line), medium feature (short dashed line) and slow feature (long dashed line). Data taken from Figures 42, 43, and 44.
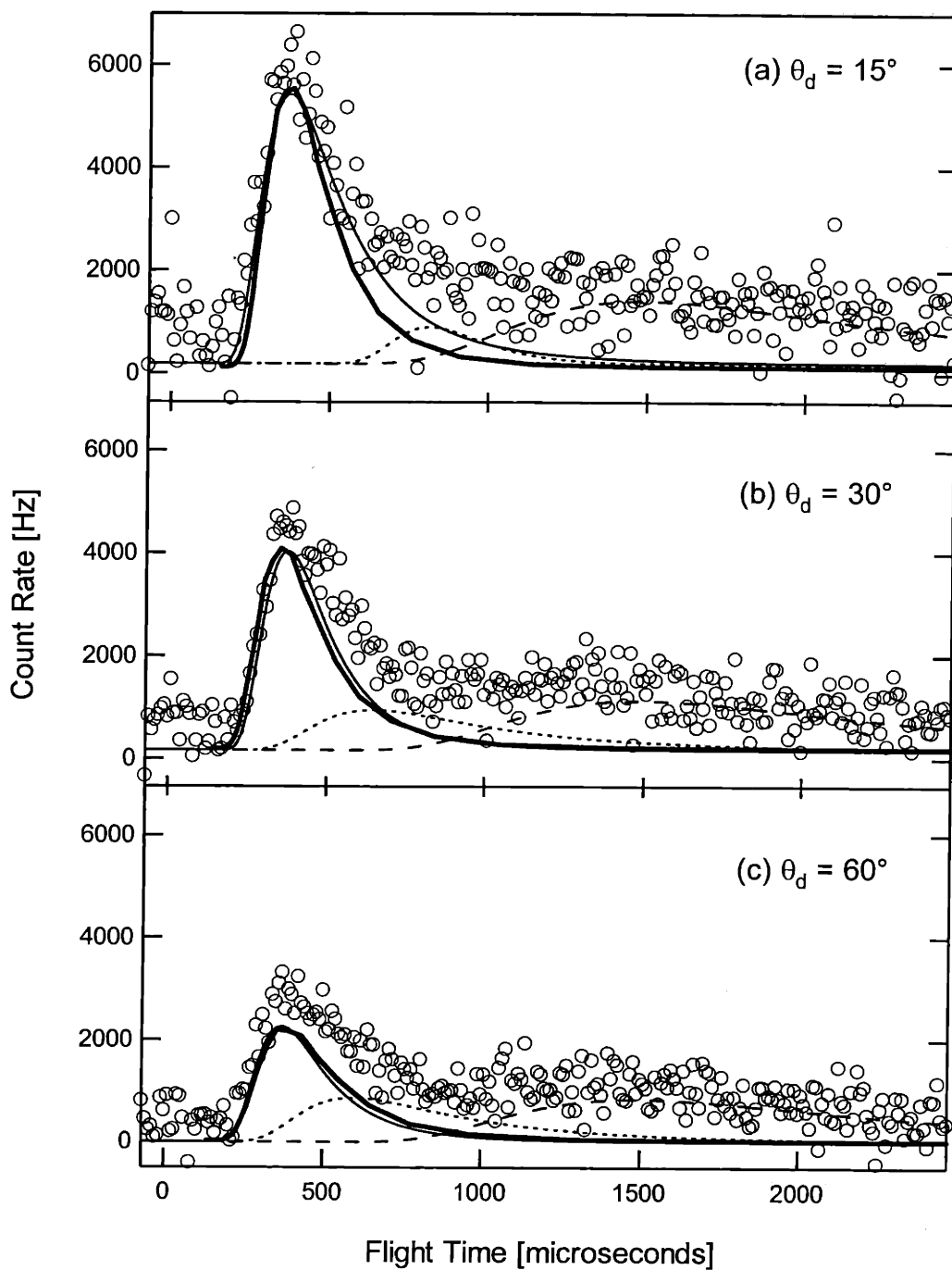
Figure 57 Predicted Xe atom TOF at 0.22 – 0.44 ML coverage with no XeF cracking subtracted

Net TOF spectra at m/e=129 for the coverage range 0.22-0.40 ML. Only cracking from XeF_2 has been subtracted. Thick solid lines show the predicted Xe atom distribution. The Maxwell-Boltzmann fits to the data are shown for the fast feature (thin solid line), medium feature (short dashed line) and slow feature (long dashed line). Data taken from Figures 45, 46, and 47.
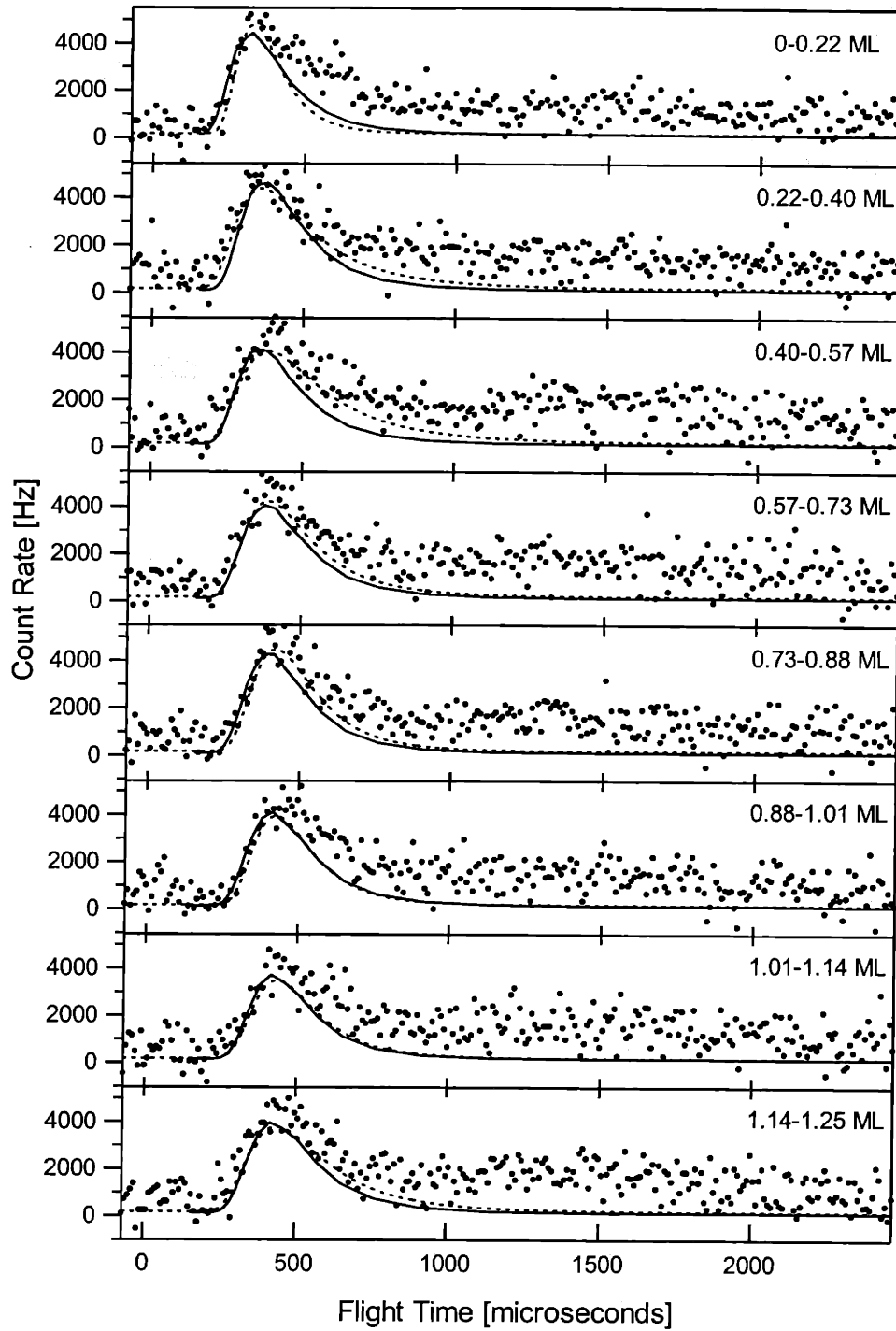
Figure 58 Predicted Xe atom TOF at $\theta_d = 15°$

Net TOF spectra at m/e=129 and a detector angle θ_d=15°. Solid lines show the predicted Xe atom distribution. The dashed line shows the fast feature of the Maxwell-Boltzmann fit to the data. Data taken from Figure 42.
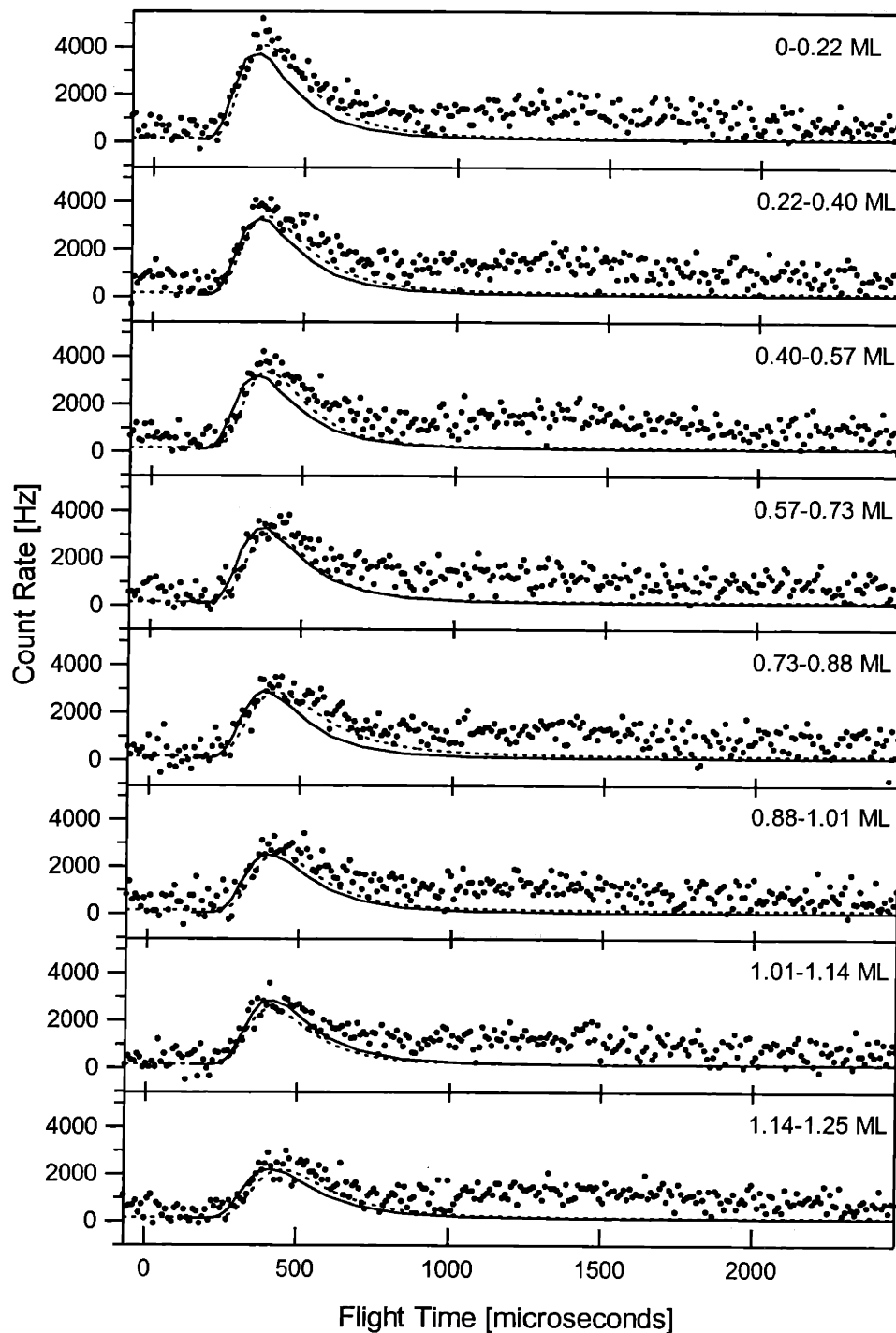
Figure 59 Predicted Xe atom TOF at $\theta_d = 30°$

Net TOF spectra at $m/e=129$ and a detector angle $\theta_d=30°$. Solid lines show the predicted Xe atom distribution. The dashed line shows the fast feature of the Maxwell-Boltzmann fit to the data. Data taken from Figure 43.
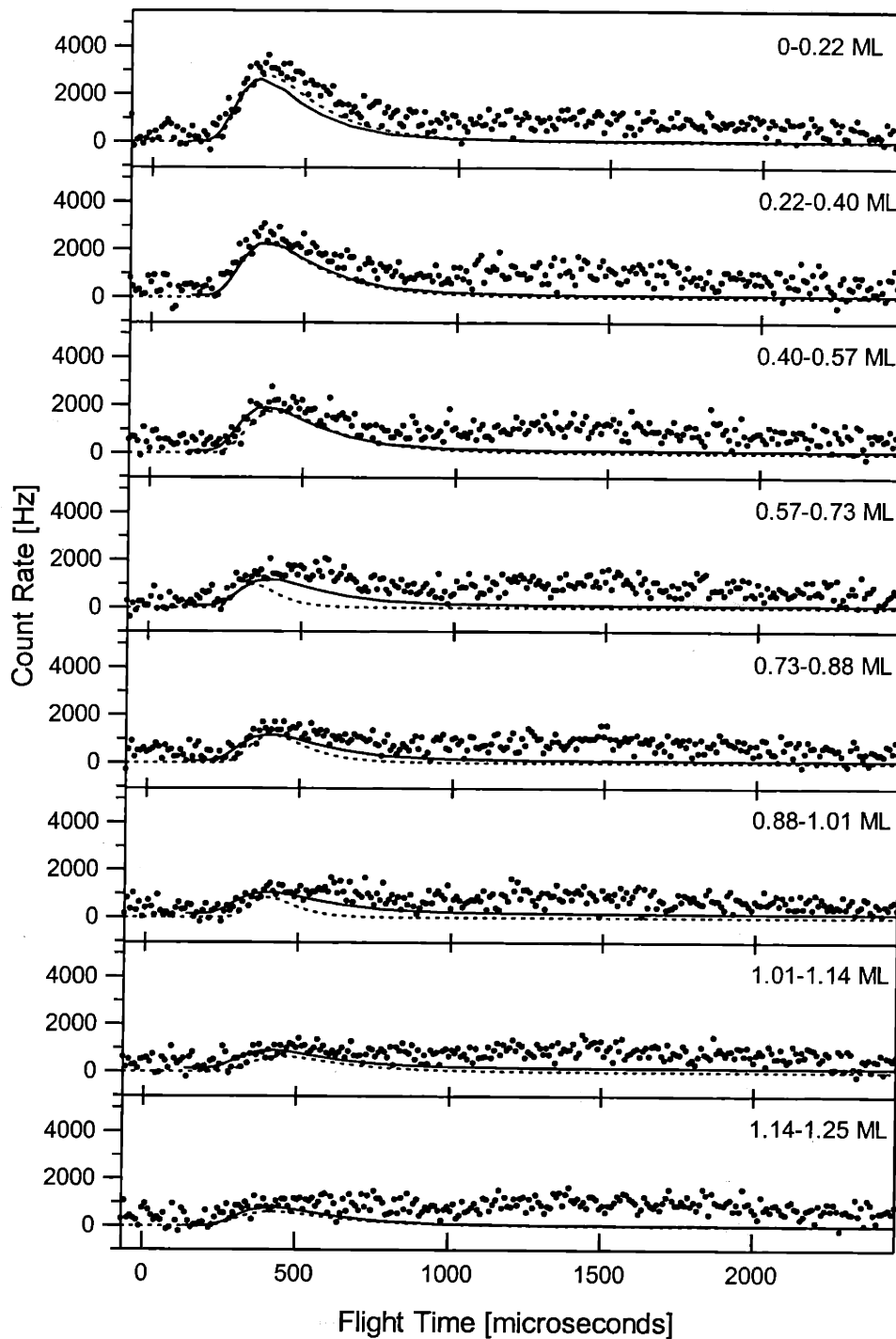
Figure 60 Predicted Xe atom TOF at θ_d = 60°

Net TOF spectra at m/e=129 and a detector angle θ_d=60°. Solid lines show the predicted Xe atom distribution. The dashed line shows the fast feature of the Maxwell-Boltzmann fit to the data. Data taken from Figure 44.
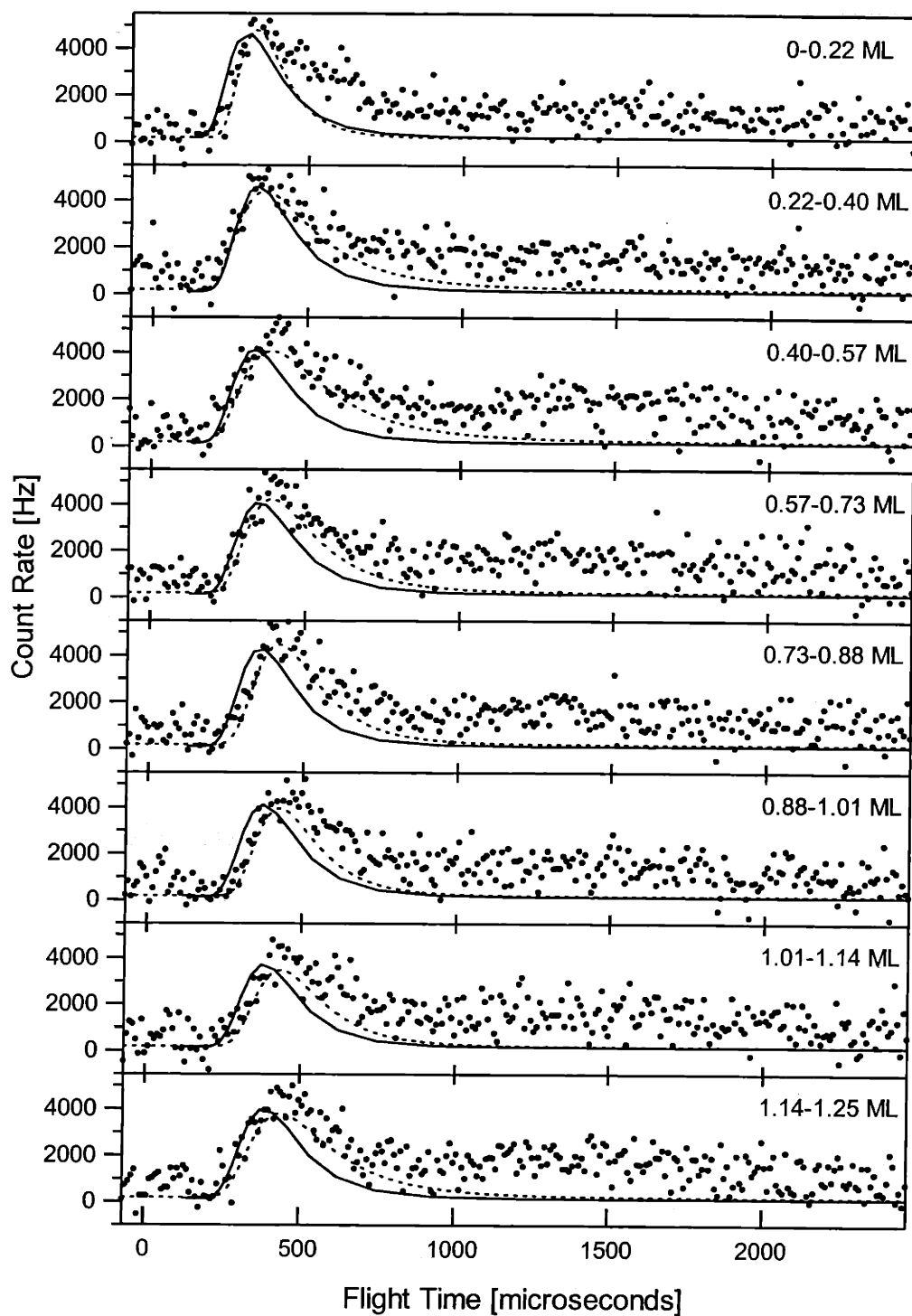
Figure 61 Predicted Xe atom TOF at $\theta_d = 15°$; $\phi = 0-2\pi$

Net TOF spectra at m/e=129 and a detector angle θ_d=15°. Solid lines show the predicted Xe atom distribution for $\phi = 0-2\pi$. The dashed line shows the fast feature of the Maxwell-Boltzmann fit to the data. Data taken from Figure 42.
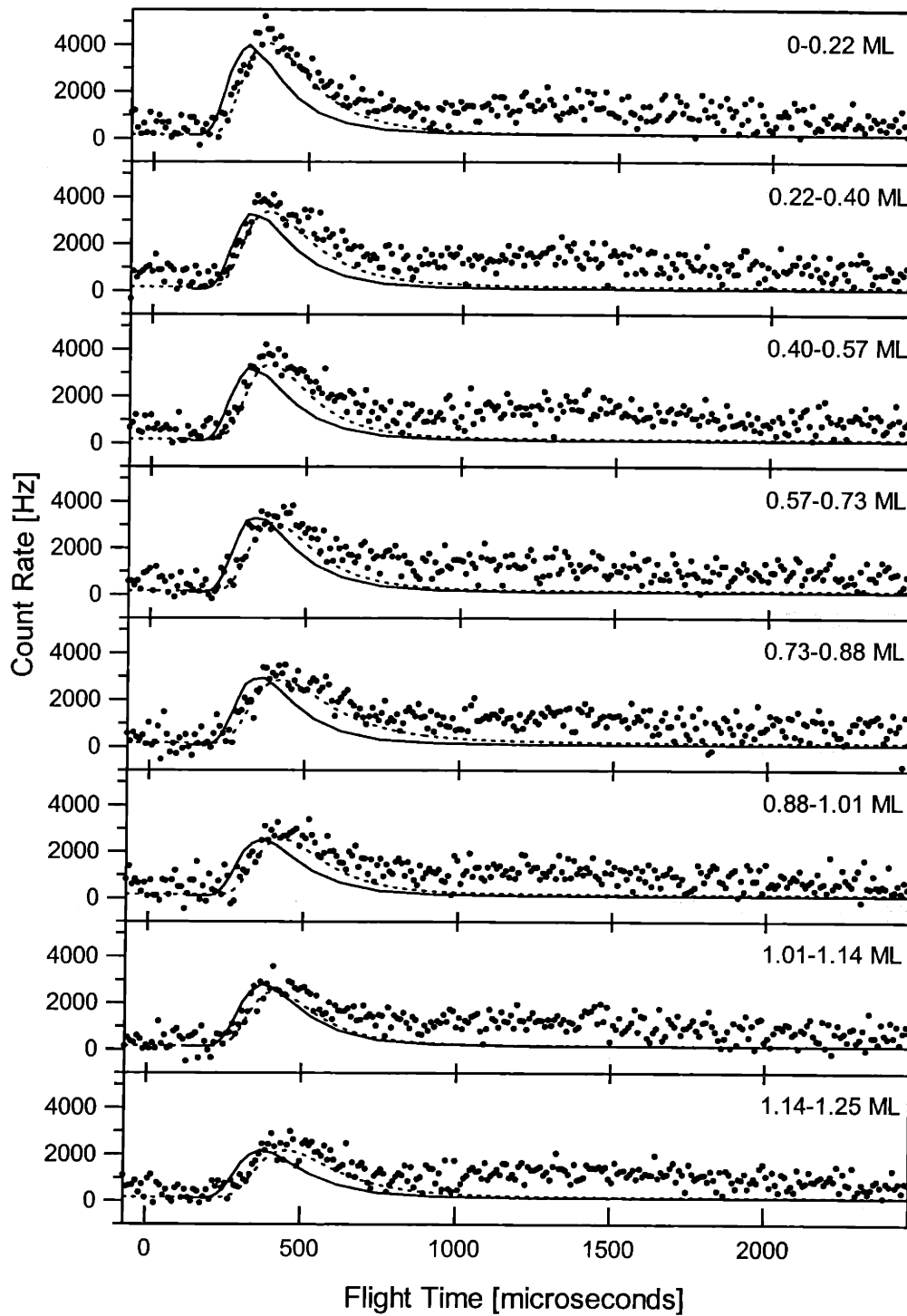
Figure 62 Predicted Xe atom TOF at $\theta_d = 30°$; $\phi = 0-2\pi$

Net TOF spectra at m/e=129 and a detector angle θ_d=30°. Solid lines show the predicted Xe atom distribution for $\phi = 0-2\pi$. The dashed line shows the fast feature of the Maxwell-Boltzmann fit to the data. Data taken from Figure 43.

Figure 63 Predicted Xe atom TOF at at θ_d = 30°; ϕ = 0–2π

Net TOF spectra at m/e=129 and a detector angle θ_d=60°. Solid lines show the predicted Xe atom distribution for ϕ = 0–2π. The dashed line shows the fast feature of the Maxwell-Boltzmann fit to the data. Data taken from Figure 44.

V. Discussion

The interaction of XeF_2 with Si(100) at 150 K has been studied in detail using the time-of-flight (TOF) technique. The main result of the present study is the observation of the TOF and angular distributions of the scattered products of the reaction, which are formed through one of three possible reaction channels. The first reaction channel is unreactive scattering, where the incident XeF_2 scatters from the surface without any bonds being broken or formed. This channel is identified by the detected time-of-flight signal at m/e=167. The unreactively scattered XeF_2 is discussed in Section V.B. The second reaction channel is single atom abstraction, which results in an adsorbed fluorine atom and a liberated XeF fragment. This XeF fragment can survive to reach the detector, where it is identified by the net TOF signal at m/e=148 after cracking from XeF_2 is subtracted. The XeF abstraction product is discussed in Section V.C. Another possible fate for the liberated XeF fragment is gas-phase dissociation, producing a F atom and a Xe atom. This dissociation is strongly suggested by the observation of the net TOF signal at m/e=19. The F and Xe atoms from the gas-phase dissociation of XeF are predicted using conservation of energy and momentum via a forward convolution calculation, as described in detail in Section IV. The F atoms from XeF dissociation are discussed in Section V.D, and the Xe atoms from XeF dissociation are discussed in Section V.E. The last possibility for the fate of the XeF fragment is to undergo a second interaction with the surface, resulting in a second adsorbed F atom and a liberated Xe atom. This reaction channel is termed two-atom adsorption, and is discussed in Section V.F.

In addition to the TOF results, the XeF_2 dissociative chemisorption probability, surface order, and etch product are determined as a function of coverage at a surface temperature of 150

K, similar to the results presented in Chapter 2 for a surface temperature of 250 K. These results are discussed in Section V.A below.

V.A. Dissociative chemisorption probability, etch product, He diffraction results

The dissociative chemisorption probability as a function of coverage for the reaction of XeF_2 with Si(100) at 150 K is determined from thermal desorption measurements and is plotted in Figure 13. The dissociative chemisorption probability starts at around 0.73 ± 0.26 on a clean surface and decreases to around 0.40 ± 0.16 just prior to the onset of etching, where the error bars represent a 95% confidence limit, or $\pm 2\sigma$. These probabilities are slightly lower than those presented in Chapter 2 for a surface temperature of 250 K, which showed a dissociative chemisorption probability of about 0.82 ± 0.14 on a clean surface, decreasing to about 0.54 ± 0.10 just prior to the onset of etching. The dissociative chemisorption probability of XeF_2 on Si(100) can be compared to the dissociative chemisorption of F_2 on Si(100), which decreases from 0.83 ± 0.14 on a clean surface to zero at a coverage of about 1 ML. By contrast, the XeF_2 dissociative chemisorption probability is only weakly dependent on coverage. The relative constancy of a chemisorption probability with coverage is usually interpreted in terms of a long lifetime of an extrinsic precursor, which is a species physisorbed on top of filled sites. An extrinsic precursor diffuses on top of the filled sites until it encounters an empty site, such as a dangling bond, and reacts or desorbs without dissociating. In short, the extrinsic precursor makes it more likely that a XeF_2 molecule will encounter an unoccupied dangling bond and hence, increases the dissociation probability. The substantially greater polarizability of XeF_2 as compared to F_2 suggests that a XeF_2 extrinsic precursor would have a longer lifetime than that of F_2. However, two aspects of the present results cannot be accounted for using a precursor mechanism. First, if a precursor mechanism were active the dissociative chemisorption

probability would be expected to be constant at approximately 1 until all the reactive sites were nearly filled. This is not observed to be the case – rather, the dissociative chemisorption probability decreases steadily over the coverage range 0-0.8 ML, although the large error bars preclude a strict interpretation of this result. Second, if a precursor mechanism were active, the dissociative chemisorption probability would be expected to be higher at 150 K than at 250 K, since the lifetime of XeF_2 on the surface is higher at lower temperatures. This is not observed to be the case – rather, the dissociative chemisorption probability is observed to be slightly lower at 150 K than it is at 250 K. Again, the large error bars preclude a strict interpretation of these results. A second explanation for the relative constancy of the dissociative chemisorption probability is the longer collision time of XeF_2 as compared to F_2. Because it is four times more massive than F_2, XeF_2 spends twice as long as F_2 in the near surface region where it may encounter an unoccupied dangling bond. It is not clear from the present study if both effects or either of them are operative.

Figure 14 shows a plot of the signal intensity at m/e=85, corresponding to SiF_3^+ arising from the etch product SiF_4, as a function of coverage during exposure of XeF_2 to Si(100) at 150 K. The signal intensity remains zero or near zero below 0.8 ML coverage. Above 0.8 ML coverage, there is a slight increase in the intensity of the signal, and after about 1.2 ML coverage the signal increases dramatically.

The evolution of the etch product with respect to coverage can be compared to the helium diffraction specular intensity as a function of coverage, shown in Figure 15b. The intensity of the specular feature decays rapidly during the initial exposure of the surface to XeF_2. This initial loss of intensity can be understood in terms of fluorination of the surface at random sites. The presence of a F atom bonded to a dangling bond changes the interaction potential of the He atom

with that surface unit cell, thereby making it different from the surrounding unit cells that do not yet include a F atom. The surface order is disrupted, thus resulting in a loss of coherency of the diffracted He beam. The specular intensity reaches a minimum at about 0.3 ML and then begins to recover. The specular intensity fully recovers around 0.7-0.8 ML, at which point etching is observed to begin, and then begins to decay rapidly between 0.8 − 1.0 ML, and reaching a minimum value at 1.1 ML, at which point the intensity of the observed etch product begins to increase dramatically. The 0.7-0.8 ML recovery at 150 K is lower than the 0.9 ML recovery reported in Chapter 2 for a surface temperature of 250 K. The fact that the 150 K recovery occurs at a lower coverage than the 250 K recovery is likely due to the presence of physisorbed XeF_2 on the surface at 150 K. Physisorbed XeF_2 disrupts the periodicity of the fluorinated surface unit cell, resulting in a loss of specular intensity.

The suggested presence of physisorbed XeF_2 on the surface at >1.0 ML coverage is in contrast to the results at 250 K, which showed no such evidence. The possible effect of physisorbed XeF_2 on the reaction can also be seen in the unreactively scattered XeF_2, as described below.

V.B. Unreactive scattering

Previously, for the interaction of high-energy (E_i=6.3 kcal/mol) XeF_2 with Si(100) at 250 K, XeF_2 was observed to unreactively scatter from the surface via both a direct inelastic (DI) scattering channel and a trapping-desorption (TD) scattering channel.[1] The DI/TD branching ratio was found to decrease dramatically with increasing coverage, in contrast to the observed DI/TD branching ratio for inert Xe scattered from the Si(100) surface over the same coverage range, which increased slightly with increasing surface coverage.

In the present experiment, performed at 150 K surface temperature, a combination of factors including lower surface temperature, lower incident beam energy, and a decrease in the flux of unreactively scattered XeF_2, has precluded a similar identification of the DI and TD features. That is, for the present results at m/e=167, only one component is apparent. The average energy of the unreactively scattered XeF_2 is 1.49±0.42 kcal/mol. This average energy matches the incident energy of 1.40±0.05 kcal/mol, but is significantly higher than the thermal energy, which is 0.7 kcal/mol at 150 K, suggesting that the majority of the observed XeF_2 is due to a direct scattering mechanism.

Shown in Figure 20 is the angular distribution of the XeF_2 flux. It can be seen that the distribution is essentially cosine at all coverages, within the errors (95% confidence limit) of the measurement. Note that the error bars reflect the uncertainty that is a result of the least-squares fitting procedure as described in Appendix B, but do not reflect the assumptions which are built into those fits. Specifically, the flow velocity, temperature, and baseline of each fit are fixed as described in detail in Section III.D, and any potential variance in those parameters does not contribute to the propagated error.

Shown in Figure 21 is the XeF_2 flux with respect to coverage at the three scattering angles. The flux of XeF_2 decreases with increasing coverage at all measured scattering angles. This is in contrast to the earlier observed results at 250 K surface temperature, which showed that the total flux, calculated by summing the flux at each scattering angle weighted by the Jacobian, $\sin\theta_d$, increased monotonically with increasing coverage. The increase in XeF_2 flux with increasing coverage at 250 K was explained by the fact that the dangling bonds are far more reactive than any other surface reactive site, and on a clean surface the concentration of dangling bonds is at its highest. By contrast, on a fluorinated surface there are fewer dangling bond reactive sites and hence decreased reactivity, which results in an increased flux in the unreactively scattered XeF_2. Although a calculation of the total flux for the data taken at 150 K is not possible because data were only taken at a limited number of scattering angles, the fact that the flux decreases with increasing coverage at all three scattering angles strongly implies that the total flux decreases as well. This discrepancy could be due to two possible causes. First, it is possible that the angular distribution at 150 K is peaked in such a way that the three detection angles used actually miss the bulk of the unreactively scattered XeF_2. This possibility is considered unlikely, given that both the DI and the TD XeF_2 angular distributions observed at 250 K were quite broad. The more likely explanation is the larger molecular adsorption probability of XeF_2 at 150 K than at 250 K because XeF_2 physisorbs to the surface. Consequently, the dynamics changes as the coverage increases. That is, the energy transfer of incident XeF_2 to a physisorbed XeF_2, or to a fluorinated surface, is more efficient, resulting in a greater trapping probability. At higher coverages there is a comparatively greater amount of physisorbed XeF_2 and fluorine bound to the dangling bonds on the surface, resulting in the observed decrease in unreactively scattered XeF_2 with increasing coverage.

V.C. Single atom abstraction

Single atom abstraction is a novel gas-surface scattering mechanism which has been only recently demonstrated for the interactions of F_2 and XeF_2 with Si(100) by the observation of the TOF signal arising from scattered F and XeF respectively. This reaction pathway is energetically allowed due to the high F-Si bond strength.

The angular distribution of the XeF flux is shown in Figure 26. The angular distribution is cosine-like on a clean surface, and becomes more peaked towards normal on a fluorinated surface. This changing angular distribution is consistent with the combined effects of steric hinderance and molecular steering. That is, on a fluorinated surface the local environment of the reactive site is more crowded due to the neighboring adsorbed fluorine atoms. The attractive interaction potential between the fluorine in a XeF_2 molecule and a reactive site on the surface could "steer" the XeF_2 into a more favorable perpendicular orientation prior to the reaction, resulting in an ejected XeF angular distribution which is more peaked towards the surface normal. The notion that the XeF_2 is oriented in a perpendicular orientation prior to the reaction is consistent with the results of the momentum matching calculation, which suggests a transition state with the fluorine atom pointed into the vacuum. That is, if the range of allowed orientations of the XeF fragment is expanded to include orientations where the F atom is pointing towards the surface, the calculation cannot successfully predict the observed Xe atom TOF distributions.

The average energy of XeF as a function of scattering angle and coverage is shown in Figure 29. The average energy at $\theta_d=15°$ decreases from ~12 kcal/mol on a clean surface to ~7 kcal/mol at a coverage of 1.3 ML. Similarly, the average energy at $\theta_d=30°$ decreases from ~10 kcal/mol on a clean surface to ~7 kcal/mol at a coverage of 1.3 ML, and the average energy at $\theta_d=60°$ decreases from ~8 kcal/mol on a clean surface to ~6 kcal/mol at a coverage of 1.3 ML.

The average energy at all angles decreases with increasing coverage, a trend observed earlier at 250 K.[1] However, the fact that the average energy decreases with increasing detector angle at all coverages is a trend that was not observed previously for XeF.

The fact that the translational energy of the XeF decreases with increasing coverage and increasing angle could be a result of a changing interaction potential. That is, if the potential energy surface of this reaction changes substantially with coverage, then it is possible that less of the reaction exothermicity is partitioned to translational excitation of XeF at higher coverages and scattering angles. However, the decrease in the translational energy of the abstraction product with increasing coverage is not observed for the reactively scattered F atoms arising from the interaction of F_2 with Si(100). Given the similarities of the two reactions, one would expect such a trend to be evident for both reactants. Another possibility is that the decrease in XeF translational energy is caused by interactions with a neighboring adsorbed fluorine atom, which slows the exiting XeF fragment. This interaction is consistent with the larger size of XeF (~4 Å in length) compared to F (~1.5 Å in diameter), and is also consistent with the fact that the XeF detected at $\theta_d=60°$ is slower than the XeF detected at $\theta_d=15°$ and 30°. That is, if the XeF is ejected at a more grazing scattering angle, it will have a greater interaction with the neighboring adsorbed fluorine atoms, and will therefore be slower.

The observation that the translational energy of the abstraction product (between 6-12 kcal/mol) is only a small fraction of the exothermicity of the reaction (~90 kcal/mol) is consistent with the idea of an attractive potential. Also known as an "early barrier" potential, this type of potential energy surface was first described by Evans and Polanyi for gas phase reactions[24]. Typically, the products of a reaction of this nature have low translational energy and high vibrational energy. Strictly speaking the "early barrier" potential predicts only that the Si-F

bond will be vibrationally excited, but the fact that XeF dissociation occurs indicates that part of the reaction exothermicity is partitioned into vibrational excitation of the XeF fragment.

V.D. F atoms from XeF dissociation

The observation of fairly energetic F atoms provides direct evidence for the gas-phase dissociation of excited XeF. The TOF distributions of the observed F atoms are well described by the results of a forward convolution calculation, which uses as inputs the observed XeF velocity and angular distribution, and a number density Maxwell-Boltzmann energy distribution for the center of mass energy, E_{CM}, with an average energy of 6.2 kcal/mol.

The angular distribution of the flux of F atoms at the eight coverage ranges is shown in Figure 34. The angular distribution becomes slightly more peaked towards normal with increasing coverage, following the trend observed for the angular distribution of the XeF. This similarity is consistent with the conclusion that the observed F atoms arise from XeF dissociation.

The average energy of the F atoms is shown in Figure 37 and is essentially constant as a function of coverage and detection angle. Although there appears to be an increase in the translational energy at $\theta_d=60°$ between 0.9-1.0 ML, a conclusive interpretation of this result is precluded by the low signal to noise ratio of those TOF spectra.

V.D.1. Center of mass energy distribution

The center of mass energy distribution $P(E_{CM})$ shown in Figure 50 can give insight as to the energy levels involved in the dissociation, shown in Figure 1. Recall from the discussion in Section I that dissociation could occur either directly via excitation onto the repulsive A state, or simply by excitation on the ground state manifold into rovibrational states lying above the dissociation limit. Electronic excitation to the B or C states followed by radiative relaxation is

most likely energetically inaccessible, as discussed in Section I. The energy gap between the minimum in the ground state well and the repulsive A state as given by the Morse potentials based on parameters from References 5 and 7 is ~27 kcal/mol, leaving ~24 kcal/mol for E_{CM}. If excitation to the repulsive A state were significant, one would expect $P(E_{CM})$ to peak at energies approximately corresponding to the calculated energy gap. That is, $P(E_{CM})$ would be expected to peak at ~27 kcal/mol, whereas in reality it is observed to peak near zero energy, suggesting that direct excitation on to the repulsive A state does not play a significant role in the gas phase dissociation of XeF. Additionally, the excitation from the ground state to the repulsive A state requires a spin flip, and is therefore a non-adiabatic transition. Therefore, the results of the present study suggest that the primary pathway for XeF dissociation is excitation into rovibrational states that are above the dissociation threshold of the ground electronic state.

It is remarkable that the same center of mass energy distribution $P(E_{CM})$ can reproduce the observed F atom TOF distributions at all angles and coverages, even past the onset of etching. Recall from Section 1 that the exothermicity of atom abstraction that occurs at a dangling bond reactive site is approximately twice as large as compared to atom abstraction when a Si-Si σ bond is broken. The fact that $P(E_{CM})$ does not change as a function of coverage, even past the onset of etching, suggests that XeF is produced primarily by reaction with the dangling bonds, not from a reaction that breaks a Si-Si σ bond. If, as suggested by these results, atom abstraction does not in general break Si-Si σ bonds, then the primary method of Si-Si σ bond breakage is two-atom adsorption.

V.E. Xe atoms from XeF dissociation

The results presented in Section III.G. show that the TOF spectra measured at m/e=129 are well fit by three Maxwell-Boltzmann distributions, fast, medium and slow (thermal). It is

found that the TOF distributions of Xe from XeF dissociation that are predicted using the forward convolution calculation match the fast feature of the observed m/e=129 TOF spectra. Changing the range of XeF orientations in the forward convolution calculation has a noticeable effect on the ability of the calculation to correctly predict the observed net m/e=129 TOF distributions. That is, if the calculation includes orientations with the F atom pointing towards the surface, the forward convolution calculation is unable to correctly predict the observed Xe TOF distributions at some coverages, whereas if the calculation includes only those orientations where the F atom is pointing into the vacuum, the predicted Xe TOF distributions match the observed net m/e=129 TOF distributions. The results of the calculation therefore suggest that the geometry of the transition state is such that the F atom points into the vacuum, which is consistent with the notion of molecular steering in which the XeF_2 is steered into a more favorable perpendicular alignment prior to the reaction. The results of the calculation are consistent with the fact that since the dissociation is expected to occur on a time scale of a vibrational period, much faster than a rotational period, the XeF is expected to dissociate before any significant rotation can occur. Since the XeF dissociates quickly, it is expected to be at most a few angstroms away from the surface when it dissociates. Specifically, the energy of the ground vibrational state in the ground electronic state is found using the parameters of Ref. 5 to be 214 cm^{-1}, including anharmonicity, which gives a vibrational period of 1.6×10^{-13} s. The average velocity of the XeF fragment at θ_d=15° at 0-0.22 ML coverage is approximately 770 m/s, which yields a value of 1.2 Å traveled in one vibrational period. At this small distance from the surface, one might expect the dissociation to be affected by the nearby presence of the surface. However, the forward convolution calculation, which is based explicitly on the fact that the dissociation is an isolated gas-phase process, successfully predicts the observed F atom and

Xe atom TOF distributions at all angles and coverage ranges. Thus, the current analysis suggests that the surface does not have a significant effect on the dissociation event.

V.E.1 Uncertainty in Xe^+:XeF^+ cracking ratio

Because the Xe^+:XeF^+ cracking ratio is not known, the net Xe TOF signal is found by subtracting the net XeF TOF signal multiplied by either the maximum (1.0:1), intermediate (0.5:1), or minimum (0.0:1) cracking ratio. It is not known a priori which of these three cracking ratios is closest to the true cracking ratio, but it is known that the true cracking ratio must lie somewhere between the maximum and minimum cracking ratio.

The flux and average energy of the fast feature of the m/e=129 TOF distributions are determined by integrating the flux distribution as described by Eq. (II. 2) and Eq. (II. 4) in the experimental section, with the flux normalized by the number of experiments taken at each angle. Figure 64 shows the angular distribution of the flux of the fast Xe feature at the eight coverage ranges, along with the Xe angular distribution predicted by the forward convolution calculation, and a cosine distribution superimposed for comparison. The angular distribution of the flux of the fast feature of the net m/e=129 TOF spectra is shown for the maximum, intermediate, and minimum Xe^+:XeF^+ cracking ratios, and these results are also shown in Figure 65 plotted with respect to coverage at each of the detection angles. The error bars on the flux are given by the propagated error from the fit parameters as described in Appendix B. In general, for the intermediate and minimum cracking values, the predicted angular distribution of Xe from XeF dissociation matches the observed angular distribution of the fast Xe feature quite well, although there are slight disagreements at the 0-0.22 ML coverage range, where the observed angular distribution is flatter than predicted, and at the 0.57-0.73 ML coverage range, where the observed distribution is slightly more peaked towards normal than predicted. This similarity

supports the identification of the fast Xe feature as being due to XeF dissociation. The observed trend in the angular distribution, that it becomes more peaked at higher coverages, is similar to the observed trend for the XeF angular distribution, shown in Figure 26. This is consistent with the fact that the Xe is the heavy body in the dissociation, and its trajectory after the dissociation is therefore expected to be similar to the initial XeF trajectory. The results of the maximum $Xe^+:XeF^+$ cracking ratio, however, do not agree as well with the predicted Xe angular distributions. It is likely, therefore, that the true $Xe^+:XeF^+$ cracking ratio is closer to the intermediate or minimum value.

It should be noted that the fast, medium and slow TOF features are quite broad. In fact, the tail of the fast feature significantly overlaps the medium feature, resulting in a certain amount of ambiguity that is not reflected in the reported error bars. This overlap can be seen in Figure 55, which shows the fits to the net Xe signal at the three detection angles after the maximum XeF cracking has been subtracted. It is evident that the tail of the fast feature still has a significant amount of signal at the maximum of the medium feature. Thus, with only a minimal change in the overall fit, a decrease or increase of the flux of the medium feature can be accounted for by broadening or narrowing the fast feature. The angular distributions of the flux of the three Xe features should be viewed with this uncertainty in mind.

The angular distribution of the average energy of the fast Xe feature is shown in Figure 66, and the average energy is also plotted with respect to coverage in Figure 67. The average energy of the fast Xe feature is reasonably insensitive to the $Xe^+:XeF^+$ cracking ratio used, and both the absolute value of the energy and the trend with respect to coverage are similar to the observed XeF energy at each detection angle. That is, in the 0-0.22 ML range, the angular distribution of the energy is peaked towards normal, and then it becomes more isotropic at the

higher coverages, although the larger error bars at higher coverage preclude a strict interpretation. The average energy decreases with increasing coverage at all detection angles, unaffected by the XeF cracking ratio. The overall trend of the energy with respect to coverage is quite similar to the energy of the XeF with respect to coverage, shown in Figure 29. The average energy decreases monotonically, from ~12 kcal/mol (θ_d=15°) or ~10 kcal/mol (θ_d=30°) or ~9 kcal/mol (θ_d=30°) on a clean surface to ~6-7 kcal/mol (all angles) at higher coverages. At θ_d=60° the uncertainty in the average energy is larger than at the other angles, but the trend is still apparent. This similarity mirrors the observed similarity in the angular distribution of the flux. This similarity is consistent with the fact that the Xe is the heavy body in the dissociation, and its trajectory after the dissociation is therefore expected to be similar to the initial XeF trajectory. The observed similarities between the flux and average energy of the fast Xe feature and the XeF support the results of the forward convolution calculation, which identifies the fast Xe feature as being due to Xe from XeF dissociation. The observed similarities also give some credence to the assumption, used in the forward convolution calculation, that the velocity distribution of the XeF that dissociates can be approximated using the velocity distribution of the XeF that does not dissociate.

It should be noted that the identification of the fast feature as consistent with Xe from XeF dissociation does not preclude the possibility that two-atom adsorption also contributes to the fast feature. In other words, it is possible that the fast Xe feature is made up of *both* Xe from XeF dissociation and also Xe from 2-atom adsorption. While this possibility cannot be ruled out, the fact that the observed fast Xe TOF distribution is well described by the results of the forward convolution calculation suggests that the effect, if any, is small.
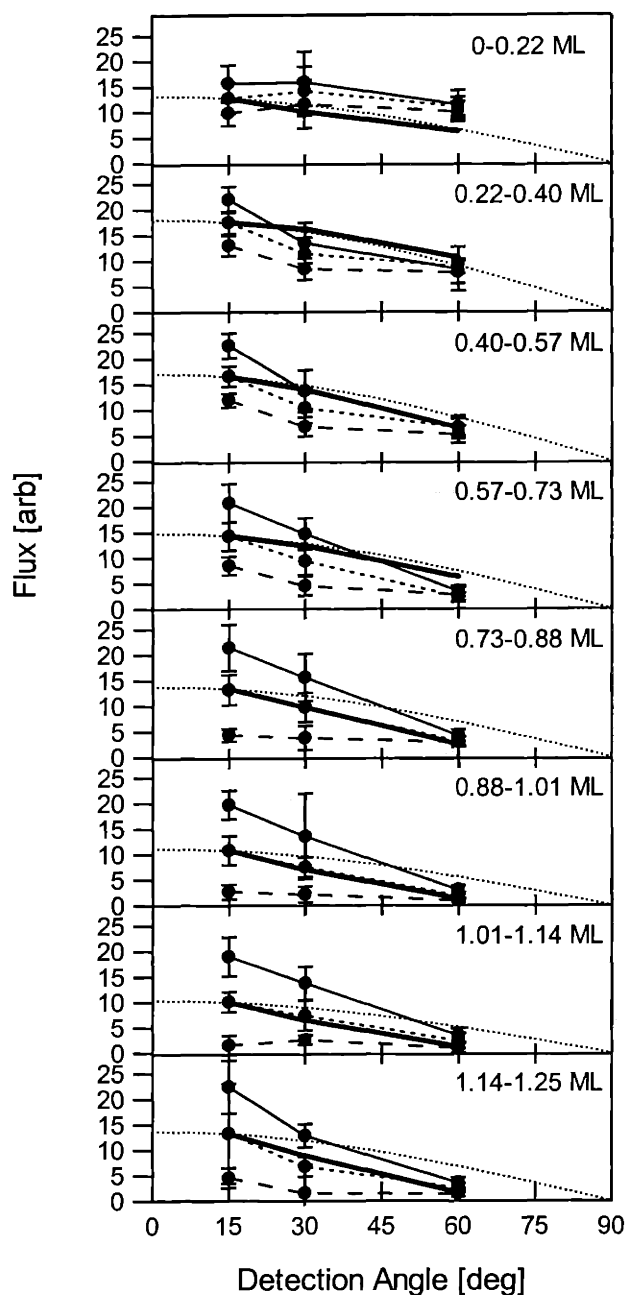
Figure 64 Angular dependence of the flux of the fast Xe feature

Scattered flux of the fast Xe feature determined from the Maxwell-Boltzmann fit to the data in Figures 39-47 for the XeF cracking ratios 1.0:1 (long dashed line), 0.5:1 (short dashed line) and no XeF cracking subtracted (solid line) using Eq. (II.2). Flux at each point is normalized to the number of experiments at that detection angle. Cosine distribution is shown as a dotted line, normalized to the flux at $\theta_d=15°$ and intermediate XeF cracking. Predicted Xe angular distribution from the forward convolution calculation is shown as a thick solid line, normalized to the flux at $\theta_d=15°$, and intermediate XeF cracking. Error bars reflect a 95% confidence limit.
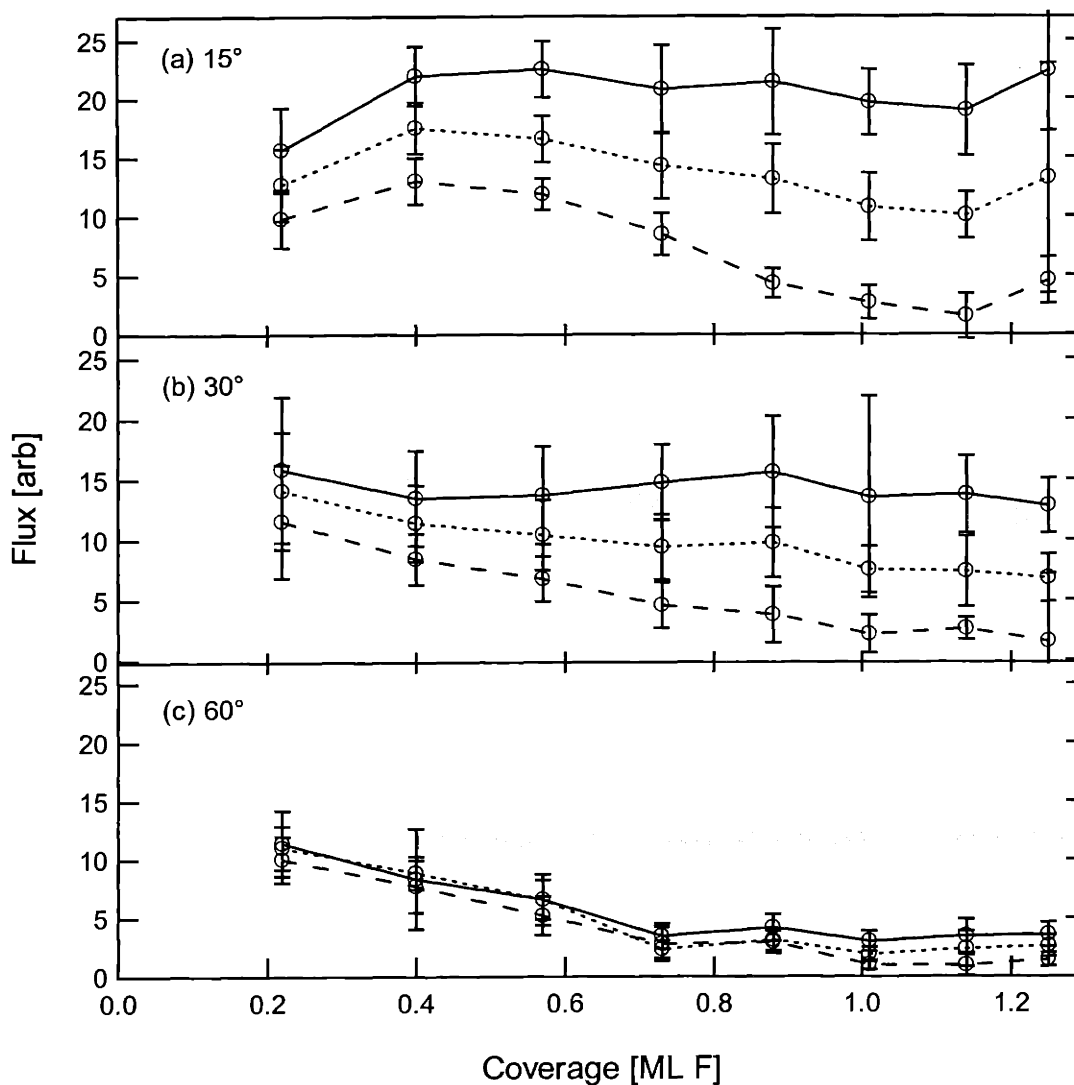
Figure 65 Coverage dependence of the flux of the fast Xe feature
Scattered flux of the fast Xe feature determined from the Maxwell-Boltzmann fit to the net Xe signal at (a) θ_d = 15°; (b) θ_d = 30°; and (c) θ_d = 60°, for the XeF cracking ratios 1.0:1 (long dashed line), 0.5:1 (short dashed line) and no XeF cracking subtracted (solid line). Flux at each point is normalized to the number of experiments taken at that detection angle. From data shown in Figures 39-47. Error bars reflect a 95% confidence limit.
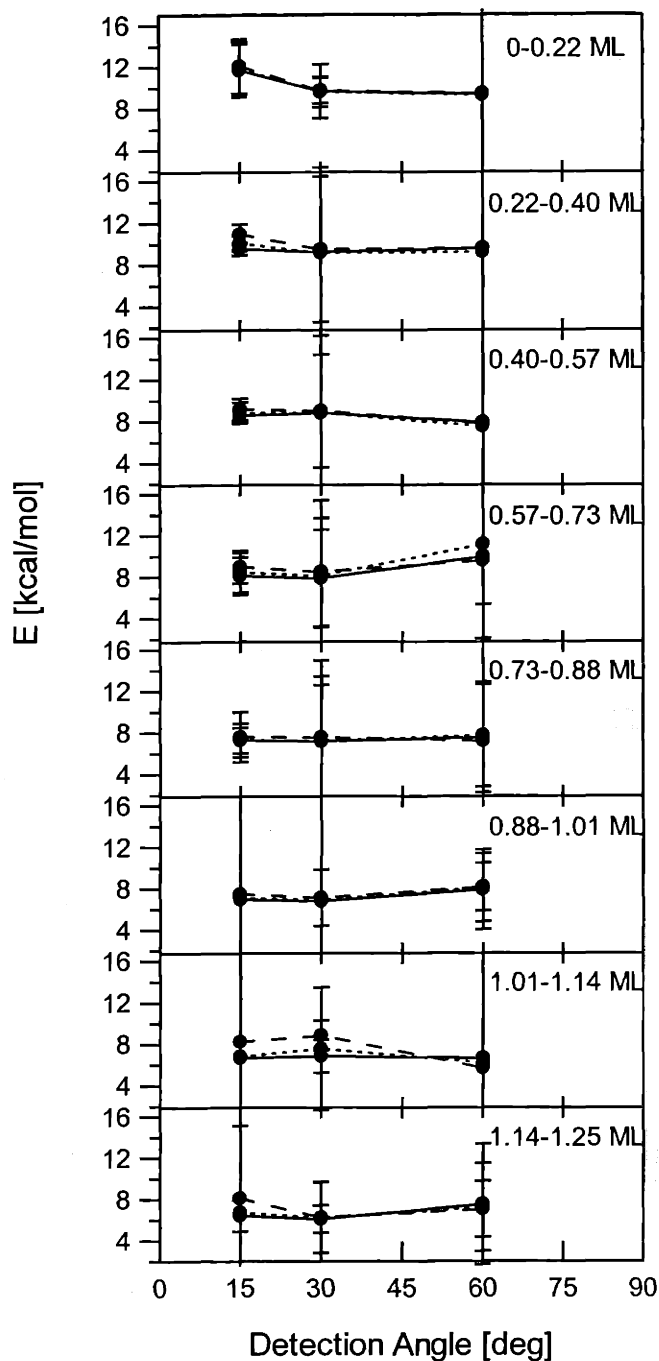
Figure 66 Angular dependence of the average energy of the fast Xe feature

Average energy of the fast Xe feature determined from the Maxwell-Boltzmann fit to the data in Figures 39-47 for the XeF cracking ratios 1.0:1 (long dashed line), 0.5:1 (short dashed line) and no XeF cracking subtracted (solid line) using Eq. (II.4). Error bars reflect a 95% confidence limit.
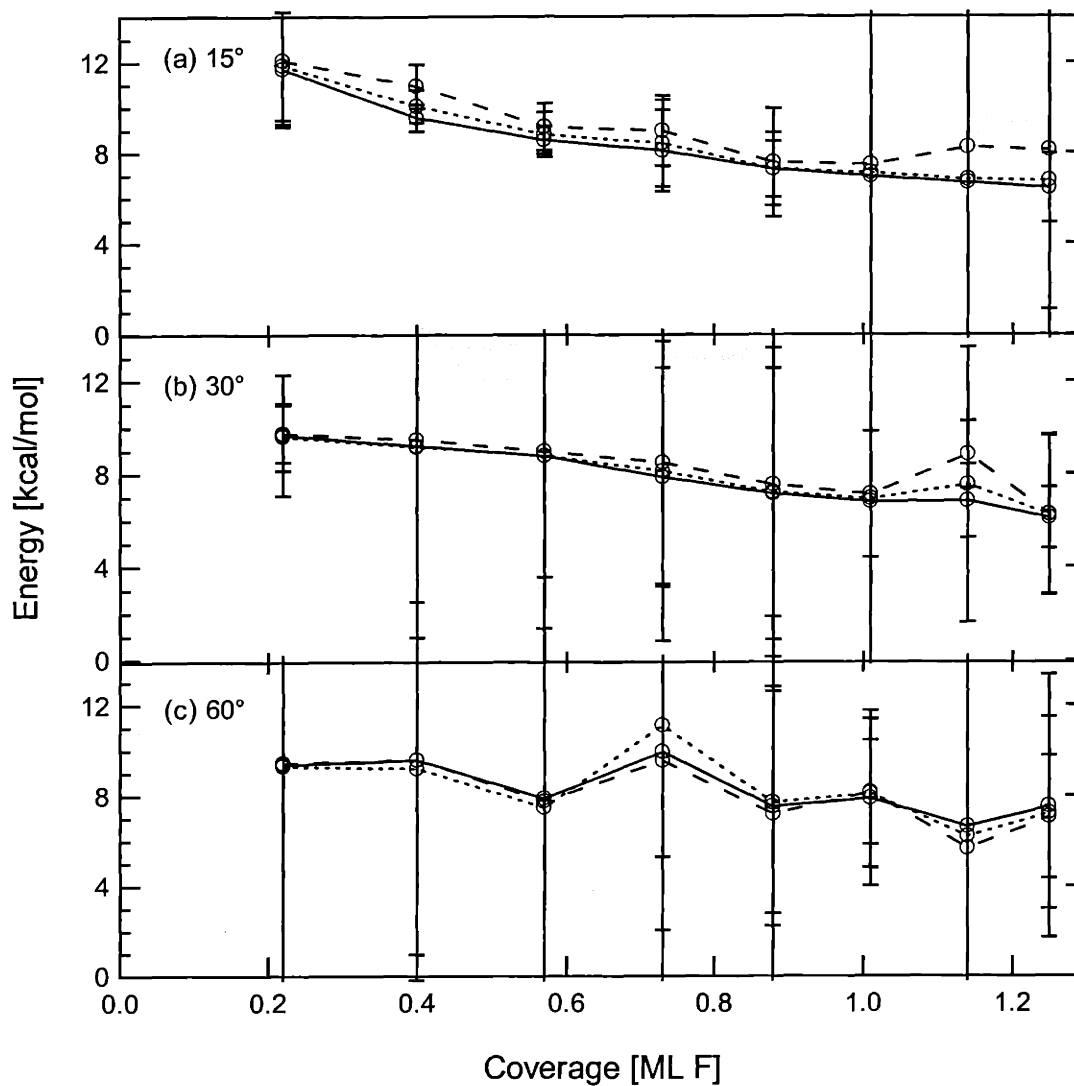
Figure 67 Coverage dependence of the average energy of the fast Xe feature

Average energy of the fast Xe feature determined from the Maxwell-Boltzmann fit to the data in Figures 39-47 at (a) $\theta_d = 15°$; (b) $\theta_d = 30°$; and (c) $\theta_d = 60°$, for the XeF cracking ratios 1.0:1 (long dashed line), 0.5:1 (short dashed line), and no XeF cracking subtracted (solid line) using Eq. (II.4). Error bars reflect a 95% confidence limit.

V.F. Two-atom adsorption

The net m/e=129 TOF spectra can be fit to three Maxwell-Boltzmann distributions, fast, medium and slow, as shown in Figures 39-47. The slow feature has a flow velocity that is fixed at zero and a temperature that is fixed at the surface temperature of 150 K. The flow velocity and temperature of the fast and medium features are freely fit by the least squares fitting algorithm. In the past, identification of two-atom adsorption from the signal at m/e = 129 was hampered by the inability to disentangle a myriad of contributions to the Xe^+ signal, including Xe from XeF dissociation, the unknown cracking from XeF, and the possibility of free Xe contamination in the incident beam. In the present study, the possibility of free Xe contamination in the incident beam is eliminated by utilizing an all-Teflon manifold and nozzle. The TOF distributions of the Xe atoms from XeF dissociation are predicted from the forward convolution calculation, and are conclusively identified as consistent with the fast Xe TOF feature, regardless of the amount of the XeF cracking ratio. This identification suggests that the medium and slow Xe features are due to two-atom adsorption. In principle, it is possible that some of the Xe from XeF dissociation receives enough translational energy that its forward motion is actually reversed so that it returns to the surface instead of scattering into the gas phase. If this were to occur, the Xe could scatter off the surface with a reduced velocity, and therefore could contribute to the medium or slow Xe features. However, a calculation based on the forward convolution calculation presented in Section IV suggests that the flux of Xe from XeF dissociation that scatters off the surface is less than 2% of the flux of Xe from XeF dissociation that scatters into the gas phase.

The angular distribution of the flux of the medium feature is shown in Figure 68 at the eight coverage ranges, where the error bars are given by the propagation of error as described in

Appendix B. From 0-0.22 ML, the angular distribution is highly peaked at $\theta_d=15°$. However, the angular distribution then changes drastically, and between 0.22 ML – 0.73 ML the angular distribution is actually peaked towards the higher detection angles. Between 0.73 ML – 1.25 ML, the angular distribution changes again and becomes more peaked towards normal. The angular distributions of the medium Xe feature are not significantly affected by the Xe^+:XeF^+ cracking ratio.

Before discussing the angular distributions in detail, it is prudent to note that, as mentioned in the previous section, the fast, medium and slow TOF features are quite broad, and the tail of the fast feature significantly overlaps the medium feature, resulting in a certain amount of ambiguity that is not reflected in the reported error bars. That is, with only a minimal change in the overall fit, a decrease or increase of the flux of the medium feature can be accounted for by broadening or narrowing the fast feature. The angular distributions of the flux of the medium Xe feature should be viewed with this uncertainty in mind.

It is intriguing that the angular distribution of the medium feature is peaked towards $\theta_d=15°$ from 0-0.22 ML, as seen in Figure 68, and as seen in the TOF spectra in Figure 39. One possible explanation is the high concentration of adjacent dangling bond sites at low coverage, which may allow for a reaction configuration where the XeF is immediately steered into an upright position upon abstraction of the fluorine atom. That is, after the initial abstraction event, the XeF fragment is steered by a neighboring dangling bond into a more favorable perpendicular orientation, with the Xe pointing into the vacuum. This orientation effect is similar to the arguments presented in Section V.C, where molecular steering of XeF_2 into a more favorable perpendicular orientation is used to account for the observed XeF angular distribution.

Between 0.22 ML – 0.73 ML the angular distribution is peaked towards θ_d=30° and 60°.

The Xe end of the XeF is expected to be more attractive to the fluorinated surface than the F end.

Therefore, it is possible that the XeF initially interacts with the surface with an orientation where

the Xe atom positioned closer to the surface than the F atom. When the XeF encounters a

dangling bond, the attraction between the dangling bond and the F atom tips the XeF onto one

side, resulting in a parallel orientation during the reaction. The Xe atom is consequently ejected

with a grazing exit trajectory, and hence greater Xe flux is observed at the higher scattering

angles.

Between 0.73 ML – 1.25 ML the angular distribution is essentially cosine, although the

larger error bars make this difficult to say for certain. Due to the fact that etching is occurring

over this coverage range, and therefore the structure of the surface is significantly altered, it is

difficult to draw any conclusions from this result.

The average energy of the medium Xe feature is shown in Figure 70 with respect to

detection angle. Although the large error bars preclude a strict interpretation, it can be seen that

the angular distribution of the average energy bears a marked similarity to the angular

distribution of the flux, shown in Figure 68. Thus, an increased flux is associated with an

increased average energy for the medium Xe feature. The average energy of the medium Xe

feature is shown in Figure 71 with respect to coverage, and ranges between 2-4 kcal/mol. The

large error bars on the average energy of the medium Xe feature make it difficult to perform a

more detailed analysis of the trends. Although there is a significant decrease in the energy at

θ_d=15° between 0.2 ML and 0.4 ML, this may be an artifact of the fitting procedure.

The fact that the average energy of two-atom adsorption is between 2-4 kcal/mol is

unexpected. Since two-atom adsorption is approximately 60 kcal/mol more exothermic than

single atom abstraction, one would expect the product of two-atom adsorption to be more translationally excited than the abstraction product, XeF. The fact that this is not observed indicates that the partitioning of energy from the exothermicity of the reaction into translational energy of the Xe atom is singularly ineffective. One possible reason for this inefficient coupling is the extremely weak Xe-F bond. It is possible that the transition state resembles a free F atom interacting with a Si atom, resulting in only weak coupling between the forming Si-F bond and the Xe atom. A more remote possibility is that the bulk of the Xe from two-atom adsorption actually has a similar energy to the Xe from XeF dissociation, and is therefore part of the fast Xe feature. This possibility cannot be ruled out.

The slow feature of the Xe TOF is mainly due to Xe that has undergone 2-atom adsorption and subsequently thermally equilibrated with the surface, although some part of this feature may be due to Xe from XeF dissociation that is directed back towards the surface. However, the results of the forward convolution calculation suggest that this contribution is less than 2%. The Xe atoms that contribute to the slow feature desorb from the surface, instead of being directly scattered into the gas phase like the Xe atoms that contribute to the medium feature. Therefore, the slow Xe feature is fit to a Maxwell-Boltzmann distribution with the flow velocity fixed at zero, and the temperature fixed at the surface temperature, 150 K. With these assumptions, the TOF spectra are well fit, as shown in Figures 39-47. However, as mentioned before, the broad and overlapping nature of the TOF features introduces an additional uncertainty that is not reflected in the reported error bars. The flux of the slow Xe feature is shown in Figure 72 as a function of detection angle. The results are nearly independent of the cracking ratio used, due to the fact that the thermal feature is well separated from the flight times at which the XeF

signal is at a maximum. The angular distribution is essentially cosine at all coverages, which is characteristic of a species that desorbs after having first equilibrated with the surface.
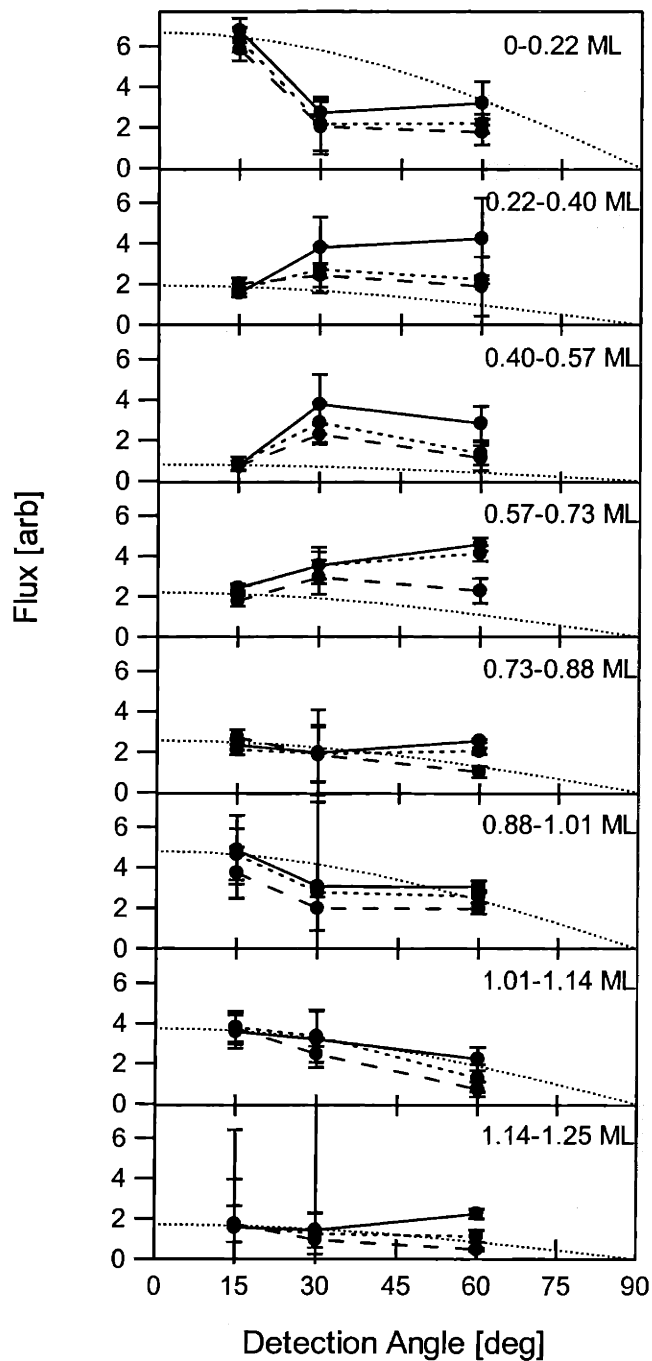
Figure 68 Angular dependence of the flux of the medium Xe feature

Scattered flux of the medium Xe feature determined from the Maxwell-Boltzmann fit to the data in Figures 39-47 for the XeF cracking ratios 1.0:1 (long dashed line), 0.5:1 (short dashed line), and no XeF cracking subtracted (solid line) using Eq. (II.2). Dotted line shows a cosine distribution normalized to match the flux at θ_d=15°. Flux at each point is normalized to the number of experiments at that detection angle. Error bars reflect a 95% confidence limit.

Figure 69 Coverage dependence of the flux of the medium Xe feature

Scattered flux of the medium Xe feature determined from the Maxwell-Boltzmann fit to the data in Figures 39-47 at (a) θ_d = 15°; (b) θ_d = 30°; and (c) θ_d = 60°, for the XeF cracking ratios 1.0:1 (long dashed line), 0.5:1 (short dashed line), and no XeF cracking subtracted (solid line) using Eq. (II.2). Flux at each point is normalized to the number of experiments at that detection angle. Error bars reflect a 95% confidence limit.
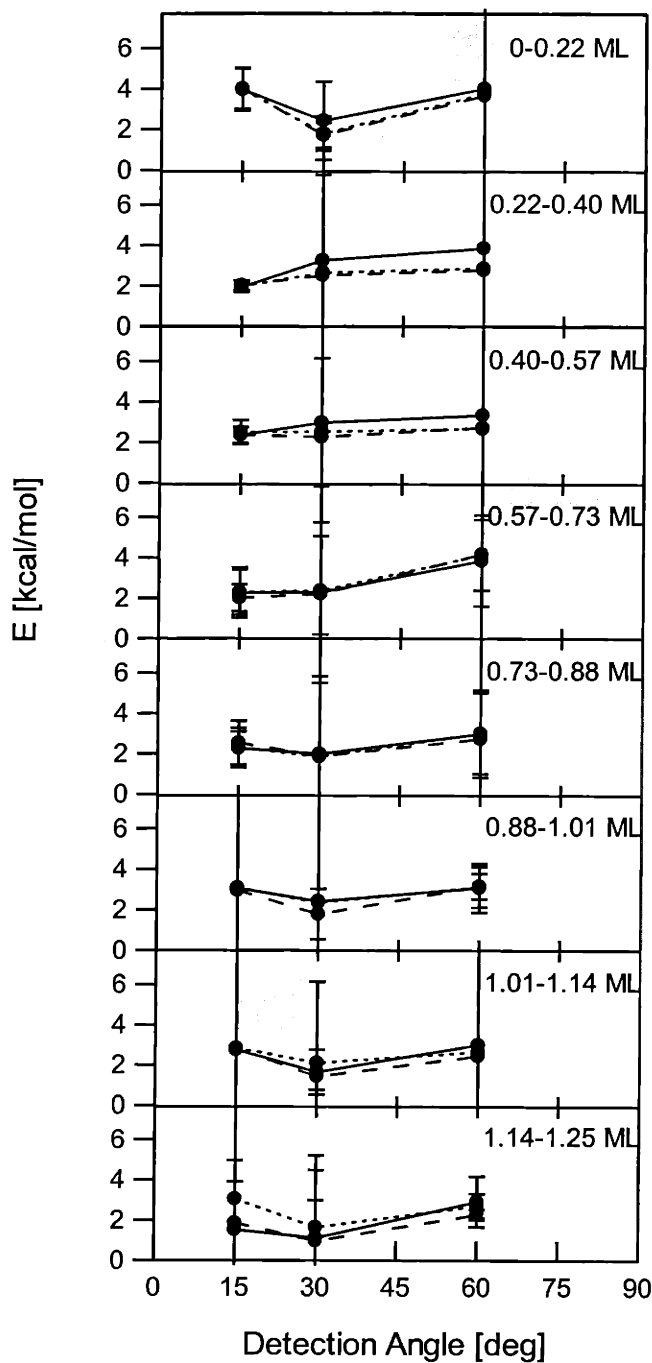
Figure 70 Angular dependence of the energy of the medium Xe feature

Average energy of the medium Xe feature determined from the Maxwell-Boltzmann fit to the data in Figures 39-47 for the XeF cracking ratios 1.0:1 (long dashed line), 0.5:1 (short dashed line), and no XeF cracking subtracted (solid line) using Eq. (II.4). Error bars reflect a 95% confidence limit.
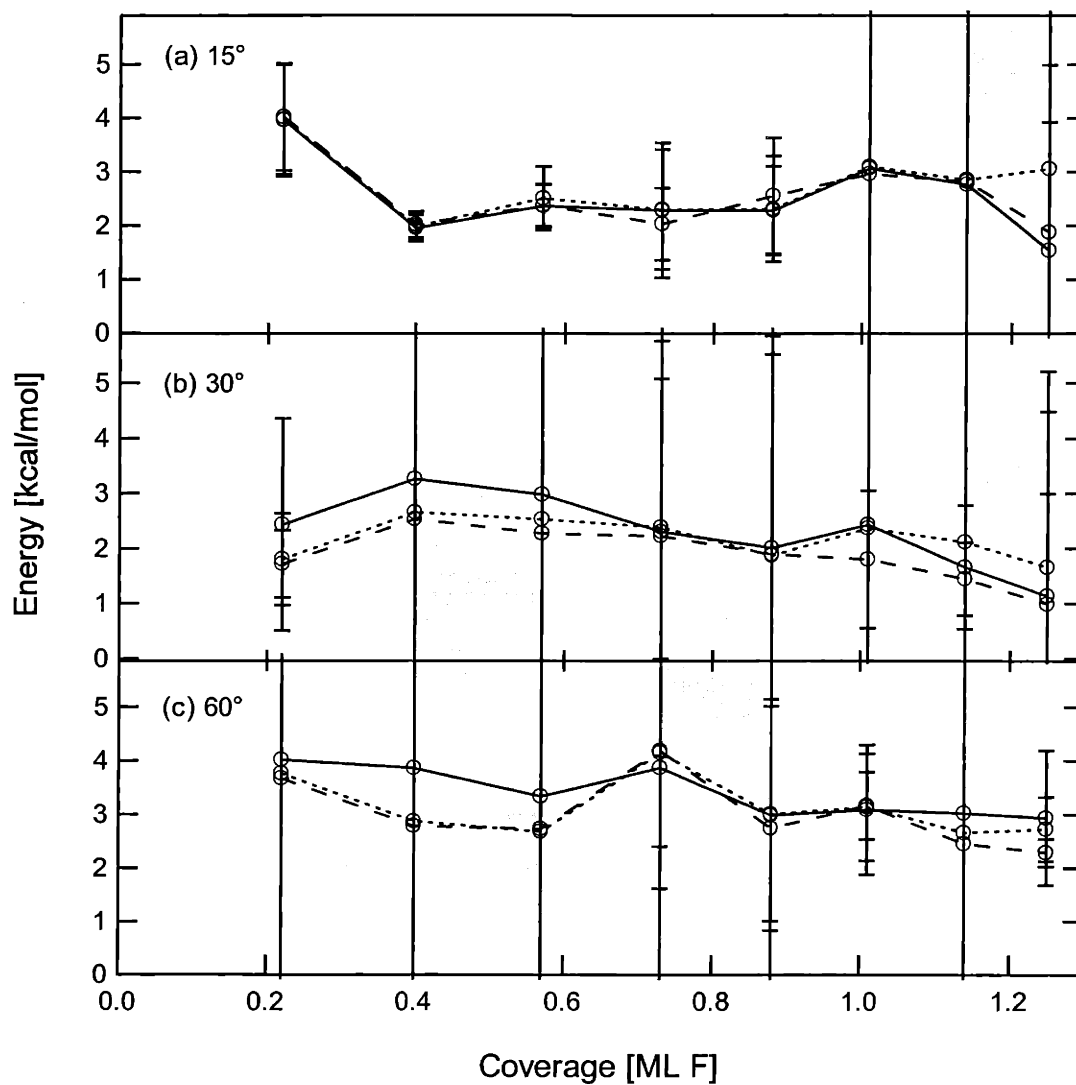
Figure 71 Coverage dependence of the average energy the medium Xe feature

Average energy of the medium Xe feature determined from the Maxwell-Boltzmann fit to the data in Figures 39-47 at (a) $\theta_d = 15°$; (b) $\theta_d = 30°$; and (c) $\theta_d = 60°$, for the XeF cracking ratios 1.0:1 (long dashed line), 0.5:1 (short dashed line) and no XeF cracking subtracted (solid line) using Eq. (II.4). Error bars reflect a 95% confidence limit.
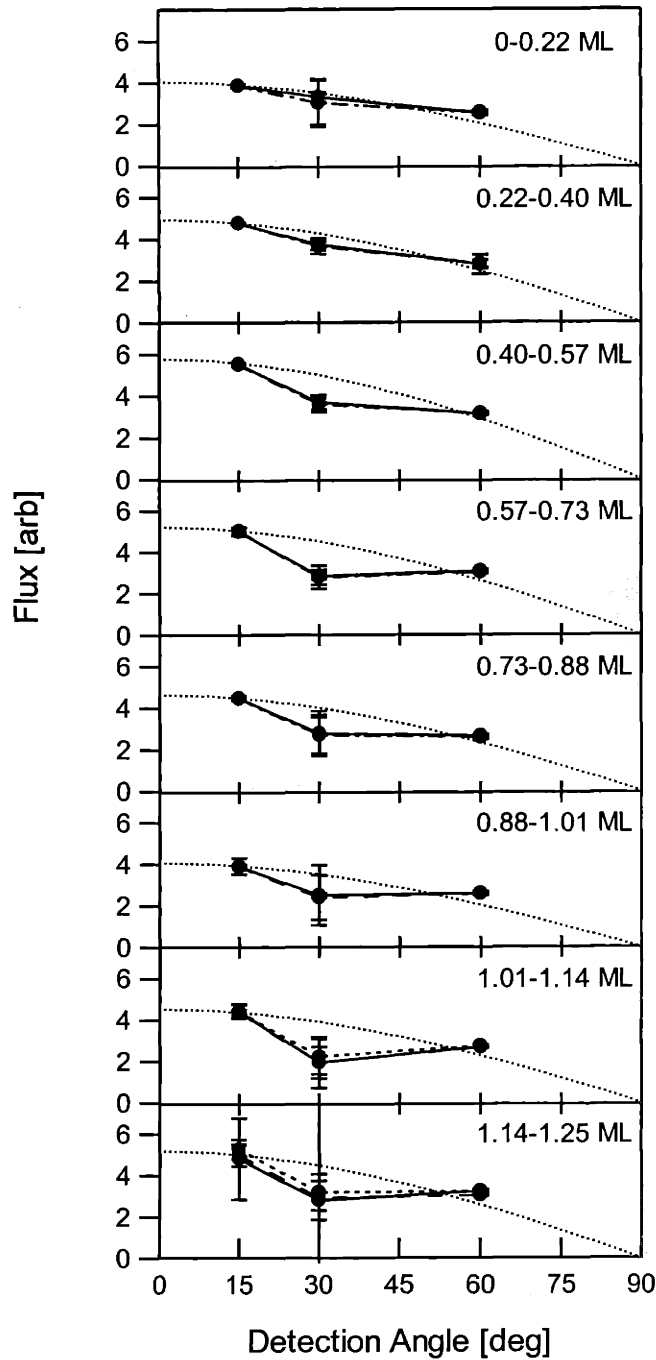
Figure 72 Angular dependence of the flux of the slow Xe feature

Scattered flux of the slow Xe feature determined from the Maxwell-Boltzmann fit to the data in Figures 39-47 for the XeF cracking ratios 1.0:1 (long dashed line), 0.5:1 (short dashed line), and no XeF cracking subtracted (solid line) using Eq. (II.2). Dotted line shows a cosine distribution normalized to match the flux at $\theta_d=15°$. Flux at each point is normalized to the number of experiments at that detection angle. Error bars reflect a 95% confidence limit.
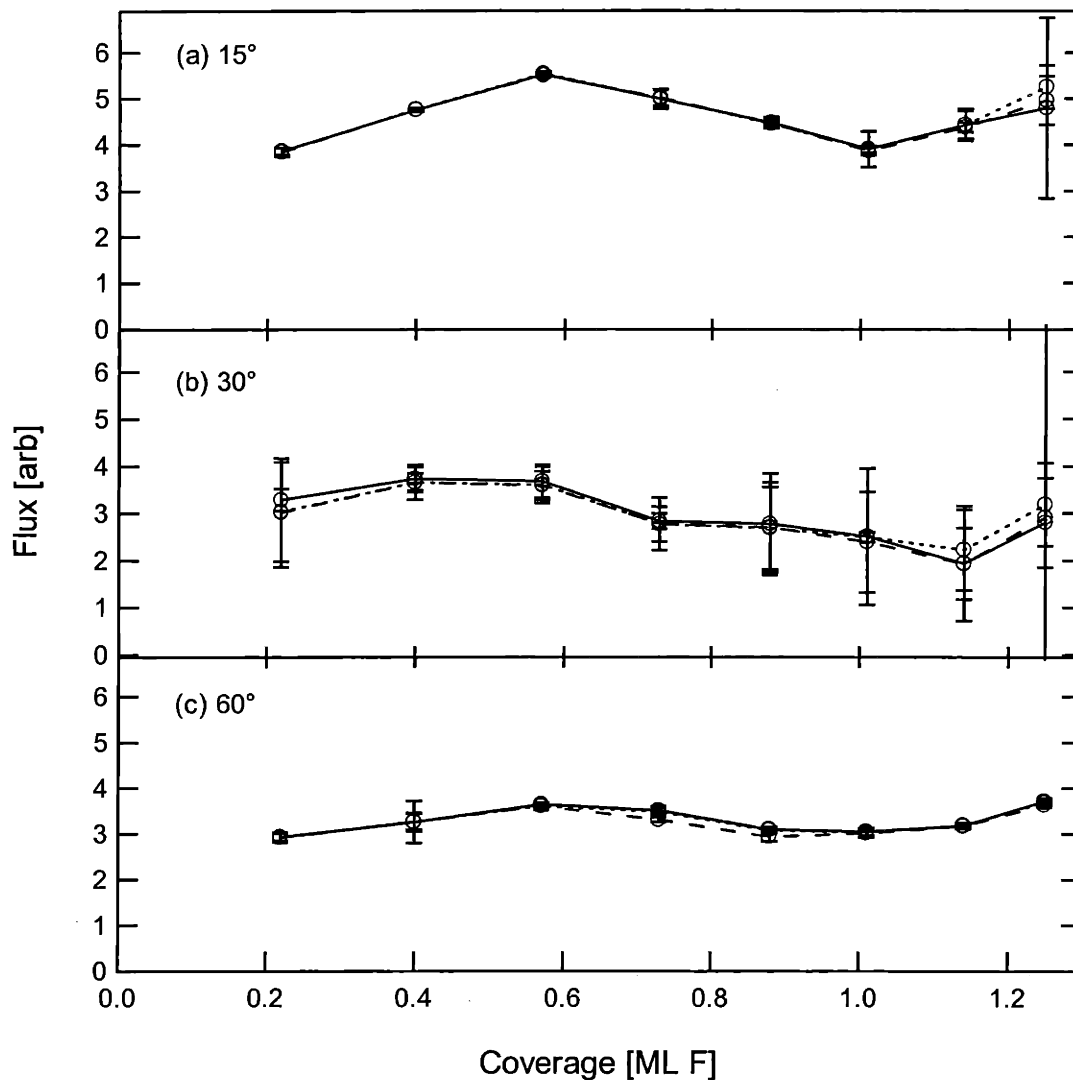
Figure 73 Coverage dependence of the flux of the slow Xe feature

Scattered flux of the slow Xe feature determined from the Maxwell-Boltzmann fit to the data in Figures 39-47 at (a) $\theta_d = 15°$; (b) $\theta_d = 30°$; and (c) $\theta_d = 60°$, for the XeF cracking ratios 1.0:1 (long dashed line), 0.5:1 (short dashed line), and no XeF cracking subtracted (solid line) using Eq. (II.2). Flux at each point is normalized to the number of experiments at that detection angle. Error bars reflect a 95% confidence limit.

VI. Conclusion

The results presented above give the following picture for the interaction of XeF_2 with Si(100). The incident XeF_2 molecule can either unreactively scatter off the Si surface, without any bonds being broken or formed, or it can react with the surface via single atom abstraction, liberating a XeF fragment. The XeF fragment has three possible fates. It can either 1) scatter into the gas phase, or 2) dissociate into a F and a Xe atom, or 3) react with the surface, resulting in two-atom adsorption. In order to gain insight into the reaction of XeF_2 with Si(100), both the surface-bound and gas-phase products of the reaction are studied.

Investigations of the surface-bound products of the reaction, presented in Chapter 2, have probed both the surface order and the dissociative chemisorption probability as a function of coverage. The initial reaction occurs solely at the Si dangling bonds, resulting in a fully ordered surface with a 2x1 periodicity at about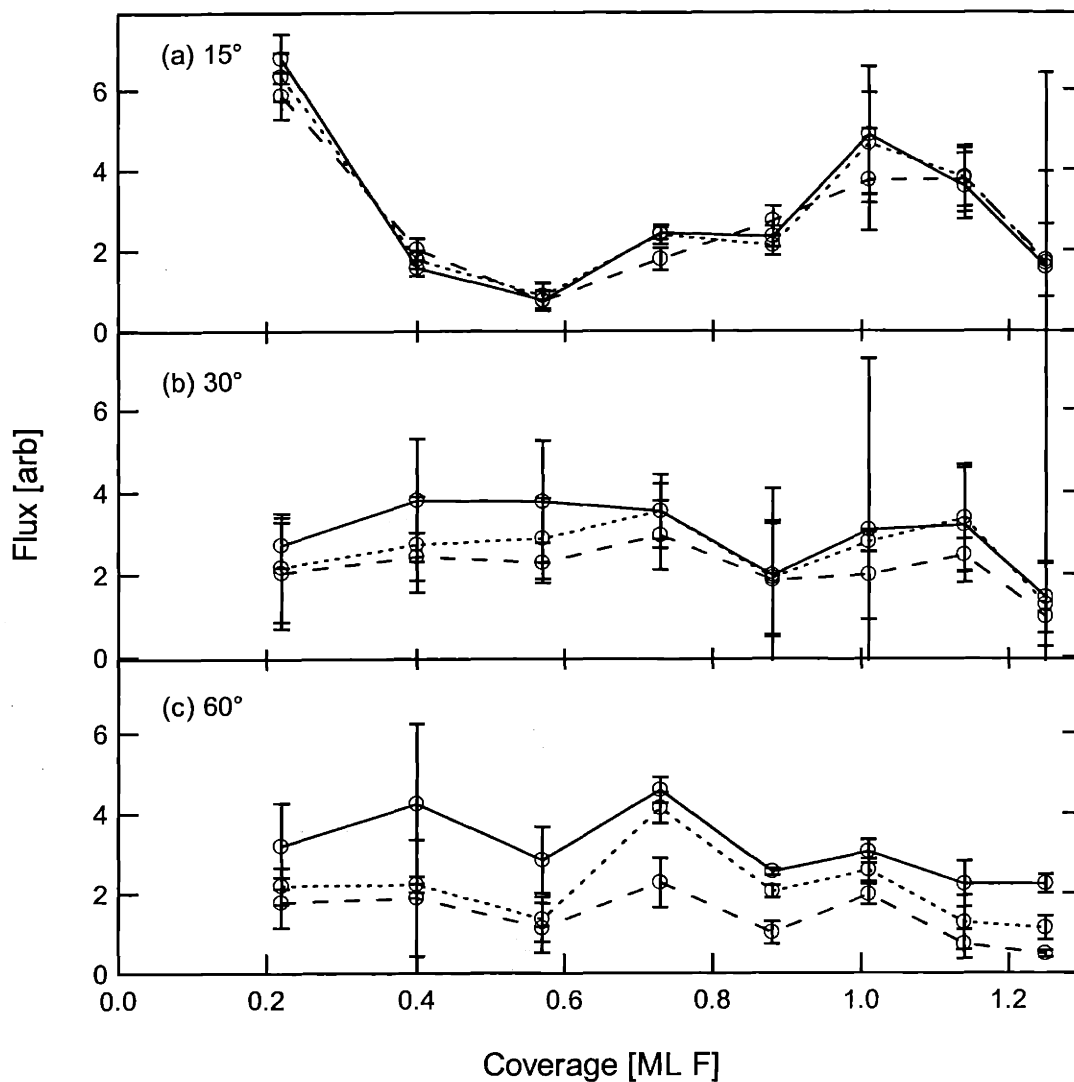 1 ML coverage. The exothermicity released during this reaction does not destroy the order of the surface. In terms of the surface order, the reaction of XeF_2 with Si(100) up to 1 ML coverage is remarkably similar to the reaction of F_2 with Si(100), which has been studied previously in our laboratory.[8,18] No Si-Si σ bonds are broken and each Si dangling bond is capped with a fluorine atom. Unlike F_2, however, XeF_2 continues to react with the surface above 1 ML coverage, breaking Si-Si bonds and etching the surface by the formation of volatile SiF_4. The dissociative chemisorption probability of XeF_2 reacting with Si(100) at 250 K is measured to be about 0.82±0.14 on a clean surface, decreasing to about 0.54±0.10 just prior to the onset of etching at about 1 ML coverage. The relatively high dissociative chemisorption probability of XeF_2 on a fluorinated surface is in stark contrast to the complete cessation of the reaction of F_2 with a fluorinated surface. In short, XeF_2 etches the surface while F_2 does not.

The decrease in the dissociative chemisorption probability with increasing coverage suggests that the reaction does not occur via a physisorbed precursor mechanism at 250 K.

Investigations of the gas-phase products of the reaction, presented in Chapter 3, have probed the fate of the XeF abstraction product. Time-of-flight spectra of the reactively scattered XeF show that only a small fraction of the exothermicity of the reaction is channeled into translational excitation of the XeF, suggesting that the transition state of this reaction lies in the entrance channel of the potential energy surface. This kind of potential energy surface leads to the channeling of most of the reaction exothermicity into vibrational energy of the Si-F bond. The fact that the XeF angular distribution becomes more peaked towards normal on a fluorinated surface suggests that the combined influence of molecular steering from the attractive interaction between the dangling bond and the fluorine atom, and steric hinderance between the large XeF_2 and the neighboring adsorbed fluorine atoms, serve to align the XeF_2 into a more favorable perpendicular orientation prior to the reaction.

The observation of reactively scattered F atoms is evidence that some of the XeF from atom abstraction dissociates to produce a gas phase F atom and a Xe atom. This conclusion is substantiated by a forward convolution calculation based on momentum-matching the F and Xe atoms from gas-phase dissociation of XeF that successfully predicts the observed F atom and Xe atom TOF distributions at all angles and coverages. The forward convolution calculation has several implications for the mechanism of XeF dissociation and atom abstraction. First, an analysis of the center of mass energy distribution of the dissociating XeF together with the potential energy curves of the XeF electronic states concludes that it is likely that the dissociation occurs primarily through an excited rovibrational state of the ground electronic state that is above the dissociation threshold. This conclusion in turn suggests that the dissociation

occurs on the time scale of a vibrational period. Second, the failure of the calculation to yield physically reasonable results when the entire range of XeF orientations are included suggests that the orientation of XeF in the transition state is such that the F atom is pointing into the vacuum. Last, because the amount of the exothermicity channeled into the internal energy of the XeF does not change with increasing coverage, it is concluded that atom abstraction occurs primarily at the dangling bond reactive sites, regardless of the coverage.

The two-atom adsorption signal is identified by that part of the Xe TOF distribution that is not predicted to be due to Xe from XeF dissociation. Although the interpretation is complicated by the broad and overlapping nature of the Xe TOF features, the angular distribution of the medium speed Xe TOF feature from two-atom adsorption suggests that molecular steering influences the orientation of the XeF during the reaction. The observed low translational energy of the Xe from two-atom adsorption may be due to the weak XeF bond, and hence weak coupling of the reaction exothermicity to the translational excitation of the Xe atom. The slow Xe TOF feature from two-atom adsorption has a cosine distribution at all coverages, as expected for a species that desorbs in thermal equilibrium with the surface. Further study of Xe from two-atom adsorption may yield further insight into the mechanism by which XeF_2 etches the Si surface.

REFERENCES

[1] M.R. Tate, Ph. D. Thesis, Massachusetts Institute of Technology (1999).

[2] M.P. D'Evelyn, Y.L. Yang, and L.F. Sutcu, *J. Chem. Phys.* **96**, 852 (1992).

[3] U. Hofer, L. Li, and T.F. Heinz, *Phys. Rev. B.* **45**, 9485 (1992).

[4] R. Walsh, *Acc. Chem. Res.* **14**, 246 (1981).

[5] P.C. Tellinghuisen, J. Tellinghuisen, J.A. Coxon, J.E. Velazco, and D.W. Setser, *J. Chem. Phys.* **68**, 5187 (1978).

[6] C.J. Wu and E.A. Carter, *J. Am. Chem. Soc.* **113**, 9061 (1991).

[7] P.J. Hay and T.H. Dunning, Jr., *J. Chem. Phys.* **69**, 2209 (1978).

[8] M.R. Tate, D. Gosalvez-Blanco, D.P. Pullman, A.A. Tsekouras, Y.L. Li, J.J. Yang, K.B. Laughlin, S.C. Eckman, M.F. Bertino and S.T. Ceyer, *J. Chem. Phys.* **111**, 3679 (1999).

[9] R.C. Hefty, PhD. Thesis, Massachusetts Institute of Technology, to be published.

[10] A. Ishizaka and Y. Shiraki, *J. Electrochem. Soc.* **133**, 666 (1986).

[11] M.T. Schulberg, Ph. D. Thesis, Massachusetts Institute of Technology (1990).

[12] Globe Motors Model #75A1646.

[13] Barden Corp. Model #SR4SSTB5.

[14] J.D. Beckerle, Ph. D. Thesis, Massachusetts Institute of Technology (1988).

[15] Lindskog Balancing Corporation, Boxborough, MA, (800) 540-2042.

[16] J.J. Yang, Ph. D. Thesis, Massachusetts Institute of Technology (1993).

[17] H.F. Winters and F.A. Houle, *J. Appl. Phys.* **54**, 1218 (1983).

[18] D.P. Pullman, A.A. Tsekouras, Y.L. Li, J.J. Yang, M.R. Tate, D.B. Gosalvez, K.B. Laughlin, M.T. Schulberg, and S.T. Ceyer, *J. Phys. Chem. B* **105**, 486 (2001).

[19] D.E. Ibbotson, D.L. Flamm, J.A. Mucha, and V.M. Donnelly, *Appl. Phys. Lett.* **44**, 1129 (1984).

[20] M.J.M. Vugts, G.L.J. Verschueren, M.F.A. Eurlings, L.J.F. Hermans, and H.C.W. Beijerinck, *J.Vac. Sci. Tech. A* **14**, 2766 (1996).

[21] B. Poelsema, G. Comsa, *Scattering of Thermal Energy Atoms from Disordered Surfaces* (Springer-Verlag, Berlin, 1989).

[22] A.M Wodtke and Y.T. Lee, *J. Phys. Chem.* **89**, 4744 (1985).

[23] Y.T. Lee, *Atomic and Molecular Beam Methods*, edited by G. Scoles (Oxford University Press, 1988), Vol. I, p. 553.

[24] M.G. Evans and M.C. Polanyi, *Trans. Faraday Soc.* **35**, 178 (1939).

Appendix A: Counting Electronics and Computer Interface

The experiments that have been described in the previous chapters have been performed utilizing a detection scheme and experimental apparatus that is to a large degree computer controlled. The purpose of this appendix is to describe two aspects of the computer-lab interface. First, the manner in which the weak current pulse from the Channeltron electron multiplier is converted into a computer-readable TTL pulse is described. In order to aid future troubleshooting efforts, the dimensions of the pulse shape at each step is given. Second, the input and output signals that allow the computer to control the experimental apparatus are summarized.

I. Pulse Counting Electronics

The use of a Channeltron electron multiplier in pulse counting experiments has been briefly described.[1] However, the current experimental setup is different in several respects from that presented earlier. Figure 1 shows a schematic of the electronic components and connections between the Channeltron electron multiplier and the computer counting board. A positive ion that survives the trajectory through the quadrupole mass selection field is incident on the Channeltron electron multiplier, causing an electron cascade. The resulting current pulse goes through a feedthrough in the lid of the machine, and is then amplified by a fast pre-amplifier, which converts the current pulse to a voltage pulse. The voltage pulse enters a discriminator, which is set to eliminate the background noise but pass legitimate counting events. The output of the discriminator passes through a pulse lengthener, which conditions the output of the discriminator for input into the counting board in the computer.

The Channeltron has the shape of a curved horn. The "input" end of the Channeltron is the flared end of the horn, and is held at a high negative bias, between -2.2 to -3.0 kV. The opposite end of the horn is the "output" end, and is held at ground, or 0 V bias. Positive ions that

survive the journey through the quadrupole mass selection region are attracted to the input region of the Channeltron and impact the inner surface of the horn at a high rate of speed. This surface is designed to emit a shower of secondary electrons. This initiates a "cascade" effect which results in a high gain current pulse at the output of the Channeltron. The Galileo Model 4870 Channeltron has been used for the current experiments. Typical test data specifications are shown in the table below.

Test bias voltage	2350 V
Dark bias current	39.2 μA
Dark counts @ 3 kV	0.017 Hz
Gain	1.08×10^8
Pulse Height Distribution (F.W.H.M.)	53%

The Channeltron signal at the output feedthrough has been observed under experimental conditions with a Tektronix model 2245A 100 MHz oscilloscope. Figure 2a shows the observed pulse distribution of a newly installed channeltron at –2.2 kV bias and 120 kHz count rate. A distribution of pulse heights is observed, with a maximum pulse height of -50 mV and a minimum pulse height of -11 mV. The full width of the pulse is 15 ns, while the full width at half maximum (F.W.H.M.) is 8 ns. In addition to the main negative peak, a much smaller secondary positive peak is observed.

The observed peak height distribution can be compared to the listed specifications. The listed gain of 1.08×10^8 means that each pulse should contain 1.08×10^8 electrons. The width of the peak is measured to be 15 ns, so each peak should have 7.2×10^{15} electrons per second, or 1.15×10^{-3} amps. When measured across the 50 ohm input impedance of the oscilloscope, this should result in a 58 mV peak. The fact that the measured peak is slightly lower than the

predicted value may be due to the fact that the experimental bias is lower than the test bias (-2200 V versus -2350 V).

The fast pre-amplifier is a Phillips Scientific Model 6931 100 MHz bipolar amplifier with a nominal voltage gain of 100 to 1. The observed output of the preamp is shown in Figure 2b, and is a -3.8 V pulse, which corresponds to a voltage gain of 75 to 1. The small positive pulse from the Channeltron is preserved, and there is an additional smaller negative pulse with a 0.4 V maximum.

The discriminator is a Phillips Scientific Model 6904D 300 MHz discriminator that has been modified for one set of TTL outputs. The setpoint of the discriminator is fixed at -0.6 V, which eliminates any possible double counting events due to the small secondary negative peak at the output of the pre-amp. The TTL output of the discriminator is shown in Figure 2c, and is a positive square pulse 1.5 V high and 52 ns in duration. However, this pulse does not meet the minimum input characteristics for the counter board input pulse, which are 2.0 V and 70 ns duration. Although the counter board can accept the pulse from the discriminator, which does not meet the minimum TTL specification, and still seem to perform adequately, detecting a pulse that is both shorter and weaker than the minimum TTL specification results in system instability, which can be exhibited as occasional spurious signal spikes or dips. For this reason, a home-built pulse lengthener is included after the discriminator.

The design of the pulse lengthener is similar to the design of the dual programmable prescaler that has been described previously.[2] However, the pulse lengthener currently in use has only a single channel, and is used exclusively with a prescale factor of 1. The output of the pulse lengthener is shown in Figure 2d. The TTL pulse from the discriminator has been amplified

slightly to +3.2 V, and the pulse duration has been lengthened to 115 ns. This signal is then counted by the counting board in the lab computer.

II. Computer Interface

The computer interface and data acquisition programs have been described in detail previously.[3] However, since that time the data acquisition and analysis hardware has been updated from a PDP-11/23 combination to a Gateway personal computer running Microsoft Windows95. This platform has many advantages over the PDP system. These advantages include the ability to keep multiple data acquisition programs running simultaneously, a larger storage capacity, and the ability to transfer large numbers of data files via the Internet.

The three component cards used to interface with the lab equipment have been preserved in the transition from PDP-11 to PC. These include a counter board and two digital to analog converter boards. One digital to analog converter board is used primarily for output purposes, while the other is used solely for input purposes. Each card is connected via a ribbon cable to a "breakout box" which has multiple BNC connectors. These breakout boxes are shown in Figure 3. The unlabeled BNC connectors are physically present in the breakout boxes, but are unused in our current experimental configuration. Table 1 summarizes the purpose of each connection.

The counter board is a Keithley Metrabyte model CTM-05 multi-function counter-timer and digital input/output (I/O) expansion board. Its capabilities include five 16 bit up/down counters, a 1 MHz crystal timebase with divider, and separate general purpose 8 bit TTL input and output ports. One of the five counters (labeled 'Sig' on the breakout box) is used to input the pulse counting signal from the pulse lengthener. The other four counters are unused. The TTL I/O bits are used for separate tasks. The input bit labeled 'In 0' on the breakout box is connected to the tuning fork chopper signal, allowing for software background subtraction of the helium

diffraction spectra. The output bit labeled 'Out 0' on the breakout box is connected to the PID temperature controller to toggle between direct current setpoint mode and feedback-stabilized temperature setpoint mode. The output bit labeled 'Out 1' on the breakout box is connected to the beam flag controller. When the beam flag controller is set to "automatic" this output bit directly controls the position of the beam flag. The output bit labeled 'Out 2' on the breakout box goes to a homemade box containing a LED and a buzzer. The purpose of this box is to give an audio signal during the acquisition of helium diffraction spectra. The user utilizes this regularly spaced audible prompt in order to calibrate the rotation rate of the detector. The rest of the TTL I/O ports are unused.

The first digital to analog converter board, which primarily is responsible for output functions, is a Keithley model DDA-06 with six independent 12 bit D/A converters providing ± 10 V input or output. Four of these converters are used to provide output. The output channel labeled 'D/A 0' on the breakout box is used to set the PID current limit, where 0-10V DC corresponds to 0-10 amps maximum current. This is useful to safeguard the equipment. For instance, if the thermocouple were to become detached from the back of the crystal, it would still read room temperature. If the PID was then instructed to ramp the crystal temperature, it would supply a steadily increasing current to the crystal, as the apparent crystal temperature would not change. This situation would almost certainly result in the destruction of the crystal, as well as possible damage to the crystal mount and heater power supply, and is therefore to be avoided. The output channel labeled 'D/A 1' is used to output the mass setpoint to the quadrupole mass spectrometer controller. The voltage that corresponds to each mass is calibrated in the data acquisition software. Generally, trial background mass spectra are collected, and the background peaks at m/e = 16 (O^+), m/e = 28 (N_2^+ and CO^+) and m/e = 44 (CO_2^+) are matched as closely as

possible to their nominal values by adjusting the mass that corresponds to +10 V (full scale output). The output channel labeled 'D/A 2' is used to directly control the xtal heater output current when the PID toggle is set to current setpoint mode. In this case, 0-10 V DC output corresponds directly to 0-20 amps current supplied to the crystal. The last output channel, labeled 'D/A 3,' outputs ± 10 V to control the PID temperature setpoint. A detailed description of this process is given elsewhere.[3] A separate connection from the main chamber pressure readout is hard-wired into the breakout box, utilizing two D/A inputs. Since the main chamber pressure is given by (for example) 4.5×10^{-10} torr, the first D/A input is used for the prefactor, in this case 4.5, and the second D/A input is used for the exponent, in this case –10.

The second digital to analog converter board is used to input the xtal temperature and the stagnation pressure as measured by a Baratron capacitance manometer. The process for inputting the xtal temperature is described in detail elsewhere.[3] The Baratron pressure input has been calibrated such that 0-10 V input corresponds to 0-5000 torr absolute pressure.

Board	Connection	Purpose
Counter	In 0	Inputs tuning fork chopper signal
	Out 0	Outputs binary PID/current limit toggle
	Out 1	Outputs binary beam flag on/off toggle
	Out 2	Outputs TTL pulse to buzzer/LED box
	Sig	Inputs signal from pulse counting electronics
D to A	D/A 0	Outputs 0-10 VDC to PID current limit
	D/A 1	Outputs 0-10 VDC to QMS external mass setting
	D/A 2	Outputs 0-10 VDC to set xtal heater current directly
	D/A 3	Outputs ± 10 VDC to set PID target temperature
A to D	A/D 0	Inputs ± 10 VDC from xtal TC temperature gauge
	A/D 1	Inputs ± 10 VDC from Baratron panel readout

Table 1. Summary of breakout boxes connections
Description of the connection made to the breakout boxes shown in Figure 3. Not shown is the main chamber pressure readout, which is hard-wired into the D to A breakout box.
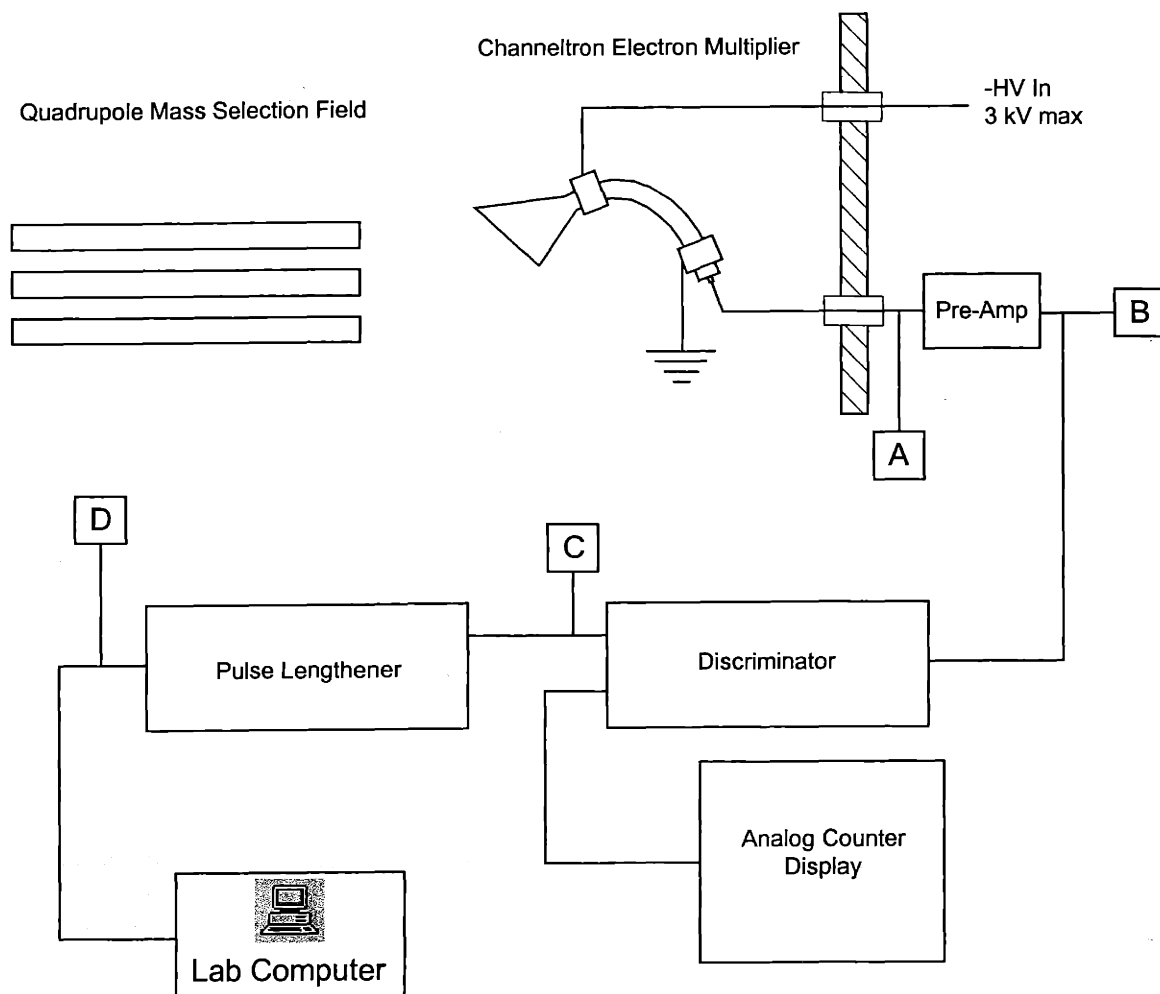
Figure 1 Pulse counting electronics schematic
Summary of the electronic components between the Channeltron electron multiplier and computer. Letters indicate oscilloscope placement for pulse shapes detailed in Figure 2.

A) Channeltron Output

6 mV

11 mV

50 mV

8 ns
FWHM

15 ns
max width

B) Pre-Amp Output

0.9 V

0.5 V

0.4 V

3.8 V

12 ns
FWHM

15 ns
max width

C) Discriminator Output

1.5 V

52 ns

D) Pulse Lengthener Output

3.2 V

115 ns
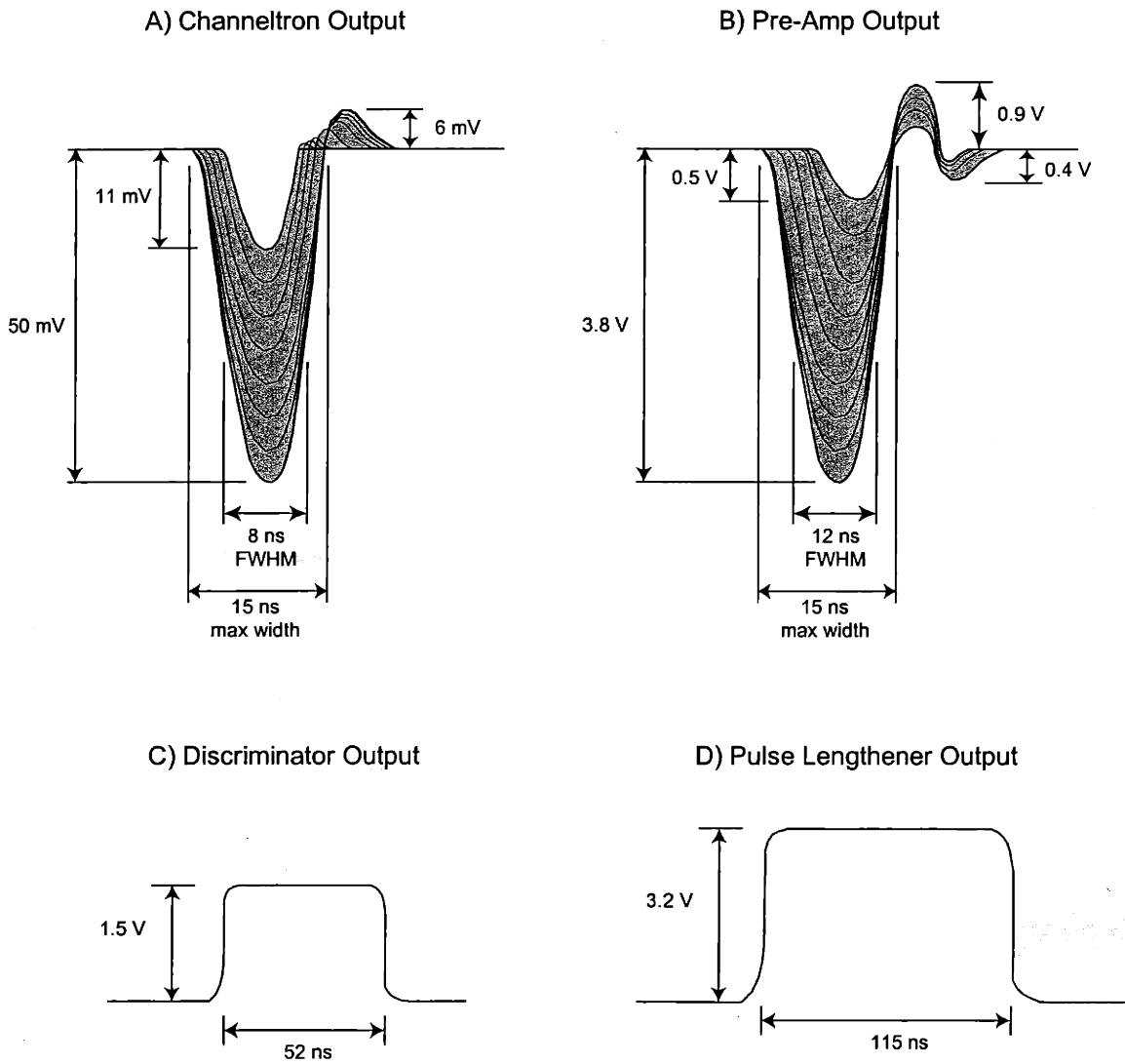
Figure 2 Pulse shapes
Detailed dimensions for the pulse shapes output from the electronic components described in
Figure 1. Grey areas indicate a distribution of peak sizes.

A) Counter

In 0   Out 0   Sig

ribbon cable
to computer

Out 1

Out 2

B) Digital to Analog

D/A 0   D/A 1   D/A 2   D/A 3

ribbon cable
to computer

C) Analog to Digital

A/D 0   A/D 1

ribbon cable
to computer
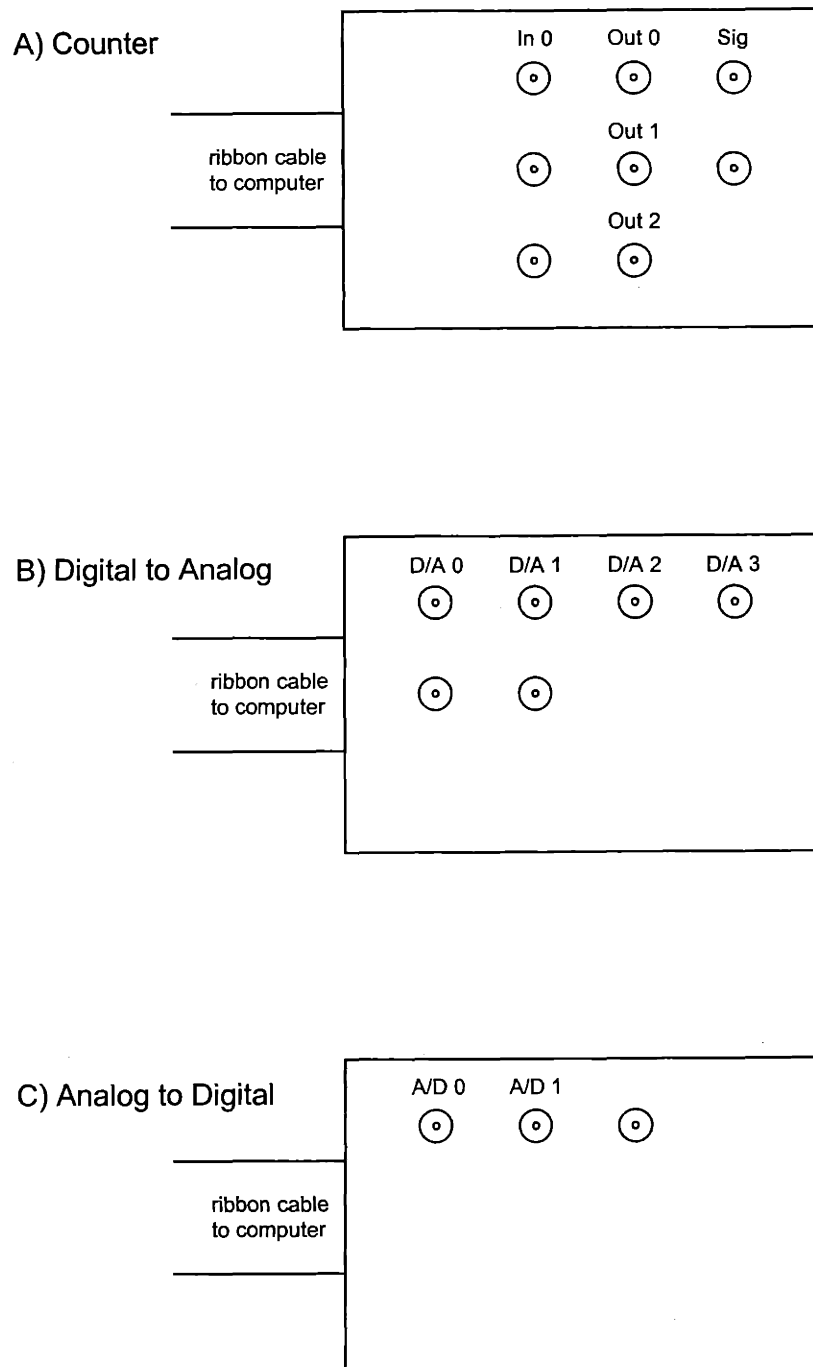
Figure 3 Breakout boxes connections diagram
Each PC interface board is connected via a ribbon cable to a breakout box, which contains multiple BNC connectors. See Table 1 for a full description as to how each connection is used. The main chamber pressure readout is hard-wired into the digital to analog breakout box.

REFERENCES

[1] J.D. Beckerle, Ph.D. thesis, Massachusetts Institute of Technology, 1988.
[2] S.P. Daley, Ph.D. thesis, Massachusetts Institute of Technology, 1994.
[3] M.T. Schulberg, Ph.D. thesis, Massachusetts Institute of Technology, 1990.

Appendix B: Error Analysis

The measurement of physical quantities in the laboratory is inevitably accompanied by variability in both the experimental conditions and also in the detected signals. It is necessary to take into account these variabilities when reporting the final uncertainty in the results of an experiment, a process known as error analysis. A good overview of the subject is given by Taylor[1].

In general, the detected signal is determined by multiple factors, including an experimentally determined independent variable, the conditions at which the experiment is performed, and unknown quantities intrinsic to the process being observed. To give a relevant example, imagine an experiment that records the intensity of the unreactively scattered XeF_2 from Si(100) as a function of exposure time. The independent variable is the exposure time. The experimental conditions include (but are not limited to) the incident flux of XeF_2, the incident energy of the XeF_2, the scattering angle where the detector is positioned, the detection efficiency of the quadrupole mass spectrometer, the acceptance angle of the detector, the temperature of the crystal, etc. The unknown quantities intrinsic to the process being studied include (but again are not limited to) the probability of unreactive scattering, the angular distribution of the scattered XeF_2, the XeF_2 velocity distribution, etc. These unknown quantities intrinsic to the process being studied may depend on the independent variable or any of the other experimental conditions. The observed signal can be represented by a function that depends on a number of parameters, $I(x;\{y,z,\ldots\};\{a_1(x,y,z,\ldots),a_2(x,y,z,\ldots),\ldots\})$, where x is the independent experimental variable, (i.e. exposure time in the example above), $\{y,z,\ldots\}$ are the experimental conditions (i.e. incident flux, detector efficiency, etc in the example above), and $\{a_1(x,y,z,\ldots),a_2(x,y,z,\ldots),\ldots\}$ are variables intrinsic to the process being observed.

There are certain rare occasions when the detected signal is the end result. More often however, it is necessary to fit the observed data to some function $I_{fit}(x;\{y,z,...\};\{A_1,A_2,...\})$ in order to derive useful parameters from the observed data. In a perfect world, the parameters of the fit to the data $\{A_1,A_2,...\}$ would exactly correspond to the intrinsic variables of the process $\{a_1,a_2,...\}$. However, in the real world this is rarely the case.

There are three major thrusts in error analysis: 1) estimating the error of the measurement itself, 2) determining the error of the fit parameters, and 3) propagating the error in any subsequent calculations. Each of these processes will be described in detail below in Section I. In Section II, these ideas will be applied to the error analysis involved in the determination of the dissociative chemisorption probability from thermal desorption data as described in chapter 2. Section III will describe the propagation of error for the calculation of flux, average velocity and average energy from the observed time of flight spectra, as described in chapter 3.

I. Theory

I.A. Estimation of the error of each measurement

The variation of an individual data point can be described by a statistical distribution. The two most common distributions are the Poisson distribution and the Gaussian, or "normal" distribution. Any measurement obtained by counting events is described by a Poisson distribution, while most other measurements are described by a Gaussian distribution. For instance, the channeltron of the mass spectrometer detector counts the number of ions, and so the number of counts in a given period of time is described by a Poisson distribution. Alternatively, the measurement of the pressure in the main chamber is governed by a Gaussian distribution. In general when the number of counts is extremely large the Poisson distribution converges to the Gaussian distribution.

The error for a measurement that is described by Poisson statistics is given by the square root of the number of counts.

$$\sigma_{I(x)} = \sqrt{I(x)} \qquad (1)$$

where x is the value of the independent variable and I(x) is the detected signal.

For measurements described by Gaussian statistics, the situation is slightly more complicated. If one makes N measurements, then the mean detected signal is given by

$$\bar{I}(x) = \frac{1}{N} \sum_{i=1}^{N} I_i(x) \qquad (2)$$

where $I_i(x)$ is the detected signal of the ith measurement.

The error of each measurement is given by the standard deviation, which is defined to be

$$\sigma_{I(x)} = \sqrt{\frac{1}{N-1} \sum_{i=1}^{N} (I_i(x) - \bar{I}(x))^2} \qquad (3)$$

However, the mean value has less error than each individual measurement. The standard deviation of the mean (SDOM) is given by

$$\sigma_{\bar{I}(x)} = \frac{\sigma_{I(x)}}{\sqrt{N}} \qquad (4)$$

I.B. Estimation of the error in the fit parameters

Non-linear least-squares fitting is a quite complicated topic. A thorough review of the issues involved is given elsewhere[2]. In general, it requires a multi-dimensional search through the phase space defined by the parameters of the fit. This phase space search attempts to minimize the discrepancy between the fit and the data, given by the chi-square value:

$$\chi^2 \equiv \sum_{i=1}^{N} \left(\frac{I_i(x) - I_{fit}(x_i)}{\sigma_{I_i(x)}} \right)^2 \qquad (5)$$

where x_i is the value of the independent variable for the ith measurement, $I_i(x)$ is the detected signal for the ith measurement, $\sigma_{I_i(x)}$ is the standard deviation of the ith measurement, and N is the total number of measurements. Note that it is necessary to supply the fitting program with the standard deviation of each measurement, $\sigma_{I_i(x)}$, using the equations given in the previous section.

The fitting is performed using the IGOR[3] data analysis program. This program uses the Levenberg-Marquardt method, which is detailed elsewhere[2]. This fitting procedure results in a set of best-fit parameters $\{A_1, A_2, \ldots\}$, and a covariance matrix, [C] which has the covariances of the parameters $\{A_1, A_2, \ldots\}$:

$$\sigma_{A_i A_j} = C_{ij} \tag{6}$$

Note that these covariances relate to the fit parameters, not the individual measurements. The main diagonal of the covariance matrix contains the variance of each parameter[4]:

$$\sigma_{A_i A_i} \equiv \sigma_{A_i}^2 = C_{ii} \tag{7}$$

and therefore, the standard deviation of each fit parameter is given by:

$$\sigma_{A_i} = \sqrt{C_{ii}} \tag{8}$$

I.B.1. Determination of the covariance matrix

This section gives an introduction to the determination of the covariance matrix, reproduced in large part from Reference 2. The interested reader should consult Reference 2 and the citations contained therein for a more complete explanation. The following description is for linear least squares fitting only. Non-linear least squares fitting follows similar lines, but the problem must be solved in an iterative manner. For a description of non-linear least squares fitting, see Reference 2.

The first step in least-squares fitting is to take the derivative of χ^2, given by Eq. 5, with respect to the M different fit parameters $\{A_1, A_2, ..., A_M\}$ to obtain a set of N equations that must hold when χ^2 is minimized:

$$0 = \sum_{i=1}^{N} \left(\frac{I_i(x) - I_{fit}(x_i)}{\sigma_{I_i(x)}^2} \right) \left(\frac{\partial I_{fit}(x_i)}{\partial A_k} \right) \quad k = 1,2,...,M \tag{9}$$

In the case of linear least-squares fitting, the data are fit to a function of the form

$$I_{fit}(x_i) = \sum_{k=1}^{M} A_k X_k(x_i) \tag{10}$$

where $X_1(x_i),...,X_M(x_i)$ are known as the basis functions, and are arbitrary fixed functions of x. Note that the term "linear" refers only to the dependence of $I_{fit}(x_i)$ on the fit parameters – the form that the basis functions may take has no restrictions. Using Eq. 10, Eq. 9 can be rewritten in the following way:

$$0 = \sum_{i=1}^{N} \frac{1}{\sigma_{I_i(x)}^2} \left(I_i(x) - \sum_{j=1}^{M} A_j X_j(x_i) \right) X_k(x_i) \quad k = 1,2,...,M \tag{11}$$

Eq. 11 can be transformed into a matrix equation using the following substitutions:

$$\alpha_{kj} = \sum_{i=1}^{N} \frac{X_j(x_i) X_k(x_i)}{\sigma_{I_i(x)}^2} \qquad \beta_k = \sum_{i=1}^{N} \frac{I_i(x) X_k(x_i)}{\sigma_{I_i(x)}^2} \tag{12}$$

which results in the following matrix form of Eq. 11:

$$\sum_{j=1}^{M} \alpha_{kj} A_j = \beta_k \tag{13}$$

This equation is called the normal equation of the least-squares problem, and can be solved using standard methods.[2] The covariance matrix is defined as the inverse matrix of $[\alpha]$. That is:

$$C_{ij} \equiv \alpha_{ij}^{-1} \tag{14}$$

I.C. Propagation of error

The best-fit parameters $\{A_1, A_2, \ldots\}$ found by fitting the data can be used in subsequent calculations. Any such calculation can be represented by the general functional form $f(\theta_1, \theta_2, \ldots, \theta_n)$, where θ can be the independent variable x, the experimental conditions $\{y, z, \ldots\}$, or the fit parameters $\{A_1, A_2, \ldots\}$. The propagated error is then given by[4]:

$$\left(\sigma_f\right)^2 = \sum_{i=1}^{n} \sum_{j=1}^{n} \sigma_{ij} \left(\frac{\partial f}{\partial \theta_i}\right)\left(\frac{\partial f}{\partial \theta_j}\right) \tag{15}$$

where σ_f is the standard deviation of $f(\theta_1, \theta_2, \ldots, \theta_n)$, and σ_{ij} is the covariance between θ_i and θ_j. If the errors are uncorrelated, then $\sigma_{ij} = 0$ for $i \neq j$, and the above formula simplifies to:

$$\left(\sigma_f\right)^2 = \sum_{i=1}^{n} \sigma_i^2 \left(\frac{\partial f}{\partial \theta_i}\right)^2 \tag{16}$$

since $\sigma_{ii} \equiv \sigma_i^2$.

II. Propagation of error in the dissociative chemisorption probability

II.A. Determination of the beam flux

The measurement of the absolute beam flux for a seeded supersonic expansion is detailed elsewhere.[5] The method used to determine the absolute flux of a neat effusive expansion follows a slightly different procedure. Briefly, a beam of neat Ar at the same stagnation pressure as the reactant beam is directed into the chamber containing the crystal. The pressure rise in the chamber P is measured with a nude Bayard-Alpert ionization gauge and calibrated to the absolute pressure by accounting for the ionization efficiency of Ar. The absolute flux of Ar into the chamber Q is then calculated using the formula

$$I_{in}^{Ar} = \frac{PC_F S}{kTA} \tag{17}$$

where P is the pressure in the main chamber, C_F is the ion gauge correction factor for the ionization efficiency of Ar, S is the pumping speed of Ar, T is the temperature of the chamber and A is the area of the crystal that the beam impinges on, defined by the incident angle of the beam as well as the geometry of the nozzle and the collimating slits. Each of these factors and their uncertainties will be considered in turn below.

The main chamber pressure is measured by a nude Bayard-Alpert ionization gauges, which determines pressure based on the ion current collected by a thin wire as the ambient gas is ionized by electron bombardment from a heated filament. The ion current collected is proportional to the density and hence the pressure of the ambient gas. The proportionality constant, however, depends on the identity of the gas being ionized. Ionization gauges are typically calibrated for N_2. A correction factor, C_F, accounting for the different ionization efficiency of the gas being measured must be used to correct the gauge reading. This correction factor is calculated by expanding a known pressure of Ar in a small calibrated volume into the larger volume of the main chamber with the gate valve closed, where the pressure of the gas in the small volume is measured using a Baratron capacitance manometer. The correction factor is determined by the ratio of the predicted main chamber pressure rise (given by the ratio of the small to large volume times the initial pressure of Ar) divided by the observed main chamber pressure rise:

$$C_F = \frac{P_{init}^{Ar} \cdot V_{small}}{P_{MC}^{obs} \cdot V_{MC}} \tag{18}$$

Since the errors are independent and therefore uncorrelated, the error in C_F can be propagated using Eq. 16:

$$\sigma_{C_F} = \sqrt{\left(\sigma_{P_{init}^{Ar}}\left(\frac{V_{small}}{P_{MC}^{obs} \cdot V_{MC}}\right)\right)^2 + \left(\sigma_{V_{small}}\left(\frac{P_{init}^{Ar}}{P_{MC}^{obs} \cdot V_{MC}}\right)\right)^2 + \left(\sigma_{P_{MC}^{obs}}\left(\frac{V_{small} \cdot P_{init}^{Ar}}{P_{MC}^{obs\,2} \cdot V_{MC}}\right)\right)^2 + \left(\sigma_{V_{MC}}\left(\frac{V_{small} \cdot P_{init}^{Ar}}{P_{MC}^{obs} \cdot V_{MC}^{2}}\right)\right)^2} \tag{19}$$

The uncertainties used in Eq. 19 have been reported previously.[6] However, the small volume has since been re-calibrated to 2.136 ± 0.008 mL by comparing the weight of the empty vessel with the weight of the vessel after the small volume has been filled with distilled water and using the known density of water. To find C_F, five experimental runs are performed at different stagnation pressures. The uncertainties shown above are propagated for each experimental run. These five experimental runs are then averaged to obtain the final value for C_F. To obtain the uncertainty in the average value of C_F, the following formula is used:

$$\sigma_{avg}^{C_F} = \frac{1}{N} \sqrt{\sum_{i=1}^{N} \left(\sigma_i^{C_F} \right)^2} \qquad (20)$$

When the error is propagated, and the five measurements are averaged, the final value is $C_F = 0.987 \pm 0.039$.

The collimating slits are rectangular in shape, and therefore the impinging beam is incident on a rectangular area of the crystal. This rectangular area is known as the "beam spot." The dimensions of the beam spot are determined from the source-aperture-crystal geometry. The uncertainty in the area of the beam spot, A, is solely due to the uncertainty in the dimensions of the defining aperture. The defining aperture has dimensions 0.142 ± 0.001 in. height and 0.100 ± 0.001 in. width. If we make the assumption that the uncertainty in the source-crystal separation is small, then the final beam spot height, h, and width, w, are given by ray tracing, and the uncertainty is given by:

$$\sigma_h = \frac{h}{h_{aperture}} \sigma_{h_{aperture}}$$

$$\sigma_w = \frac{w}{w_{aperture}} \sigma_{w_{aperture}} \qquad (21)$$

The area of the beam spot is then given by:

$$A = h \cdot w \qquad (22)$$

Since the uncertainty in h and w are independent and therefore uncorrelated, the error in A can be propagated using Eq. 16:

$$\sigma_{Aspot} = \left| A_{spot} \right| \sqrt{\left(\frac{\sigma_h^{Aspot}}{h_{Aspot}} \right)^2 + \left(\frac{\sigma_w^{Aspot}}{w_{Aspot}} \right)^2} \qquad (23)$$

The thermal desorption studies shown in Chapter 2 were performed with the Teflon nozzle and an incident angle of 35°. For this experimental configuration A=6.878±0.084x10^{-5} m^2. The time-of-flight studies shown in Chapter 3 were performed with the Teflon nozzle and an incident angle of 20°. For this experimental configuration A=5.995±0.069x10^{-5} m^2. The calculations below are given only for the experimental configuration used for the thermal desorption experiments shown in Chapter 2. However, the calculations for the time-of-flight experiments in Chapter 3 are entirely analogous.

The values and the uncertainties for each of the parameters used in Eq. 17 and Eq. 25 to calculated the beam flux and the uncertainty in the beam flux are given below:

Quantity	Symbol	Measured value
Observed Ar MC pressure rise	P	7.2±0.1x10^{-10} torr
Ar ion gauge correction factor	C_F	0.987±0.039
Pumping speed of Ar	S	1070±11 liters/s
Area of beam spot on crystal	A	6.878±0.084x10^{-5} m^2 (tef. noz. TDS)

Beam fluxes are expressed in units of particles per unit time per unit area (typically particles s^{-1} cm^{-2}). A particularly well-suited unit for flux impinging onto a single crystal surface is ML s^{-1}, were a monolayer (ML) is defined as one particle per surface site. This unit conversion is calculated using the density of Si atoms on the Si(100) surface, 6.84x10^{14} Si atoms cm^{-2}, giving the flux of the incident Ar beam:

$$I_{in}^{Ar} = \frac{PC_F S}{kTA} = 0.0520 \pm 0.0023 \text{ ML/s} \tag{24}$$

Since the errors are independent and therefore uncorrelated, the propagated error can be calculated using Eq. 16:

$$\sigma_{I_{in}^{Ar}} = \sqrt{\left(\sigma_P \frac{C_F S}{kTA}\right)^2 + \left(\sigma_{C_F} \frac{PS}{kTA}\right)^2 + \left(\sigma_S \frac{PC_F}{kTA}\right)^2 + \left(\sigma_{A_{spot}} \frac{PC_F S}{kTA^2}\right)^2} \tag{25}$$

In the case of a purely effusive expansion, the flux of a F_2 or XeF_2 beam is given by

$I_{in} = I_{in}^{Ar} \sqrt{\dfrac{M_{Ar}}{M_{beam}}}$ where M_{Ar} and M_{beam} are the molar masses of Ar and the F_2 or XeF_2 beam,

respectively. However, since we have a quasi-effusive expansion, we cannot use this formula directly. Instead, the average velocity of each molecular beam must be measured, and since the flux is directly proportional to the velocity, the difference in the flux of two beams is given by

the ratio of their average velocities: $I_{in} = I_{in}^{Ar} \dfrac{v_{avg}^{beam}}{v_{avg}^{Ar}}$. Since there are two F atoms per molecule for

both F_2 and XeF_2, the incident flux in terms of F atoms is:

$$I_{in}(\text{F atoms/s}) = 2 \cdot I_{in}^{Ar} \frac{v_{avg}^{beam}}{v_{avg}^{Ar}} \tag{26}$$

And the propagated uncertainty is given by:

$$\sigma_{I_{in}^{beam}} = 2 \cdot \sqrt{\left(\sigma_{I_{in}^{Ar}} \frac{v_{avg}^{beam}}{v_{avg}^{Ar}}\right)^2 + \left(\sigma_{v_{avg}^{Ar}} \frac{I_{in}^{Ar} \cdot v_{avg}^{beam}}{\left(v_{avg}^{Ar}\right)^2}\right)^2 + \left(\sigma_{v_{avg}^{beam}} \frac{I_{in}^{Ar}}{v_{avg}^{Ar}}\right)^2} \tag{27}$$

where the uncertainties in the average velocities are found from the Maxwell-Boltzmann fit to the observed time-of-flight distributions of the incident beams using Eq. 77, as described in Section III.B of the current Appendix. For the thermal desorption measurements shown in Chapter 2, the molecular beams were expanded from the Teflon nozzle at a stagnation pressure

of 0.62 torr as measured by the Baratron capacitance manometer. For these experimental conditions, the average velocities of the incident Ar, F_2 and XeF_2 beams are 499.6±7.8, 514.9±8.7, and 256.2±6.1 respectively. These velocities give F_2 and XeF_2 beam fluxes of 0.1072±0.0054 and 0.0534±0.0028 ML/s respectively.

II.B. Analysis of TDS calibration curves

II.B.1. Determination of the total thermal desorption yield

The amount of fluorine on the surface is determined from the raw counts of the thermal desorption spectrum integrated over the entire temperature range. Thermal desorption spectra, such as shown in Figure 1 of Chapter 2, are measured by monitoring the SiF_3^+ and SiF_2^+ signals, corresponding to SiF_4 and SiF_2 desorption products, as a function of surface temperature. The baseline of a thermal desorption spectrum is determined by fixing the endpoints of the baseline at the average of the first fifty points and the last fifty points. The integrated desorption signals for SiF_3^+ and SiF_2^+ are determined by summing the recorded signal over the entire temperature range after the baseline has been subtracted. The uncertainty in the integrated desorption signal is determined by fitting the thermal desorption features, and propagating the error in the integrated area of these functions. It should be emphasized that the fits to the thermal desorption spectra are only used to find the error – the integrated desorption signal is taken directly from the data.

The function used to fit the SiF_3^+ thermal desorption spectra is the sum of two Gaussian features:

$$F^{SiF_3^+}(T) = \text{baseline} + A_1 \cdot \exp\left(-\left(\frac{(T-B_1)}{C_1}\right)^2\right) + A_2 \cdot \exp\left(-\left(\frac{(T-B_2)}{C_2}\right)^2\right) \tag{28}$$

where the fit parameters are A_1, B_1, C_1, A_2, B_2, and C_2. The baseline is fixed as described above.

The function used to fit the SiF_2^+ thermal desorption spectra is the sum of a Gaussian and a composite exponential function, given by two exponential decays on either side of T_{max}:

$$F^{SiF_2^+}(T) = baseline + A_1 \cdot exp\left(-\left(\frac{(T-B_1)}{C_1}\right)^2\right) + A_2 \cdot exp((T-T_{max}) \cdot D_1) \qquad (T \leq T_{max}) \qquad (29)$$

$$F^{SiF_2^+}(T) = baseline + A_1 \cdot exp\left(-\left(\frac{(T-B_1)}{C_1}\right)^2\right) + A_2 \cdot exp(-(T-T_{max}) \cdot D_2) \qquad (T > T_{max}) \qquad (30)$$

where the fit parameters are A_1, B_1, C_1, A_2, D_2, and T_{max}.

The spectra are fit using $\sqrt{N}$ for the standard deviation of each point, where N is the number of counts recorded at each temperature during the temperature ramp. Once the best-fit parameters are found, the integrated SiF_3^+ counts is given by:

$$\int_0^\infty F^{SiF_3^+}(T)dT = \int_0^\infty A_1 \cdot exp\left(-\left(\frac{(T-B_1)}{C_1}\right)^2\right)dT + \int_0^\infty A_2 \cdot exp\left(-\left(\frac{(T-B_2)}{C_2}\right)^2\right)dT \qquad (31)$$

Given that the thermal desorption features go to zero at low temperatures, it is a good approximation to extend the limits of integration on the integrals shown above:

$$\int_0^\infty F^{SiF_3^+}(T)dT \cong \int_{-\infty}^\infty A_1 \cdot exp\left(-\left(\frac{(T-B_1)}{C_.}\right)^2\right)dT + \int_{-\infty}^\infty A_2 \cdot exp\left(-\left(\frac{(T-B_2)}{C_2}\right)^2\right)dT \qquad (32)$$

The definite integral of a Gaussian function is given by:

$$\int_{-\infty}^\infty exp(-ax^2)dx = \sqrt{\frac{\pi}{a}} \qquad (33)$$

which yields, after some relatively simple algebra:

$$\int_0^\infty F^{SiF_3^+}(T)dT \cong \sqrt{\pi}(A_1 C_1 + A_2 C_2) \qquad (34)$$

The integrated SiF_2^+ counts is given by:

$$\int_0^\infty F^{SiF_2^+}(T)dT = \int_0^\infty A_1 \cdot \exp\left(-\left(\frac{(T-B_1)}{C_1}\right)^2\right)dT + \int_0^{T_{max}} A_2 \cdot \exp((T-T_{max})\cdot D_1)dT + \int_{T_{max}}^\infty A_2 \cdot \exp(-(T-T_{max})\cdot D_2)dT \qquad (35)$$

Again, since the thermal desorption features go to zero at low temperature, it is a good approximation to extend the limits of integration:

$$\int_0^\infty F^{SiF_2^+}(T)dT \cong \int_{-\infty}^\infty A_1 \cdot \exp\left(-\left(\frac{(T-B_1)}{C_1}\right)^2\right)dT + \int_{-\infty}^{T_{max}} A_2 \cdot \exp((T-T_{max})\cdot D_1)dT + \int_{T_{max}}^\infty A_2 \cdot \exp(-(T-T_{max})\cdot D_2)dT \qquad (36)$$

$$\int_0^\infty F^{SiF_2^+}(T)dT \cong A_1 C_1 \sqrt{\pi} + \left(\frac{A_2}{D_1}\exp((T-T_{max})\cdot D_1)\right)_{-\infty}^{T_{max}} + \left(-\frac{A_2}{D_2}\exp(-(T-T_{max})\cdot D_2)\right)_{T_{max}}^\infty \qquad (37)$$

$$\int_0^\infty F^{SiF_2^+}(T)dT \cong A_1 C_1 \sqrt{\pi} + A_2\left(\frac{1}{D_1}+\frac{1}{D_2}\right) \qquad (38)$$

The propagation of error for the integrated signals is found using Eq. 15 and the covariance matrix, which is reported by the fitting algorithm:

$$\sigma_{\int_0^\infty F^{SiF_3^+}(T)dT} = \sqrt{\pi}\cdot\sqrt{\begin{array}{l}(\sigma_{A_1}C_1)^2+(\sigma_{C_1}A_1)^2+(\sigma_{A_2}C_2)^2+(\sigma_{C_2}A_2)^2+\sigma_{A_1C_1}C_1A_1+\sigma_{A_1A_2}C_1C_2+\\ \sigma_{A_1C_2}C_1A_2+\sigma_{C_1A_2}A_1C_2+\sigma_{C_1C_2}A_1A_2+\sigma_{A_2C_2}C_2A_2\end{array}} \qquad (39)$$

$$\sigma_{\int_0^\infty F^{SiF_2^+}(T)dT} = \sqrt{\begin{array}{l}(\sigma_{A_1}C_1\sqrt{\pi})^2+(\sigma_{C_1}A_1\sqrt{\pi})^2+\left(\sigma_{A_2}\left(\frac{1}{D_1}+\frac{1}{D_2}\right)\right)^2+\left(\sigma_{D_1}A_2\frac{1}{D_1^2}\right)^2+\left(\sigma_{D_2}A_2\frac{1}{D_2^2}\right)^2+\\[2mm]\sigma_{A_1C_1}C_1A_1\sqrt{\pi}+\sigma_{A_1A_2}C_1\left(\frac{1}{D_1}+\frac{1}{D_2}\right)\sqrt{\pi}+\sigma_{A_1D_1}C_1A_2\frac{1}{D_1^2}\sqrt{\pi}+\sigma_{A_1D_2}C_1A_2\frac{1}{D_2^2}\sqrt{\pi}+\\[2mm]\sigma_{C_1A_2}A_1\left(\frac{1}{D_1}+\frac{1}{D_2}\right)\sqrt{\pi}+\sigma_{C_1D_1}A_1A_2\frac{1}{D_1^2}\sqrt{\pi}+\sigma_{C_1D_2}A_1A_2\frac{1}{D_2^2}\sqrt{\pi}+\\[2mm]\sigma_{A_2D_1}\left(\frac{1}{D_1}+\frac{1}{D_2}\right)A_2\frac{1}{D_1^2}\sqrt{\pi}+\sigma_{A_2D_2}\left(\frac{1}{D_1}+\frac{1}{D_2}\right)A_2\frac{1}{D_2^2}\sqrt{\pi}\end{array}} \qquad (40)$$

Although this procedure is used for the results presented in Chapters 2 and 3, a simpler approach is given as follows. Explicitly, the integrated counts are given by the sum of the thermal desorption signal minus the baseline:

$$\text{integrated counts} = \sum_{i=1}^N I_i - N\left(\frac{I_{avg}^{T_0}+I_{avg}^{T_{max}}}{2}\right) \qquad (41)$$

where N is the number of bins, I_i is the number of counts in the ith bin, and $I_{avg}^{T_0}$ and $I_{avg}^{T_{max}}$ are the average of the first fifty points and the last fifty points respectively. The propagated error is then given by:

$$\sigma_{\text{integrated counts}} = \sqrt{\sum_{i=1}^{N}\left(\sqrt{I_i}\right)^2 + \left(\frac{N}{2}\sigma_{I_{avg}^{T_0}}\right)^2 + \left(\frac{N}{2}\sigma_{I_{avg}^{T_{max}}}\right)^2} = \sqrt{\sum_{i=1}^{N}I_i + \left(\frac{N}{2}\sigma_{I_{avg}^{T_0}}\right)^2 + \left(\frac{N}{2}\sigma_{I_{avg}^{T_{max}}}\right)^2} \qquad (42)$$

where the error in the number of counts in each bin is given by Poisson statistics and the error in the average of the first fifty points and the last fifty points is given by Eq. 4. This method is obviously much simpler than the fitting-based method given above, and therefore should be used in future thermal desorption analysis.

The SiF_3^+ and the SiF_2^+ integrated counts are converted to a total thermal desorption yield, as described briefly in Chapter 2.[6] The total thermal desorption yield, $\zeta(t)$, is given by:

$$\zeta(t) = (SiF_2^+ \text{ integrated counts}) + 0.12 * (SiF_3^+ \text{ integrated counts}) \qquad (43)$$

where the factor of 0.12 takes into account the relative detection sensitivities of SiF_2 and SiF_4, the factor of two more fluorine atoms that SiF_4 has relative to SiF_2, the different velocity and angular distributions of the desorbing SiF_2 and SiF_4 species, and their relative ionization cross sections and quadrupole transmissions. The uncertainty in $\zeta(t)$ is given by the propagated uncertainty from the SiF_3^+ and the SiF_2^+ integrated signals. The uncertainty in the weighting factor 0.12 is not propagated. Specifically,

$$\left(\sigma_{\zeta(t)}\right)^2 = \left(\sigma_{(SiF_2^+ \text{ integrated desorption signal})}\right)^2 + \left(0.12 * \sigma_{(SiF_3^+ \text{ integrated desorption signal})}\right)^2 \qquad (44)$$

II.B.2. Determination of the coverage calibration curves

The total desorption yield, $\zeta(t)$, shown in Chapter 2, Figure 2, is fit to a single exponential function:

$$\zeta(t) = A + Be^{-Ct} \qquad (45)$$

The fit results in a set of best-fit parameters and a covariance matrix. The thermal desorption yields are converted to coverage using the average thermal desorption yields of the long-time F_2 exposure, ζ_{sat}, which is known to be a measure of the saturation coverage, θ_{sat}:

$$\theta(t) = \frac{\zeta(t)}{\zeta_{sat}} \theta_{sat} = \frac{\left(A + Be^{-Ct}\right)}{\zeta_{sat}} \theta_{sat} \tag{46}$$

The determination of θ_{sat} has been described previously, and was found to be $\theta_{sat}^{F_2} = 0.94 \pm 0.11$ ML[5]. However, this error reflects a 95% confidence limit, which is essentially $\pm 2\sigma$. To be consistent with the rest of the error analysis, the standard deviation should be used, not the 95% confidence limit. Therefore, $\theta_{sat}^{F_2} = 0.94 \pm 0.06$ ML (standard deviation) is used to calculate the propagated error. The propagated error is converted back to a 95% confidence limit at the end of the calculation.

The propagated error can be calculated using Eq. 15:

$$\sigma_{\theta(t)} = \sqrt{\left(\frac{\theta_{sat}}{\zeta_{sat}}\right)^2 \left(\begin{array}{c} \sigma_A^2 + \left(\sigma_B e^{-Ct}\right)^2 + \left(\sigma_C Bte^{-Ct}\right)^2 + 2\sigma_{AB}e^{-Ct} \\ -2\sigma_{AC}Bte^{-Ct} - 2\sigma_{BC}Bte^{-2Ct} \end{array}\right) + \left(\sigma_{\zeta_{sat}} \frac{\theta(t)}{\zeta_{sat}}\right)^2 + \left(\sigma_{\theta_{sat}} \frac{\theta(t)}{\theta_{sat}}\right)^2} \tag{47}$$

Since the uncertainties in ζ_{sat} and θ_{sat} are independent of each other and of the uncertainties in the fit parameters, any covariance involving ζ_{sat} and θ_{sat} is zero.

II.C. Error in the coverage at the helium diffraction specular recovery

The recovery of the helium diffraction specular feature is shown in Chapter 2, Figure 6. Theoretically, since the expression for the coverage with respect to exposure time is known, the exposure time at which the specular recovery occurs could be used to calculate the coverage at the recovery peak. However, there is a complicating factor, which is that the helium diffraction data were measured using a different beam flux, I_{in}^{He}, than the TDS data, I_{in}^{TDS}. Note that I_{in}^{He} refers to the beam flux of F_2 or XeF_2 for the He diffraction experiments, not the incident flux of

the He beam. In order to find the nominal exposure time at the recovery peak, the difference in the fluxes must be taken into account by multiplying the observed dose time at the recovery peak by the ratio of the fluxes:

$$t^{TDS} = \frac{I_{in}^{He}}{I_{in}^{TDS}} t^{He} \tag{48}$$

where t^{He} is the exposure time in the He diffraction measurement and t^{TDS} is the exposure time in the TDS measurement. This substitution results in the following equation for the coverage:

$$\theta(t^{He}) = \frac{\left(A + Be^{-C\frac{I_{in}^{He}}{I_{in}^{TDS}}t^{He}} \right)}{\zeta_{sat}} \theta_{sat} \tag{49}$$

The propagated error can be calculated using Eq. 15:

$$(\sigma_{\theta(t^{He})})^2 = \left(\frac{\theta_{sat}}{\zeta_{sat}}\right)^2 \cdot \left[\sigma_A^2 + \left(\sigma_B e^{-C\left(\frac{I_{in}^{He}}{I_{in}^{TDS}}t^{He}\right)}\right)^2 + \left(\sigma_C B\left(\frac{I_{in}^{He}}{I_{in}^{TDS}}t^{He}\right)e^{-C\left(\frac{I_{in}^{He}}{I_{in}^{TDS}}t^{He}\right)}\right)^2 + \right.$$
$$\left. 2\sigma_{AB}e^{-C\left(\frac{I_{in}^{He}}{I_{in}^{TDS}}t^{He}\right)} - 2\sigma_{AC}B\left(\frac{I_{in}^{He}}{I_{in}^{TDS}}t^{He}\right)e^{-C\left(\frac{I_{in}^{He}}{I_{in}^{TDS}}t^{He}\right)} - 2\sigma_{BC}B\left(\frac{I_{in}^{He}}{I_{in}^{TDS}}t^{He}\right)e^{-2C\left(\frac{I_{in}^{He}}{I_{in}^{TDS}}t^{He}\right)} \right]$$

$$+\left(\sigma_{\zeta_{sat}}\frac{\theta(t^{He})}{\zeta_{sat}}\right)^2 + \left(\sigma_{\theta_{sat}}\frac{\theta(t^{He})}{\theta_{sat}}\right)^2 + \left(\sigma_{I_{in}^{He}}\frac{\theta_{sat}}{\zeta_{sat}}\left(\frac{BCt^{He}e^{-C\left(\frac{I_{in}^{He}}{I_{in}^{TDS}}t^{He}\right)}}{I_{in}^{TDS}}\right)\right)^2 + \left(\sigma_{I_{in}^{TDS}}\frac{\theta_{sat}}{\zeta_{sat}}\left(\frac{BCI_{in}^{He}t^{He}e^{-C\left(\frac{I_{in}^{He}}{I_{in}^{TDS}}t^{He}\right)}}{(I_{in}^{TDS})^2}\right)\right)^2 \tag{50}$$

Again, since the uncertainties in I_{in}^{He} and I_{in}^{TDS} are independent of each other and the other uncertainties, the covariance is zero for any of these cross terms. The uncertainty in the exposure times is negligible because the shutter response time (0.01s, as shown in Chapter 3 Section II) is small with respect to the exposure times (between 0.5s – 60s). Equations 49 and 50 yield 0.89±0.07 ML for the coverage at the recovery peak shown in Chapter 2, Figure 6. The major

contribution to this uncertainty is the uncertainty of the saturation coverage. The 95%

confidence limit for the uncertainty in the coverage, which is essentially $\pm 2\sigma$, is 0.89$\pm$0.14 ML.

II.D. Error in the dissociative chemisorption probability

The dissociative chemisorption probability, also known as P_{ads}, is defined as the derivative of

coverage with respect to exposure:

$$P_{ads} = \frac{d\theta}{d\varepsilon} \qquad (51)$$

where θ is the coverage and ε is the exposure. In the case of classic dissociative chemisorption,

P_{ads} is also the total reaction probability, P_{rxn}, defined as the probability that an incident particle

will react with the surface. However, this is not the case in the interaction of F_2 and XeF_2 with Si

due to the presence of atom abstraction, which is a reactive event that only leaves half of the

incident reactant flux on the surface. A more complete description of any reaction that involves

atom abstraction involves the determination of P_0, P_1 and P_2, which are the probabilities of

unreactive scattering, single atom abstraction and two-atom adsorption respectively. The

reaction probabilities P_0, P_1 and P_2 can be related to P_{ads} using the formula $P_{ads} = 0.5*P_1 + P_2$. In

the case of the interaction of XeF_2 with Si, two factors preclude a determination of P_1. First, the

absolute ionization cross section of XeF cannot be determined due to the fact that a source of

pure XeF is unavailable. Second, some of the XeF produced from single atom abstraction

dissociates, leaving a gas-phase Xe atom and a gas-phase F atom. On the other hand, P_{ads} is

quite simple to obtain from the integrated thermal desorption spectra, and gives a lower bound to

the total reaction probability due to the fact that any abstraction event will leave only half the

incident reactant flux on the surface.

To determine P_{ads} from Eq. 51 the exposure time must be converted to absolute exposure

in monolayers using the incident flux:

$$\varepsilon = I_{in}t \tag{52}$$

With this definition for the absolute exposure, Eq. 46 becomes:

$$\theta(\varepsilon) = \frac{\left(A + Be^{-C\varepsilon/I_{in}}\right)}{\zeta_{sat}}\theta_{sat} \tag{53}$$

To find P_{ads} from Eq. 51, the derivative of coverage with respect to exposure is calculated:

$$P_{ads}(\varepsilon) = \frac{d}{d\varepsilon}\frac{\left(A + Be^{-C\varepsilon/I_{in}}\right)}{\zeta_{sat}}\theta_{sat} = -\frac{BCe^{-C\varepsilon/I_{in}}}{I_{in}\zeta_{sat}}\theta_{sat} \tag{54}$$

Since parameter B is negative, this formula yields an overall positive value for P_{ads}. To find P_{ads} as a function of coverage, Eq. 53 is solved for $\varepsilon(\theta)$ and plugged into Eq. 54:

$$\varepsilon(\theta) = -\frac{I_{in}}{C}\ln\left(\frac{\zeta_{sat}\theta}{B\theta_{sat}} - \frac{A}{B}\right) \tag{55}$$

$$P_{ads}(\theta) = -\frac{BC\left(\frac{\zeta_{sat}\theta}{B\theta_{sat}} - \frac{A}{B}\right)}{I_{in}\zeta_{sat}}\theta_{sat} = \frac{C}{I_{in}}\left(\frac{A\theta_{sat}}{\zeta_{sat}} - \theta\right) \tag{56}$$

In order to find the propagated error in P_{ads}, Eq. 46 (reproduced below in a slightly modified form) is plugged into Eq. 56 in order to determine $P_{ads}(t)$:

$$\theta(t) = \frac{A\theta_{sat}}{\zeta_{sat}} + \frac{Be^{-Ct}\theta_{sat}}{\zeta_{sat}} \tag{Eq. 46}$$

$$P_{ads}(t) = -\frac{BCe^{-Ct}\theta_{sat}}{I_{in}\zeta_{sat}} \tag{57}$$

This results in the following remarkably simple formula for the propagated error:

$$\sigma_{P_{ads}} = P_{ads}\sqrt{\left(\frac{\sigma_B}{B}\right)^2 + \left(\sigma_C\left(\frac{1}{C} - t\right)\right)^2 + \frac{2\sigma_{BC}}{B}\left(\frac{1}{C} - t\right) + \left(\frac{\sigma_{\theta_{sat}}}{\theta_{sat}}\right)^2 + \left(\frac{\sigma_{I_{in}}}{I_{in}}\right)^2 + \left(\frac{\sigma_{\zeta_{sat}}}{\zeta_{sat}}\right)^2} \tag{58}$$

This formula gives the error bars shown in Chapter 2, Figure 4. Again, the uncertainty in the dose times is negligible because the shutter response time (0.01s, as shown in Chapter 3 Section II) is small with respect to the exposure times used (between 0.5s – 60s).

III. Propagation of error in time-of-flight spectra

One of the capabilities of our apparatus is the measurement of the time-of-flight (TOF) spectra of various species. It is often desirable to fit these spectra to a Maxwell-Boltzmann distribution that has been modified to include a flow velocity. Since our detector is sensitive to number density, this distribution is given by the formula:

$$F(t) = A \frac{L^3}{t^4} \exp\left[-\left(\frac{mL^2}{2kT}\right)\left(\frac{1}{t} - \frac{1}{t_f}\right)^2 \right] \tag{59}$$

where t is the flight time, L is the path length as measured between the chopper wheel and the ionization region of the detector, m is the mass, and t_f is the flow time, which is related to the flow velocity by $t_f = L/v_f$. It has been shown that for cross-correlation time-of-flight measurements, the standard deviation is the same for all points in the deconvoluted spectrum, and is equal to the square root of the total counts collected in the time of flight spectrum[6]. The flux, average velocity, and average energy of the distributions can be calculated using the following:

$$I = \int_0^\infty v \cdot F(t) \, dt \tag{60}$$

$$v_{avg} = \frac{\int_0^\infty v^2 \cdot F(t) \, dt}{I} \tag{61}$$

$$E_{avg} = \frac{\int_0^\infty \frac{1}{2} mv^3 \cdot F(t) \, dt}{I} \tag{62}$$

where v = L/t. These values are calculated by numerical integration. Note that the integrals are performed with respect to time, while the functions to be integrated are expressed in terms of velocity. From the perspective of numerical integration this substitution is transparent. That is, at each time point t, the distribution can be calculated using F(t) or F(L/t) and the resulting distribution is the same either way, and the integrals are also the same. Due to the nature of the Levenberg-Marquardt fitting method, the functional form F(t) turns out to be quite difficult for the fitting algorithm to deal with. While it is unclear as to what exactly causes the difficulty, one problem may be that small changes in the flow time tend to produce disproportionately large changes in F(t). The fitting algorithm attempts to find a local minimum in χ^2 by finding that area in phase space where the gradient of χ^2 with respect to the fit parameters goes to zero, so it may be that the gradient of χ^2 with respect to the flow time varies too quickly for the local minimum search to converge properly. However, the equivalent function form F(L/t) works well:

$$F\left(\frac{L}{t}\right) = A\frac{\left(\frac{L}{t}\right)^4}{L}\exp\left[-\left(\frac{m}{2kT}\right)\left(\left(\frac{L}{t}\right)-\left(\frac{L}{t_f}\right)\right)^2\right] = A\frac{v^4}{L}\exp\left[-\left(\frac{m}{2kT}\right)(v-v_f)^2\right] \quad (63)$$

It will be shown in section III.A. below that this alternate formulation does not affect the propagated error.

III.A. Propagated error in the flux

The error in the flux is due to the propagated error from the three fit parameters, A, v_f, and T, and the error in the path length, L. The mass is assumed to be exact. The three fit parameters will in general have non-zero covariances, while the error in the path length is independent. Therefore,

$$\sigma_I = \sqrt{\left(\sigma_A\frac{\partial I}{\partial A}\right)^2 + \left(\sigma_{v_f}\frac{\partial I}{\partial v_f}\right)^2 + \left(\sigma_T\frac{\partial I}{\partial T}\right)^2 + 2\sigma_{Av_f}\frac{\partial I}{\partial A}\frac{\partial I}{\partial v_f} + 2\sigma_{AT}\frac{\partial I}{\partial A}\frac{\partial I}{\partial T} + 2\sigma_{v_fT}\frac{\partial I}{\partial v_f}\frac{\partial I}{\partial T} + \left(\sigma_L\frac{\partial I}{\partial L}\right)^2} \quad (64)$$

where the variances and co-variances of the fit parameters are given by the fitting algorithm, and the uncertainty in the path length is given by the measured length of the ionizer region. The derivatives in the above equation must be calculated from the functional form of the flux given by Eq. 60, and the functional form of F(t) given by Eq. 59. To calculate those derivatives, it will be useful to have the partial derivatives of F with respect to each of the three fit parameters and L. For the fit parameters A, v_f and T it turns out to be easier to work with F(L/t).

$$\frac{\partial F(L/t)}{\partial A} = \frac{v^4}{L} \exp\left[-\left(\frac{m}{2kT}\right)(v - v_f)^2\right] = \frac{1}{A} \cdot F(L/t)$$ (65)

$$\frac{\partial F(L/t)}{\partial v_f} = A \frac{v^4}{L} \frac{\partial}{\partial v_f} \exp\left[-\left(\frac{m}{2kT}\right)(v - v_f)^2\right] = \left(\frac{m}{kT}(v - v_f)\right) \cdot F(L/t)$$ (66)

$$\frac{\partial F(L/t)}{\partial T} = A \frac{v^4}{L} \frac{\partial}{\partial T} \exp\left[-\left(\frac{m}{2kT}\right)(v - v_f)^2\right] = \left(\frac{m}{2kT^2}(v - v_f)^2\right) \cdot F(L/t)$$ (67)

However, for the propagated error in the path length it is critical to work with F(t), not F(L/t), since each L/t contains a hidden factor of L. After the derivative with respect to L is taken the results are transformed back to F(L/t).

$$\frac{\partial F(t)}{\partial L} = \frac{\partial}{\partial L} A \frac{L^3}{t^4} \exp\left[-\left(\frac{mL^2}{2kT}\right)\left(\frac{1}{t} - \frac{1}{t_f}\right)^2\right] = \frac{A}{t^4}\left(3L^2 - \frac{mL^4}{kT}\left(\frac{1}{t} - \frac{1}{t_f}\right)^2\right) \exp\left[-\left(\frac{mL^2}{2kT}\right)\left(\frac{1}{t} - \frac{1}{t_f}\right)^2\right]$$

$$= \left(\frac{3}{L} - \frac{m}{kTL}\left(\left(\frac{L}{t}\right) - \left(\frac{L}{t_f}\right)\right)^2\right) \cdot F(L/t)$$ (68)

With the above formulas, the derivative of the flux with respect to the three fit parameters and L is calculated from the functional form of the flux given by Eq. 60:

$$I = \int_0^\infty v \cdot F \, dt$$

$$\frac{\partial I}{\partial A} = \int_0^\infty v \cdot \frac{\partial F}{\partial A} \, dt = \int_0^\infty \frac{v}{A} \cdot F \, dt$$ (69)

$$\frac{\partial I}{\partial v_f} = \int_0^\infty v \cdot \frac{\partial F}{\partial v_f} \, dt = \int_0^\infty v \cdot \left(\frac{m}{kT} (v - v_f) \right) \cdot F \, dt \tag{70}$$

$$\frac{\partial I}{\partial T} = \int_0^\infty v \cdot \frac{\partial F}{\partial T} \, dt = \int_0^\infty v \cdot \left(\frac{m}{2kT^2} (v - v_f)^2 \right) \cdot F \, dt \tag{71}$$

$$\frac{\partial I}{\partial L} = \int_0^\infty \frac{\partial}{\partial L} \left(\frac{L}{t} \cdot F \right) dt = \int_0^\infty \left(\frac{F}{t} + \frac{L}{t} \frac{\partial F}{\partial L} \right) dt = \int_0^\infty \left(\frac{1}{t} + \frac{L}{t} \left(\frac{3}{L} - \frac{m}{kTL} (v - v_f)^2 \right) \right) \cdot F \, dt$$

$$= \int_0^\infty \frac{L}{t} \left(\frac{4}{L} - \frac{m}{kTL} \left(\frac{L}{t} - \frac{L}{t_f} \right)^2 \right) \cdot F \, dt \tag{72}$$

These derivatives are then used in Eq. 64, along with the variances and co-variances of the fit parameters given by the fitting algorithm, and the uncertainty in the path length given by the measured length of the ionizer region to give the propagated error in the flux.

To show that the use of v_f instead of t_f does not affect the error propagation, the error propagation of the flux with respect to t_f is shown below.

$$\frac{\partial I}{\partial t_f} = A \int_0^\infty L^4 \cdot t^{-5} \frac{\partial}{\partial t_f} \exp\left[-\left(\frac{mL^2}{2kT} \right) \cdot \left(\frac{1}{t} - \frac{1}{t_f} \right)^2 \right] dt \tag{73}$$

$$= A \int_0^\infty L^4 \cdot t^{-5} \left(\frac{mL^2}{kT} \left(\frac{1}{t} - \frac{1}{t_f} \right) \right) \left(-\frac{1}{t_f^2} \right) \exp\left[-\left(\frac{m}{2kT} \right) \cdot \left(\frac{L}{t} - \frac{L}{t_f} \right)^2 \right] dt$$

$$= \int_0^\infty \frac{v}{L} \cdot \left(\frac{m}{kT} (v - v_f) \right) \cdot v_f^2 \cdot F\left(\frac{L}{t} \right) dt \tag{74}$$

The standard deviation σ_{t_f} can be related to σ_{v_f}:

$$\sigma_{t_f} = \left| \frac{dt_f}{dv_f} \right| \cdot \sigma_{v_f} = \frac{L}{v_f^2} \cdot \sigma_{v_f} \tag{75}$$

and therefore,

$$\sigma_{t_f} \frac{\partial I}{\partial t_f} = \frac{L}{v_f^2} \sigma_{v_f} \int_0^\infty \frac{v}{L} \cdot \left(\frac{m}{kT} (v - v_f) \right) \cdot v_f^2 \cdot F\left(\frac{L}{t} \right) dt = \sigma_{v_f} \int_0^\infty v \cdot \left(\frac{m}{kT} (v - v_f) \right) \cdot F\left(\frac{L}{t} \right) dt = \sigma_{v_f} \frac{\partial I}{\partial v_f} \tag{76}$$

showing that the two approaches are in fact equivalent.

III.B. Propagated error in the average velocity

Similar to the flux equations shown above, the propagation of error in the average velocity is given by:

$$\sigma_{v_{avg}} = \sqrt{\left(\sigma_{v_f}\frac{\partial v_{avg}}{\partial v_f}\right)^2 + \left(\sigma_T\frac{\partial v_{avg}}{\partial T}\right)^2 + 2\sigma_{v_f T}\frac{\partial v_{avg}}{\partial v_f}\frac{\partial v_{avg}}{\partial T} + \left(\sigma_L\frac{\partial v_{avg}}{\partial L}\right)^2} \quad (77)$$

Note that there is no propagated error due to the normalization constant A. The average energy does not depend on A since it cancels out, as can be seen by substituting the full distribution into the integral.

$$v_{avg} = \frac{\int\limits_0^\infty v^2\cdot F(t)\,dt}{I} = \frac{\int\limits_0^\infty v^2\cdot F(t)\,dt}{\int\limits_0^\infty v\cdot F(t)\,dt} = \frac{\int\limits_0^\infty \left(\frac{L}{t}\right)^2\cdot\frac{L^3}{t^4}\exp\left[-\left(\frac{m}{2kT}\right)\left(\frac{L}{t}-\frac{L}{t_f}\right)^2\right]dt}{\int\limits_0^\infty \frac{L}{t}\cdot\frac{L^3}{t^4}\exp\left[-\left(\frac{m}{2kT}\right)\left(\frac{L}{t}-\frac{L}{t_f}\right)^2\right]dt} \quad (78)$$

To derive the propagated error it will be useful to use the quotient rule:

$$\frac{\partial}{\partial x}\left[\frac{f}{g}\right] = \frac{g\frac{\partial f}{\partial x} - f\frac{\partial g}{\partial x}}{g^2} \quad (79)$$

Therefore,

$$\frac{\partial v_{avg}}{\partial v_f} = \frac{I\left(\int\limits_0^\infty v^2\cdot\frac{\partial F}{\partial v_f}\,dt\right) - \left(\int\limits_0^\infty v^2\cdot F\,dt\right)\frac{\partial I}{\partial v_f}}{I^2} = \frac{1}{I}\left(\int\limits_0^\infty v^2\cdot\left(\frac{m}{kT}(v-v_f)\right)\cdot F\,dt - v_{avg}\frac{\partial I}{\partial v_f}\right) \quad (80)$$

$$\frac{\partial v_{avg}}{\partial T} = \frac{I\left(\int\limits_0^\infty v^2\cdot\frac{\partial F}{\partial T}\,dt\right) - \left(\int\limits_0^\infty v^2\cdot F\,dt\right)\frac{\partial I}{\partial T}}{I^2} = \frac{1}{I}\left(\int\limits_0^\infty v^2\cdot\left(\frac{m}{2kT^2}(v-v_f)^2\right)\cdot F\,dt - v_{avg}\frac{\partial I}{\partial T}\right) \quad (81)$$

$$\frac{\partial v_{avg}}{\partial L} = \frac{I\left(\int_0^\infty \frac{\partial}{\partial L}\left(\frac{L^2}{t^2}\cdot F\right)dt\right) - \left(\int_0^\infty v^2 \cdot F\, dt\right)\frac{\partial I}{\partial L}}{I^2} = \frac{1}{I}\left(\int_0^\infty v^2\left(\frac{5}{L} - \frac{m}{kTL}(v - v_f)^2\right)\cdot F\, dt - v_{avg}\frac{\partial I}{\partial L}\right) \qquad (82)$$

III.C. Propagated error in the average energy

Similar to the average velocity equations shown above, the propagation of error in the average energy is given by:

$$\sigma_{E_{avg}} = \sqrt{\left(\sigma_{v_f}\frac{\partial E_{avg}}{\partial v_f}\right)^2 + \left(\sigma_T\frac{\partial E_{avg}}{\partial T}\right)^2 + 2\sigma_{v_f T}\frac{\partial E_{avg}}{\partial v_f}\frac{\partial E_{avg}}{\partial T} + \left(\sigma_L\frac{\partial E_{avg}}{\partial L}\right)^2} \qquad (83)$$

Note that again there is no propagated error due to the normalization constant A.

$$E_{avg} = \frac{\int_0^\infty \frac{1}{2}mv^3 \cdot F\, dt}{I}$$

Using the quotient rule:

$$\frac{\partial E_{avg}}{\partial v_f} = \frac{I\left(\int_0^\infty \frac{1}{2}mv^3 \cdot \frac{\partial F}{\partial v_f}dt\right) - \left(\int_0^\infty \frac{1}{2}mv^3 \cdot F\, dt\right)\frac{\partial I}{\partial v_f}}{I^2} = \frac{1}{I}\left(\int_0^\infty \frac{1}{2}mv^3 \cdot \left(\frac{m}{kT}(v - v_f)\right)\cdot F\, dt - E_{avg}\frac{\partial I}{\partial v_f}\right) \qquad (84)$$

$$\frac{\partial E_{avg}}{\partial T} = \frac{I\left(\int_0^\infty \frac{1}{2}mv^3 \cdot \frac{\partial F}{\partial T}dt\right) - \left(\int_0^\infty \frac{1}{2}mv^3 \cdot F\, dt\right)\frac{\partial I}{\partial T}}{I^2} = \frac{1}{I}\left(\int_0^\infty \frac{1}{2}mv^3 \cdot \left(\frac{m}{2kT^2}(v - v_f)^2\right)\cdot F\, dt - E_{avg}\frac{\partial I}{\partial T}\right) \qquad (85)$$

$$\frac{\partial E_{avg}}{\partial L} = \frac{I\left(\int_0^\infty \frac{\partial}{\partial L}\left(\frac{1}{2}m\frac{L^3}{t^3}\cdot F\right)dt\right) - \left(\int_0^\infty \frac{1}{2}mv^3 \cdot F\, dt\right)\frac{\partial I}{\partial L}}{I^2} = \frac{1}{I}\left(\int_0^\infty \frac{1}{2}mv^3\left(\frac{6}{L} - \frac{m}{kTL}(v - v_f)^2\right)\cdot F\, dt - E_{avg}\frac{\partial I}{\partial L}\right) \qquad (86)$$

REFERENCES

[1] J.R. Taylor, *An Introduction to Error Analysis* (University Science Books, 1982).
[2] W.H. Press, S.A. Teukolsky, W.T. Vetterling and B.P. Flannery, *Numerical Recipes in C: The Art of Scientific Computing*, 2nd ed., (Cambridge University Press, Cambridge, 1992), Chapter 15, *Modeling of Data* and references contained therein.
[3] IGOR Pro Version 3.16 (WaveMetrics, Inc., Lake Oswego, OR, 1998).

[4] B.R. Martin, *Statistics for Physicists* (Academic Press, New York, 1971).

[5] M.R. Tate, D. Gosalvez-Blanco, D.P. Pullman, A.A. Tsekouras, Y.L. Li, J.J. Yang, K.B. Laughlin, S.C. Eckman, M.F. Bertino, and S.T. Ceyer, *J. Chem. Phys.* **111**, 3679 (1999).

[6] D. Gosalvez-Blanco, Massachusetts Institute of Technology, Ph.D. thesis, 1997.

Appendix C: Data Sources

CHAPTER 1
See M.R. Tate, Ph. D. Thesis, Massachusetts Institute of Technology (1999), Appendix E.

CHAPTER 2
Figure 1
Neat XeF_2, θ_i=35°, θ_d=0°, T_s=250 K:
$\quad$ TD2101-9.202

Figure 2
Neat F_2, θ_i=35°, θ_d=0°, T_s=250 K:
$\quad$ TD1101-30.D01
θ_i=35°, θ_d=0°, T_s=250 K, Neat XeF_2:
$\quad$ TD1201-20.D01

Figure 3
Neat XeF_2, θ_i=20°, θ_d=15°, T_s=250 K.
Average of four experiments:
$\quad$ ST0904.401
$\quad$ ST0908.401
$\quad$ ST0911.401
$\quad$ ST0914.401

Figure 4
See Figure 2.

Figure 5
θ_i=40°, θ_d=15-55°, T_s=250 K, 75% He/Ar.
$\quad$ HE1202.301
$\quad$ HE1203.301
$\quad$ HE1702.301

Figure 5
Neat F_2, θ_i=20°; 75% He/Ar, θ_i=40°; θ_d=40°, T_s=250 K:
Average of two experiments:
$\quad$ ST1801-2.301
Neat XeF_2, θ_i=20°; 75% He/Ar, θ_i=40°; θ_d=40°, T_s=250 K:
Average of five experiments:
$\quad$ ST1301-5.301

Figure 6
Neat XeF_2, θ_i=20°; 75% He/Ar, θ_i=40°; θ_d=21.5°, T_s=250 K:
Average of two experiments:
$\quad$ ST1401-2.301
Neat XeF_2, θ_i=20°; 75% He/Ar, θ_i=40°; θ_d=51.25°, T_s=250 K:
Average of two experiments:
$\quad$ ST1404-5.301

Figure 10
Neat XeF_2:
      TF0805.401
Neat F_2:
      TF0807.401

Figure 11
Neat XeF_2:
      TF1709.D01
Neat F_2:
      TF1410.D01

Figure 12
75% He/Ar:
      TF0401.501

Figure 13
See Figure 5.

Figure 14
50% He/Ar, $\theta_i=30°$; $\theta_d=25\text{-}60°$, $T_s=250$ K:
      HE1401-2.N00

CHAPTER 3
Figure 4
Neat XeF_2:
      TF1702.D01

Figure 5
Neat XeF_2:
      MS1610.399
      MS1508.102

Figure 6
Neat XeF_2:
      MS0701-2.801

Figure 10
Neat Ar:
Average of 10 experiments:
      ST1201-10.402

Figure 11
Neat XeF_2, $\theta_i=35°$, $\theta_d=0°$, $T_s=150$ K:
      TD2901-8.302

Figure 12
Neat XeF_2, $\theta_i=20°$, $\theta_d=0°$, $T_s=150$ K:
      TD0101-15.N01

Figure 13
See Figure 12.

Figure 14
Neat XeF_2, $\theta_i=20°$, $\theta_d=15°$, $T_s=150$ K:
Average of 4 experiments:
      ST1702.901
      ST1801.901
      ST1901.901
      ST2001.901

Figure 15
Neat XeF_2, $\theta_i=20°$; 75% He/Ar, $\theta_i=40°$; $\theta_d=40°$, $T_s=150$ K:
      ST2502.302

Figure 16
Neat XeF_2, $\theta_i=20°$ $\theta_d=15°$, $T_s=150$ K:
Average of 40 experiments taken between 9/25/01 – 10/3/01

Figure 17
Neat XeF_2, $\theta_i=20°$ $\theta_d=30°$, $T_s=150$ K:
Average of 81 experiments taken between 8/8/01 – 8/16/01

Figure 18
Neat XeF_2, $\theta_i=20°$ $\theta_d=60°$, $T_s=150$ K:
Average of 40 experiments taken between 9/24/01 – 9/25/01

Figures 19-21
See Figures 16-18.

Figure 22
Neat XeF_2, $\theta_i=20°$ $\theta_d=15°$, $T_s=150$ K:
Average of 40 experiments taken between 9/17/01 – 9/18/01

Figure 23
See Figure 22.

Figure 24
Neat XeF_2, $\theta_i=20°$ $\theta_d=30°$, $T_s=150$ K:
Average of 81 experiments taken between 8/9/01 – 8/17/01

Figure 25
Neat XeF_2, $\theta_i=20°$ $\theta_d=60°$, $T_s=150$ K:
Average of 40 experiments taken between 9/13/01 – 9/16/01

Figures 26-29
See Figures 23-25.

Figure 30
Neat XeF_2, $\theta_i=20°$ $\theta_d=15°$, $T_s=150$ K:
Average of 40 experiments taken between 9/19/01 – 9/20/01

Figure 31
See Figure 30.

Figure 32
Neat XeF_2, $\theta_i=20°$ $\theta_d=30°$, $T_s=150$ K:
Average of 81 experiments taken between 8/20/01 – 10/3/01

Figure 33
Neat XeF_2, $\theta_i=20°$ $\theta_d=60°$, $T_s=150$ K:
Average of 40 experiments taken between 9/20/01 – 9/21/01

Figures 34-37
See Figures 31-33.

Figure 38
Neat XeF_2, $\theta_i=20°$ $\theta_d=15°$, $T_s=150$ K:
Average of 80 experiments taken between 8/23/01 – 9/7/01

Figure 39
See Figure 30.

Figure 40
Neat XeF_2, $\theta_i=20°$ $\theta_d=30°$, $T_s=150$ K:
Average of 160 experiments taken between 7/18/01 – 10/16/01

Figure 41
Neat XeF_2, $\theta_i=20°$ $\theta_d=60°$, $T_s=150$ K:
Average of 160 experiments taken between 9/9/01 – 10/17/01

Figures 42-47
See Figures 39-41.

Figures 51-54
See Figures 31-33.

Figures 55-73
See Figures 39-41.

Appendix D: Curriculum Vitae

Judson Robert Holt

Education

Massachusetts Institute of Technology, Cambridge MA
Ph.D. in Physical Chemistry, May, 2002. Thesis title: "The Interaction of Xenon Difluoride with Si(100)" Thesis advisor: Professor S. T. Ceyer. Research is focused on understanding the dynamics of the reaction of XeF_2 with Si(100), a reaction with implications for industrial semiconductor processing.
GPA: 5.0/5.0

Rice University, Houston TX
Bachelor of Arts in Physical Chemistry, May, 1996.
GPA: 3.7/4.0

Research Experience

Massachusetts Institute of Technology, Cambridge MA
Research with Professor S.T. Ceyer in experimental physical chemistry.
Gas-surface scattering is used to probe the dynamics of the reaction of XeF_2 with silicon. Experience in apparatus design including technical drawing using MiniCAD and AutoCAD, and machine shop experience constructing various custom components. Experience with the use and maintenance of ultrahigh vacuum systems, molecular beam techniques, quadrupole mass spectrometry, time-of-flight velocity measurement, thermal desorption spectroscopy, helium diffraction and Auger electron spectroscopy. Experience with many different computer operating systems and software packages, including UNIX, Windows and Macintosh operating systems; Matlab, Mathematica, Igor Pro, LabVIEW, Word and Excel software packages. Teaching responsibilities included Teaching Assistant (TA) for advanced undergraduate Physical Chemistry and Head TA for undergraduate Thermodynamics. As Head TA my duties included coordinating a team of ten TAs, organizing exams and grading sessions, and acting as liaison to the professor, in addition to a regular teaching schedule.

Rice University, Houston TX
Research with Professor P.R. Brooks in experimental physical chemistry.
Investigated aspects of gas-phase reactions of oriented molecules. Characterized the angular momentum quantum state distribution in a beam of oriented molecules using molecular beam electric resonance spectroscopy. Teaching responsibilities included Teaching Assistant for undergraduate Introductory Chemistry and Physical Chemistry.

Publications

J.R. Holt, R.C. Hefty, M.R. Tate, and S.T. Ceyer, "Comparison of the Interactions of XeF_2 and F_2 with Si(100)2x1"
To be published.

Poster Presentation, "Mechanism for and Site of the Dissociative Chemisorption of Xenon Difluoride on Si(100)2x1 Below 1 ML Coverage"; J.R. Holt, R.C.

Hefty, M.R. Tate, S.T. Ceyer. Presented at the American Vacuum Society 47th International Symposium (2000).

Poster Presentation, "The Reactive Scattering of Xenon Difluoride from Si(100)"; J.R. Holt, R.C. Hefty, M.R. Tate, S.T. Ceyer. Presented at the Chemistry of Electronic Materials Gordon Conference (1999).

S.D. Wiediger, P.W. Harland, J.R. Holt, and P.R. Brooks, "Characterization of Oriented Molecule Beams by Radio Frequency Spectroscopy" J. Phys. Chem. A **102**, pg. 1112 (1998)

Awards   Awarded a $1200 research grant for an independent research proposal submitted to the Rice Undergraduate Scholars Program.
Awarded the Zevi and Bertha Salsburg Memorial Award for outstanding scholarship in Chemistry (1996).
Symposium talk, Rice Undergraduate Research Symposium (1996), Awarded First Place.